



**HAL**  
open science

# Chain conformation of cellulose, a sustainable biopolymer, and its derivatives in ionic liquid studied by small-angle neutron and X-ray scattering

Qiang Zhang

► **To cite this version:**

Qiang Zhang. Chain conformation of cellulose, a sustainable biopolymer, and its derivatives in ionic liquid studied by small-angle neutron and X-ray scattering. *Polymers*. Université Paris-Saclay, 2024. English. NNT : 2024UPASF075 . tel-04926220

**HAL Id: tel-04926220**

**<https://theses.hal.science/tel-04926220v1>**

Submitted on 3 Feb 2025

**HAL** is a multi-disciplinary open access archive for the deposit and dissemination of scientific research documents, whether they are published or not. The documents may come from teaching and research institutions in France or abroad, or from public or private research centers.

L'archive ouverte pluridisciplinaire **HAL**, est destinée au dépôt et à la diffusion de documents scientifiques de niveau recherche, publiés ou non, émanant des établissements d'enseignement et de recherche français ou étrangers, des laboratoires publics ou privés.

Chain conformation of cellulose, a sustainable biopolymer, and its derivatives in ionic liquid studied by small-angle neutron and X-ray scattering

*Conformation d'une chaîne de cellulose, un biopolymère durable, et de ses dérivés dans un liquide ionique observée par diffusion aux Petits Angles (neutron, RX)*

**Thèse de doctorat de l'université Paris-Saclay**

École doctorale n° 571

Sciences Chimiques : Molécules, Matériaux, Instrumentation et Biosystèmes (2MIB)

Spécialité de doctorat : Chimie

Graduate School : Chimie. Référent : Faculté des sciences d'Orsay

Thèse préparée dans l'unité de recherche **LLB (Université Paris-Saclay, CEA, CNRS)**, sous la direction de **Patrick JUDEINSTEIN**, Directeur de recherche, et le co-encadrement de **François BOUÉ**, Directeur de recherche émérite

**Thèse soutenue à Paris-Saclay, le 9 Décembre 2024, par**

**Qiang ZHANG**

**Composition du Jury**

Membres du jury avec voix délibérative

**Philippe ROGER**

Professeur des universités, Université Paris-Saclay

Président

**Ruigang LIU**

Professeur, Chinese Academy of Science

Rapporteur & Examineur

**Bruno JEAN**

Directeur de recherche, Université de Grenoble

Rapporteur & Examineur

**Benoît DUCHEMIN**

Ingénieur de recherche, Université du Havre

Examineur

**Isabelle CAPRON**

Directrice de recherche, Université de Nantes

Examinatrice

**Titre :** Conformation d'une chaîne de cellulose, un biopolymère durable, et de ses dérivés dans un liquide ionique observée par diffusion aux Petits Angles (neutron, RX)

**Mots clés :** Biopolymères renouvelables, Cellulose, Liquide ionique, Conformation d'une chaîne polymère, Diffusion de rayons X aux Petits Angles, Diffusion de neutrons aux Petits Angles

**Résumé :** La cellulose, un biopolymère renouvelable, peut remplacer les matériaux non biodégradables dans les applications industrielles. Elle est d'abord dissoute, puis transformée (par exemple en fibres) et enfin « régénérée » (recristallisation par ajout d'eau). Cependant, la dissolution de la structure cristalline très stable nécessite des solvants agressifs et polluants, au contraire des liquides ioniques (IL). Cette thèse étudie le processus de dissolution et l'état dissous pour deux liquides ioniques sélectionnés comme solvants efficaces. Nous étudions la structure et la conformation des chaînes de cellulose par la diffusion des rayons X et des neutrons. Les signaux sont très faibles ( $< 1 \text{ cm}^{-1}$ ), en raison de la forme fine des bâtonnets, du faible contraste et de la difficulté à mesurer en raison de la grande sensibilité à l'eau.

Le chapitre 1 résume l'état de l'art sur les solutions dans des solvants industriels et dans les liquides ioniques, et sur les études de diffusion, de la lumière, des rayons X et des neutrons, montrant des situations diverses.

Le chapitre 2 présente la préparation des échantillons et les techniques.

Le chapitre 3 présente des études de Diffusion des rayons X aux Petits Angles (DXPA), réalisées à l'aide de spectromètres sur synchrotron, à flux élevé et à faisceau étroit. Nous avons d'abord étudié la cellulose microcristalline (MCC, degré de polymérisation  $DP = 200$  unités) dans deux IL à base de butyl-méthyl-imidazolium : acétate (BmimAc) ou chlorure (BmimCl). Différents régimes sont attendus à partir d'études rhéologiques.

- Dans le régime dilué (0,005 - 0,02 g/g). La diffusion est ajustée au facteur de forme  $P(q)$  d'une chaîne en forme de bâtonnet, entourée d'une coquille de

densité différente de celle du solvant, avec éventuellement une grande longueur de persistance ( $> 7 \text{ nm}$ ).

- Pour des concentrations plus importantes, dans des cas encore bien dissous, un facteur de structure révèle des répulsions inter-chaînes faibles, sans alignement fort.

- A des concentrations plus élevées, la diffusion suggère une séparation de phase liquide-liquide.

- Enfin, aux concentrations les plus élevées, des cristaux non dissous sont détectés à grand  $q$  (WAXS), un grand avantage de notre technique.

La coexistence avec les cristaux a été étudiée pendant le gonflement de films ou de fibres de cristaux de nanocellulose, par balayage en faisceau étroit d'un gradient de concentration.

L'effet d'un faible pourcentage d'eau ajoutée a été testé, les IL bons solvants étant assez hygroscopiques. Au-delà de quelques pour cent d'eau, une diffusion beaucoup plus forte suggère de fortes fluctuations de concentration, ou une structure biphasique, utile pour comprendre les premières étapes de la « régénération » (recristallisation) par ajout d'eau.

Les courbes de diffusion de cellulose d'autre origine et de poids moléculaire également faible (rayonne, nanocristaux - CNC) sont similaires à celles du MCC. Celle de la cellulose bactérienne montre aussi une identité complète à l'échelle locale, mais avec des agrégats indépendants visibles aux moyens  $q$ .

Le chapitre 4 présente les mesures:

- de Diffusion des Neutrons aux Petits Angles (DNPA) aux faibles concentrations, le profil de DNPA est celui de la DXPA, ce qui permet une évaluation complémentaire des densités de longueur de diffusion. Par extrapolation à la fraction zéro de cellulose deutérée, nous avons tenté d'extraire la fonction intra-chaîne  $S_1(q) \sim P(q)$ , et la fonction inter-chaîne  $S_2(q)$ . Des difficultés sont apparues à faible  $q$  en raison de la forte remontée de la cellulose deutérée bactérienne. A  $q$  élevé il y a accord avec la DXPA.

- de Diffusion de Neutrons aux Grands Angles (DNGA) suit les corrélations à courte échelle. Nous avons effectué différentes deutériations : soit le cation Bmim, soit l'anion Ac, soit les deux. Par comparaison nous discutons de l'absorption possible des anions acétate sur les chaînes.

**Title :** Chain conformation of cellulose, a sustainable biopolymer, and its derivatives in ionic liquid studied by small-angle neutron and X-ray scattering

**Keywords :** Sustainable biopolymers, Cellulose, Ionic liquid, Polymer chain conformation, Small angle X rays scattering, Small angle neutron scattering

**Abstract :** Cellulose, a renewable bio-polymer, can replace non-biodegradable materials in various technological applications. Industrially, it is first dissolved, then processed (e.g. by spinning), and finally "regenerated" (recrystallization by adding water). However, dissolution from the very stable crystal structure requires harsh, pollutant solvents for individual chains to stay in solution. Ionic liquids (ILs) have emerged as non-polluting effective solvents. This thesis aims at the dissolution process and dissolved state checking how the two selected ILs are successful solvents, which is controversial. Our approach is to study structure and conformation of cellulose chains by X-Ray and neutron scattering, which are very weak ( $< 1 \text{ cm}^{-1}$ ), due to the small volume of the thin rod, the low contrast and difficult to measure due to high sensitivity to water.

Chapter 1 summarizes the state of the art on solutions of cellulose in different widely-used solvents, in ionic liquids, and in scattering studies, light, X-rays and neutrons, showing various states of dispersion.

Chapter 2 presents the preparation of the samples and the techniques.

Chapter 3 reports Small Angle X rays Scattering (SAXS) studies, using high flux and narrow beam synchrotron spectrometers. We first monitored MicroCrystalline Cellulose (MCC, Degree of Polymerisation  $DP \approx 200$  units) in two Butyl-methylimidazolium based ILs: acetate (BmimAc), or Chloride (BmimCl). Different regimes are assumed from rheological studies.

-In the dilute regime (0.005 – 0.02 g/g). Scattering is fitted to the form factor  $P(q)$  of a rod-like chain, surrounded by a shell of density different from the

one of the solvent, with possibly a large persistence length ( $> 7 \text{ nm}$ ).

-For larger concentrations, in yet well dissolved cases, a structure factor unveils soft interchain repulsions, without strong alignment.

-At higher concentration, the scattering suggests a liquid-liquid phase separation

-Finally, at the highest concentrations, non-dissolved crystals are detected at large  $q$  (WAXS), a great advantage of our technique.

The coexistence with crystals was also investigated during swelling in nanocellulose crystals films or fibers, through narrow beam scanning of a concentration gradient.

The effect of a small percentage of added water was tested, the IL good solvents for cellulose being quite hygroscopic. Above a few per cent of water, much stronger scattering suggests strong concentration fluctuations, or biphasic structure, useful to understand the first stages of the "regeneration" (recrystallization) step performed by adding water, to obtain the final products.

Cellulose of other origin and similarly small molecular weights (in rayon, and CNC), superimpose their scattering on the one of MCC. Bacterial cellulose scattering superposes only at large  $q$  (hence a complete identity at local scale), but shows an additional strong low  $q$  upturn, due to independent aggregates. This opens the way to neutron scattering experiments using deuterated cellulose, which is available only in a bacterial form.

Chapter 4 reports the measurements of:

-Small Angle Neutron Scattering (SANS) shows for low concentrations a profile similar to SAXS, allowing a complementary evaluation of the Scattering Length Density of cellulose. Using extrapolation at Zero Deuteriated Cellulose Fraction, we attempted the extraction of the intrachain function  $S_1(q) \sim P(q)$ , the interchain function  $S_2(q)$ . Difficulties appeared at low  $q$  due to the strong upturn, while high  $q$  showed agreement with the SAXS measurement of the form factor below  $c^*$ .

-Wide Angle Neutron Scattering (WANS) was used to track the correlations at short scale. Different solvents were used in which either the Bmim cation, or the anion Ac, or both, were deuteriated using our own synthesis processes. Comparisons enable us to discuss about possible absorption of the acetate anions on the cellulose chains.

# Chain conformation of cellulose, a sustainable biopolymer, and its derivatives in ionic liquid studied by small-angle neutron and X-ray scattering

*Conformation d'une chaîne de cellulose, un biopolymère durable, et de ses dérivés dans un liquide ionique observée par diffusion aux Petits Angles (neutron, RX)*

## Thèse de doctorat de l'université Paris-Saclay

École doctorale n° 571

Sciences Chimiques : Molécules, Matériaux, Instrumentation et Biosystèmes (2MIB)

Spécialité de doctorat : Chimie

Graduate School : Chimie. Référent : Faculté des sciences d'Orsay

Thèse préparée dans l'unité de recherche **LLB (Université Paris-Saclay, CEA, CNRS)**, sous la direction de **Patrick JUDEINSTEIN**, Directeur de recherche, et le co-encadrement de **François BOUÉ**, Directeur de recherche émérite

Thèse soutenue à Paris-Saclay, le 9 Décembre 2024, par

**Qiang ZHANG**

## Composition du Jury

Membres du jury avec voix délibérative

**Philippe ROGER**

Professeur des universités, Université Paris-Saclay

Président

**Ruigang LIU**

Professeur, Chinese Academy of Science

Rapporteur & Examineur

**Bruno JEAN**

Directeur de recherche, Université de Grenoble

Rapporteur & Examineur

**Benoît DUCHEMIN**

Ingénieur de recherche, Université du Havre

Examineur

**Isabelle CAPRON**

Directrice de recherche, Université de Nantes

Examinatrice

**Yoshiharu NISHIYAMA**

Directeur de recherche, Université de Grenoble

Invité

## Acknowledgements

First and foremost, I want to thank my supervisors Patrick Judeinstein and François Boué, who gave me continuous mentorship, through their knowledge and plentiful experience. Thank both of you for your engagement, professional and support, and patience throughout my PhD studies. Patrick, thank you for all the kindness, friendly encouragement and the scientific insights and thinking during my studies. François, thank you for all the extensive scientific discussions, the help for applying the beamline and the company of experiments and all the helps in both academic and personal matters during the PhD journey. I am also thankful to the MOPGA-CHINE (Campus France) and Laboratoire Léon Brillouin for the financial support during the whole duration of my thesis. Also, thanks to LLB director Arnaud Desmedt's constant support.

I would like to thank all the people who contributed in some way to the work described in this thesis, particularly: Doru Constantin (Institut Charles Sadron, Strasbourg), for the discussion on the structure factor and all the details for the data analysis. Yoshiharu Nishiyama (CERMAV, Grenoble), for all the critical and innovative scientific discussion, his rich presence and shrewd eye during experiments in ILL and ESRF, and the supporting of the deuterated bacterial cellulose by you along with Howard Wang from UMD (also thanks to Christopher J. Garvey, TUM for the ANSTO deuterated bacterial cellulose). Thanks to Benoît Duchemin (LOMC, Le Havre) for all the discussion of the crystal structures and the nanocrystal cellulose films. Also, thanks to Jun Zhang and Guangjie Song (ICCAS, Beijing) for the discussion on the thesis topic and helps with density measurements.

Furthermore, I thank all the people who helped me scientifically along the research path. Thanks to MMB group to give me access at SWAXS laboratory, to the XEUSS X-ray spectrometer. In particular: Annie Brûlet and Alexis Chennevière, for helping with SAXS experiments and data treatment. Fabrice Cousin and Marion Grzelka, for helping for the SANS studies. I thank the different facilities for beam time and support. Especially, I thank Javier Perez's for his great help in synchrotron (most measurements are in SWING, SOLEIL) and Evelyne Lutton's company during the synchrotron experiments; Arnaud Helary for the professional technical help with the SAXS sample environment; Lionel Porcar, Anne Martel and Apostolos Vagias, for their help with the SANS measurements (D22 of ILL) and data treatments. Bruno Demé, for his close and careful assistance during the WANS measurements (D16 of ILL). Isabelle Morfin, Theyencheri Narayanan and Gouranga Manna, for their help on D2AM and ID02 of ESRF; Sylvio Haas' help in the beamline of P62 (DESY, Hamburg). Also thanks to the people who help me in the other characterizations: Daniel Dudzinski, for his expertise along the rheology experiments, and



Oriana Osta's help for her guidance of the FTIR measurements; former PhD Maja Napieraj, for having time to answer my questions at the beginning of my PhD. And former PhD Tiago Outerelo Corvo, for his help with Python and programming study.

I would like to thank my Jury members, Ruigang Liu, Bruno Jean, Isabelle Capron, Philippe Roger, Benoît Duchemin, Yoshiharu Nishiyama, thank all of you for the time coming to my Jury, as well as your understanding and support regarding the thesis processing, and offering invaluable insights and guidance. Also thanks to Giang Vo-thanh to be my first year Jury member.

I would also thank all the help for the administrative staff from LLB: Aurore Verdier, Sarah Môme, Olivier Sineau who deserve credit for their assistance with administrative work. And Gaston Exil and Remy Lautie, who provided support for IT problems. I thank all my colleagues from the lab LLB helping me through the toughest of times, Christelle Saade, Cécile Rerzki-Vérité, Lee Lay-Theng, Daniel Dudzinski, Sophie Combet, Sumit Mehan, Marion Grzelka, Zorana Jovanovic, Manon Pépin, Sarah Môme, Antoine Roll, Olivier Demortier, Christiane Alba-Simionesco, Clémence Lecoœur, former technical assistant Marianne Bombléd. Particular thanks to Stéphane Longeville (head of MMB group), and to the former LLB director Eric Eliot. Your concern and support made my work a great pleasure, giving me encouragement and motivation, help me through the challenging times, with all your friendship and unyielding support. Special thanks to Antoine Pallandre (Ecole Doctorale 2MIB) for his listening and care during the writing period of my PhD.

Finally, thanks to my best friend Yue, and my fellow scholars Dong and Xiaodan, who gave me the encouragement and motivation during my PhD. Also thanks to my family and all my friends for their support through my studies.

# TABLE OF CONTENTS

<b>INTRODUCTION (EN FRANÇAIS) .....</b>	<b>1</b>
<b>INTRODUCTION .....</b>	<b>3</b>
<b>CHAPTER 1 LITERATURE REVIEW .....</b>	<b>6</b>
<b>1.1 Cellulose and solvent.....</b>	<b>7</b>
1.1.1 Cellulose.....	7
1.1.2 Former solvents .....	10
1.1.3 Ionic liquids as solvent.....	13
<b>1.2 Cellulose chains in solutions: current discussion .....</b>	<b>16</b>
1.2.1 Models of dissolution mechanisms in ionic liquids .....	16
1.2.2 NMR.....	20
1.2.3 WANS .....	21
1.2.4 Rheology .....	22
<b>1.3 Cellulose chains in solution: scattering .....</b>	<b>25</b>
1.3.1 Scattering for Non-IL solvents.....	25
1.3.1.1 Static Light Scattering for non-IL solvents .....	25
1.3.1.2 DLS for non-IL solvents.....	29
1.3.1.3 Small Angle Scattering for non-IL solvents.....	32
1.3.2 Scattering from solutions in Ionic Liquids.....	37
1.3.2.1 SLS and DLS.....	37
1.3.2.2 SAXS .....	38
1.3.2.3 SANS.....	41
<b>1.4 Conclusion.....</b>	<b>44</b>
<b>References .....</b>	<b>45</b>
<b>CHAPTER 2 MATERIALS AND METHODS .....</b>	<b>57</b>

<b>2.1 Different types of cellulose used.....</b>	<b>57</b>
2.1.1 Short chains: Micro-Crystalline Cellulose (MCC).....	57
2.1.2 Long chains: Bacterial Cellulose.....	57
2.1.3 Deuteriated Bacterial Cellulose: preparation .....	58
<b>2.2 Solvents.....</b>	<b>58</b>
2.2.1 Non-deuteriated ionic liquids .....	58
2.2.2 Deuteriated ionic liquids: synthesis.....	59
2.2.3 Deuteriated and non-deuteriated ionic liquids: NMR and FTIR characterization .....	61
2.2.4 Other solvents and materials .....	64
2.2.5 Preparation of cellulose solution .....	65
<b>2.3 NMR procedure.....</b>	<b>66</b>
<b>2.4 FTIR procedure.....</b>	<b>67</b>
<b>2.5 Rheometry.....</b>	<b>69</b>
2.5.1 Steady shear.....	69
2.5.2 Frequency sweep .....	69
2.5.3 Result: Cox-Merz rule and power laws.....	69
<b>2.6 Scattering techniques .....</b>	<b>72</b>
2.6.1 Laboratory X rays.....	74
2.6.2 Synchrotron Radiation (SR) .....	74
2.6.3 Energy dependence of the transmission of samples.....	75
2.6.4 Small-Angle Scattering Data processing and analysis.....	76
2.6.5 Neutron scattering: SANS/WANS .....	79
<b>References .....</b>	<b>81</b>
 <b>CHAPTER 3 X-RAY SCATTERING .....</b>	 <b>85</b>
<b>3.1 From raw data to treated data: displaying the difficulties.....</b>	<b>86</b>

<b>3.2 Dilute solution .....</b>	<b>90</b>
3.2.1 Difficulties in data treatment.....	90
3.2.2 Description .....	91
3.2.3 Direct estimate of the chain parameters: unit length, cross-section.....	93
3.2.3.1 Unit length - cross-section.....	93
3.2.3.2 Unit cross-section area.....	96
3.2.4 Rod scattering: equations .....	97
3.2.5 Fit to a model form factor .....	99
3.2.5.1 Cylinder form factor in BmimAc .....	99
3.2.5.2 Core-shell cylinder form factor in BmimAc.....	100
3.2.5.3 Flexible cylinder model in BmimAc .....	101
3.2.5.4 Core-shell model in BmimAc and BmimCl discussion .....	102
<b>3.3 Higher cellulose concentration (semi-dilute regime) .....</b>	<b>105</b>
3.3.1 Description .....	105
3.3.2 Effective structure factor .....	108
3.3.2.1 Principle.....	108
3.3.2.2 Calculations .....	110
3.3.3 Hard cylinder 2D structure factor: comparison with data.....	112
<b>3.4 Higher concentrations: biphasic state .....</b>	<b>115</b>
<b>3.5 Solutions in BmimCl: similarities and differences, a check .....</b>	<b>121</b>
3.5.1 BmimCl solutions at different concentrations.....	121
3.5.2 Comparison between BmimCl and BmimAc.....	122
<b>3.6 Effects of water and temperature in BmimAc and BmimCl.....</b>	<b>123</b>
3.6.1 Effect of water for BmimAc at large $q$ .....	123
3.6.2 Effect of water for BmimAc - cellulose solution at low $q$ .....	124
3.6.3 Effects of water: comparison with BmimCl solutions .....	125
3.6.4 Absence of temperature effect in BmimAc.....	127
3.6.5 Effect of temperature: case of BmimCl.....	128
<b>3.7 Influence of the cellulose origin .....</b>	<b>129</b>
3.7.1 Other microcrystalline cellulose.....	129
3.7.2 Bacterial cellulose .....	129

<b>3.8 Influence of co-solvent .....</b>	<b>131</b>
<b>3.9 Discussion and conclusion .....</b>	<b>133</b>
<b>References .....</b>	<b>135</b>
<b>Chapter 4 NEUTRON SCATTERING .....</b>	<b>138</b>
<b>4.1 Small angle scattering .....</b>	<b>138</b>
4.1.1 Introduction .....	138
4.1.2 Solutions scattering in different solvents. Effect of deuteration on the contrast .....	140
4.1.2.1 Values of Scattering Length Densities .....	140
4.1.2.2 In [d-Bmim][Cl] .....	141
4.1.2.3 In [d-Bmim][d-Ac] .....	142
4.1.2.4 In [d-Bmim][h-Ac] .....	143
4.1.2.5 In [h-Bmim][d-Ac] .....	144
4.1.2.6 Ionic liquids with few water added: H <sub>2</sub> O – D <sub>2</sub> O mixtures .....	145
4.1.2.7 Phase separation due to moisture effects .....	146
4.1.2.8 Aqueous solutions: NaOH/urea mixture solvent .....	147
4.1.2.9 Summary .....	147
4.1.3 Extrapolation at zero fraction of deuteriated chains by matching H chains: getting the intrachain scattering function $S_1(q)$ and the interchain scattering function $S_2(q)$ .....	149
4.1.3.1 Principle .....	149
4.1.3.2 Determination of the contrast conditions .....	150
4.1.3.3 Zero $\phi_D$ extrapolation: results .....	151
4.1.4 Zero Average contrast .....	155
4.1.4.1 Principle .....	155
4.1.4.2 ZAC matching conditions .....	156
4.1.4.3 Results .....	157
4.1.5 Conclusion on SANS .....	161
<b>4.2 Wide Angle Neutron Scattering .....</b>	<b>162</b>
4.2.1 Results .....	162
4.2.1.1 All samples with 5mm beam .....	162
4.2.1.2 All samples with 10 mm beam .....	164

4.2.1.3 Focus on [d-Bmim][h-Ac] series .....	165
4.2.2 Summary .....	167
<b>4.3 Conclusion.....</b>	<b>168</b>
<b>References .....</b>	<b>169</b>
<b>CHAPTER 5: DIFFERENT SITUATION OF</b>	
<b>DISSOLUTION .....</b>	<b>171</b>
<b>5.1 Swelling gradient measurements using SAXS (SWING) .....</b>	<b>171</b>
5.1.1 Method .....	171
5.1.2 Results .....	172
<b>5.2 Conclusion.....</b>	<b>177</b>
<b>Supporting information .....</b>	<b>178</b>
<b>CONCLUSION.....</b>	<b>181</b>

## **Introduction (*en français*)**

La consommation croissante et l'épuisement des ressources non renouvelables dans la société moderne conduisent à l'utilisation de polymères naturels. Les polymères biodégradables et les composites biocompatibles créés à partir de ressources renouvelables suscitent un intérêt croissant pour le remplacement des polymères non recyclables. La prise de conscience mondiale de la responsabilité environnementale a stimulé la recherche de produits et de procédés plus respectueux de l'environnement.

La cellulose, en tant que matériau naturel et renouvelable, est particulièrement prisée pour ses avantages environnementaux et son potentiel en tant que ressource durable. Cependant, la cellulose se trouve principalement sous une forme cristalline, alors que les applications nécessitent qu'elle soit dissoute avant d'être régénérée dans différentes formes cristallines et formes d'objets. En pratique, elle résiste à l'eau et à la plupart des solvants organiques simples. La dissolution efficace devient donc une étape importante pour les applications de la cellulose, permettant des modifications structurelles et des propriétés du matériau telles que la résistance mécanique.

La plupart des solvants aqueux contiennent des acides forts, des bases fortes ou des ions spécifiques ; ils sont agressifs et dangereux pour la santé et l'environnement. Les liquides ioniques, récemment apparus, sont plus respectueux de l'environnement, notamment parce qu'ils peuvent être récupérés à partir du mélange avec l'eau utilisé pour la régénération.

Plusieurs études utilisant des techniques de diffusion, notamment la diffusion de lumière et la diffusion de rayons X et de neutrons aux petits angles, ont été menées depuis quelque temps sur les solvants aqueux traditionnels, mais peu sur les solutions dans les liquides ioniques. Les solutions aqueuses étaient souvent perturbées, voire dominées, par l'agrégation ou la gélification des chaînes. On peut supposer que l'agrégation pourrait être limitée pour des solvants IL suffisamment bons.

Nous avons donc recherché et heureusement trouvé un solvant particulièrement favorable, permettant d'atteindre des concentrations élevées. Cependant, le fait que les IL absorbent l'eau (de l'atmosphère), ce qui a un effet fortement dégradant sur la solution, restait un problème. Nous avons donc choisi un second IL, avec le même cation et des anions différents, plus hygroscopique que l'autre, pour comparaison.

Cette étude utilise un liquide ionique à température ambiante pour dissoudre la cellulose, permettant d'étudier les conformations de chaîne dans différentes conditions de concentration. À faible concentration, dans ou proche du régime dilué ( $c < c^*$ ), la chaîne unique de cellulose existe en solution, permettant une étude détaillée de sa structure géométrique et de la taille des chaînes individuelles.

Des concentrations plus élevées ( $c > c^*$ ) peuvent être atteintes avec notre système, ce qui est rare. Les chaînes de cellulose dissoute interagissent et forment une structure multi-chaînes d'une solution semi-diluée, offrant l'opportunité d'étudier les effets possibles d'alignement des chaînes au sein de la solution.

Au-delà de la comparaison des deux IL de différentes hygroscopies, il semble nécessaire de vérifier l'effet de l'eau, ce qui sera réalisé ici en ajoutant de l'eau dans la solution.

Enfin, en augmentant encore la concentration, nous atteignons la région de dispersion biphasique, que nous avons également atteinte par le gonflement progressif d'un film sec.

La plupart des travaux sont prévus avec l'utilisation des rayons X. Nous essayerons de confirmer ces résultats en utilisant les neutrons, par deutériation des différentes entités, en particulier pour détecter une possible corrélation entre les ions et les chaînes, ce qui permettrait de mieux analyser le processus de solvation.

Nous espérons que cette recherche apportera une compréhension approfondie du comportement de la cellulose dans un liquide ionique dans des conditions pertinentes pour une utilisation à grande échelle.



# Introduction

Growing consumption and exhaustion of non-renewable resources in modern society lead to the utilization of natural polymers. Biodegradable polymers and biocompatible composites created from renewable resources get growing esteem for the substitution of unrecyclable polymers. Global awareness of environmental responsibility has pushed the research into more environmentally friendly products and processes.

Cellulose, as a natural and renewable material, is highly regarded for its environmental benefits and potential as a sustainable resource. However, cellulose is mostly in crystalline form, whilst applications require it to be dissolved – before to be regenerated in different crystalline forms and objects shape. In practice, it resists water and most simple organic solvents. Effective dissolution becomes an important step in cellulose applications. It enables further application and modification of its regenerated structure, and consequently material properties such as mechanical strength.

Most of aqueous solvents contain strong acid, or strong bases, or special ions; they are harsh, dangerous for health, and for environment. Recently appeared Ionic Liquids (IL), which are more environmentally friendly, in particular because they can be recovered from the mixture with water used for regeneration.

Several studies using scattering, more precisely Light Scattering and Small Angle X rays and Neutron Scattering, were achieved some time ago, on traditional aqueous solvents, but few on solutions in ionic liquids. Aqueous solutions were often perturbed, if not dominated, by aggregation, or gelation, of the chains. We could speculate that aggregation could be limited, for sufficiently good IL solvents.

We therefore looked and fortunately found a particularly favorable solvent, allowing to reach high concentrations. However, was remaining the fact that ILs absorb water (from atmosphere), which has a strong decremental effect on the solution. Therefore, we chose a second IL, with same cation and different anions, more hygroscopic than the other, for comparison.

This study takes a room temperature ionic liquid to dissolve cellulose, allowing investigation of the chain conformations under different concentration conditions. At low concentrations, inside or close to the dilute regime ( $c < c^*$ ), cellulose single chain exists in the solution, enabling a close study of its geometric structure and the size of individual chains.

Higher concentrations ( $c > c^*$ ) could be attained with our system, which is rare. The dissolved cellulose chains interact and form a multi-chain structure of a semi-dilute solution. This provides the opportunity to study possible effects of chain alignment within the solution.

Beyond comparison of the two IL of different hygroscopy, it seems necessary to check the effect of water, which will be achieved here by adding water on the solution.

Finally, still increasing concentration, we met the region of biphasic dispersion, which we also attained by progressive swelling of a dry film.

Most of the work is planned to be using X Rays. We will try to confirm it by using neutrons, through deuteration of the different entities, in particular to detect a possible correlation between ions and with the chain which could enable to better analyze the solvation process.

We hope that this research provides a comprehensive understanding of how cellulose behaves in an IL under conditions relevant for scalable processing.

<b>CHAPTER 1 LITERATURE REVIEW .....</b>	<b>6</b>
<b>1.1 Cellulose and solvent .....</b>	<b>7</b>
1.1.1 Cellulose .....	7
1.1.2 Former solvents .....	10
1.1.3 Ionic liquids as solvent .....	13
<b>1.2 Cellulose chains in solutions: current discussion .....</b>	<b>16</b>
1.2.1 Models of dissolution mechanisms in ionic liquids.....	16
1.2.2 NMR .....	20
1.2.3 WANS .....	21
1.2.4 Rheology.....	22
<b>1.3 Cellulose chains in solution: scattering.....</b>	<b>25</b>
1.3.1 Scattering for Non-IL solvents .....	25
1.3.1.1 Static Light Scattering for non-IL solvents.....	25
1.3.1.2 DLS for non-IL solvents .....	29
1.3.1.3 Small Angle Scattering for non-IL solvents .....	32
1.3.2 Scattering from solutions in Ionic Liquids .....	37
1.3.2.1 SLS and DLS .....	37
1.3.2.2 SAXS .....	38
1.3.2.3 SANS .....	41
<b>1.4 Conclusion .....</b>	<b>44</b>
<b>References.....</b>	<b>45</b>

## Chapter 1 Literature Review

Due to growing concerns over non-degradable plastic waste, the development of sustainable materials derived from renewable biomass resources is gaining significant attention. Cellulose, as the most abundant natural polymer on Earth, is a cornerstone for producing innovative and sustainable materials, which can be transformed into various biodegradable materials, and have the potential to substitute many plastics. However, unlike most polymers, cellulose cannot be melted, which means its processing largely depends on effective dissolution followed by shaping processes. Hence one of the main challenges for cellulose-based materials is the success of the dissolution of cellulose. In a second step, to obtain a solid material, the cellulose is re-crystallized by adding water, which is called “regenerated”. The properties of regenerated cellulose materials are closely linked to the efficiency of the dissolution step, making it a critical focus in material science.

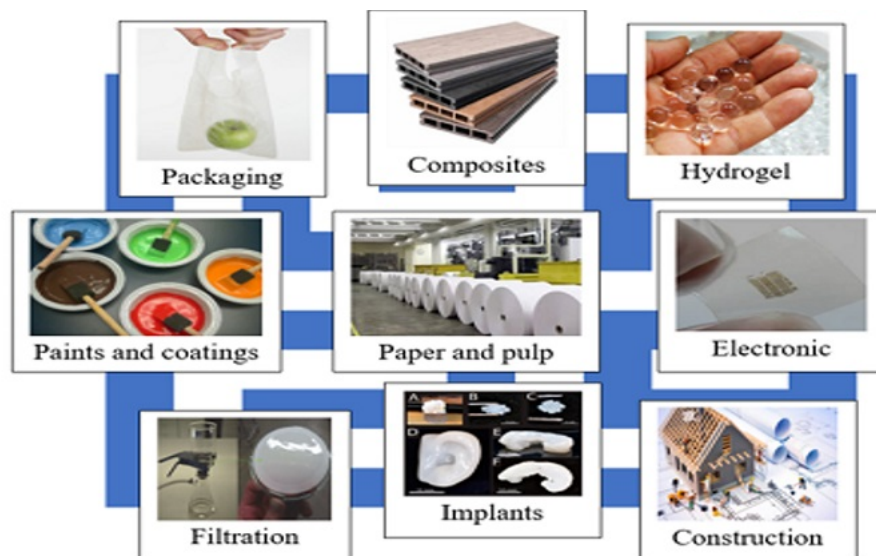


**Figure 1.1.0:** Application of cellulose in versatile uses, showing its adaptability and sustainability across various industries (Aziz et al., 2022)

**Applications.** Due to the renewability, biodegradability and versatility, cellulose is widely used in food packaging films (Wan et al., 2021), biomedical materials (Ruan et al., 2006), high-performance materials (Singh et al., 2019), environmental sensing (Galamba et al., 2021), and textiles (Bierhalz, 2021), showing its great potential for sustainable development (Fig 1.1.0).

Despite its polar structure, cellulose is well known to have an extremely low solubility in water, due to a combination of entropy, van der Waals interactions, an extended network of hydrogen bonds (for 30% as evaluated recently), and hydrophobic interactions.

## 1.1 Cellulose and solvent

### 1.1.1 Cellulose

Cellulose is often regarded as an “inexhaustible” natural resource. The most well-known source of cellulose is **plants** (such as stock native cellulose: cotton linter). In the native plant cell wall, cellulose is intricately structured into microfibrils, which are typically associated with other matrix components such as hemicelluloses and lignin. This hierarchical organization not only imparts critical structural properties to plants but also presents challenges for cellulose dissolution. **Bacterial cellulose** is different, in molecular weight in particular, depending on which bacteria it comes from. It is mostly obtained from *Acetobacter xylinum* species (Brown, 1886; Skočaj, 2019), which is a Gram-negative bacteria. Other Gram-negative, but also Gram-positive bacteria, and also fungi, including yeast-like fungi, were found to also produce cellulose. Microbial cellulose has a significantly higher degree of polymerization and crystallinity compared to the plant sources. It is a purer cellulose, without matrix components or impurities present in plant-derived cellulosic products, lignin and hemicellulose (Betlej et al., 2021; Muthu and Rathinamoorthy, 2021).

**Molecular structure.** At the molecular scale, cellulose is a polysaccharide homopolymer, which is a linear condensation formed from D-anhydro-glucopyranose (AGU) units, by  $\beta(1-4)$  glycosidic bonds, with degrees of polymerization (DP) from 100 to 20,000. The 1st carbon of one glucose ring is linked to the 4-th carbon of another ring with an acetal linkage. The glucopyranose ring adopts C14 chair conformation with all the hydroxyls equatorial and hydrogens axial. The cellulose molecule repeats the monosaccharide glucose units by rotate through  $180^\circ$  with previous unit (Figure 1.1.1).

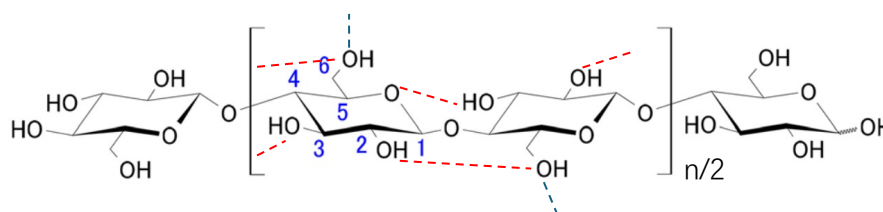


**Figure 1.1.1:** Molecular structure of cellulose. Red dotted line: intra-H bond; blue dotted line: inter-H bond

Although cellulose has a polar structure, it is widely known for its extremely low solubility in water. This was primarily attributed to dispersion forces, to its extensive hydrogen bonding network, recently evaluated as a contribution 30%, as said above, and to the presence of hydrophobic interactions.

Cellulose exists as semi-crystalline microfibrils, characterized by a three-dimensional structure with crystalline interiors (Figure 1.1.2). Both crystalline and amorphous regions are present, and the ratio between these regions varies depending on the source of the cellulose. There are four main crystalline polymorphs of cellulose: I, II, III, and IV. Native cellulose exists primarily in the form of cellulose I, which can be irreversibly converted into cellulose II through regeneration or so-called mercerization (using sodium hydroxide) processes. Cellulose III can be produced by a reversible reaction involving cellulose I or II and liquid ammonia. Further heating of cellulose III results in the formation of cellulose IV. **Figure 1.1.2** shows the width of thick fibrils is  $5 \pm 0.05$  nm and that of fine fibrils is 0.3 - 0.4 nm by TEM, both of which being consistent with the dimension of a single cellulose chains (Luo et al., 2012).

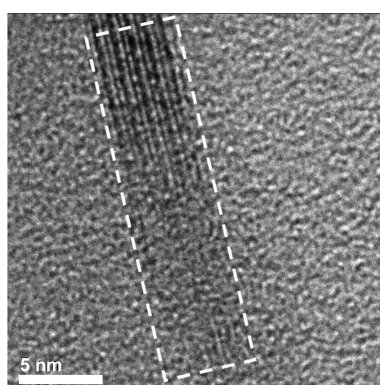


**Figure 1.1.2 a:** TEM of cellulose fibril (Luo et al., 2012)

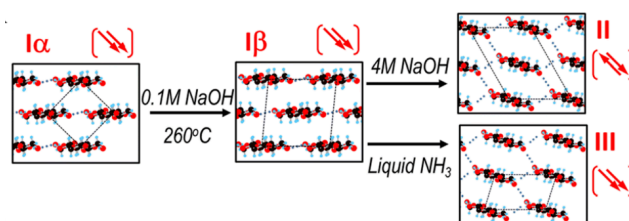


**Figure 1.1.2 b:** The 4 types of cellulose crystals (Szabó et al., 2023)

The industrially produced microcrystalline cellulose powder (Avicel PH-101) was used the most for our solution studies. Avicel PH-101 is from the plant sources (primarily from wood), and is produced by alkaline treatment to remove non-cellulosic components (such as lignin and hemicellulose), followed by acid treatment to reduce it into shorter chains; it is so called Micro-

Crystalline Cellulose (**MCC**). It consists mostly of cellulose  $I_{\beta}$  (triclinic crystal lattice) from the plant sources. Cellulose  $I_{\alpha}$  (monoclinic crystal lattice) is widely found in the cell wall of some algae and in bacteria. The difference between these polymorphs arises from their distinct hydrogen-bonding networks, where alternating glucose units are oriented oppositely and held together by intra-molecular hydrogen bonds. The intrachain hydrogen bonds hold alternating glucose units together within the same chain, while interchain hydrogen bonds stabilizing interactions between adjacent cellulose chains, further contributing to the crystalline structure (Nishiyama et al., 2010).

Cellulose nanocrystals (**CNC**), also known as whiskers, are generated by removing amorphous regions of a purified cellulose by acid hydrolysis, followed by ultrasonic treatment. They consist of polydisperse clusters made of a small number of rod-like cellulose crystals of nanometer size. The CNCs show higher crystallinity and shorter chains than MCC (Klemm et al., 2011). Bacterial cellulose possesses much larger molecular weights and chains connections (but no chemical branching) built during the synthesis, which create clusters difficult to dissolve.

The dissolution process is complicated by the need to break the complex network of inter- and intramolecular hydrogen bonds and hydrophobic interactions among cellulose molecules, often requiring multistep pretreatments and the use of hazardous chemicals (**Figure 1.1.3**). The treated cellulose shows lower DP than the natural cellulose source, due to the chemical pretreatment, which makes that most cellulose samples consist of a broader distribution of chain length or molecular weight, which measurements require dedicated techniques (Oberlerchner et al., 2015).

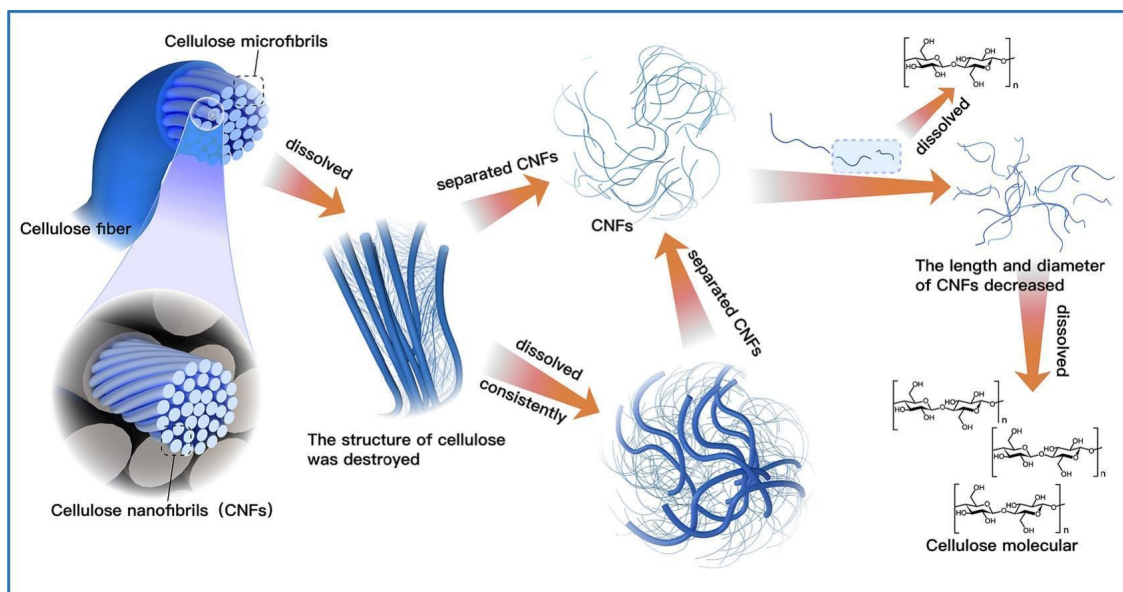


**Figure 1.1.3:** Cellulose fiber dissolution process (Peng et al., 2023)

### 1.1.2 Former solvents

Cellulose's crystalline structure is insoluble in most conventional solvents, whether polar or non-polar. Despite extensive research over the past century, only a limited number of solvents have proven effective in dissolving cellulose. Comparison in this thesis between ionic liquids and other solvents requires a brief description.

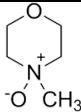
In late 19th century, in order to create an affordable and versatile substitute for silk, a cellulose solution was designed using a mixture of sodium hydroxide and carbon disulfide **NaOH/CS<sub>2</sub>**. The regenerated cellulose fibers can be extruded through a spinner and regenerated in an acid bath. Soon this “viscose process” was applied leading to the industrial production and commercialization of rayon (Cross et al., 1902). With the significant mass production of viscose fiber, the environmental and health impacts attracted more and more attention, due to the heavy usage of disulfide CS<sub>2</sub>, highly toxic and volatile (Forsberg et al., 2024). In the 1920s, the **Schweizer's Reagent** (Copper (II) hydroxide in aqueous ammonia, Cuen) has been developed to dissolve cellulose. This led to high-quality fibers productions, especially popular for delicate textiles (Burchard et al., 1994). In turn, the use of copper and ammonia led to significant environmental challenges. The recovery and recycling of these chemicals was complex and costly, leading to pollution concerns when no elaborate recovery system was used (Burchard et al., 1994). Searching for an environmentally friendly cellulose solvent was desperate.



In the 1960s, a more environmentally friendly solvent *N*-Methylmorpholine *N*-oxide (**NMMO**) was found, which is largely non-toxic and can be recycled almost completely. This safer and more sustainable alternative to the viscose process, dissolved cellulose without derivatization, nor toxic chemicals, lead to fewer chemical reactions and less waste. In 1992, Lyocell fibers began to the commercial production with brand name Tencel<sup>®</sup>, as a sustainable alternative viscose rayon. It shows softness and strength for high-quality textiles and technical applications, applied to everything from fashion and home textiles to industrial applications (Luo et al., 2001). It represents a significant step forward in sustainable textile production. However, the Lyocell process relies on the NMMO solvent which is sensitive to high temperature and can undergo or trigger oxidative side reactions. Hence recovery may produce **uncontrolled explosive reaction**. NMMO is also expensive (Reddy and Yang, 2015).

Efforts have been made to improve existing solvents and find new environmentally safe solvents. In 2002, the use of Ionic Liquids (**ILs**) for cellulose dissolution was published by Rogers's group (Swatloski et al., 2002). The possibility to have solvents with various cations and anions is an advantage for scientific study. ILs have vanishingly small vapor pressure, low flammability, and high thermal, oxidative and chemical stability. Degradability problems exist also. In 2004 the newer class of solvents, the Deep Eutectic Solvents (**DESs**), was also applied in cellulose solution by Abbott (Abbott et al., 2004), which are combinations of two species such as choline chloride and urea. Solubility of cellulose in DESs can be limited, often requiring higher temperatures or prolonged dissolution times compare to ionic liquids; it also exhibits high viscosity and is a challenge for recyclability when the separation of DESs from the mixtures or productions needs complex and energy-intensive processes (Zhong et al., 2022).

**Table 1.1.0:** Industrial processes for cellulose dissolution

Process	Reagent	Chemical formula
Viscose process	NaOH/CS <sub>2</sub>	NaOH/CS <sub>2</sub>
	Schweizer's Reagent	[Cu(NH <sub>3</sub> ) <sub>4</sub> (H <sub>2</sub> O) <sub>2</sub> ][OH] <sub>2</sub>
Tencel <sup>®</sup>	NMMO	

Over time, various solvent systems have been developed to address the challenge of cellulose dissolution, but each comes with significant drawbacks. For example, DMAc/LiCl (Striegel, 1997; Zhang et al., 2014), DMF/N<sub>2</sub>O<sub>4</sub> (Portnoy and Anderson, 1977), and DMSO/TBAF

(Östlund et al., 2009) have been investigated as potential solvents, but they are often associated with high toxicity, cost, difficulties in solvent recovery and instability during processing, which limits their broader industrial use. For example, in the case of DMAc/LiCl, cellulose is degraded by high temperature (Potthast et al., 2002).

Tetrabutylammonium hydroxide (TBAH), a highly basic, low-viscous solvent is also used, being commercially available solvated in different weight percentages of water, TBAH(aq).

Nowadays, competitive development of various modified or mixed solvents for cellulose (Sayyed et al., 2019) occurs. Among them, the basic solvents containing hydroxide ions were widely studied. Traditional solvents like concentrated NaOH(aq) have been employed, particularly in the viscose process since the early 20th century, but they function under very narrow conditions, often requiring low temperatures, which limits their practical application.

The mixture of NaOH/urea in aqueous solution was used in dissolving cellulose at low  $-5^{\circ}\text{C}$  by Zhang's group (Ruan et al., 2006), which avoid the use of toxic  $\text{CS}_2$ . Except the fact that the solution remains highly temperature-sensitive fluctuations, the NaOH/urea gain more attention in 2010s, being popular for its low-temperature processing and reduction of the environmental impact. In NaOH/urea aqueous solution, the random self-association of the cellulose chains having the exposed hydroxyl promotes physical cross-linking and therefore thermal gelation (Weng et al., 2004).

Other alkali solvents were also developed, such as LiOH/urea (Cai and Zhang, 2005; Isobe et al., 2013), in which  $\text{Li}^+$  ions – there can be 4 states of dissolved  $\text{Li}^+$  - improve the ability of dissolution of cellulose. The coordination ability of alkali metal ions ( $\text{Li}^+$ ,  $\text{Na}^+$ ,  $\text{K}^+$ ), e.g. for LiBr aqueous system (Yang et al., 2014)) with cellulose, probably determines the ability to dissolve cellulose (Huang et al., 2019; Wang et al., 2017). NaOH/TBAH, NaOH/TMAH were also examined, using SAXS, see below (Swensson et al., 2020). We can end the list with LiCl/*N,N*-dimethylacetamide (DMAc), and tetrabutylammonium fluoride/dimethyl sulfoxide (TBAF/DMSO).

On the other side of pH, a strong acid,  $\text{H}_3\text{PO}_4(\text{aq})$  shows good potential for solubility, as shown using a less common technique, cryo-EM (Alves et al., 2021). However, it is fragile with respect to aging (gelification).

### 1.1.3 Ionic liquids as solvent

Some inorganic melt salt as solvent was studied to dissolve cellulose (Fischer et al., 2003), but cellulose solubility in organic molten salts was discovered as early as 1934 by (Charles, 1934). The search for more efficient and environmentally benign solvents has led to the discovery of ionic liquids (ILs) as promising alternatives. ILs, first reported as cellulose solvents by (Swatloski et al., 2002), have opened up new avenues for cellulose dissolution. The vast combination of cations and anions that can dissolve cellulose, without chemical modification, has been extensively studied by (Fukaya et al., 2008; Swatloski et al., 2002).

Ionic liquids (ILs) are composed of ions. The relatively bulky organic cation paired with an anion, that leads to poor lattice packing, results in a purely ionic compound with low melting point. Due to the low vapor pressure, a negligible evaporation occurs when heating at the industrial scale. This leads also to high chemical stability and high solvation ability. They can dissolve organic molecules, inorganic ones, and salts, depending on their composition and can be often purified in industrial processes to be recycled and used few times

Ionic liquids were applied in industrial scale (Hermanutz et al., 2008) for application in various fields, including catalysis, extraction, electrochemistry, organic synthesis, etc.

**Potential.** ILs can dissolve significant amounts of cellulose, up to 25 wt%, under relatively mild conditions, which is a significant improvement over traditional solvent. Their application is still limited by factors such as high cost, viscosity, and toxicity, as well as recycling and reducing their environmental impact.

Progress in recovery has nevertheless been published (Zhang et al., 2022), and included in some industrial development (Zhang Jun, communication, 2nd International Symposium on Cellulose and Renewable Materials, Chengdu, China, Sept. 20-23, 2024).

Understanding the mechanisms by which ILs interact with cellulose at the molecular level is crucial for the development of new, industrially viable processes for producing cellulose-based materials. These advancements could significantly enhance the sustainability and scalability of cellulose applications in industries ranging from textiles to biomedical materials, or aerogels (Ci et al., 2023; Druel et al., 2018).

**Ions' combinations.** The ionic liquid, in general simply refers to a salt with a low-melting-temperature in recent literature, mostly generally less than 100 °C. The high number of potential combinations (or the inherent tunability) of anions and cations can lead us to design the ionic

liquids for a specific task to achieve the property. Plenty of ionic liquids were designed to dissolve cellulose (Wang et al., 2012). Most generally organic cations such as imidazolium, ammonium, phosphonium, pyridinium, pyrrolidinium are paired with inorganic or organic anions, such as halides, carboxylates (such as acetate), triflates or sulfates and phosphates. This combination includes imidazolium cations with various anions such as Cl<sup>-</sup>, Br<sup>-</sup>, formate, acetate, and dialkylphosphates. Mixtures with DMSO have been studied also, for example, of quaternary ammonium-based ionic liquids and DMSO (Kostag et al., 2020).

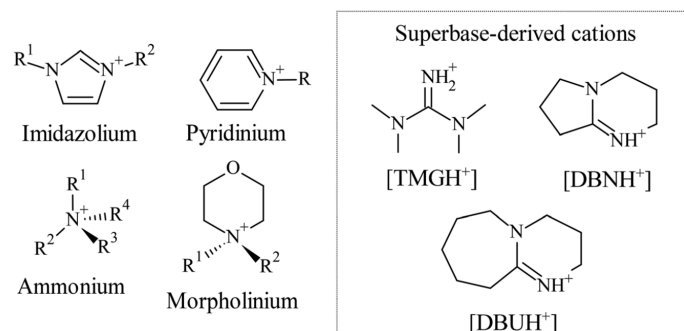


**Figure 1.1.4:** Different cations in ionic liquids salts for dissolving cellulose

With heating to ~100 °C, cellulose could be dissolved in ionic liquids which contained some anions Cl<sup>-</sup>, Br<sup>-</sup>, SCN<sup>-</sup>, etc. Cl<sup>-</sup> and OAc<sup>-</sup> of ionic liquids commonly used in dissolve cellulose (Li et al., 2018). Also quoted are formate, acetate, and dialkylphosphates.

The novel solvents for cellulose dissolution can also be classified by cation of ionic liquids: heterocyclic amines (imidazolium, pyridinium, etc.), quaternary cations (ammonium- and phosphonium-based cores), and superbases (DBNH, DBUH, etc.) (Xu and Wang, 2020). Among all ionic liquids, imidazolium-based ionic liquids are the most used to dissolve cellulose. 1-Allyl-3-methylimidazolium chloride (AmimCl) was found a powerful solvent for cellulose solution by Zhang's group (Zhang et al., 2005). "Inexpensive" mixtures of levulinic acid (LevA) and 1,8-diaza-bicyclo [5,4,0] undec-7-ene (DBU) were used by Ci (Ci et al, 2023).

There are a very good reviews of ionic liquid types, and size of hydrogen bonds for cellulose (Gupta and Jiang, 2015), and, on the engineering point of view, of ionic liquid-cellulose interaction dissolution mechanism (Pinkert et al., 2009). (Yuan and Cheng, 2015) giving insights on how the cellulose dissolution in ionic liquids can be made more efficient.

To end this long list, superbase-derived ionic liquids, namely 1,5-diazabicyclo [4.3.0] non-5-enium acetate ([DBNH][OAc]) were studied by Sixta (Sixta et al., 2015). The regenerated cellulose from [DBNH][OAc] shows high oriented fibers (called Ioncell-F) and higher tenacity

values than commercial rayon and Lyocell fibers. Systematic investigations revealed that the combination of electron-donating groups, small steric hindrance groups, and short-chain groups in carboxylate anions combined with a larger ring in superbase cations facilitated cellulose dissolution (Li et al., 2020). (Kuzmina et al., 2017) derived six different cations and obtained good results in fibers fabrication.

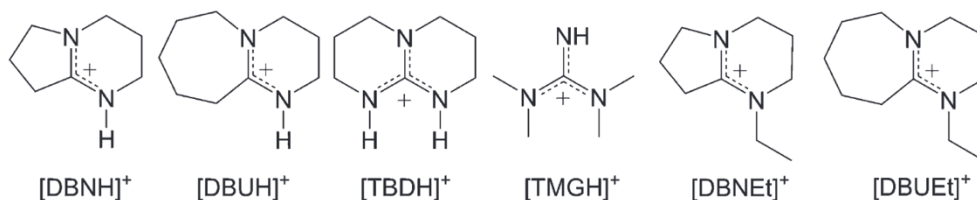


**Figure 1.1.5:** Superbase derived cations for ionic liquids (Kuzmina et al., 2017).

As a final remark, the high cellulose solubility in some ionic liquids could open up new functionalization pathways that are not accessible in traditional solvents.

## 1.2 Cellulose chains in solutions: current discussion

We will first report very briefly the state of art acquired by other techniques than scattering. Cellulose chain conformation in solution can be first studied by rheology, which can distinguish different concentration regimes, indirectly suggesting conformation changes in cellulose chain spatial arrangement and interaction between chain segments. Also, molecular dynamics (MD) has been developed to evaluate the interactions between solvent molecules and cellulose chains through time-evolving conformation of cellulose chains in solution by computer simulation.

### 1.2.1 Models of dissolution mechanisms in ionic liquids

An abundant literature has treated the dissolution process, since it is necessary both for a basic understanding, and all practical applications! This includes also regeneration, a key step to obtain the desired properties. To all kinds of molecule present in the various solvents, have been attributed some insertion mechanisms separating cellulose chains from each other by suppressing their physical links, as shown on the cartoon of **Figure 1.2.1**, of mostly visual character.

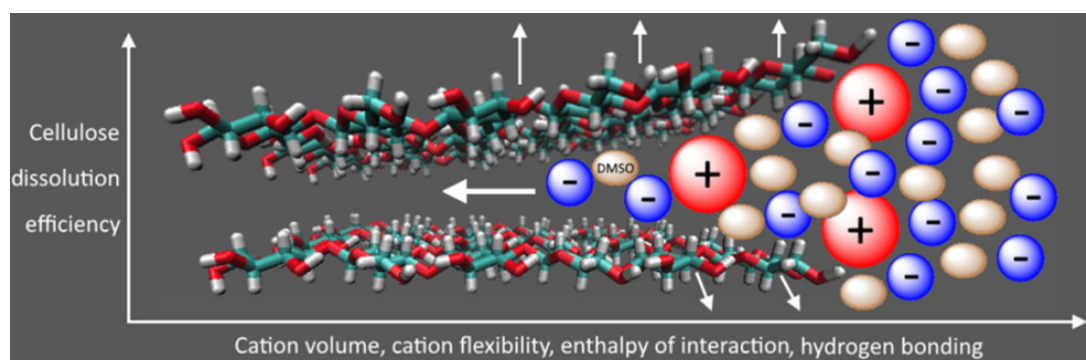


**Figure 1.2.1:** Scheme of effect on dissolution (Kostag et al., 2020).

In view of the many possible interactions, it seems sensible to account for most of them in a model, but it is a huge task (**Figure 1.2.2**). Probe molecules using the Abraham parameters of a linear free energy relationship for solvation process (Anderson et al., 2002) can be utilized. Solvatochromic probes are another possibility (El Seoud et al., 2019).

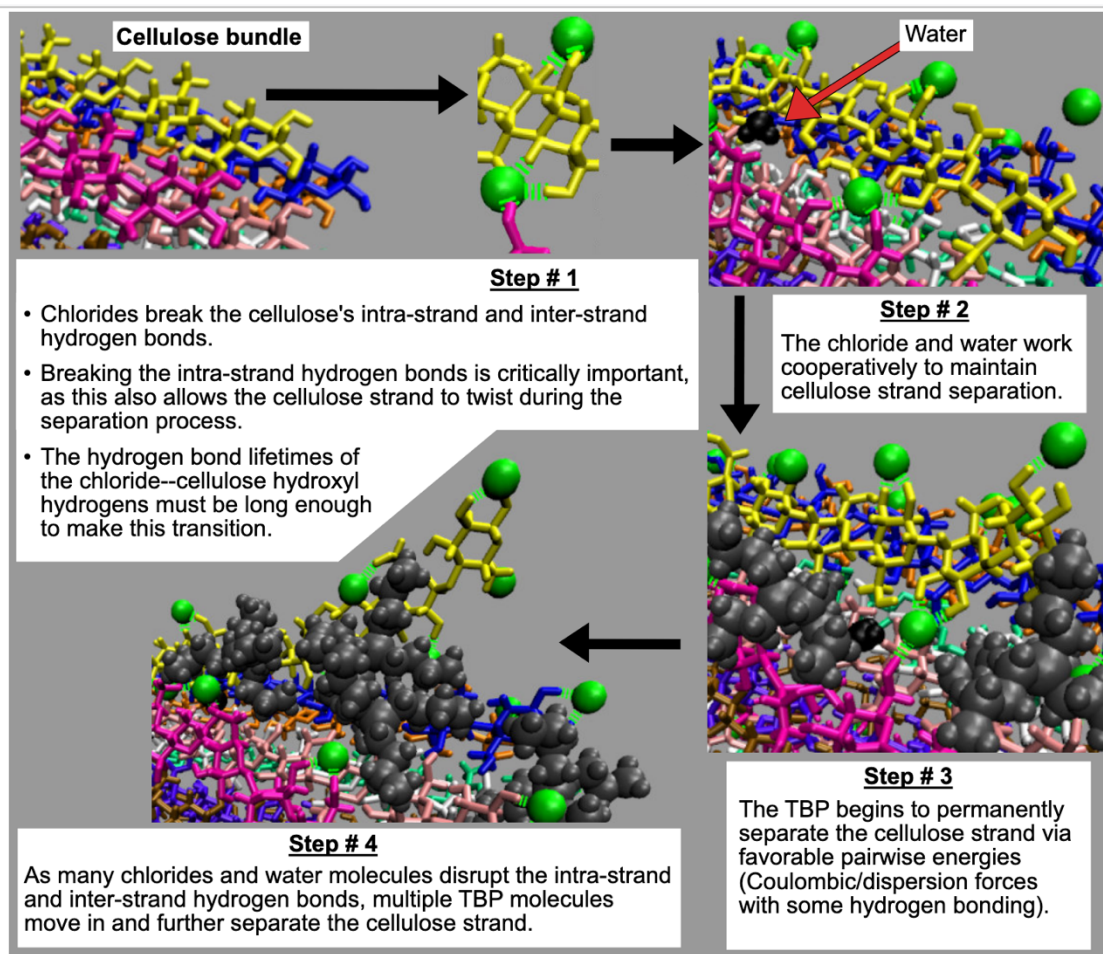


**Figure 1.2.2:** Summarized mechanism for cellulose dissolution (Tetrabutylphosphonium Chloride-Water Mixture) in the TBPCl-water solution. (Crawford and Ismail, 2020).

**H bonds.** The good abilities of ionic liquids to dissolve cellulose have been attributed by many authors to the possibility of forming hydrogen bonds with cellulose chains, instead of the bonds formed between chains, hence leading to a rupture of hydrogen bonds between chains - in EmimAc (Liu et al., 2012)), see **Figure 1.2.3**.

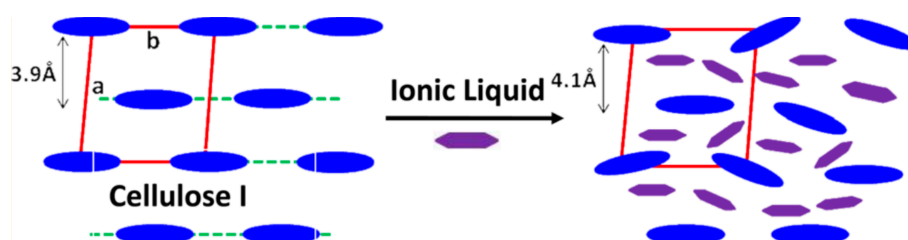


**Figure 1.2.3:** Schematic effect of IL on H bonds disruption (Cheng et al., 2012).

The impact of a Pretreatment by 1-Ethyl-3-methylimidazolium Acetate Ionic Liquid on the Cellulose Crystalline Structure has also been studied by (Cheng et al., 2012).

That has been the subject of long going controversies, occurring in the interpretation of different techniques, such as NMR (see below). In an often-cited work, (Medronho and Lindman, 2014) have struck the importance of hydrophobicity.

One could split the problem of the contribution of H bonds in two.

**In the crystals:** e.g., some calculations of the contribution of H bonds with respect with the other contributions, most of the time present for polymer dissolutions, has been estimated to only 30% (Pan Chen, communication, 2nd International Symposium on Cellulose and Renewable Materials, Chengdu, China, Sept. 20-23, 2024).

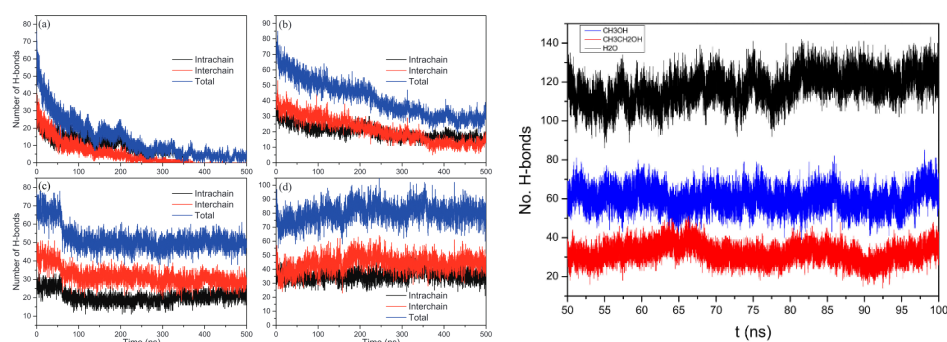


**Figure 1.2.4:** Number of bonds between different chains in different 80% antisolvents at 293 K. Left: (Li et al., 2015). Right: (Ju et al., 2022).

Crystallographic studies (Nishiyama et al., 2010, 2002), enable understanding the topology of the H bonds. They conclude that, although hydrogen bonding may not be the most important factor in the stabilization of cellulose I, it is essential for stabilizing cellulose III, which is the activated form, and preventing it from collapsing back to the more stable cellulose I.

**In solutions.** Essentially, a very spread claim is that the hydrogen of the ionic liquid anions would bond with the hydroxyl groups in the cellulose chains, while ionic liquid cations bond with the cellulose ether oxygens. This would disrupt H bonds.

For example, **the association between cellulose and acetate anions** was studied by different methods, in particular MD, NMR (see below), WANS, SAXS and SANS (see corresponding sections).



It was also found that acidic protons on the heterocyclic rings of the cations are essential for the dissolution of cellulose in the ILs, using  $^{13}\text{C}$  NMR and the Kamlet–Taft parameters, which describes solvent polarity, including hydrogen bonding ability (Lu et al., 2014)<sup>1</sup>.

The localization of the ions was studied by several MD calculations: see (Crawford and Ismail, 2020), and Figure below, for example.

It was also studied experimentally by NMR and WANS, see **section 1.2.1**.

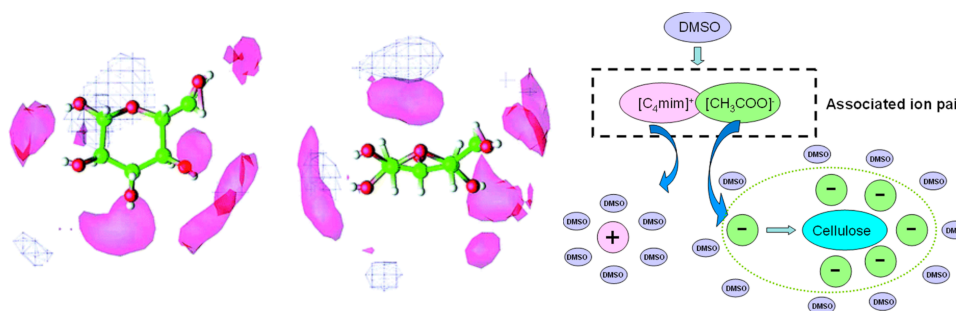


**Figure 1.2.5:** Left: Three-dimensional probability distributions of anions (red/solid surface) and cations (blue/wireframe surface) around an isolated glucose molecule (Gupta and Jiang, 2015), (Li et al, 2018). Right: insertion of DMSO (Zhao et al., 2013).

This is far beyond the purpose of our studies, apart a connection with the immediate surroundings of the chains, as probed by SAXS in the form of a shell of solvent, often proposed to fit data, see section SAXS.

---

<sup>1</sup> Kamlet-Taft solvent parameters are hydrogen bond acidity  $\alpha$  (hydrogen bond donor), hydrogen bond basicity  $\beta$  (hydrogen bond acceptor), and dipolarity/ polarizability effects  $\pi^*$  (polarizability). The  $\alpha$  and  $\beta$  can express the ability of solvent to act as hydrogen donors and acceptors, that means the strength of the hydrogen bond provided by the solvent to the solute and received by solvent from solute respectively;  $\pi^*$  is the ability of solvent molecules to affect solutes through electrostatic interactions.

**Table 1.2.0:** Different types of Ionic liquids and the ability to dissolve cellulose.

Groups	Types	Examples	Ability
heterocyclic amines	Imidazolium-based (Uto et al., 2018)	[Bmim]Cl, [Emim][OAc], [Amim]Cl ...	High solubility; mild conditions
	Pyridinium-based (Sashina et al., 2016)	N-Butylpyridinium Chloride...	
quaternary cations	Ammonium-based	Tetrabutylammonium Fluoride (TBAF)/DMSO (Rebière et al., 2017) ...	Thermal stability; low solubility
	Phosphonium-based (Abe et al., 2012)	Tetraphosphonium Chloride (Crawford and Ismail, 2020) ...	
superbases	Superbase-derived (Kuzmina et al., 2017)	[DBNH][OAc] (Crawford and Ismail, 2020), [DBUH][OAc] (Ci et al., 2023) ...	High solubility; corrosiveness

### 1.2.2 NMR

In Cl and Bmim, (Remsing 2006) followed the differential behavior of relaxation times of Cl and Bmim, to probe the "local mobility" of Bmim ( $^{13}\text{C}$ ) and Cl ( $^{35/37}\text{Cl}$ ). Bmim is not affected by cellulose, while Cl relaxation, which suggests affinity of  $\text{Cl}^-$  anion to the cellulose chains. That was interpreted by the authors as hydrogen bonding between carbohydrate hydroxyl protons and the chloride anion in a 1:1 stoichiometry. See **Figure 1.2.4**.

Zhang et al (Zhang, J., 2010) proposed the variation of  $^1\text{H}$  chemical shifts to interpreted as H-bonding variations. The observed stoichiometric ratio of EmimAc/hydroxyl is between 3:4 and 1:1 in the primary solvation shell, implying that there should be one anion or cation to form hydrogen bonding with two hydroxyl groups simultaneously.

This was commented by Remsing et al 2010 pointing that chemical shifts are very sensitive to any variations and are never "direct evidence" of the presence or absence of H-bonding interactions. Remsing et al concluded that "*As we and others have shown, both experimental and theoretical studies indicate that the imidazolium ion is NOT involved in H-bonding with*

*the sugar solute as proposed in the manuscript. It is worth noting, however, that the structure of the IL cation is known to have an effect on cellulose solubility."*

In (Youngs et al., 2011), in mixture of Glucose and BmimAc, Pulsed Field Gradient- PFG-NMR experiments are used to measure diffusion coefficients of cation, acetate and glucose, compared with MD. One can read that diffusion coefficient of anion is quicker than cellulose, so we propose that complexation is probably very labile (quick exchange between H bond with glucose and bulk IL). NOESY (Nuclear Overhauser Effect Spectroscopy) (cross-correlation) experiments (which measure spatial correlation between hydrogen sites) do not show any significant interaction between cation ring and glucose hydroxyls. Youngs et al conclude: "*Therefore, from both the previous chloride and current acetate studies, the predominant interactions of the ionic liquid with cellulose as a solute, in terms of dissolution, are likely to be with the anion and that not any cation–solute interactions are not structure forming.*", see

**Figure 1.2.6.**

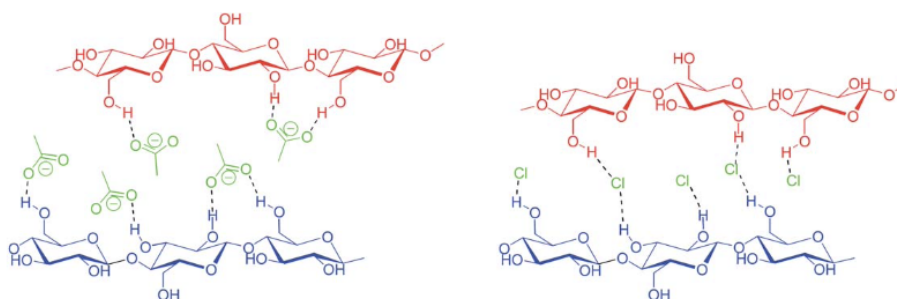


**Figure 1.2.6:** Scheme of acetate ion penetration and separation of cellulose strands (acetate) compared to potential formation of intra-sheet hydrogen bonds with chloride (Youngs, 2011).

### 1.2.3 WANS

Youngs also measured the correlations between the different ions of the IL and glucose, taken as a model of cellulose unit. His conclusions meet the one inspired by NMR. (Youngs, 2011), see **Figure 1.2.7** and **Figure 1.2.8**.

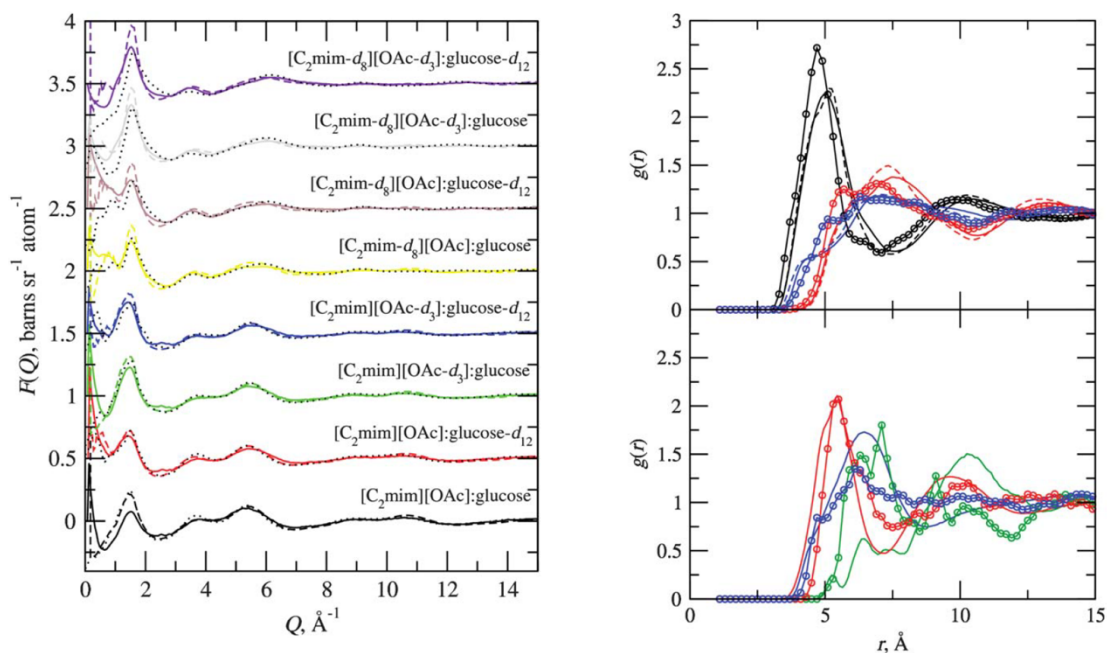


**Figure 1.2.7 (left):** Experimental (solid lines), EPSR (Empirical Potential Structure Refinement) refined (dotted lines) and MD simulated (dashed lines) distinct scattering profiles of all isotopically substituted 6:1  $[\text{C}_2\text{mim}][\text{OAc}]:\text{glucose}$  mixtures examined (Youngs et al, 2011).

**Figure 1.2.8 (right):** Centre-of-mass radial distribution functions for a 6:1  $[\text{C}_2\text{mim}][\text{OAc}]:\text{glucose}$  system, as determined by EPSR fitting of experimental neutron diffraction data (solid lines with symbols) and MD simulation (solid line). MD data for the neat ionic liquid is also shown for comparison (dashed line). Top panel shows ionic liquid cation–anion (black), cation–cation (blue) and anion–anion (red) distributions. Bottom panel shows glucose–glucose (green), glucose–cation (blue) and glucose–anion (red) correlations.

## 1.2.4 Rheology

Several studies concern different IL of the Emim or Bmim type- BmimAc, (Lefroy et al., 2021), or with cosolvent – DMSO (Lv et al., 2012). They show similar behavior, which we illustrate with one paper (Chen, X., 2011), see **Figure 1.2.9**. Successive concentration regimes appear, with increasing power laws, when concentration is increased. The concentration dependence of specific viscosity was used to define the three concentration regimes: dilute, semidilute unentangled, and entangled solutions. All the observed concentration dependences of specific viscosity, relaxation time, and plateau modulus are similar to the scaling predictions for neutral

polymers in a solvent, with overlap concentration  $c = 0.5$  wt % and entanglement concentration  $c_e = 2$  wt %, see **Figure 1.2.9 a**.

Important rheo-fluidification is also observed at large shear gradient, or high angular frequency, see **Figure 1.2.9 b**.

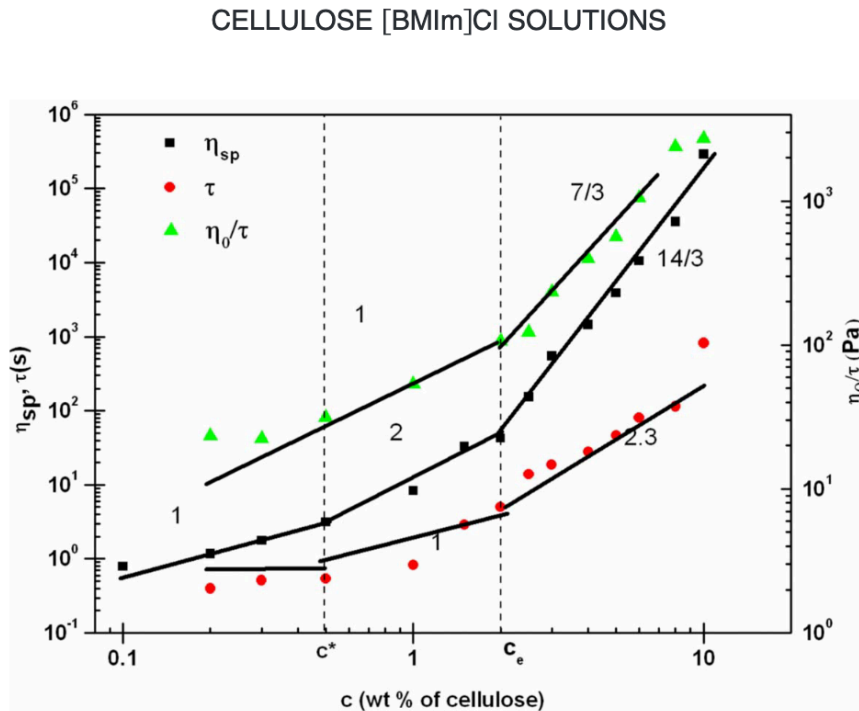


**Figure 1.2.9 a.** Concentration dependence of specific viscosity  $\eta_{sp} = (\eta - \eta_0)/\eta_0$ ,  $\tau_s$ , terminal relaxation time, and terminal modulus,  $\eta/\tau$  for solutions of cellulose ( $M_w = 120\,000$ ) in BmimCl at 25 °C with overlap concentration  $c^* = 0.5$  wt % and entanglement concentration  $c_e = 2$  wt % indicated by vertical dashed lines.  $\eta/\tau$  for  $c > c_e$  is the plateau modulus  $G_e$ , and for  $c < c_e$  this is the terminal modulus of the Rouse/Zimm models without entanglement,  $kT$  per chain. The numbers are the slope of the different linear part in log-log, e.g. the apparent power laws  $c^m$ , in agreement with predictions of polymer dynamics (Chen et al., 2009)

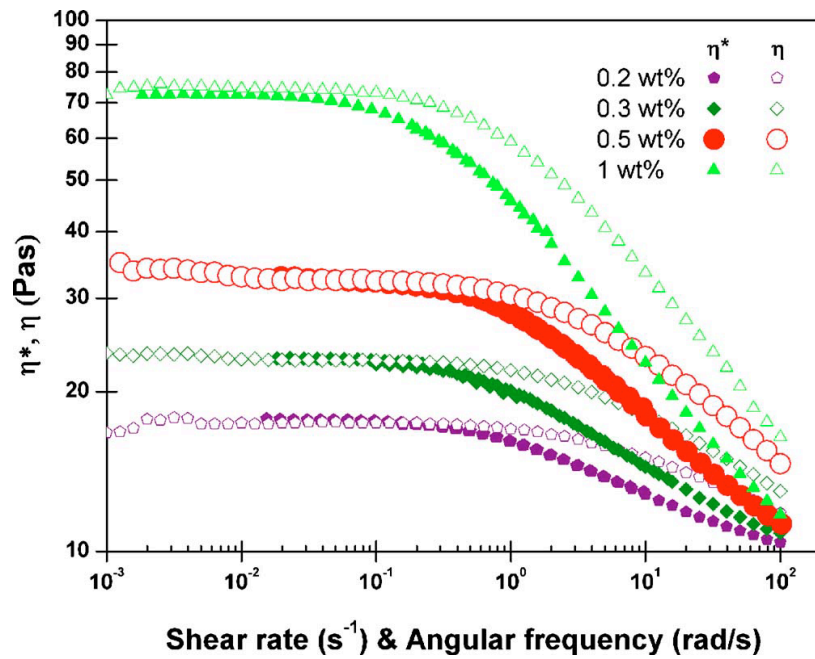


**Figure 1.2.9 b.** Shear rate dependence of steady shear viscosity and frequency dependence of complex viscosity of two dilute cellulose/BmimCl solutions, a solution at  $c^*$  (red circles), and a semidilute unentangled solution at  $2c^*$  (green triangles) at 25 °C. Open symbols are the shear rate dependence of steady shear viscosity; filled symbols are the frequency dependence of complex viscosity. From (Chen et al., 2009).

## 1.3 Cellulose chains in solution: scattering

Cellulose solutions, first in non-ionic (mostly aqueous) liquids then in ionic liquids, were also studied at the microscopic scale by Dynamic Light Scattering (DLS) and Static Light Scattering (SLS), and more recently by Small Angle Scattering (SAS), using either X-ray (SAXS) or neutron (SANS)

### 1.3.1 Scattering for Non-IL solvents

#### 1.3.1.1 Static Light Scattering for non-IL solvents

**Dilute regime. Kuhn length, persistence length, chain stiffness:** Beyond viscometry, the cellulose conformation and stiffness was, as generally, studied, by SLS in dilute solution. The worm-like chain (WLC) model introduces the persistence length  $L_p$ . The characteristic ratio ( $C_\infty$ ) - which expresses the chain stiffness, is the ratio of the actual end-to-end distance of the polymer chain to the expected distance if the polymer units were freely jointed to characterize the semiflexible or rigid chains in many papers. In other words, we can consider the chain made of freely jointed chains of length the Kuhn length  $L_K = 2 \times L_p = C_\infty \times A$ , where  $A$  is the average monomer length or contour segment length along the polymer backbone. It can be obtained either from the radius of gyration  $R_g$  for chains short enough (with the additional difficulty of addressing the polydispersity), or better by fitting of the SLS using the wormlike chain model, with a persistence length  $L_p$  calculated by Yamakawa - Fujii model.

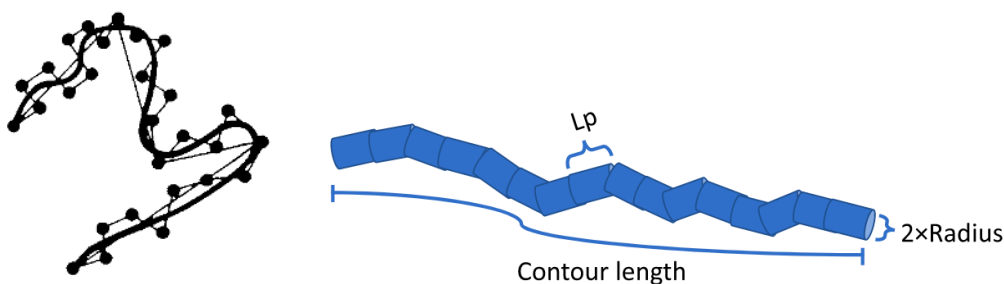


**Figure 1.3.1:** Wormlike chain schemes for dissolved cellulose: left, (Burchard et al., 1994) right (Swensson et al., 2021)

**Light scattering** measurements were first attempted, with aqueous solvents. Saito, in 1983 reports values of the Benoit-Doty persistence length around 5 nm (Saito, 1983) in Cadoxen and FeTNa (iron sodium tartrate). Kamide et al (Kamide 1987) use the ratio  $a = A/A_{free}$ , of the

measured size  $A$  over  $A_{free}$  (where  $A$  represents the unperturbed chain dimension of the polymer chain;  $A_{free}$  represents the chain dimension for a free rotating chain model), the dimension of the corresponding free rotating chain, and the characteristic ratio  $C_\infty$  characteristic, and conclude these are characteristics of a semi-flexible chain.

A next set of measurements started 30 years ago with Burchard group (Burchard et al., 1994; Saalwächter et al., 2000; Seger et al., 1996; Seger and Burchard, 1994). They used a good visualization of such fit to the WLC model, using the Casassa-Holtzer plot ( $qI(q)$  versus  $q$ ). (Casassa, 1955; Holtzer, 1955). **Figure 1.3.2** shows the reduced scattering intensities  $R_0/K_c = P(q)M$ , multiplied by  $q/\pi$ , for five celluloses and five amyloses of different chain length as examples. The full circles (cellulose) and shaded (amylose) circles represent the experimental data, and the lines demonstrate the fits by the Koyama theory. Both the maximum and the plateau at large  $u = qR_g$ , have a simple physical meaning:

- the large  $qR_g$  plateau: only the internal structure of the chain is seen. The chain appears as a rigid rod, which results in a plateau. Its height gives the linear mass density  $M/L$  of the rod like segment sections.
- The low  $q$  part is increasing, because it corresponds to the Guinier plateau ( $q \cdot (1 - q^2 R_g^{2/3})$ ) is an increasing function).
- a maximum appears only for a variation in  $q^{-a > 1}$ ; in particular for  $a = 2$  this corresponds to the Gaussian behavior. i.e. the wormlike chain (WLC) for  $q > 1/L_p$ . For pure rods, this regime does not exist, there is no maximum. The ratio of the maximum height to the plateau height measures the number of Kuhn segments  $N_{kw}$  (weight average). The position of the maximum depends on the polydispersity, from  $u = 1.41$  for uniform chain length, up to  $u = 1.71$  when  $M_w/M_n = 2$  (most probable Schulz-Flory distribution).

As seen on the Casassa-Holtzer plot of **Figure 1.3.2**, the obtained data show a clear decrease, i.e.  $a > 1$  This can be fitted by the theoretical curve for WLC. It should reach a plateau related to a  $I \sim q^{-1}$  power-law, but with SLS the maximum attainable  $q$  is too small. The Burchard group and following authors therefore *assume* the WLC conformation and deduce a value of  $L_p$ .



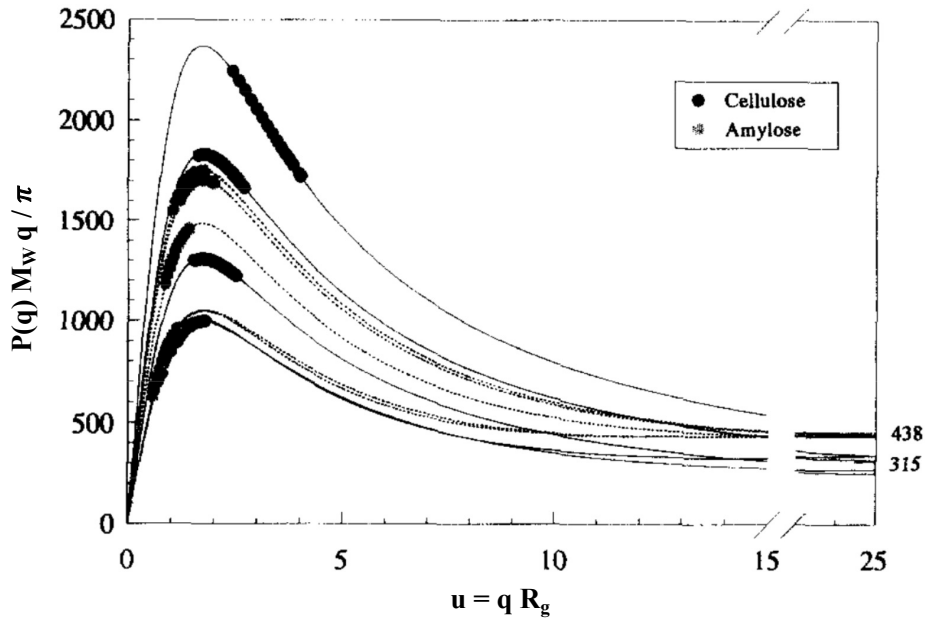


**Figure 1.3.2:** Casassa-Holtzer plot  $R_\theta/K_c = P(q)M_w q/\pi$  versus  $qR_g$  for five cellulose and five amylose samples. The solid and dashed lines represent the calculated fit curves (Seger-Burchard, 1996).

Obtained values of  $L_p$  are given in the **Table 1.3.1**. Most values vary in between 6 and 9, except two cases reaching 13 nm, and an even larger value of 25 nm calculated based on quasi-elastic light scattering and viscosity data in LiCl/DMAc solvent. As a reference the monomer length is estimated to 0.5515 nm - with a diameter of 0.8 nm (Gilbert and Patton, 1983). This corresponds to  $C_\infty \sim 20$ .

**Table 1.3.1:** Persistence lengths obtained by Static Light Scattering (WLC model) from cellulose solutions in different solvents.

persistence length $L_p$ ( $L_p = \frac{1}{2}L_k$ )	molar mass per unit contour length ( $M_L$ )	characteristic ratio ( $C_\infty$ )	Diameter of the chain (d)	solvent	reference
$6.0 \pm 0.2$ nm	$360 \pm 10$ nm <sup>-1</sup>	20.9	–	6 wt% NaOH/4 wt%	(Zhou et al., 2004)
6.0 nm	$365$ nm <sup>-1</sup>	20.8	–	LiOH/urea	(Cai et al., 2006) (Saito 1983)
25.2 nm	–	91.9	$8 \times 10^{-8}$ cm	LiCl/DMAc	(McCormick et al., 1985)
4.7 nm	–	–	–	Cuen	(Kes and
8.2 nm	–	–	–	0.5% DMAc/LiCl	Christensen, 2013)
6.25 nm	–	–	–	LiCl/DMAc	(Bianchi et al., 1985)
7.9 nm	–	–	–	Cd-tren	(Saalwächter et
5.1 nm	–	–	–	Ni-tren	al., 2000)
6.55 nm	–	–	–	cuoxam	
13 nm	–	–	–	Schweizer's Reagent	(Burchard et al., 1994)
12.8 nm	–	$49.6 \pm 12$	–	cuoxam	(Seger and Burchard, 1994)

Note that in most cases, the points falling on the Casassa-Holtzer plot cover a rather narrow range, and could be, in our opinion also interpreted also by some power law  $q^{-a>1}$  scattering due to aggregates. Indeed, later, the idea of branched gelled structures, or fractal aggregates, or “significant attractive cellulose-cellulose interactions” (Hagman et al., 2017). For NaOH solutions can show very nicely a  $q^{-2}$  law all over the SLS and the SAXS  $q$  range (this was also observed by us from neutron experiments) at ILL.

### Semi-dilute regime for non-IL solvents

Above the overlapping concentration  $c^*$ , Gaussian chains – or excluded chains, interpenetrate and form a sea of blobs of size  $\xi < R_g$ . The zero  $q$  limit of intensity should decrease with  $c$ . In reality, for cellulose solutions, it is much higher, showing aggregates of high number of chains

in most cellulose solutions. This led to the proposition by the Burchard group, that they are created by links between some linear parts of the chains, as shown in **Figure 1.3.3**, for several different aqueous solvents. More recent work confirms this: non-substituted cellulose dissolved in the monohydrate of *N*-methylmorpholine-*N*-oxide was investigated by static light scattering measurements by Arndt et al (Arndt, 2000). Apparent molecular masses of the cellulose of several millions g/mol were observed. The overall particle scattering function  $I(q)$  can be separated into two individually scattering contributions, due either to large and small aggregates, or to the different parts of a fringed micelle, the core and the fringes.

“Similarly, in (Röder and Morgenstern, 1999), the solution state of cellulose dissolved in *N*-methylmorpholine-*N*-oxide-mono-hydrate (NMMNO·MH) was investigated by static laser-light scattering. Molar masses of the order of several million  $\text{g mol}^{-1}$  were observed ( $R_g > 160 \text{ nm}$ ). The overall scattering functions can be separated into two partial scattering contributions of large and small aggregates. The activation of cellulose prior to dissolution leads to particles consisting of significantly fewer cellulose molecules lower mass, but with similar size.”

We will see below that Dynamic Light Scattering brings more evidence.

### 1.3.1.2 DLS for non-IL solvents

**Dynamic light scattering** contribution has also been measured. Slow modes appear, particularly in semi-dilute cases. They may also be due to the structures just evoked (same papers), as well as other types of aggregates or gels, initial and subsequent to the dissolution, reported later in time by Hirosawa, Hashimoto, and Shibayama (Hirosawa et al., 2017).

To cope with this picture, it was proposed earlier, a picture of chains rigid over nanometer scale (until  $L_p$ , most likely), which aggregate together in small fibrils, themselves arranged in a kind of random walk by (Burchard et al., 1994). Seger et al compared, together with SLS (see above), the DLS of amylose and cellulose in iron tartrate. A slow mode appeared for cellulose much sooner, at concentration lower than  $c^*$  (Seger et al., 1996). This confirms the proposal that for cellulose dissolved in NMMO, forms a supramolecular structure, described by the so-called model of fringed micelle.

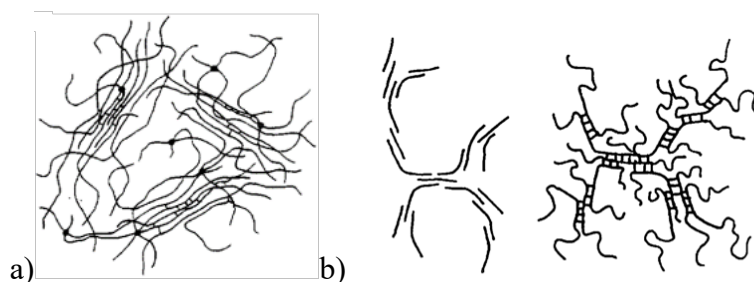


**Figure 1.3.3:** Suggested solution structures above the overlap concentration  $c^*$  of cellulose: a) in Iron Sodium Tartrate – FeTNa (Seger-Aberle-Burchart, 1996), and b) in *N*-morpholine-*N*-oxide monohydrate (NMMNO) (Schulz-Seger-Burchard, 2000).

Slow modes were also observed and well described for mixtures of solvent and "cosolvent" for chloride-based and acetate-based ionic liquids with co-solvent (DMSO, DMF, DMAc, and DMH). DLS (see Figure below) shows a double size distribution attributed to the coexistence of dissolved cellulose chains and aggregated or undissolved chains (Zhou et al., 2022).

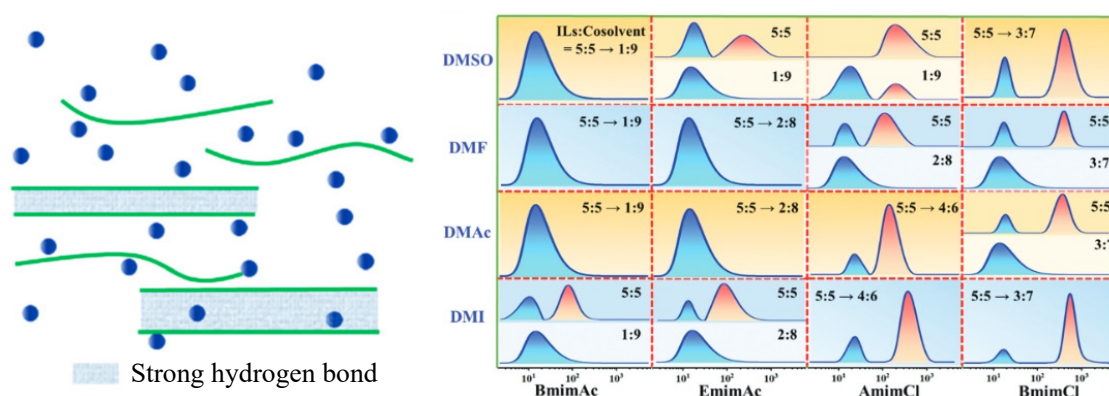


**Figure 1.3.4:** DLS from mixtures of ILs (BmimAc, EmimAc, AmimCl, BmimCl) with co-solvents (DMSO, DMF, DMAc, DMI) at one or two different fractions (Zhou et al., 2022)

SLS - DLS at the exit of separation columns, so-called **SEC-MALS-QELS** (Size Exclusion Chromatography - Multi Angle Light Scattering - Quasi Elastic Light Scattering) method was applied by Masahiro Yanagisawa and Akira Isogai (Yanagisawa and Isogai, 2005) to many different kinds of cellulose (from MCC to tunicate) of various average DP values, and a derivative, cellulose tricarbonyl (CTC), with LiCl/ amide solvents and THF as the mobile phases. SLS gives both the mass  $M_w$ , hence the contour length and the  $R_g$ . For relatively high-

$L_w$  (the weight average counter length)  $>1000$  nm and CTC samples, the good consistency was observed between the conformation plots of  $R_g$  vs  $L_w$  for cellulose and CTC samples in LiCl/amide solvents, indicating that cellulose and CTC molecules adopt nearly identical conformations. In the “normal” good solvents for cellulose, the  $R_g$  versus  $L_w$  log-log plots were almost linear and their slopes commonly yielded  $R_g \sim L_w^{0.55-0.58}$ , as expected for flexible chains, surprisingly (see **Figure 1.3.5**).

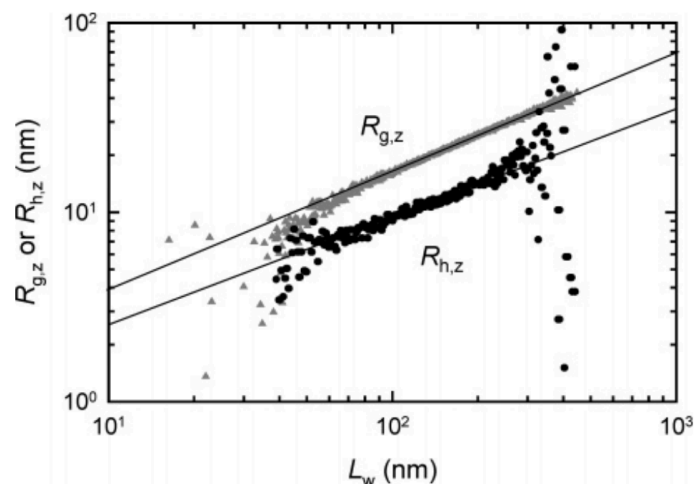


**Figure 1.3.5:** SEC-MALS-QELS: double-logarithmic plots of  $L_w$  vs  $R_{g,z}$  (z- average radius of gyration) or  $R_{h,z}$  (hydro-dynamics radius) for tricarbonylated microcrystalline cellulose powder (c-MCC) in THF (Yanagisawa and Isogai, 2005).

To conclude this part on light scattering in aqueous solvents:

- in dilute regime, there is a possible agreement with a WLC (Worm-Like Chain) model, giving some values of persistence length  $L_p$  centered on the 6 -10 nm range
- in semidilute regime, and light scattering gives information on density fluctuations, but no direct information on their shape anymore. In practice, the main result is the presence of aggregates, for which pictures were first given in term of aggregation of rigid parts, and later in term of fractal aggregates.

Let us point that light scattering is, for our purpose of understanding chain conformation, firstly interesting in the dilute regime. However, it corresponds to very low concentration, not much used in applications. At higher concentration, the chains are very interpenetrated, and light scattering gives information on density fluctuations, but no direct information on their shape anymore. It seems that aggregates are present but that does not prevent to make observations at larger  $q$  using SAS, where these aggregates are observed at a lower scale.

### 1.3.1.3 Small Angle Scattering for non-IL solvents

**SAXS.** SAXS (see Small-Angle Scattering corrections methods (Pauw, 2013)), allows us to access to more local scale and observe the effect on chain-chain interaction. This has been done in a second generation of papers which examined the range of larger  $q_s$  more recently.

SAXS was used for MicroCrystalline Cellulose (MCC) solutions in aqueous solvents, such as tetrabutylammonium hydroxyde by Olsson group (A. Behrens et al., 2016; Gubitosi et al., 2016) and tetrabutylammonium acetate/dimethylsulfoxyde mixtures (Idström et al., 2017).

Briefly summarizing, the intensity appears as varying like the scattering of a cylinder ( $q^{-1}$ , for  $q > 1/R_g$ ), followed in log-log by a clear-cut shoulder signaling the cross-section of the rod, at  $10^{-2} < q < 10^{-1} \text{ \AA}^{-1}$ , while at lower  $q_s$ , for concentrations higher than  $0.004 \text{ g/cm}^3$ , the apparent slope increases and approaches  $q^{-2}$ ; it is modelled by the scattering of large fractal aggregates. (A. Behrens et al., 2016) give a core-shell  $5 \text{ \AA}$ , shell  $5 \text{ \AA}$ , which is same as our fitting using core shell model, with  $R_{g,c=0.1 \text{ g/cm}^3}=270 \text{ \AA}$ , get the averaged single chain  $R_g \approx (Ll_p/3)^{1/2} \approx 160 \text{ \AA}$  due to the average aggregation number, see **Figure 1.3.6**.

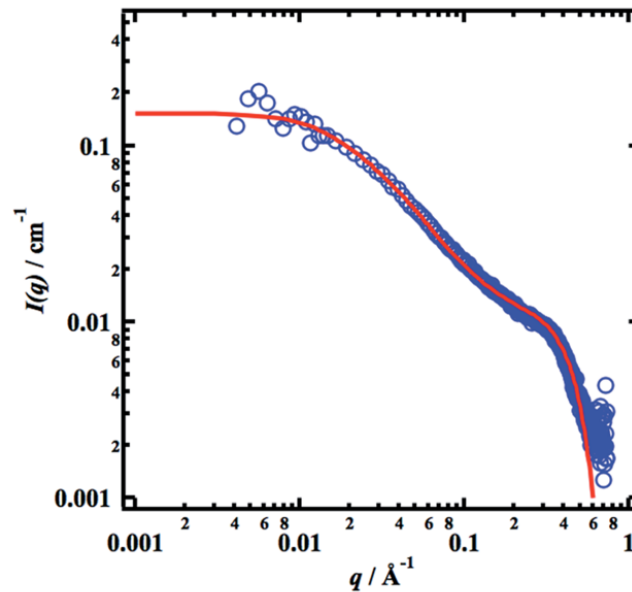


**Figure 1.3.6:** SAXS pattern (blue circles) from a  $0.02 \text{ g/cm}^3$  sample together with a model calculation (red line) (A. Behrens et al., 2016), for a core-shell cylinder with core radius  $5 \text{ \AA}$  and shell thickness  $5 \text{ \AA}$ .

With pulp cellulose, stronger scattering was also found by the same group, and also attributed to aggregates, however smaller and more compacts (Gubitosi et al., 2016). Such transition from exponent 1 and 2 at lower  $q_s$  was also found by Trulove *et al* in ionic liquid (Trulove et al., 2019).

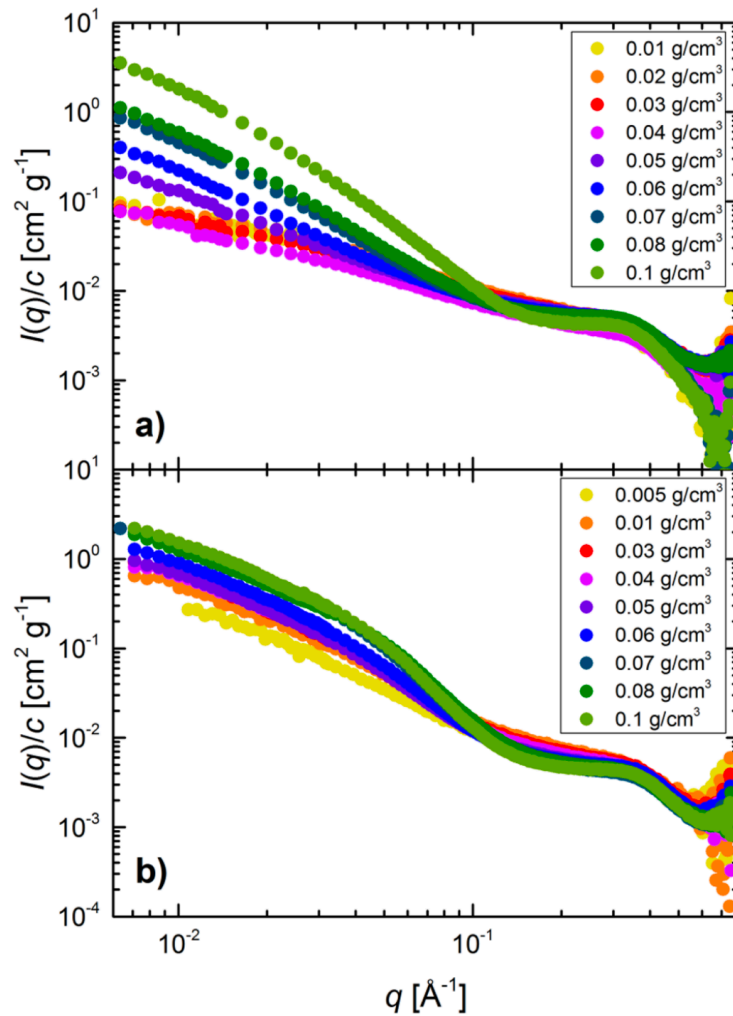


**Figure 1.3.7:** SAXS patterns (Gubitosi et al., 2016) for 0.01–0.10 g/cm<sup>3</sup> MCC (a) and 0.005–0.10 g/cm<sup>3</sup> pulp (b) solutions in 40 wt % TBAH(aq) at 30 °C. The curves are in absolute scale, normalized with cellulose concentrations. The data for MCC has been adapted from (A. Behrens et al., 2016) except the lowest concentration 0.01 g/cm<sup>3</sup>, which was measured in this study.

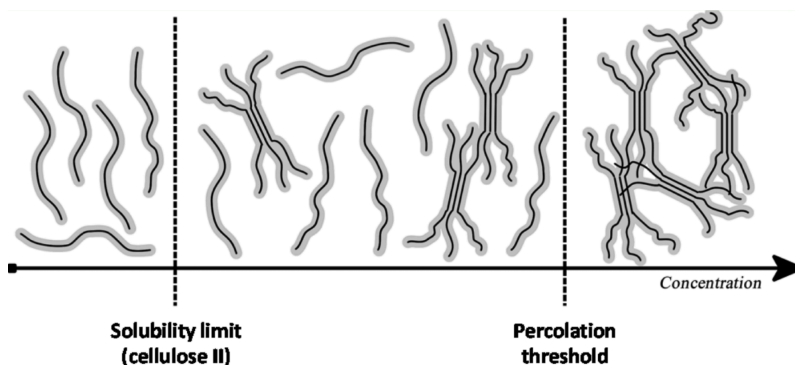


**Figure 1.3.8:** Scheme of cellulose in TBAH (Gubitosi et al., 2016)

In aqueous solutions of NaOH, tetramethylammonium hydroxide (TMAH), benzyltrimethylammonium hydroxide (Triton B) and previously studied equimolar solutions of NaOH/TMAH and NaOH/Triton B, (Swenson et al 2021) found two quite distinct power-law exponents: close to -1 for pure TMA and pure Triton, and with a low  $q$  increase with slope close to -2 for NaOH pure or mixed with TMAH and Triton B, signaling additional structures or objects, less extended. Cellulose in NaOH(aq) is largely aggregated while the more hydrophobic TMAH and Triton are capable of molecularly dissolving cellulose into worm-like conformations.

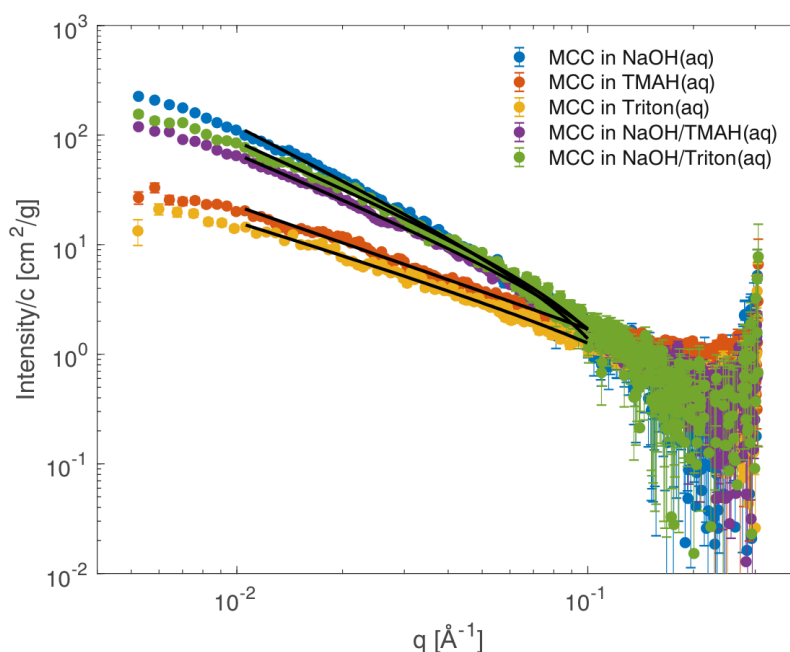


**Figure 1.3.9:** SAXS data normalized by concentration with the black lines showing the linear parts (power laws) fitted within a certain  $q$  range between 0.01 and 0.1 Å<sup>-1</sup> (Swenson et al 2021).



An interesting recent study (Martin-Bertelsen et al., 2020) combines SAXS and SLS from aqueous NaOH, dissolving up to 2 wt % MCC in 8 wt % NaOH. At  $q > 10^{-1} \text{ \AA}^{-1}$  SAXS can be characterized as due to semi-flexible cylinders with relatively long, stiff segments (radius of 4.1 Å, persistence length of 10 nm and total contour length of 60 nm). At lower  $q$ , SAXS shows a slope which increases strongly, signaling aggregates (see **Figure 1.3.10**). SLS confirms, with good connection (after rescaling by the contrast), with SAXS. An estimate of the observed weight-averaged molecular weight  $M_w$  was determined from the Guinier approximation by using  $R(q > 0) = K_{SLS} \cdot c \cdot M_w$  (assuming negligible interactions), which corresponds to a  $M_w = 95 \text{ kg/mol}$ , significantly larger than expected (35.3 kg/mol), but close to a value determined previously for dissolved MCC in TBAH by (A. Behrens et al., 2016). Nicely, the addition of 0.7 wt % ZnO demonstrates that it is aggregation by reducing its level compared to cellulose in neat NaOH.

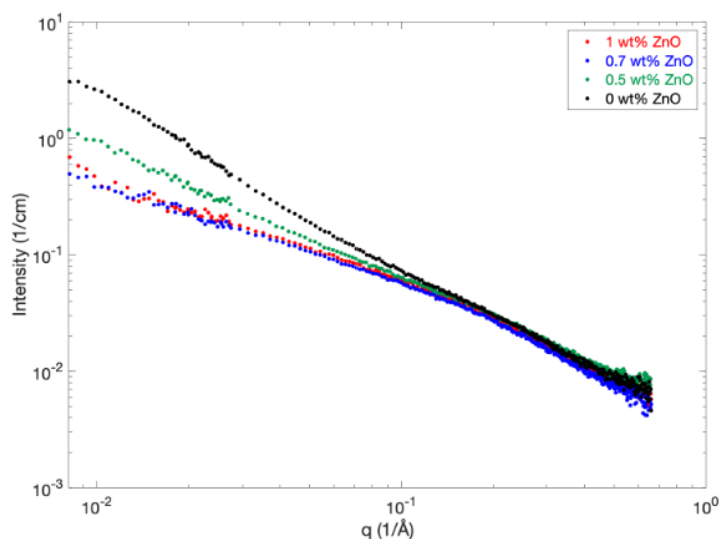


**Figure 1.3.10:** SAXS patterns for 4% MCC dissolved in 8% NaOH with/without a varying content of ZnO (Martin-Bertelsen et al., 2020).

**SANS.** Also in aqueous solvent, namely deuterated phosphoric acid (d-PA), using this time SANS, (Alfassi et al., 2024) obtained again, in water solution of d-PA (85 to 97 % with insignificant differences, see **Figure 1.3.11 a**), a  $q^{-1}$  variation at high  $q$ , with at low  $q$  a clear  $q^{-2}$  for high  $c$  cellulose chains, as found in several other studies. Interestingly, lower content of PA led to a completely different scattering (**Figure 1.3.11 b**), of the biphasic type, indicative of disordered aggregates of rod-like fibrils, with possible surface fractal dimension (2.5), or

simply compact. They may be composed of segments emanating from partially dissolved fibrils, forming smaller-scale structures of gyration radius  $\sim 30 \text{ \AA}$ ).

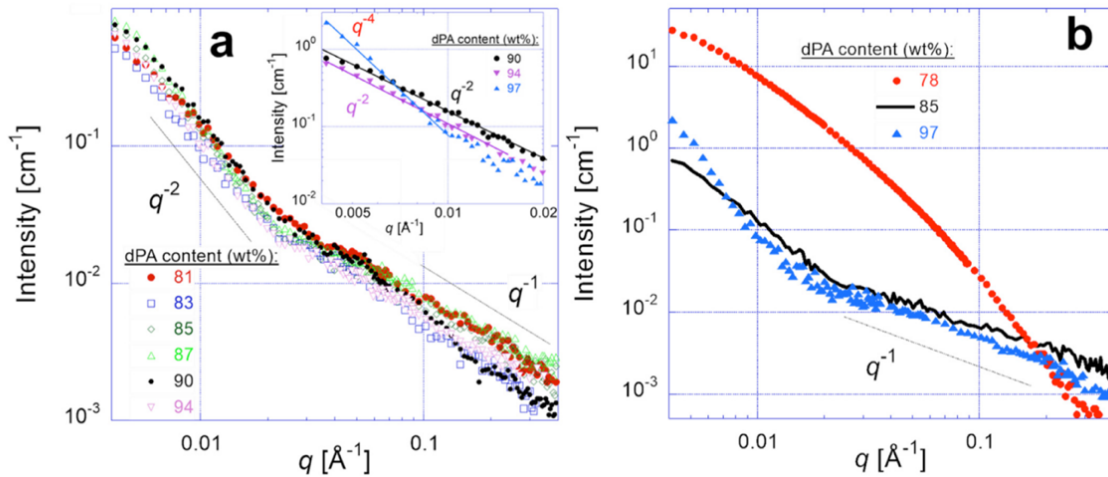


**Figure 1.3.11:** SANS patterns (Alfassi, 2024) from 2 wt% cellulose solutions in d-PA/D2O solvents composed of: (a) 81, 83, 85, 87, 90 and 94 wt% d-PA, exhibiting nearly similar patterns (note, no discernible differences are meant to be demonstrated). Insert: Patterns at low- $q$  from solution in 90, 94 and 97 %; and (b) 78, 85 and 97 wt% d-PA, exhibiting dissimilar patterns (that of 85 % PA solution is repeated for comparison).

Using neutrons and SAXS, Nishiyama and Wang studied the scattering from short chains (oligocellulose hydrolyzed from cellulose in LiOH (Jiang et al., 2021)). In this case, they do not observe aggregation.

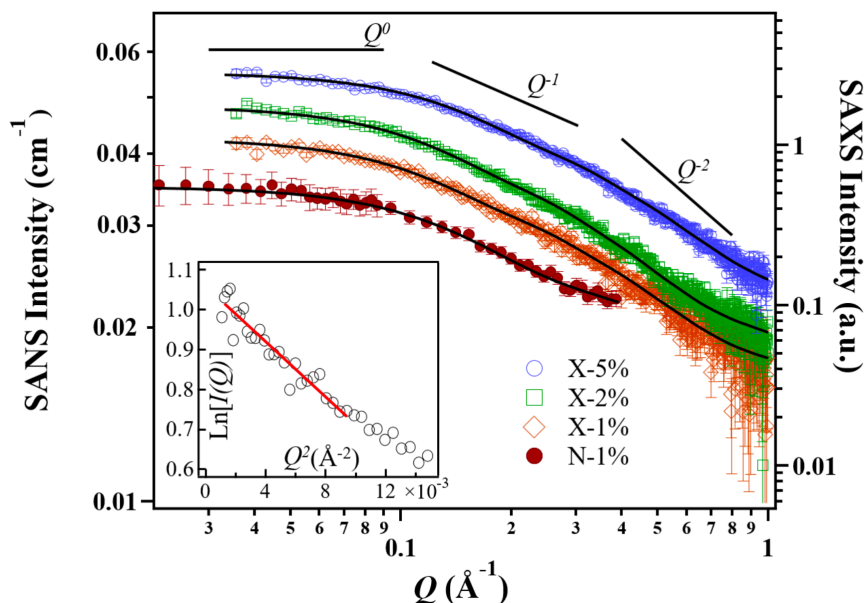


**Figure 1.3.12:** SANS for solutions of oligocellulose in LiOH aqueous solvent (Jiang et al., 2021).

## 1.3.2 Scattering from solutions in Ionic Liquids

### 1.3.2.1 SLS and DLS

In a rather complete study Hirosawa, Hashimoto and Shibayama associated SLS, MD and local structure in a phosphonate-based ionic liquid,  $[C_2mIm][CH_3(H)PO_3]$  (Hirosawa et al., 2017), as well as SAXS (detailed in next section). Based on the high-energy Xray total scattering experiment and MD simulations, a predominant interaction between cellulose and the IL was established, i.e., hydrogen bonding between the IL anion species and hydroxyl groups of cellulose (Figure 1.3.13). In addition, it was found that intramolecular hydrogen bonds existed within cellulose molecules, even when dissolved in the IL. In dynamic light scattering experiments, a speckle pattern was observed for concentrated cellulose solutions. This indicated the existence of a physical-gel-like frozen inhomogeneity. Authors proposed that they arise from pseudo-crosslinks between cellulose molecules.

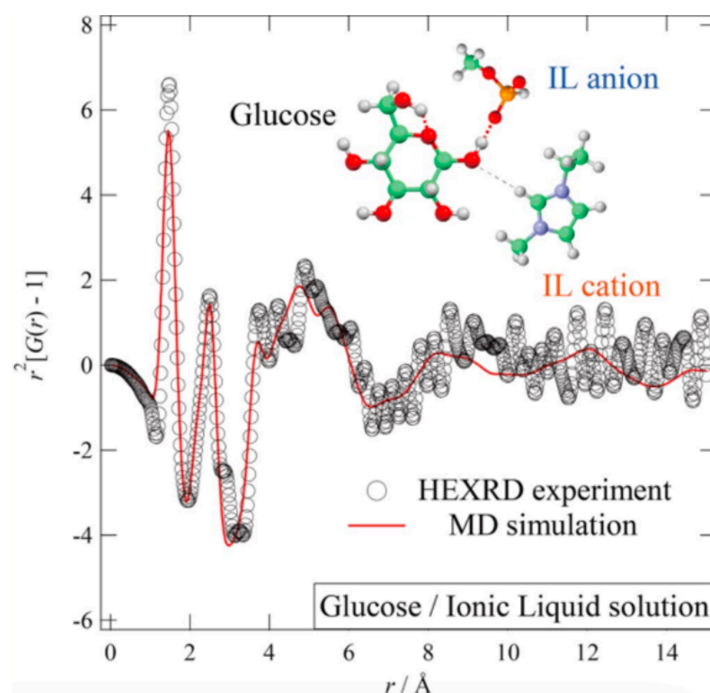


**Figure 1.3.13:** Correlation density function as measured by high-energy X-ray total scattering (Hirosawa et al., 2015).

### 1.3.2.2 SAXS

In the same paper, the conformation of cellulose chains in the IL was investigated by a small-angle X-ray scattering experiment. At very low investigated volume fractions  $\phi$ , the SAXS is the one of a rod, indicating that chains are dispersed in  $[\text{C}_2\text{mIm}][\text{CH}_3(\text{H})\text{PO}_3]$ . It is proposed, erroneously in our opinion, that cellulose molecules existed as rigid-rod-like polymers because of the intramolecular hydrogen bonds within the cellulose molecules.

However as soon as  $\phi \sim 0.01$ , a plateau develops at low  $q$ , while the large  $q^{-1}$  becomes visible only at very large  $q$ . Moreover, as soon as  $\phi > 0.02$ , a strong upturn develops, signaling the aggregates.

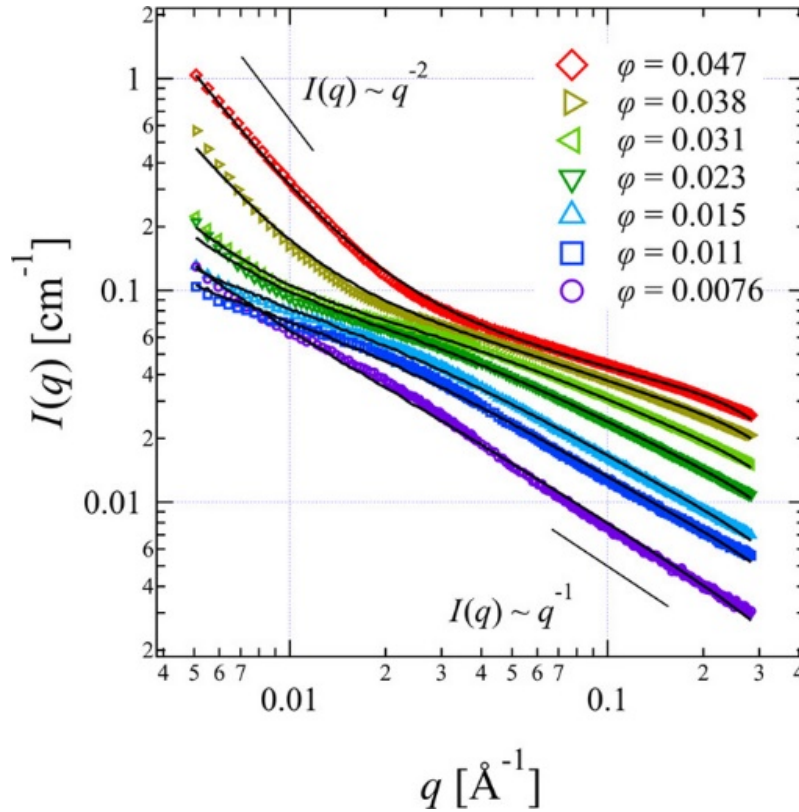


**Figure 1.3.14:** SAXS from a cellulose solution in a phosphonate-based ionic liquid (IL) (Hirosawa et al., 2017), showing an isolated behavior at low volume fraction, and aggregation at higher one. In dynamic light scattering experiments, a speckle pattern for concentrated cellulose solutions indicates the existence of a physical-gel-like frozen inhomogeneity.

Other papers report SAXS or SANS for Ionic Liquids.

A first one has interest of the persistence length. In  $[C_4C_1Im]Cl$  (more developed formula of BmimCl), Jiang-Terao (Jiang et al., 2017) investigated with different polymer mass concentrations  $c$  ranging from  $5 \times 10^{-3}$  to  $5 \times 10^{-2}$  g/cm<sup>3</sup>, Chain Dimensions and Stiffness of Cellulosic and Amylose Chains. They used only SAXS ( $10^{-2} < q < 1.7 \times 10^{-1}$  Å<sup>-1</sup>). The aim was to determine the z-average mean-square radius of gyration  $\langle S^2 \rangle_z$  and the particle scattering function  $P(q)$ . The same analysis as for SLS was applied, namely using the Holzer plot of  $P(q)$ . Here we observe the plateau since we reach much larger  $q_s$  than in SLS.

But the Holzer plot also evidences a slight increase from the  $q^{-1}$  plateau at lower  $q$ , which is analyzed in terms of the wormlike chain model giving Kuhn segment length  $L_k = 2L_p$  at  $7 \pm 1$  nm for cellulose (and  $3.5 \pm 0.5$  nm for amylose). It corresponds to about 14 monomers in cellulose assuming a length of 0.5 nm for one glucose unit. Of course, other origin for the

increase in the slope of the log-log plot can be produced by aggregation, as discussed above and below.

*NOTE: The Holzer plot for our data for 0.5% MCC in BmimAc is very similar to the one of JIANG et al in BmimCl, see Chapter on SAXS!*

In two other ionic liquids, the interest is extended towards larger  $q$ . 1-ethyl-3-methylimidazolium acetate (Emim-OAc) and 1-ethyl-3-methylimidazolium diethyl phosphate (Emim-DEP) Avicel cellulose was observed through SAXS by Koide et al (Koide et al., 2019). They show some aggregation at low  $q$ , while suffering also from the impact of the strong synchrotron X-ray irradiation, and from temperature effect. However at large  $q$  the scattering could be described by a coaxial double cylinder model where the sheath (an outer shell) and the core are constituted of EMIm-OAc or EMIm-DEP solvent molecules and the solute cellulose, respectively. Since the molecular size of Emim-DEP is larger than that of Emim-OAc, the sheath thickness was consequently found to be larger (6.6 Å) than that of cellulose/Emim-OAc solution (4.1 Å).

To end this review, let us quote the paper of Napso, Cohen et al (Napso et al, 2017) for Ethyl Methylimidazolium Acetate (EmimAc), at moderate concentration above overlapping. They did not observe low  $q$  increase, but on the contrary the onset of a plateau when  $q \rightarrow 0$ . This led them to describe the intensity in reference to the one of flexible polymer chains in semi-dilute solution with a correlation length,  $\zeta$  (see below), with a  $q$  dependence not too far from the one of flexible chains. This is surprising, since the exponent  $m$  of  $q^m$  power law observed at a close length scale, i.e. slightly larger  $q$ , was close to the one for a rigid conformation.

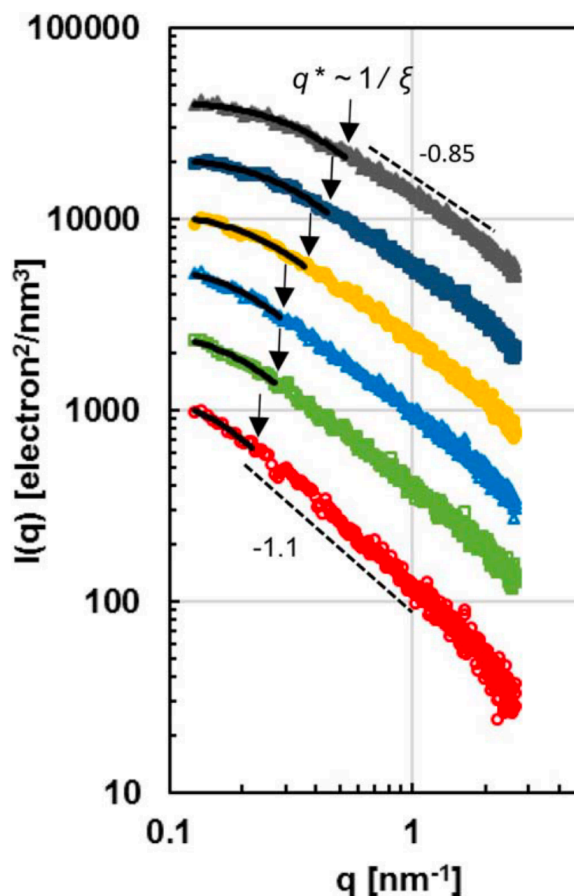


**Figure 1.3.15:** SAXS from cellulose solution in EthylMethylAcetate (EmimAc), at moderate concentration above overlapping, interpreted with a correlation length (Napso et al., 2017).

### 1.3.2.3 SANS

Using neutrons, Raghuwanshi, Garnier, Garvey, and Cohen (Raghuwanshi et al., 2018) obtained similar scattering profiles for MCC cellulose. They observed a surprisingly low intensity, which they attributed to a low contrast, due to adsorption of the deuterated Acetate on the chain. The highly tight binding of acetate and AGU of cellulose in EmimAc was studied by contrast variation of SANS, which show the molar absorption ratio of acetate per AGU were fitted by lower limit  $\approx 0.6$  (Raghuwanshi et al., 2018).

(Annamraju, 2021), in [Emim]acetate and [Amim]formate by SAXS, calculated that formate binds to 4.6 anhydroglucose units (AGUs), while one acetate anion would bind to 2.8 and 4.6 AGUs, with mean radius 2.85 Å. They used the same approach as Raghuwanshi et al to estimate -through fitting of scattering of a rod - the difference between experimental and theoretical contrast. Similarly to the description of Raghuwanshi et al, the acetate anions are proposed by (Idström et al., 2017) to create a “ionic atmosphere” around the cellulose chain with core 5 Å,

shell 5 Å in aqueous solvent implying tetrabutylammonium acetate/dimethyl sulfoxide. The SAXS was described by the Pedersen–Schurtenberger model for semi-flexible polymer chains with excluded volume.

We therefore see that we have a lot of concomitant conclusions in this matter.

Returning to SANS, (Raghuwanshi et al., 2018) also considered the dissolution in h-IL (non deuteriated) of **deuteriated bacterial cellulose**, d-BC. An important upturn at low  $q$  is observed, with a  $q^{-3.4}$  power-law which the authors interpret by surface fractal. However, it is accepted as a modified  $q^{-4}$  law (Porod law) for compact objects with imperfect surfaces. In the dimethylformamide/IL-h solvent mixture, the SANS curve shows a power law of  $q^{-2.5}$ . At larger  $q$ , a  $q^{-1}$  power law is indicative of rigid segments of dissolved d-BC chains. We will observe similar effects in our Chapter on neutron scattering.

Finally, we would like to cite a dynamics measurement associating inelastic neutron scattering (Mean Square Displacement) to SANS. MCC cellulose solutions in mixtures of DiMethylFormamide (DMF) and IL (EmimAc) were investigated by Wang H. et al. (Zhang et al., 2019). They show that MCC can be fully dissolved in solvent mixtures, but also a molecular partitioning of IL into coexisting states, in a phase diagram of ternary cellulose mixtures of MC/IL/DMF (Figure 1.3.16). Dynamics partitioning shows dynamical heterogeneities of the IL with slow dynamics resembling neat IL and fast dynamics being coupled with the DMF solvent.



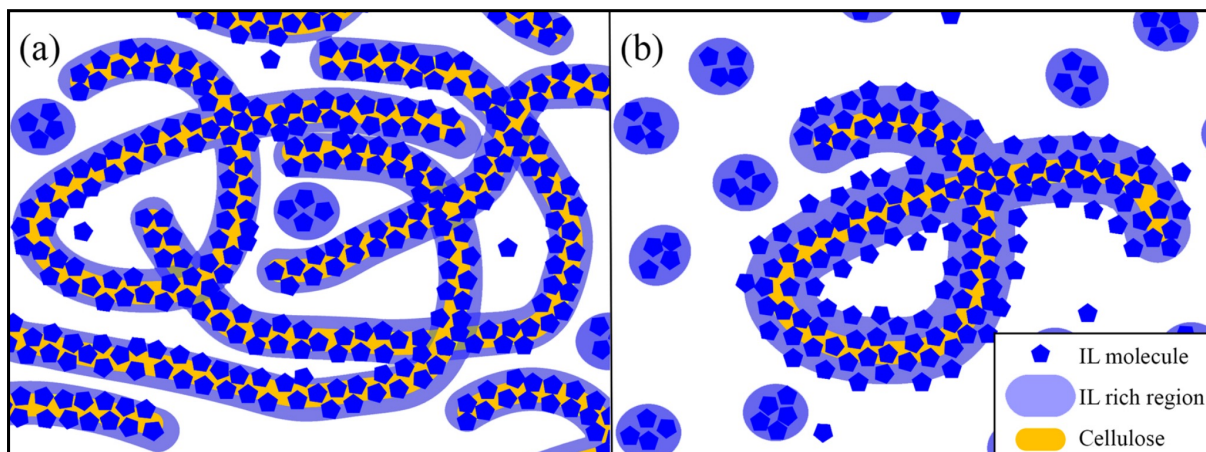


**Figure 1.3.16:** Schematic illustration of the cellulose dissolution in a mixture of ionic liquid and organic solvent (DMF). (a) At high cellulose concentration, IL tightly-bond to cellulose chains to form a thin shell, resulting in a network of worm-like micelles. As most ILs are bonded to cellulose, few clusters form due to limited concentration of free ILs. (b) At low cellulose concentrations, the IL shell is made of the tight-binding ILs directly on cellulose and loose outskirts layers, and clusters form relatively extensively in the continuous liquid phase (Zhang et al., 2019).

## 1.4 Conclusion

We will first give a crude summary, focused on scattering, which applies to aqueous solvents and a few ionic liquids:

- cellulose chains are soluble individually in dilute solutions in many solvents, aqueous ones or ionic liquids, so that a chain form factor  $P(q)$  is involved in the scattering.
- at large  $q$ , Small Angle X Ray Scattering observation of  $P(q)$  converges toward a  $q^{-1}$  (rod) behavior in dilute regime
- at low  $q$ , the SAXS intensity is quite difficult to measure. In former SLS work in aqueous solvents in dilute regime, a flexible chain behavior is reported, and a persistence length of order 10 nm can be obtained from the radius of gyration (with polydispersity issues) or from a crossover observed from  $q^{-1}$  (rod) to  $q^{-2}$  (coil), with the difficulty that the crossover occurs at the limit between the two techniques.
- In semi-dilute regime, observation shows most often chain aggregation both for SLS and SAXS. The system is a model system of semiflexible chains for dilute solutions only, in most of the cases.

In our following studies, we will see how to bring more information when working on our first cellulose/IL solvent system, MCC in BmimAc. Our aim is to describe it, addressing a large range of concentration and temperature. We will show that there is a range of concentration in which it has a simple structure. This model system. is also a departure point to understand a transition to more complex situations, for high concentrations, and for the unavoidable effect of humidity. We will extend the study in parallel to another solvent, of neighbor structure, with the same cation, BmimCl, It will be a way to confirm results, since a similar transition appears shifted towards lower solubility.

## References

- Abbott, A.P., Boothby, D., Capper, G., Davies, D.L., Rasheed, R.K., **2004**. Deep Eutectic Solvents Formed between Choline Chloride and Carboxylic Acids: Versatile Alternatives to Ionic Liquids. *J. Am. Chem. Soc.* *126*(29), 9142–9147. <https://doi.org/10.1021/ja048266j>
- Abe, M., Fukaya, Y., Ohno, H., **2012**. Fast and facile dissolution of cellulose with tetrabutylphosphonium hydroxide containing 40 wt% water. *Chem. Commun.* *48*, 1808–1810. <https://doi.org/10.1039/C2CC16203B>
- A. Behrens, M., A. Holdaway, J., Nosrati, P., Olsson, U., **2016**. On the dissolution state of cellulose in aqueous tetrabutylammonium hydroxide solutions. *RSC Advances.* *6*, 30199–30204. <https://doi.org/10.1039/C6RA03547G>
- Alfassi, G., Radulescu, A., Lifshiz-Simon, S., Rappoport, S., Cohen, Y., **2024**. Small-angle neutron scattering from cellulose solutions in phosphoric acid at different water content. *Giant.* *17*, 100246. <https://doi.org/10.1016/j.giant.2024.100246>
- Alves, L., Medronho, B., Filipe, A., Romano, A., Rasteiro, M.G., Lindman, B., Topgaard, D., Davidovich, I., Talmon, Y., **2021**. Revisiting the dissolution of cellulose in H<sub>3</sub>PO<sub>4</sub>(aq) through cryo-TEM, PTssNMR and DWS. *Carbohydrate Polymers.* *252*, 117122. <https://doi.org/10.1016/j.carbpol.2020.117122>
- Anderson, J.L., Ding, J., Welton, T., Armstrong, D.W., **2002**. Characterizing Ionic Liquids On the Basis of Multiple Solvation Interactions. *J. Am. Chem. Soc.* *124*(47), 14247–14254. <https://doi.org/10.1021/ja028156h>
- Arndt, K.F., Morgenstern, B., Röder, T., **2000**. Scattering function of non-substituted cellulose dissolved in N-methylmorpholine-N-oxide-monohydrate. *Macromol. Symp.* *162*(1), 109–120. [https://doi.org/10.1002/1521-3900\(200012\)162:1<109::AID-MASY109>3.0.CO;2-1](https://doi.org/10.1002/1521-3900(200012)162:1<109::AID-MASY109>3.0.CO;2-1)
- Aziz, T., Farid, A., Haq, F., Kiran, M., Ullah, A., Zhang, K., Li, C., Ghazanfar, S., Sun, H., Ullah, R., Ali, A., Muzammal, M., Shah, M., Akhtar, N., Selim, S., Hagagy, N., Samy, M., Al Jaouni, S.K., **2022**. A Review on the Modification of Cellulose and Its Applications. *Polymers.* *14*, 3206. <https://doi.org/10.3390/polym14153206>
- Betlej, I., Zakaria, S., Krajewski, K.J., Boruszewski, P., **2021**. Bacterial Cellulose - Properties and Its Potential Application. *Sains Malaysiana.* *50*(2), 493–505. <https://doi.org/10.17576/jsm-2021-5002-20>

- Bianchi, E., Ciferri, A., Conio, G., Cosani, A., Terbojevich, M., **1985**. Mesophase formation and chain rigidity in cellulose and derivatives. 4. Cellulose in *N,N*-dimethylacetamide-lithium chloride. *Macromolecules*. 18(4), 646–650. <https://doi.org/10.1021/ma00146a012>
- Bierhalz, A., **2021**. Cellulose nanomaterials in textile applications. *Cellulose Chem. Technol.* 55(7-8), 725–741. <https://doi.org/10.35812/CelluloseChemTechnol.2021.55.61>
- Brown, A.J., **1886**. XIX.—The chemical action of pure cultivations of bacterium aceti. *J. Chem. Soc., Trans.* 49, 172–187. <https://doi.org/10.1039/CT8864900172>
- Burchard, W., Habermann, N., Klüfers, P., Seger, B., Wilhelm, U., **1994**. Cellulose in Schweizer's Reagent: A Stable, Polymeric Metal Complex with High Chain Stiffness. *Angew. Chem. Int. Ed. Engl.* 33(8), 884–887. <https://doi.org/10.1002/anie.199408841>
- Cai, J., Liu, Y., Zhang, L., **2006**. Dilute solution properties of cellulose in LiOH/urea aqueous system. *J. Polym. Sci. B Polym. Phys.* 44(21), 3093–3101. <https://doi.org/10.1002/polb.20938>
- Cai, J., Zhang, L., **2005**. Rapid Dissolution of Cellulose in LiOH/Urea and NaOH/Urea Aqueous Solutions. *Macromolecular Bioscience*. 5(6), 539–548. <https://doi.org/10.1002/mabi.200400222>
- Charles, G., **1934**. Cellulose solution. US1943176A.
- Chen, X., Zhang, Y., Cheng, L., Wang, H., **2009**. Rheology of Concentrated Cellulose Solutions in 1-Butyl-3-methylimidazolium Chloride. *J Polym Environ.* 17, 273–279. <https://doi.org/10.1007/s10924-009-0149-4>
- Chen, X., Zhang, Y.M., Wang, H.P., Wang, S.W., Liang, S.W., Colby, R.H., **2011**. Solution rheology of cellulose in 1-butyl-3-methyl imidazolium chloride. *Journal of Rheology*. 55(3), 485–494. <https://doi.org/10.1122/1.3553032>
- Cheng, G., Varanasi, P., Arora, R., Stavila, V., Simmons, B.A., Kent, M.S., Singh, S., **2012**. Impact of Ionic Liquid Pretreatment Conditions on Cellulose Crystalline Structure Using 1-Ethyl-3-methylimidazolium Acetate. *J. Phys. Chem. B.* 116(33), 10049–10054. <https://doi.org/10.1021/jp304538v>
- Ci, Y., Chen, T., Li, F., Zou, X., Tang, Y., **2023**. Cellulose dissolution and regeneration behavior via DBU-levulinic acid solvents. *International Journal of Biological Macromolecules*. 252, 126548. <https://doi.org/10.1016/j.ijbiomac.2023.126548>
- Crawford, B., Ismail, A.E., **2020**. Insight into Cellulose Dissolution with the Tetrabutylphosphonium Chloride-Water Mixture using Molecular Dynamics Simulations. *Polymers*. 12(3), 627. <https://doi.org/10.3390/polym12030627>

- Cross, C.F., Bevan, E.J., Beadle, C., **1902**. Treatment of Viscose for the Preparation of Useful Products therefrom. GB190103592A.
- Druel, L., Niemeyer, P., Milow, B., Budtova, T., **2018**. Rheology of cellulose-[DBNH][CO<sub>2</sub>Et] solutions and shaping into aerogel beads. *Green Chem.* *20*, 3993–4002. <https://doi.org/10.1039/C8GC01189C>
- El Seoud, O.A., Kostag, M., Jedvert, K., Malek, N.I., **2019**. Cellulose in Ionic Liquids and Alkaline Solutions: Advances in the Mechanisms of Biopolymer Dissolution and Regeneration. *Polymers.* *11*(12), 1917. <https://doi.org/10.3390/polym11121917>
- Elsayed, S., Viard, B., Guizani, C., Hellsten, S., Witos, J., Sixta, H., **2020**. Limitations of Cellulose Dissolution and Fiber Spinning in the Lyocell Process Using [mTBDH][OAc] and [DBNH][OAc] Solvents. *Ind. Eng. Chem. Res.* *59*(45), 20211–20220. <https://doi.org/10.1021/acs.iecr.0c04283>
- Fischer, S., Leipner, H., Thümmler, K., Brendler, E., Peters, J., **2003**. Inorganic Molten Salts as Solvents for Cellulose. *Cellulose.* *10*, 227–236. <https://doi.org/10.1023/A:1025128028462>
- Forsberg, D.C.R., Bengtsson, J., Hollinger, N., Kaldéus, T., **2024**. Towards Sustainable Viscose-to-Viscose Production: Strategies for Recycling of Viscose Fibres. *Sustainability.* *16*(10), 4127. <https://doi.org/10.3390/su16104127>
- Fukaya, Y., Hayashi, K., Wada, M., Ohno, H., **2008**. Cellulose dissolution with polar ionic liquids under mild conditions: required factors for anions. *Green Chem.* *10*, 44–46. <https://doi.org/10.1039/B713289A>
- Galamba, J., Alves, V., Jordão, N., Neves, L., **2021**. Development of cellulose-based polymeric structures using dual functional ionic liquids. *RSC Advances.* *11*, 39278–39286. <https://doi.org/10.1039/D1RA03204F>
- Gilbert, R.D., Patton, P.A., **1983**. Liquid crystal formation in cellulose and cellulose derivatives. *Progress in Polymer Science.* *9*(2-3), 115–131. [https://doi.org/10.1016/0079-6700\(83\)90001-1](https://doi.org/10.1016/0079-6700(83)90001-1)
- Gubitosi, M., Duarte, H., Gentile, L., Olsson, U., Medronho, B., **2016**. On cellulose dissolution and aggregation in aqueous tetrabutylammonium hydroxide. *Biomacromolecules.* *17*(9), 2873–2881. <https://doi.org/10.1021/acs.biomac.6b00696>
- Gupta, K.M., Jiang, J., **2015**. Cellulose dissolution and regeneration in ionic liquids: A computational perspective. *Chemical Engineering Science.* *121*, 181–189. <https://doi.org/10.1016/j.ces.2014.07.025>

- Hagman, J., Gentile, L., Jessen, C.M., Behrens, M., Bergqvist, K.-E., Olsson, U., **2017**. On the dissolution state of cellulose in cold alkali solutions. *Cellulose*. *24*, 2003–2015.  
<https://doi.org/10.1007/s10570-017-1272-3>
- Hermanutz, F., Gähr, F., Uerdingen, E., Meister, F., Kosan, B., **2008**. New Developments in Dissolving and Processing of Cellulose in Ionic Liquids. *Macromolecular Symposia*. *262*(1), 23–27. <https://doi.org/10.1002/masy.200850203>
- Hirosawa, K., Fujii, K., Hashimoto, K., Shibayama, M., **2017**. Solvated Structure of Cellulose in a Phosphonate-Based Ionic Liquid. *Macromolecules*. *50*(17), 6509–6517.  
<https://doi.org/10.1021/acs.macromol.7b01138>
- Hirosawa, K., Fujii, K., Hashimoto, K., Umebayashi, Y., Shibayama, M., **2015**. Microscopic Solvation Structure of Glucose in 1-Ethyl-3-methylimidazolium Methylphosphonate Ionic Liquid. *J. Phys. Chem. B*. *119*(20), 6262–6270. <https://doi.org/10.1021/acs.jpcc.5b00724>
- Huang, H., Ge, H., Song, J., Yao, Y., Chen, Q., Xu, M., **2019**. NMR Study on the Roles of Li<sup>+</sup> in the Cellulose Dissolution Process. *ACS Sustainable Chem. Eng.* *7*(1), 618–624.  
<https://doi.org/10.1021/acssuschemeng.8b04177>
- Idström, A., Gentile, L., Gubitosi, M., Olsson, C., Stenqvist, B., Lund, M., Bergqvist, K.-E., Olsson, U., Köhnke, T., Bialik, E., **2017**. On the dissolution of cellulose in tetrabutylammonium acetate/dimethyl sulfoxide: a frustrated solvent. *Cellulose*. *24*, 3645–3657.  
<https://doi.org/10.1007/s10570-017-1370-2>
- Isobe, N., Noguchi, K., Nishiyama, Y., Kimura, S., Wada, M., Kuga, S., **2013**. Role of urea in alkaline dissolution of cellulose. *Cellulose*. *20*, 97–103. <https://doi.org/10.1007/s10570-012-9800-7>
- Jiang, F., Zhang, X., Hwang, W., Nishiyama, Y., Briber, R.M., Wang, H., **2021**. Oligocellulose from acid hydrolysis: A revisit. *Applied Surface Science*. *537*, 147783.  
<https://doi.org/10.1016/j.apsusc.2020.147783>
- Jiang, X., Kitamura, S., Sato, T., Terao, K., **2017**. Chain Dimensions and Stiffness of Cellulosic and Amylosic Chains in an Ionic Liquid: Cellulose, Amylose, and an Amylose Carbamate in BmimCl. *Macromolecules*. *50*(10), 3979–3984.  
<https://doi.org/10.1021/acs.macromol.7b00389>
- Ju, Z., Yu, Y., Feng, S., Lei, T., Zheng, M., Ding, L., Yu, M., **2022**. Theoretical Mechanism on the Cellulose Regeneration from a Cellulose/EmimOAc Mixture in Anti-Solvents. *Materials*. *15*(3), 1158. <https://doi.org/10.3390/ma15031158>

- Kamide, K., Saito, M., Kowsaka, K., **1987**. Temperature Dependence of Limiting Viscosity Number and Radius of Gyration for Cellulose Dissolved in Aqueous 8% Sodium Hydroxide Solution. *Polym J.* *19*, 1173–1181. <https://doi.org/10.1295/polymj.19.1173>
- Kes, M., Christensen, B.E., **2013**. A re-investigation of the Mark–Houwink–Sakurada parameters for cellulose in Cuen: A study based on size-exclusion chromatography combined with multi-angle light scattering and viscometry. *Journal of Chromatography A.* *1281*, 32–37. <https://doi.org/10.1016/j.chroma.2013.01.038>
- Klemm, D., Kramer, F., Moritz, S., Lindström, T., Ankerfors, M., Gray, D., Dorris, A., **2011**. Nanocelluloses: A New Family of Nature-Based Materials. *Angewandte Chemie International Edition.* *50*(24), 5438–5466. <https://doi.org/10.1002/anie.201001273>
- Koide, M., Wataoka, I., Urakawa, H., Kajiwara, K., Henniges, U., Rosenau, T., **2019**. Intrinsic characteristics of cellulose dissolved in an ionic liquid: the shape of a single cellulose molecule in solution. *Cellulose.* *26*, 2233–2242. <https://doi.org/10.1007/s10570-018-02238-3>
- Kostag, M., Pires, P.A.R., El Seoud, O.A., **2020**. Dependence of cellulose dissolution in quaternary ammonium acetates/DMSO on the molecular structure of the electrolyte: use of solvatochromism, micro-calorimetry, and molecular dynamics simulations. *Cellulose.* *27*, 3565–3580. <https://doi.org/10.1007/s10570-020-03050-8>
- Kuzmina, O., Bhardwaj, J., Vincent, S.R., Wanasekara, N.D., Kalossaka, L.M., Griffith, J., Potthast, A., Rahatekar, S., Eichhorn, S.J., Welton, T., **2017**. Superbase ionic liquids for effective cellulose processing from dissolution to carbonisation. *Green Chem.* *19*, 5949–5957. <https://doi.org/10.1039/C7GC02671D>
- Lefroy, K.S., Murray, B.S., Ries, M.E., **2021**. Rheological and NMR Studies of Cellulose Dissolution in the Ionic Liquid BmimAc. *J. Phys. Chem. B.* *125*(29), 8205–8218. <https://doi.org/10.1021/acs.jpcc.1c02848>
- Li, X., Li, H., Ling, Z., Xu, D., You, T., Wu, Y.-Y., Xu, F., **2020**. Room-Temperature Superbase-Derived Ionic Liquids with Facile Synthesis and Low Viscosity: Powerful Solvents for Cellulose Dissolution by Destroying the Cellulose Aggregate Structure. *Macromolecules.* *53*(9), 3284–3295. <https://doi.org/10.1021/acs.macromol.0c00592>
- Li, Y., Liu, X., Zhang, S., Yao, Y., Yao, X., Xu, J., Lu, X., **2015**. Dissolving process of a cellulose bunch in ionic liquids: a molecular dynamics study. *Phys. Chem. Chem. Phys.* *17*, 17894–17905. <https://doi.org/10.1039/C5CP02009C>

- Li, Y., Wang, J., Liu, X., Zhang, S., **2018**. Towards a molecular understanding of cellulose dissolution in ionic liquids: anion/cation effect, synergistic mechanism and physicochemical aspects. *Chem. Sci.* *9*, 4027–4043. <https://doi.org/10.1039/C7SC05392D>
- Liu, H., Cheng, G., Kent, M., Stavila, V., Simmons, B.A., Sale, K.L., Singh, S., **2012**. Simulations Reveal Conformational Changes of Methylhydroxyl Groups during Dissolution of Cellulose I<sub>β</sub> in Ionic Liquid 1-Ethyl-3-methylimidazolium Acetate. *J. Phys. Chem. B.* *116*(28), 8131–8138. <https://doi.org/10.1021/jp301673h>
- Lu, B., Xu, A., Wang, J., **2014**. Cation does matter: how cationic structure affects the dissolution of cellulose in ionic liquids. *Green Chem.* *16*, 1326–1335. <https://doi.org/10.1039/C3GC41733F>
- Luo, M., Roscelli, V.A., Neogi, A.N., Sealey, I.J.E., Jewell, R.A., **2001**. Lyocell fibers, and compositions for making same. US6210801B1.
- Luo, N., Lv, Y.X., Wang, D.X., Zhang, J.M., Wu, J., He, J.S., Zhang, J., **2012**. Direct visualization of solution morphology of cellulose in ionic liquids by conventional TEM at room temperature. *Chemical Communications.* *48*(50), 6283–6285. <https://doi.org/10.1039/C2CC31483E>
- Lv, Y.X., Wu, J., Zhang, J.M., Niu, Y.H., Liu, C.Y., He, J.S., Zhang, J., **2012**. Rheological properties of cellulose/ionic liquid/dimethylsulfoxide (DMSO) solutions. *Polymer.* *53*(12), 2524–2531. <https://doi.org/10.1016/j.polymer.2012.03.037>
- Martin-Bertelsen, B., Andersson, E., Köhnke, T., Hedlund, A., Stigsson, L., Olsson, U., **2020**. Revisiting the Dissolution of Cellulose in NaOH as “Seen” by X-rays. *Polymers.* *12*(2), 342. <https://doi.org/10.3390/polym12020342>
- McCormick, C.L., Callais, P.A., Hutchinson, B.H., **1985**. Solution studies of cellulose in lithium chloride and *N,N*-dimethylacetamide. *Macromolecules.* *18*(12), 2394–2401. <https://doi.org/10.1021/ma00154a010>
- Medronho, B., Lindman, B., **2014**. Competing forces during cellulose dissolution: From solvents to mechanisms. *Current Opinion in Colloid & Interface Science.* *19*(1), 32–40. <https://doi.org/10.1016/j.cocis.2013.12.001>
- Muthu, S.S., Rathinamoorthy, R., **2021**. Bacterial Cellulose: Sustainable Material for Textiles. *Springer Singapore.* <https://doi.org/10.1007/978-981-15-9581-3>
- Napso, S., Rein, D.M., Khalfin, R., Cohen, Y., **2017**. Semidilute solution structure of cellulose in an ionic liquid and its mixture with a polar organic co-solvent studied by small-angle X-ray scattering. *J. Polym. Sci. Part B: Polym. Phys.* *55*(11), 888–894. <https://doi.org/10.1002/polb.24337>



- Nishiyama, Y., Langan, P., Chanzy, H., **2002**. Crystal Structure and Hydrogen-Bonding System in Cellulose I<sub>β</sub> from Synchrotron X-ray and Neutron Fiber Diffraction. *J. Am. Chem. Soc.* *124*(31), 9074–9082. <https://doi.org/10.1021/ja0257319>
- Nishiyama, Y., Langan, P., Wada, M., Forsyth, V.T., **2010**. Looking at hydrogen bonds in cellulose. *Acta Crystallogr. D66*, 1172–1177. <https://doi.org/10.1107/S0907444910032397>
- Östlund, Å., Lundberg, D., Nordstierna, L., Holmberg, K., Nydén, M., **2009**. Dissolution and Gelation of Cellulose in TBAF/DMSO Solutions: The Roles of Fluoride Ions and Water. *Biomacromolecules*. *10*(9), 2401–2407. <https://doi.org/10.1021/bm900667q>
- Pauw, B.R., **2013**. Everything SAXS: small-angle scattering pattern collection and correction. *J. Phys.: Condens. Matter*. *25*, 383201. <https://doi.org/10.1088/0953-8984/25/38/383201>
- Peng, J., Huang, Y., Fu, R., Lu, J., Wang, W., Zhu, W., Yu, Y., Guo, F., Mai, H., **2023**. Microscopic dissolution process of cellulose in alkaline aqueous solvents and its application in CNFs extraction - Investigating temperature as a variable. *Carbohydrate Polymers*. *322*, 121361. <https://doi.org/10.1016/j.carbpol.2023.121361>
- Pinkert, A., Marsh, K.N., Pang, S., Staiger, M.P., **2009**. Ionic Liquids and Their Interaction with Cellulose. *Chem. Rev.* *109*(12), 6712–6728. <https://doi.org/10.1021/cr9001947>
- Portnoy, N.A., Anderson, D.P., **1977**. Chemistry of the Cellulose-N<sub>2</sub>O<sub>4</sub>-DMF Solution: Recovery and Recycle of Raw Materials. Chapter 5: Solvent Spun Rayon, Modified Cellulose Fibers and Derivatives. *ACS Symposium Series*. *58*, 52–70. <https://doi.org/10.1021/bk-1977-0058.ch005>
- Potthast, A., Rosenau, T., Sixta, H., Kosma, P., **2002**. Degradation of cellulosic materials by heating in DMAc/LiCl. *Tetrahedron Letters* *43*(43), 7757–7759. [https://doi.org/10.1016/S0040-4039\(02\)01767-7](https://doi.org/10.1016/S0040-4039(02)01767-7)
- Raghuwanshi, V.S., Cohen, Y., Garnier, G., Garvey, C.J., Russell, R.A., Darwish, T., Garnier, G., **2018**. Cellulose Dissolution in Ionic Liquid: Ion Binding Revealed by Neutron Scattering. *Macromolecules* *51*(19), 7649–7655. <https://doi.org/10.1021/acs.macromol.8b01425>
- Rebière, J., Rouilly, A., Durrieu, V., Violleau, F., **2017**. Characterization of Non-Derivatized Cellulose Samples by Size Exclusion Chromatography in Tetrabutylammonium Fluoride/Dimethylsulfoxide (TBAF/DMSO). *Molecules*. *22*(11), 1985. <https://doi.org/10.3390/molecules22111985>
- Reddy, N., Yang, Y., **2015**. The *N*-Methylmorpholine-*N*-Oxide (NMMO) Process of Producing Regenerated Fibers. In: Innovative Biofibers from Renewable Resources. *Springer, Berlin, Heidelberg*. 65–71. [https://doi.org/10.1007/978-3-662-45136-6\\_18](https://doi.org/10.1007/978-3-662-45136-6_18)

- Röder, T., Morgenstern, B., **1999**. The influence of activation on the solution state of cellulose dissolved in *N*-methylmorpholine-*N*-oxide-monohydrate. *Polymer*. *40*(14), 4143–4147. [https://doi.org/10.1016/S0032-3861\(98\)00674-0](https://doi.org/10.1016/S0032-3861(98)00674-0)
- Ruan, D., Zhang, L., Lue, A., Zhou, J., Chen, H., Chen, X., Chu, B., Kondo, T., **2006**. A Rapid Process for Producing Cellulose Multi-Filament Fibers from a NaOH/Thiourea Solvent System. *Macromolecular Rapid Communications*. *27*(17), 1495–1500. <https://doi.org/10.1002/marc.200600232>
- Saalwächter, K., Burchard, W., Klüfers, P., Kettenbach, G., Mayer, P., Klemm, D., Dugarmaa, S., **2000**. Cellulose Solutions in Water Containing Metal Complexes. *Macromolecules*. *33*(11), 4094–4107. <https://doi.org/10.1021/ma991893m>
- Saito, M., **1983**. Wormlike Chain Parameters of Cellulose and Cellulose Derivatives. *Polym J*. *15*, 213–223. <https://doi.org/10.1295/polymj.15.213>
- Sashina, E., Kashirskii, D., Busygin, K.N. **2016**. Dissolution of cellulose with pyridinium-based ionic liquids: effect of chemical structure and interaction. *Cellulose Chem. Technol.* *50*(2), 199–211.
- Sayyed, A.J., Deshmukh, N.A., Pinjari, D.V., **2019**. A critical review of manufacturing processes used in regenerated cellulosic fibres: viscose, cellulose acetate, cuprammonium, LiCl/DMAc, ionic liquids, and NMMO based lyocell. *Cellulose*. *26*, 2913–2940. <https://doi.org/10.1007/s10570-019-02318-y>
- Seger, B., Aberle, T., Burchard, W., **1996**. Solution behaviour of cellulose and amylose in iron-sodiumtartrate (FeTNa). *Carbohydrate Polymers*. *31*(1-2), 105–112. [https://doi.org/10.1016/S0144-8617\(96\)00080-X](https://doi.org/10.1016/S0144-8617(96)00080-X)
- Seger, B., Burchard, W., **1994**. Structure of cellulose in cuoxam. *Macromolecular Symposia*. *83*(1), 291–310. <https://doi.org/10.1002/masy.19940830124>
- Singh, P., Magalhães, S., Alves, L., Antunes, F., Miguel, M., Lindman, B., Medronho, B., **2019**. Cellulose-based edible films for probiotic entrapment. *Food Hydrocolloids*. *88*, 68–74. <https://doi.org/10.1016/j.foodhyd.2018.08.057>
- Sixta, H., Michud, A., Hauru, L., Asaadi, S., Ma, Y., King, A.W.T., Kilpeläinen, I., Hummel, M., **2015**. Ioncell-F: A High-strength regenerated cellulose fibre. *Nordic Pulp & Paper Research Journal*. *30*(1), 43–57. <https://doi.org/10.3183/npprj-2015-30-01-p043-057>
- Skočaj, M., **2019**. Bacterial nanocellulose in papermaking. *Cellulose*. *26*, 6477–6488. <https://doi.org/10.1007/s10570-019-02566-y>

- Striegel, AndréM., **1997**. Theory and applications of DMAc/LiCl in the analysis of polysaccharides. *Carbohydrate Polymers*. *34*(4), 267–274. [https://doi.org/10.1016/S0144-8617\(97\)00101-X](https://doi.org/10.1016/S0144-8617(97)00101-X)
- Swatloski, R.P., Spear, S.K., Holbrey, J.D., Rogers, R.D., **2002**. Dissolution of Cellulose with Ionic Liquids. *J. Am. Chem. Soc.* *124*(18), 4974–4975. <https://doi.org/10.1021/ja025790m>
- Swensson, B., Lages, S., Berke, B., Larsson, A., Hasani, M., **2021**. Scattering studies of the size and structure of cellulose dissolved in aqueous hydroxide base solvents. *Carbohydrate Polymers*. *274*, 118634. <https://doi.org/10.1016/j.carbpol.2021.118634>
- Swensson, B., Larsson, A., Hasani, M., **2020**. Dissolution of cellulose using a combination of hydroxide bases in aqueous solution. *Cellulose*. *27*, 101–112. <https://doi.org/10.1007/s10570-019-02780-8>
- Szabó, L., Milotskyi, R., Sharma, G., Takahashi, K., **2023**. Cellulose processing in ionic liquids from a materials science perspective: turning a versatile biopolymer into the cornerstone of our sustainable future. *Green Chem.* *25*, 5338–5389. <https://doi.org/10.1039/D2GC04730F>
- Trulove, P.C., Reichert, W.M., De Long, H.C., Kline, S., Rahatekar, S., Gilman, J., Muthukumar, M., **2019**. The Structure and Dynamics of Silk and Cellulose Dissolved in Ionic Liquids. *ECS Trans.* *16*, 111–117. <https://doi.org/10.1149/1.3159315>
- Uto, T., Yamamoto, K., Kadokawa, J., **2018**. Cellulose Crystal Dissolution in Imidazolium-Based Ionic Liquids: A Theoretical Study. *J. Phys. Chem. B.* *122*(1), 258–266. <https://doi.org/10.1021/acs.jpcc.7b09525>
- Wan, J., Diao, H., Yu, J., Song, G., Zhang, J., **2021**. A biaxially stretched cellulose film prepared from ionic liquid solution. *Carbohydrate Polymers*. *260*, 117816. <https://doi.org/10.1016/j.carbpol.2021.117816>
- Wang, H., Gurau, G., Rogers, R.D., **2012**. Ionic liquid processing of cellulose. *Chem. Soc. Rev.* *41*, 1519. <https://doi.org/10.1039/c2cs15311d>
- Wang, S., Sun, P., Zhang, R., Lu, A., Liu, M., Zhang, L., **2017**. Cation/macromolecule interaction in alkaline cellulose solution characterized with pulsed field-gradient spin-echo NMR spectroscopy. *Phys. Chem. Chem. Phys.* *19*, 7486–7490. <https://doi.org/10.1039/C6CP08744B>
- Weng, L., Zhang, L., Ruan, D., Shi, L., Xu, J., **2004**. Thermal Gelation of Cellulose in a NaOH/Thiourea Aqueous Solution. *Langmuir*. *20*(6), 2086–2093. <https://doi.org/10.1021/la035995o>

- Xu, A., Wang, F., **2020**. Carboxylate ionic liquid solvent systems from 2006 to 2020: thermal properties and application in cellulose processing. *Green Chem.* *22*, 7622–7664. <https://doi.org/10.1039/D0GC02840A>
- Yanagisawa, M., Isogai, A., **2005**. SEC–MALS–QELS Study on the Molecular Conformation of Cellulose in LiCl/Amide Solutions. *Biomacromolecules.* *6*(3), 1258–1265. <https://doi.org/10.1021/bm049386m>
- Yang, Y.J., Shin, J.M., Kang, T.H., Kimura, S., Wada, M., Kim, U.J., **2014**. Cellulose dissolution in aqueous lithium bromide solutions. *Cellulose.* *21*, 1175–1181. <https://doi.org/10.1007/s10570-014-0183-9>
- Youngs, T.G.A., Holbrey, J.D., Mullan, C.L., Norman, S.E., Lagunas, M.C., D'Agostino, C., Mantle, M.D., Gladden, L.F., Bowron, D.T., Hardacre, C., **2011**. Neutron diffraction, NMR and molecular dynamics study of glucose dissolved in the ionic liquid 1-ethyl-3-methylimidazolium acetate. *Chemical Science.* *2*(8), 1594–1605. <https://doi.org/10.1039/c1sc00241d>
- Yuan, X., Cheng, G., **2015**. From cellulose fibrils to single chains: understanding cellulose dissolution in ionic liquids. *Phys. Chem. Chem. Phys.* *17*, 31592–31607. <https://doi.org/10.1039/C5CP05744B>
- Zhang, C., Liu, R., Xiang, J., Kang, H., Liu, Z., Huang, Y., **2014**. Dissolution Mechanism of Cellulose in N,N-Dimethylacetamide/Lithium Chloride: Revisiting through Molecular Interactions. *J. Phys. Chem. B.* *118*(31), 9507–9514. <https://doi.org/10.1021/jp506013c>
- Zhang, H., Ionita, A., Serriñan, P., Ferrer, M.L., Rodríguez, M., Tamayo, A., Alons, F., Monte, F., Gutiérrez, M., **2022**. Easy and Efficient Recovery of EMIMCl from Cellulose Solutions by Addition of Acetic Acid and the Transition from the Original Ionic Liquid to an Eutectic Mixture. *Molecules.* *27*(3), 987. <https://doi.org/10.3390/molecules27030987>
- Zhang, H., Wu, J., Zhang, J., He, J., **2005**. 1-Allyl-3-methylimidazolium Chloride Room Temperature Ionic Liquid: A New and Powerful Nonderivatizing Solvent for Cellulose. *Macromolecules.* *38*(20), 8272–8277. <https://doi.org/10.1021/ma0505676>
- Zhang, X., Mao, Y., Tyagi, M., Jiang, F., Henderson, D., Jiang, B., Lin, Z., Jones, R.L., Hu, L., Briber, R.M., Wang, H., **2019**. Molecular partitioning in ternary solutions of cellulose. *Carbohydrate Polymers.* *220*, 157–162. <https://doi.org/10.1016/j.carbpol.2019.05.054>
- Zhao, Y., Liu, X., Wang, J., Zhang, S., **2013**. Insight into the Cosolvent Effect of Cellulose Dissolution in Imidazolium-Based Ionic Liquid Systems. *J. Phys. Chem. B.* *117*(30), 9042–9049. <https://doi.org/10.1021/jp4038039>

Zhong, Y., Wu, J., Kang, H., Liu, R., **2022**. Choline hydroxide based deep eutectic solvent for dissolving cellulose. *Green Chem.* *24*, 2464–2475. <https://doi.org/10.1039/D1GC04130D>

Zhou, J., Zhang, L., Cai, J., **2004**. Behavior of cellulose in NaOH/Urea aqueous solution characterized by light scattering and viscometry. *J. Polym. Sci. B Polym. Phys.* *42*(2), 347–353. <https://doi.org/10.1002/polb.10636>

Zhou, Y., Zhang, X., Yin, D., Zhang, J.M., Mi, Q., Lu, H., Liang, D., Zhang, J., **2022**. The solution state and dissolution process of cellulose in ionic-liquid-based solvents with different hydrogen-bonding basicity and microstructures. *Green Chem.* *24*, 3824–3833. <https://doi.org/10.1039/D2GC00374K>

<b>CHAPTER 2 MATERIALS AND METHODS.....</b>	<b>57</b>
<b>2.1 Different types of cellulose used .....</b>	<b>57</b>
2.1.1 Short chains: Micro-Crystalline Cellulose (MCC).....	57
2.1.2 Long chains: Bacterial Cellulose .....	57
2.1.3 Deuteriated Bacterial Cellulose: preparation.....	58
<b>2.2 Solvents .....</b>	<b>57</b>
2.2.1 Non-deuteriated ionic liquids .....	58
2.2.2 Deuteriated ionic liquids: synthesis .....	59
2.2.3 Deuteriated and non-deuteriated ionic liquids: NMR and FTIR characterization.....	61
2.2.4 Other solvents and materials.....	64
2.2.5 Preparation of cellulose solution .....	65
<b>2.1 NMR procedure .....</b>	<b>66</b>
<b>2.4 FTIR procedure .....</b>	<b>67</b>
<b>2.5 Rheometry .....</b>	<b>69</b>
2.5.1 Steady shear .....	69
2.5.2 Frequency sweep .....	69
2.5.3 Result: Cox-Merz rule and power laws .....	69
<b>2.6 Scattering techniques .....</b>	<b>72</b>
2.6.1 Laboratory X rays .....	74
2.6.2 Synchrotron Radiation (SR) .....	74
2.6.3 Energy dependence of the transmission of samples .....	75
2.6.4 Small-Angle Scattering Data processing and analysis .....	76
2.6.5 Neutron scattering: SANS/WANS .....	79
<b>References.....</b>	<b>81</b>

## CHAPTER 2 Materials and methods

### 2.1 Different types of cellulose used

#### 2.1.1 Short chains: Micro-Crystalline Cellulose (MCC)

“Avicel® PH101” is the form we mostly use as a Micro-Crystalline Cellulose (MCC),  $(C_6H_{10}O_5)_n$ , as it was received from Sigma-Aldrich. (BCCF5370 source,  $d: 0.600 \text{ g/cm}^3$ , CAS-No: 9004-34-6, made in Ireland), It is made from cotton linters, DP~200, with powder particle size ~50  $\mu\text{m}$ ). The water content of the cellulose material was estimated to be approximately 3.8 wt% using thermo-gravimetric analysis. The molecular fraction density of  $(C_6H_{10}O_5)_n$   $1.5 \text{ g/cm}^3$  (Sun, 2005) was used in SAXS treatment.

Two other sources were employed:

- viscose cellulose (VC) (DP~250-350) from the brand Le Chinois, available in supermarkets.
- cellulose from CNC films donated by Benoit Duchemin, Le Havre Université.

#### 2.1.2 Long chains: Bacterial Cellulose

**Bacterial cellulose**, was extracted from **Nata de coco** (which was purchased in supermarket, Nata de coco white, brand: Buenas, product of the Philippines), which is harvested from static fermentation by using coconut water as nutrient source and the use of acetobacter xylinum bacteria in industrial production (Halib et al., 2012; Herawati et al., 2020; Rusdi et al., 2022), cellulose content with 0.7-1% in Nata de coco.

The nata de coco bought from market was cut into small pieces to ~8 ( $2 \times 2 \times 2$ )  $\text{cm}^3$  cube with a knife, then was squeezed to remove most of the water. The small piece was washed and soaked a large amount of distilled water at least 3 weeks to remove most of the sugars, adjust the pH to neutral (pH ~ 6-7) by 5% NaOH solution, then wash it by repeatedly changing distilled water was at least 5 times per week. Then the cleaned nata de coco was put in a Petri dish and was dried in oven at ~ 80 °C for 1 day to remove the water. The small piece stuck together and form a dry film (sheet) due to the loss of water under the oven. In order to facilitate dissolution experiments, the cellulose film was then pulverized with a coffee grinder to produce a fluffy cellulose powder. The cellulose powder was kept in a Petri dish with an aluminum foil, stored in the vacuum box for further uses.

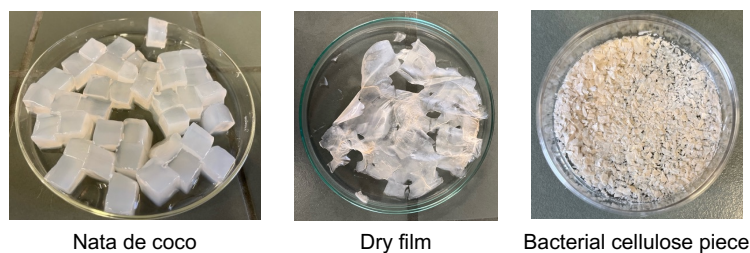


**Figure 2.1.0:** Samples of bacterial cellulose derived from Nata de coco, shown in three stages. From left to right: left) Nata de coco cubes before treatment; middle) Dry film of bacterial cellulose after processing; and right) Pulverized bacterial cellulose piece post-treatment.

### 2.1.3 Deuteriated Bacterial Cellulose: preparation

Deuteriated bacterial cellulose was kindly donated by Prof. Howard Wang and Dr. Yoshiharu Nishiyama. It was elaborated from cell cultures in Oakridge, in Guangdong or in ANSTO. Deuteriated cellulose was prepared by feeding acetobacters with deuteriated glycerol using the classical method (Bali et al., 2013; Chumpitazi-Hermoza et al., 1983, 1978).

Some other deuteriated cellulose was donated by Chris Garvey (ANSTO), which is prepared by growing *Gluconacetobacter xylinus* (ATCC 53524) in deuteriated medium as reported (Raghuwanshi et al., 2017; Su et al., 2016), also used in his papers recently (Raghuwanshi et al., 2021, 2018).

## 2.2 Solvents

### 2.2.1 Non-deuteriated ionic liquids

Two types of Ionic liquid were used: 1-Butyl-3-methylimidazolium Acetate (BmimAc) (> 98%) and 1-Butyl-3-methylimidazolium Chloride (BmimCl) were obtained from IoLiTec (Ionic Liquids Technologies GmbH, Im Zukunftspark 9, D-74076 Heilbronn, Germany).

**BmimAc** is a transparent liquid, claimed to have a BmimAc content of 99.7% with 0.1264% moisture, which was kept in a vacuum chamber before use together with the vials (with melting point: -20 °C, flash point: 153 °C (Safarov et al., 2014)). The BmimAc is a viscous liquid at room temperature, with light yellow color and was stored in vacuum box.



**BmimCl** is a super-cooled liquid (Nishikawa et al., 2007), which is a crystalline solid state at room temperature with melting point:  $\sim 70$  °C, flash point: 192 °C. The commercial BmimCl is a white crystalline powder at room temperature, which is absorbing water quickly and easily. Hence a small amount of BmimCl powder was changed to small liquid droplet in several seconds in the air condition. For using it as a liquid, the BmimCl was heated to 90°C for one day to melt all the crystals. When sample was melted completely, it kept a viscous liquid state for several months when back to the room temperature, which is a colorless transparent viscous liquid. The liquid state BmimCl enables a dissolution at room temperature.

### 2.2.2 Deuteriated ionic liquids: synthesis

Before synthesis of the deuteriated ionic liquids, all the procedures were checked and optimized on the standard hydrogenated (natural abundancy) compounds. The synthesized ionic liquids were detected by  $^1\text{H}$  NMR to compare to the commercial ionic liquids.

**BmimCl** were synthesized using reflux method according to the literature (Cammarata et al., 2001; Clough et al., 2014; Dharaskar et al., 2013a), 1-chlorobutane (10.29 g, 0.11 mol, small stoichiometric excess to compensate evaporation of 1-chlorobutane) was added to a vigorously stirred solution of 1-methylimidazole (8.30 g, 0.10 mol) in toluene (10 ml) with a magnetic stirring on the heating plate at room temperature, the mixture was then heated to 110 °C with reflux for approximately 24 hours. After reflux and reaction, ethyl acetate was added to the solution and then was placed in a freezer set to -20 °C for 12 hours. Subsequently, we get a mixture of crystallized crystals and liquid with toluene and ethyl acetate. The liquid was decanted, and repeatedly re-crystallized from ethyl acetate to yield a soft crystalline solid, which then was dried in vacuum to produce hard white BmimCl crystals with 90% yield characterized by  $^1\text{H}$ -NMR spectroscopy.

The deuteriated BmimCl was synthesized with the same method, replacing 1-chlorobutane by 1-chlorobutane-d9 (1.9867 g, 0.0255 mol), 1-methylimidazole by 1-methylimidazole-d6 (1.5 g, 0.017 mol), the molar ratio of 1-methylimidazole-d6 and 1-chlorobutane-d9 is 1:1.15, toluene (mL). All the other chemical reagents and experimental procedures are the same as described above. This leads to a hard yellow solid [d-Bmim][Cl].

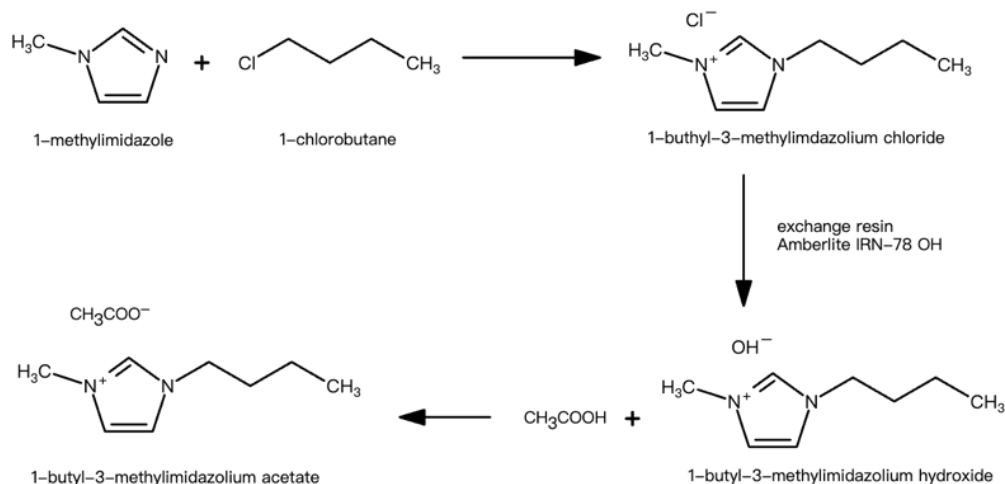


**Figure 2.2.1:** Scheme of the synthesis pathway of 1-butyl-3-methylimidazolium-based ionic liquids. The reaction starts with 1-methylimidazole and 1-chlorobutane to form 1-butyl-3-methylimidazolium chloride (BmimCl). The chloride anion is then exchanged with hydroxide using an Amberlite IRN-78 OH resin to produce 1-butyl-3-methylimidazolium hydroxide (BmimOH). Finally, 1-butyl-3-methylimidazolium acetate (BmimAc) was yielded by the hydroxide reacts between BmimOH and acetic acid.

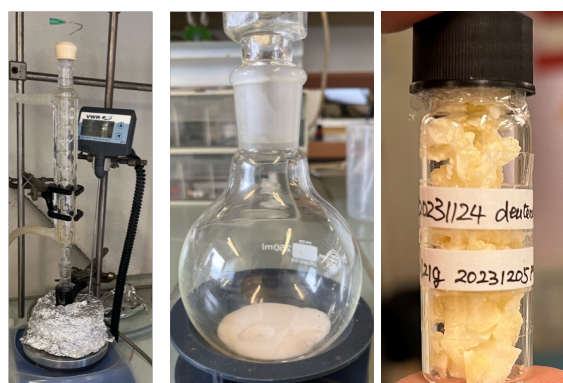


**Figure 2.2.2:** Left: The reflux apparatus used for the synthesis of BmimCl (1-Butyl-3-methylimidazolium chloride) at 70 °C; middle: the purified hydrogenated BmimCl product after synthesis and extraction, with visible residue at the bottom of the flask indicating successful crystallization; right: the purified and dried deuterated [d-Bmim][Cl], which shows the white yellow color.

The synthesis of **BmimAc**, was obtained by an anion exchange on an ion-exchange resin adapted from the procedure described by (Bonhôte et al., 1996; Xu et al., 2012). An aqueous solution of BmimCl was allowed to pass through a column filled with anion exchange resin (amberlite IRN-78 OH) to obtain BmimOH. The progress of the anion exchange was monitored

using aqueous  $\text{AgNO}_3$ , ensuring that once the chloride ions were fully replaced by hydroxide ions, no white  $\text{AgCl}$  precipitation occurred. The resulting aqueous  $\text{BmimOH}$  solution was then neutralized with an equimolar amount of acetic acid. The pH of the solution was carefully monitored using a pH test paper to maintain neutrality and avoid excess acetic acid. Following neutralization, water was removed by evaporation under reduced pressure. The viscous liquid  $\text{BmimAc}$  was obtained after drying under vacuum at  $70^\circ\text{C}$  for at least 2h to remove the residual moisture and characterized by  $^1\text{H-NMR}$ , which gave an estimated amount of water.

The method was also applied to prepare the deuteriated and half deuteriated  $\text{BmimAc}$ , including:

[d- $\text{Bmim}$ ][d- $\text{Ac}$ ]: deuteriated  $\text{BMIm}$  + deuteriated acetate

[d- $\text{Bmim}$ ][h- $\text{Ac}$ ]: deuteriated  $\text{BMIm}$  + hydrogenated acetate

[h- $\text{Bmim}$ ][d- $\text{Ac}$ ]: hydrogenated  $\text{BMIm}$  + deuteriated acetate

For synthesizing [d- $\text{Bmim}$ ][h- $\text{Ac}$ ], precursor ionic liquid  $\text{BmimCl}$  replaced by [d- $\text{Bmim}$ ][ $\text{Cl}$ ], other conditions and reagents remain the same; for [h- $\text{Bmim}$ ][d- $\text{Ac}$ ], replaced acetic acid by acetic acid- $\text{d}_4$  during the synthesis; for [d- $\text{Bmim}$ ][d- $\text{Ac}$ ], we replaced  $\text{BmimCl}$  by [d- $\text{Bmim}$ ][ $\text{Cl}$ ] and acetic acid by acetic acid- $\text{d}_4$ .

#### **Nomenclature used in the following:**

**BAc:** 1-(1,1,1,2,2,3,3,4,4- $\text{H}_9$ )-Butyl-3-(1,1,1- $\text{H}_3$ )-Methyl-imidazolium (1,1,1- $\text{H}_3$ )-acetate

**hBdAc-d3:** 1-(1,1,1,2,2,3,3,4,4- $\text{H}_9$ )-Butyl-3-(1,1,1- $\text{H}_3$ )-Methyl-imidazolium (1,1,1- $\text{D}_3$ )-acetate

**dBhAc-d12:** 1-(1,1,1,2,2,3,3,4,4- $\text{D}_9$ )-Butyl-3-(1,1,1- $\text{D}_3$ )-Methyl-imidazolium (1,1,1- $\text{H}_3$ )-acetate

**dBdAc-d15:** 1-(1,1,1,2,2,3,3,4,4- $\text{D}_9$ )-Butyl-3-(1,1,1- $\text{D}_3$ )-Methyl-imidazolium (1,1,1- $\text{D}_3$ )-acetate

H: hydrogen, D: deuterium.

### **2.2.3 Deuteriated and non-deuteriated ionic liquids: NMR and FTIR characterization**

The  $^1\text{H}$  NMR spectra of  $\text{BmimCl}$  and  $\text{BmimAc}$  are shown in **Figure 2.2.3a**. The assignment of the chemical shift for each peak labeled 2-10, is made with reference to the chemical structure of  $\text{BmimCl}$ . In our work, the proton H(2) signal served as a reference point. The chemical shift of all other signals was determined through the distance from the peak. The proportion of the signal area is correct and agrees well with the corresponding number of protons. This suggests

that NO aggregates are formed in pure BmimCl. The resolved peak at 3.0 ppm in the spectra was assigned to water molecules based on the calculation of the area of this signal (Kaszyńska et al., 2017).

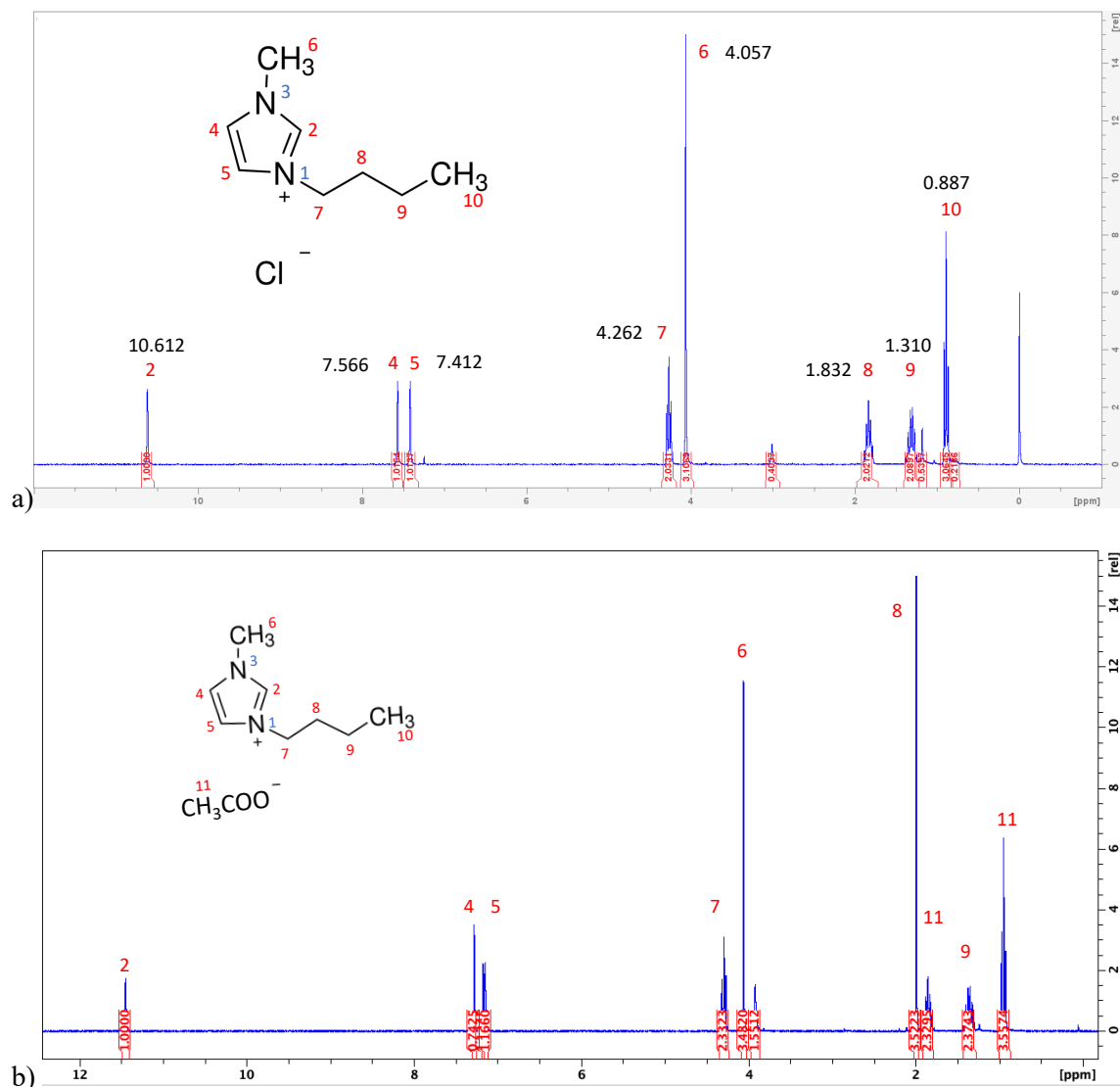


**Figure 2.2.3:** <sup>1</sup>H NMR spectra of non deuteriated ionic liquids. a) non deuteriated BmimCl; b) non deuteriated BmimAc

**Figure 2.2.3b** shows the NMR spectrum of pure hydrogenated BmimCl with full peak assignments, corresponding to the different proton environments (Lefroy et al., 2022). It should be noted that an external reference DMSO-d<sub>6</sub> was added to the NMR tube as a capillary (to ensure accuracy in determining minor peak shifts), since the presence of DMSO may also affect the BmimAc proton environments. The resolved peak at 3.9 ppm in the spectra was assigned to water molecules based on the calculation of the area of this signal.

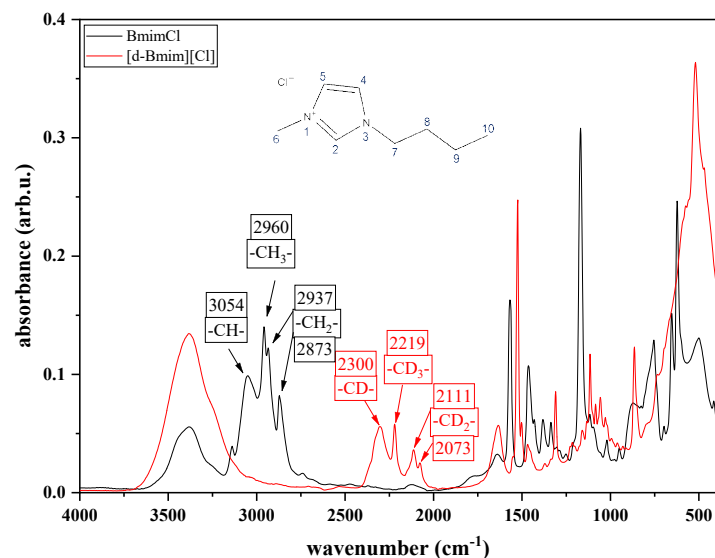


**Figure 2.2.4:** FT-IR (ATR) absorption spectrum of the BmimCl (black) and [d-Bmim][Cl] (red) within the sampling interval of wavenumbers 4000-400  $\text{cm}^{-1}$ .

**Table 2.2.1:** FTIR peak position comparison for C-H and C-D stretching vibrations in BmimCl and [d-Bmim][Cl].

BmimCl	$\tilde{\nu}_{C-H}$	[d-Bmim][Cl]	$\tilde{\nu}_{C-D}$	$\tilde{\nu}_{C-D}/\tilde{\nu}_{C-H}$
-CH	3054	-CD	2300	75.3%
-CH <sub>3</sub> -	2960	-CD <sub>3</sub> -	2219	75.0%
-CH <sub>2</sub> -	2937	-CD <sub>2</sub> -	2111	71.9%
	2873		2073	72.2%

Going now to FTIR: in **Figure 2.2.4**, for hydrogenated BmimCl, the bands in the 3200-2800  $\text{cm}^{-1}$  region were observed, which were attributed to C-H stretching vibrations and overtones of the aromatic ring (Dharaskar et al., 2013b). The 3054  $\text{cm}^{-1}$  peak corresponds to the C-H stretching vibration in the -CH group on the imidazolium ring of BmimCl. The 2960  $\text{cm}^{-1}$  peak corresponds to the C-H stretching vibration in the -CH<sub>3</sub> group on the alkyl chain. The peaks at 2937  $\text{cm}^{-1}$  and 2873  $\text{cm}^{-1}$  correspond to asymmetric and symmetric C-H stretching vibrations in the -CH<sub>2</sub> groups on the alkyl chain. Comparing deuteriated [d-Bmim][Cl], the corresponding peaks exhibit a red shift, the C-D stretching vibrations appear at lower wavenumbers than the corresponding C-H vibrations. The frequency (wavenumber) ratios  $\tilde{\nu}_{C-D}/\tilde{\nu}_{C-H}$  range around 72-75%, consistent with the expected 73.4% (see **Equation 2.4.5**), and decrease in vibrational frequency after deuteriated. This shift is primarily due to deuterium's mass being twice that of

hydrogen, affecting the bond vibrational frequencies, which providing evidence that the [d-Bmim][Cl] has been effectively deuteriated.

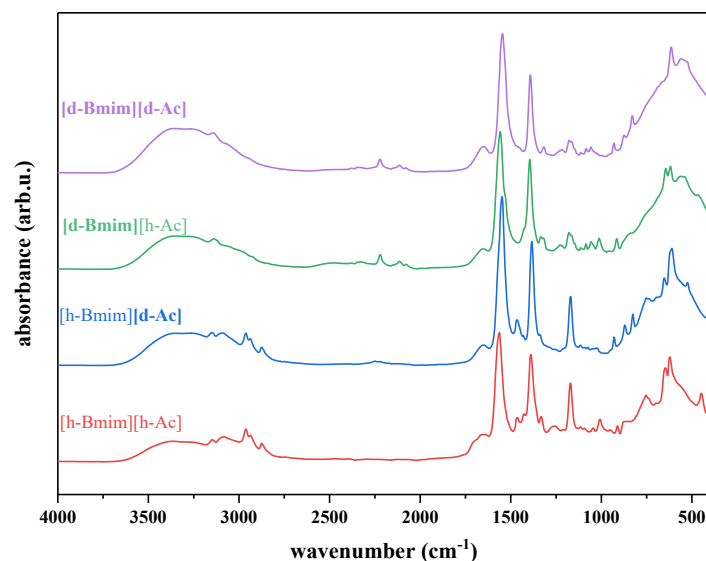


**Figure 2.2.5:** The FT-IR (ATR) absorption spectrum of the hydrogenated, partially deuteriated and fully deuteriated BmimAc within the sampling interval of wavenumbers 4000-400 cm<sup>-1</sup>.

For BmimAc, in **Figure 2.2.5**, it is clear that all the -CH peaks of [1-butyl-3-methylimidazolium]<sup>+</sup> (3100-2800 cm<sup>-1</sup>) of non-deuteriated [h-Bmim][h-Ac] and partially deuteriated [h-Bmim][d-Ac] show a red shift to the low wavenumber (2300-2000 cm<sup>-1</sup>) of partially deuteriated [d-Bmim][h-Ac] and fully deuteriated [d-Bmim][d-Ac].

But comparisons between non-deuteriated and deuteriated acetate are not easy due to the fact that the peaks of -CH<sub>3</sub> are mixed with the peaks of [1-butyl-3-methylimidazolium]<sup>+</sup>.

## 2.2.4 Other solvents and materials

Reagents: 1-methylimidazole (99%), 1-chlorobutane, acetic acid ( $\geq 99\%$ ), toluene ( $\geq 99.8\%$ ), ethyl acid, anion exchange resin (amberlite IRN-78 OH) and deuterium reagent acetic acid-d<sub>4</sub> (ref. 151785) ( $\geq 99.5$  atom % D) was purchased from Sigma-Aldrich. Deuterium reagent 1-methylimidazole-d<sub>6</sub> (98%-d<sub>6</sub>) and 1-chlorobutane-d<sub>9</sub> (99.2%-d<sub>9</sub>) were purchased from CIL (Cluzeau Info Labo). *N,N*-Dimethylacetamide ( $\geq 99.9\%$ ) was purchased from Sigma-Aldrich, dimethyl sulfoxide dried (max 0.03% H<sub>2</sub>O) purchased from Sigma-Aldrich, acetonitrile from Sigma-Aldrich, ethyl acetate purchased from R.P Normapur. 1-Methylimidazole (99%) from

Sigma-Aldrich, 1-chlorobutane from Sigma-Aldrich, sodium hydroxide from Rectapur, urea ( $\geq 99.5\%$ ) from Sigma-Aldrich, and deuterium oxide from Eurisotop.

## 2.2.5 Preparation of cellulose solution

**Cellulose solution:** to obtain the cellulose solution in BmimAc (or BmimCl), the cellulose powder and ionic liquid BmimAc were removed from the vacuum box at the last time to limit moisture, the amount of MCC powder was measured in the 2 mL vial first to prevent the powder to stick on the surface of vial, then BmimAc was added in the vial using pipette gun till 0.3g, shaken using a vortex quickly to make the cellulose powder dispersion homogenous in the BmimAc. Immediately a magnetic stirrer bar was stirred in the vial and the vial was closed by a cap. The sample was stirred on a heating plate with 400 rpm at constant temperature 70 °C, at the atmosphere air condition of the lab. Dissolution was dried over at suitable different times. For example, the stirring was continuous drying 3 h for 0.5-5 wt% MCC solution in BmimAc. For higher concentration than 5 wt%, the dispersion was stirred manually with a needle and heated in the oven at constant temperature, due to the high viscosity. Then we obtained a transparent cellulose/BmimAc solution, and the samples were heated below than 70 °C in a heating desiccator under vacuum to remove residual moisture. The visual determination of solubility is shown in the **Figure 2.2.6** below.

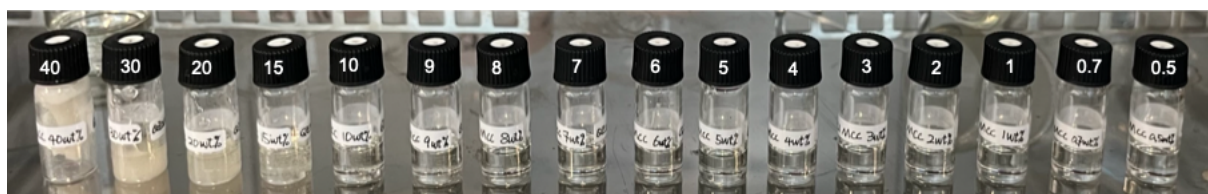


**Figure 2.2.6:** Serial dissolutions of MCC/BmimAc in vials, with concentrations ranging from 40 to 0.5 wt%, as labeled on the vial caps. The decreasing turbidity across the vials indicates progressively lower concentrations of the cellulose suspensions, which are prepared for SAXS characterization.

## 2.3 NMR procedure

**Preparation of  $^1\text{H}$  NMR samples:** In order to characterize the ionic liquid,  $^1\text{H}$ -NMR analyses were carried out for characterization of ILs. The ILs was characterized by  $^1\text{H}$ -NMR using  $\text{CDCl}_3$  as solvent on a spectrometer for determination of molecular structures and conformations. For all NMR analysis, approximately 30 mg of the ILs were transferred into 5 mm NMR tubes. A stem coaxial capillary tube was loaded with 0.5 mL of solute. Ionic liquids were identified by  $^1\text{H}$  NMR spectrometer. NMR spectra were obtained on Bruker Fourier 300 spectrometer with 16-32 scans for  $^1\text{H}$  NMR, with deuteriated DMSO as a solvent and TMS as an internal standard.



## 2.4 FTIR procedure

The (Fourier transform infrared spectroscopy, FTIR) infrared spectra of ionic liquids and cellulose were obtained with a Bruker TENSOR equipped with a Platinum ATR (Attenuated-Total-Reflectance, for the liquids, powders, and solid samples, which are difficult to press into pellets, resulting in unknown thickness), and equipped with a diamond internal reflection element, from 4000 to 400  $\text{cm}^{-1}$ . Spectra acquisition with a resolution of 2  $\text{cm}^{-1}$ , was done at room normal temperature and pressure condition. A spectrum of surrounding atmosphere (moisture vapor) was subtracted from each acquired spectra, and linear baseline and ATR were corrected subsequently. That deals with the interaction between a molecule and radiation from the electromagnetic region ranging (4000-400 $\text{cm}^{-1}$ ).

To estimate the frequency shift of the deuteriated samples, the harmonic vibration equation was used, the radiation was expressed in wavenumbers (Bellisola and Sorio, 2011):

$$\tilde{\nu} = \frac{1}{2\pi c} \sqrt{\frac{k}{m_{reduced}}} \quad (2.4.1)$$

where  $\tilde{\nu}$  is the wavenumber ( $\text{cm}^{-1}$ );  $c$  is the speed of light;  $k$  is the force constant bond (N/m);  $m_{reduced}$  is the reduced mass of the vibrating atoms.

Assume the force constant  $k$  is unchanged between C-H and C-D, the wavenumber ratio between C-H and C-D bonds only depends on the ratio:

$$\frac{\tilde{\nu}_{C-D}}{\tilde{\nu}_{C-H}} = \sqrt{\frac{m_{C-H}}{m_{C-D}}} \quad (2.4.2)$$

where  $m_{C-H}$  and  $m_{C-D}$  are reduced masses. A reduced mass  $m_{reduced}$  is given by:

$$m_{reduced} = \frac{m_{atom_1} \cdot m_{atom_2}}{m_{atom_1} + m_{atom_2}} \quad (2.4.3)$$

where  $m_{atom_1}$  and  $m_{atom_2}$  are the masses of the two atoms involved in the vibration. For the C-H and C-D bonds, the reduced mass will change due to the mass difference between hydrogen (H) and deuterium (D), which affects the vibrational frequency of the bond.

Then,

$$m_{C-H} = \frac{m_C \cdot m_H}{m_C + m_H} = \frac{12 \cdot 1}{12 + 1} \approx 0.923 \text{ amu} \quad (2.4.4a)$$

$$m_{C-D} = \frac{m_C \cdot m_D}{m_C + m_D} = \frac{12 \cdot 2}{12 + 2} \approx 1.714 \text{ amu} \quad (2.4.4b)$$

Thus, estimate the wavenumber ration between C-D and C-H bonds:

$$\frac{\tilde{\nu}_{C-D}}{\tilde{\nu}_{C-H}} = \sqrt{\frac{m_{C-H}}{m_{C-D}}} \approx \sqrt{\frac{0.923}{1.714}} \approx 73.4\% \quad (2.4.5)$$

## 2.5 Rheometry

Rheological measurements were carried out using a Modular Compact Rheometer MCR 302 (Anton Paar GmbH, Austria) with Rheocompass<sup>®</sup> software (v.1.20) for instrument control and data recording. Measurements used a stainless-steel cone-plate geometry (diameter 25 mm, with cone angle 2°) to prevent slippage. The torque was measured by the rheometer; it is generated by the resistance of the sample to shearing and the deflection angle. The elastic moduli ( $G'$ ) and viscous moduli ( $G''$ ) are calculated automatically by the Rheocompass<sup>®</sup> software. Combination of a cone and parallel plate (both Anton Paar GmbH, Austria) was used as upper and lower plateaus, respectively. Since ionic liquids are hygroscopic and the absorption of atmospheric water can result in coagulation of cellulose solution, dry air flux was applied near the measurement cell to avoid the local gelation of the solution. Evaporation at the air-sample-interface was also limited by this device.

### 2.5.1 Steady shear

The shear rheology of cellulose-IL solutions, at increasing shear rate  $\dot{\gamma}$  shows the viscosity results as a function of shear rate  $\eta(\dot{\gamma})$ .

### 2.5.2 Frequency sweep

Directly after the unidirectional shear measurements, an amplitude sweep followed by a frequency sweep, were carried out with the same sample. In the amplitude sweep, the frequency was fixed to 1 Hz and the measurement time to 20s, the amplitude was chosen below the apparition of slippage and the angular frequency and various, leading to  $\eta^*(\omega)$ .

### 2.5.3 Result: Cox-Merz rule and power laws

As a result, the steady shear viscosity  $\eta(\dot{\gamma})$  as the function of the shear rate  $\dot{\gamma}$ , the complex viscosity  $\eta^*(\omega)$  as a function of angular frequency  $\omega$  were measured for cellulose solution over a range of concentrations, for each concentration. The steady shear viscosity overlaps the complex viscosity well, indicating that the empirical Cox-Merz rule,

$$|\eta^*(\omega)| \approx \eta(\dot{\gamma})_{\dot{\gamma}=\omega},$$

where  $\eta^*$  represents the complex viscosity and  $\omega$  the angular frequency, holds well for various cellulose solution in ionic liquids. The pure BmimAc solvent has a viscosity of  $\eta_s \approx 0.2$  Pa. s

at 25 °C, which is invariant with shear rate. The agreement with well-characterized BmimAc sample confirms the high purity and low water content of the ionic liquid solvent.

The zero-shear viscosity ( $\eta_0$ ) as a function of cellulose concentration showed a linear region - proportional to  $c$  at dilute cellulose concentration ( $c < 0.5$  wt%) followed by a power dependence,

$$\eta_0 = c^n$$

which is similar with some previously reported scaling for cellulose solutions at a similar temperature in the same IL solvent (Chen-Colby et al, 2011).

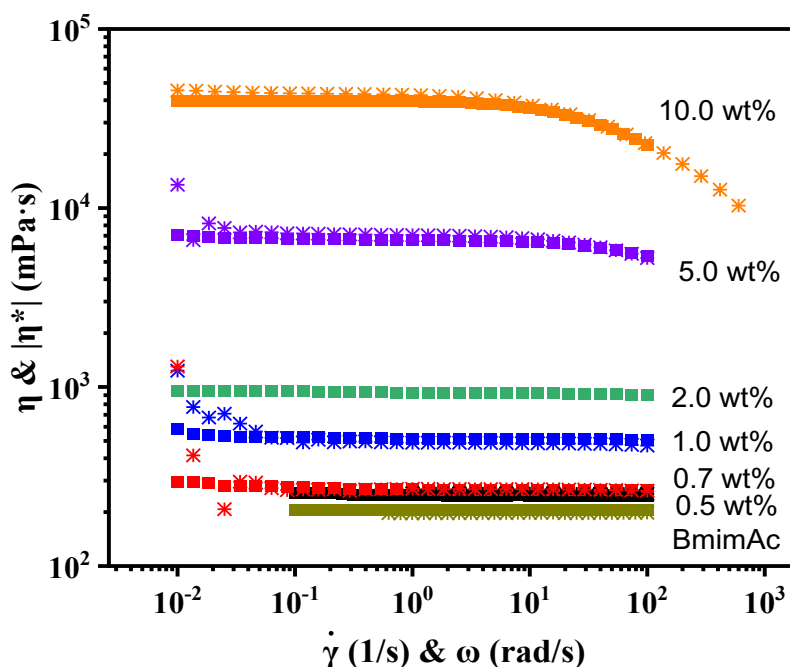


**Figure 2.5.1:** Complex viscosity,  $\eta^*(\omega) = (G'(\omega) + iG''(\omega))/\omega$  of MCC solutions in BmimAcetate at different concentrations: frequency sweep (\*) (viscosity  $\eta(\dot{\gamma})$  with shear rate(1/s)), and comparison with continuous sweep ( $\square$ ) (complex viscosity  $|\eta^*(\omega)|$  with angular frequency (rad/s)). Both overlaps.

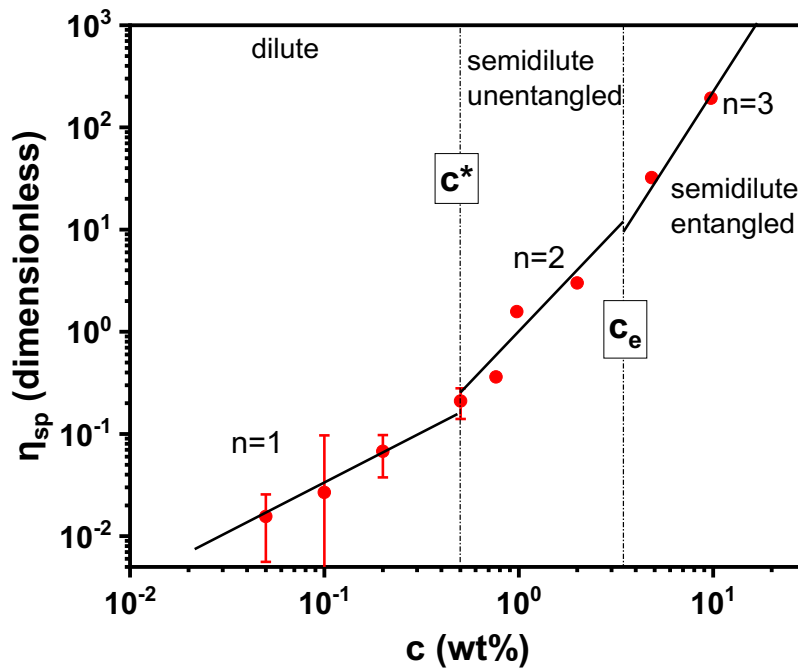


**Figure 2.5.2:** Dependence of the specific viscosity ( $\eta_{sp}$ ) on cellulose concentration in BmimAc solutions at 25 °C, with power-law. The  $c^*$  and  $c_e$  represent the overlap and entanglement concentrations respectively.

From the variation of the viscosity with concentration, we can estimate an apparent exponent always larger than 1 for  $c > 0.7\%$ . For  $c < 0.7\%$ , the accuracy is low. However, all measurements show that the slope 2 is no longer observed. More accurate measurements would be useful. We conclude at this stage that the  $c^*$  is inferior to 1 %.

## 2.6 Scattering techniques

Small Angle Scattering (SAS) techniques, including X-ray (SAXS) and neutron scattering (SANS), investigate the nanoscale structure of materials by measuring the elastically scattered intensity as a function of the scattering vector modulus  $q$ . The scattering vector  $q$  is related to the scattering angle  $2\theta$  and the wavelength  $\lambda$  of the photons or neutrons used. The scattered intensity  $I(q)$  represents the Fourier transform of the correlation function of the electron or nuclear density within the sample. This relationship provides insights into the spatial correlations in the sample, illustrating a connection between the size of the scattering entities and the scattering vector  $q$ .

The scattering vector  $q$  is defined as the difference between the incident wave vector  $k_i$  and the scattered wave vector  $k_j$ :

$$q = k_j - k_i \quad (2.6.1)$$

The modulus of  $q$  is given by:

$$q = \frac{4\pi}{\lambda} \sin\left(\frac{\theta}{2}\right) \quad (2.6.2)$$

where  $\lambda$  is the wavelength of the incident radiation, and  $\theta$  is the scattering angle.

The scattering intensity  $I(q)$  is related to the spatial distribution of the scattering length density (electron density in X-ray or nuclear density in neutrons) within the samples. It is given by the square of the modulus of Fourier transform of the autocorrelation function of the scattering length density:

$$I(\mathbf{q}) = \left| \int_V \rho(\mathbf{r}) e^{i\mathbf{q}\cdot\mathbf{r}} d\mathbf{r} \right|^2 \quad (2.6.3)$$

where  $\rho(\mathbf{r})$  is the scattering length density at position  $\mathbf{r}$ ;  $V$  is the volume of the sample.

For the system of discrete scattering centers (polymer solution system), Debye's formula expresses the scattering intensity as:

$$I(\mathbf{q}) = \frac{1}{N} \sum_{i=1}^N \sum_{j=1}^N \langle f_i f_j \rangle \frac{\sin(qr_{ij})}{qr_{ij}} \quad (2.6.4)$$

where  $N$  is the number of scattering centers,  $f_i$  and  $f_j$  are the scattering amplitudes of the  $i$ -th and  $j$ -th centers and  $r_{ij}$  is the distance between  $i$  and  $j$ .

Most of the samples were solutions measured in capillaries of different nature : i) Kapton capillary with diameter 1.5 mm wall thickness 0.015 mm, ii) borosilicate glass capillary with diameter 1.5 mm wall thickness 0.01 mm, iii) quartz glass capillary with diameter 1.5 mm wall thickness 0.01 mm, and iv) square Borosilicate tube 0.8 mm thickness with wall thickness 0.16 mm. Exceptions are films and fibers, standing by themselves, but also gels which could hold in between windows of Kapton films with spacer to get a thickness 0.015 mm.

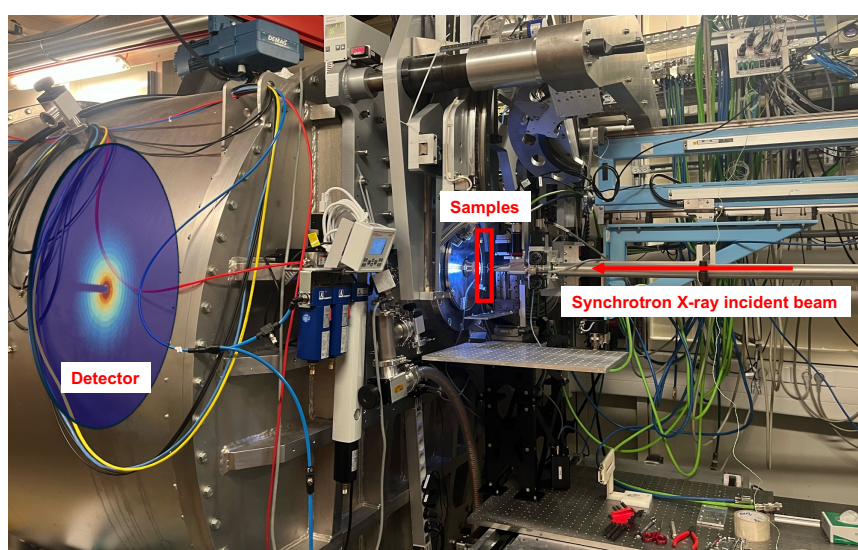


**Figure 2.6.1:** SAXS instrument from SWING beamline of Soleil Synchrotron

2D data were normalized to the sample thickness and transmission. Absolute intensity (not intrinsic intensity, so we did not divide by the cellulose concentration, unless specified) per sample volume ( $\text{cm}^{-1}$ ) was obtained using either a reference sample (a capillary filled of water with the absolute scattering intensity of  $0.016325 \text{ cm}^{-1}$ , or a glassy carbon standard sample) or using the direct incident flux measurement method. The background also has been corrected.

### 2.6.1 Laboratory X rays

SAXS and WAXS initial measurements of first samples were carried out on the XEUSS 2.0 apparatus of Laboratoire Léon Brillouin, installed in the SWAXS lab (Saclay, France). The instrument uses a micro focused Genix source with a Cu K $\alpha$  wavelength of 1.54 Å with energy 8 keV, coupled with scatter slits (Xenocs, France) and a Pilatus3 1M detector (Dectris, Switzerland). The sample to detector distance can be set 0.539m with a collimated beam size of  $0.8 \times 0.8 \text{ mm}^2$ , to achieve a good resolution in a  $q$  range from  $2 \times 10^{-2} \text{ \AA}^{-1}$  to approximately  $3 \times 10^{-1} \text{ \AA}^{-1}$ . Each measurement was performed in the middle (x and z axis) of the capillary at ambient environment, with the acquisition time of 1h. The 2D images were processed for azimuthal averaging and background subtraction using the [pygdatax](#) software.

### 2.6.2 Synchrotron Radiation (SR)

We used the **SWING** (<https://www.synchrotron-soleil.fr/en/beamlines/swing>) beamline at the Synchrotron Soleil (Saint Aubin, France), with Eiger X4M detector. The sample-to-detector distance can be fixed at 0.5m and 6m, the X-ray energy was set most of the time to 12 keV (sometimes 16 keV), giving scattering vector  $q$  range from  $0.0018 \text{ \AA}^{-1}$  to  $0.22 \text{ \AA}^{-1}$ . The samples were vertically scanned (always in the x-axis center) by a narrow beam ( $50 \text{ \mu m} \times 300 \text{ \mu m}$ , height  $\times$  width), the acquisition time was 200 ms, with a 1000 ms interval, due to the high flux  $5.10^{12} \text{ ph/s}$  for 12 keV. The data treatment used the [Foxtrot](#) software.

Ultra-Small Angle X-ray Scattering (USAXS) measurements were performed on the **ID02** (<https://www.esrf.fr/home/UsersAndScience/Experiments/CBS/ID02.html>) beamline at the European Synchrotron Radiation Facility (ESRF) in Grenoble, France. The X-ray wavelength was 0.1 nm at 12 keV and sample to detector distance was fixed at 31 m or 10 m to cover a  $q$  range about  $0.0004 - 0.02 \text{ \AA}^{-1}$ . At the sample position, the photon flux was about 1010 photons/s, and the beam size was  $120 \text{ \mu m} \times 63 \text{ \mu m}$  (horizontal and vertical dimensions). Scattering patterns were recorded on a flight tube-enclosed EIGER2 4M detector (Dectris) with a 0.1 s (not sure) exposure time to avoid beam damage by X-ray overexposure. Radial integration of 2D SAXS patterns was performed to obtain 1D plots by [SAXSutilities](#).



### 2.6.3 Energy dependence of the transmission of samples

The curve below shows that for low energy (8 keV) as used in our laboratory, the transmission can be very low (in particular for BmimCl). SR SAXS ensures much higher transmission at larger wavelength, 12 keV and 16 keV. BmimCl contains chlorine, which makes it a material with high x-ray absorption. That means that only a few ratios of incident X-rays are transmitted and scattered through BmimCl. In an energy range of X-ray experiments 8 keV in XEUSS, the scattering (coherent and incoherent) contribution is small, the X-ray transmission is around 0.03, making the uncertainties too big. In comparison, at higher photon energy, as accessible on SWING beamline with 12 keV (Soleil Synchrotron SAXS), increases the transmission to ~ 0.3 for 12 keV (see BmimCl X-ray transmission relation with energy in **Figure 2.6.2**), and this problem disappears. We can also decrease the thickness of the samples to increase the transmission, but it will decrease the scattering contribution, while the background scattering from the Kapton capillary remains the same.

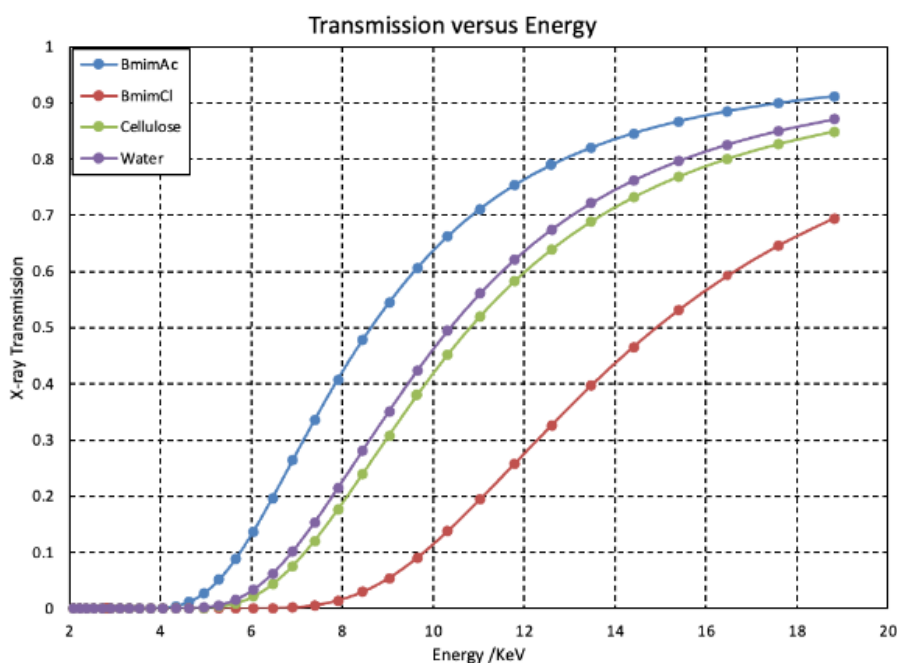


**Figure 2.6.2:** The plot of transmission of ionic liquid, [Bmim][Chloride], [Bmim][OAc], cellulose and standard water with X ray energy. The transmission is calculated by the thickness of 0.15 cm which is the diameter of Kapton capillary. X-ray transmission dependence of X-ray energy, Calculated by [X-Ray Transmission Calculator](#), using Beer-Lambert Law:  $T = e^{-\mu \cdot d}$ , where T is X-ray transmission and  $\mu$  the absorption coefficient which depends on the materials' properties, density and X-ray energy E ( $\mu \propto E^3$ ); d is the sample thickness.

The relationship between the imaginary part of the form factor  $f_2$  (which represents the component associated with photon absorption or inelastic scattering) and X-ray scattering energy [ $f_2$  (e/atom) vs  $E$  (keV)], was calculated by [NIST attenuation calculator](#) based on [NIST X-ray attenuation database](#).

The mass attenuation coefficient  $\mu/\rho$  (which represents the attenuation of X-ray radiation per unit mass of the material) is calculated by the imaginary part of the form factor  $f_2$ :

$$\mu/\rho = f_2 \times constant \quad (2.6.5)$$

with *constant* based on the material and experiment condition.

Linear Attenuation Coefficient  $\mu$  (which represents the degree of attenuation the X-ray undergoes when passing through a unit thickness of the material):

$$\mu = (\mu/\rho) \times \rho \quad (2.6.6)$$

$\rho$  is the density of sample.

The X-ray transmission  $T$  is calculated using the attenuation coefficient:

$$T = e^{-\mu d} \quad (2.6.7)$$

$d$  is the thickness of the material (0.15 cm for Kapton capillary)

The **Figure 2.6.3** illustrates the fact that synchrotron SAXS with 12 keV provide higher transmission compared to Lab SAXS (8 keV). This reduces the impact of absorption effect of X-ray, improves the signal quality (signal-to-noise ratio). It also provides higher brightness, and ensures sufficient scattering intensity is collected, which is essential for obtaining accurate and reliable SAXS data. Also to account is the possibility of heating the sample, leading to degradation or boiling.

## 2.6.4 Small-Angle Scattering Data processing and analysis

Small Angle X-Ray Scattering (SAXS) is a technique used to derive low resolution structural information about the shape and conformational changes of macromolecules in solution by taking advantage of the scattering intensities at different angles. For getting the information of conformational cellulose chain, the SAXS data were processed and analyzed as follows.

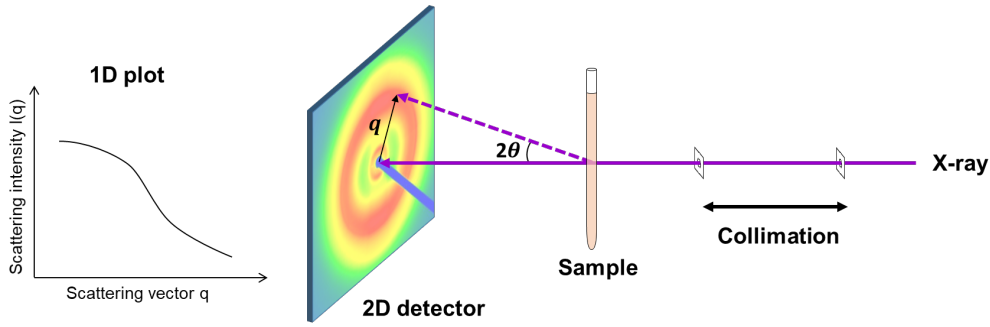


**Figure 2.6.3:** The procedure of SAXS data treatment from 2D to 1D

The samples were irradiated by the incident X-ray (or neutron) beam which is collimated by several slits. The elastic scattering signals from the inhomogeneous structures within the samples were captured by the pixels of the detector to obtain the intensity. The modulus of scattering vector  $q$  was calculated by  $q = \frac{4\pi}{\lambda} \sin \theta$ , with  $2\theta$  the scattering angle (see below) and  $\lambda$  the photon (or neutron) wavelength. That expression of the scattering vector  $q$  assumes elastic scattering (no change of energy/wavelength). The averaged intensity  $I(q)$ , is the square of the amplitude, which is the Fourier Transform of the spatial correlation function of all photons (or neutron) scattering length density (SLD) fluctuations in the sample.

**2D->1D:** The two-dimensional raw SAXS patterns were detected by collecting counts in each pixel of the 2D detector, which is under vacuum to avoid the air effect and light scattering. We **mask** the shadow of the beam stop and bad areas (or points) in the 2D SAXS pattern. Then after checking that scattering is isotropic, the 1D raw data were obtained through **azimuthal radial integration** from 2D SAXS pattern in rings with the scattering center as the beam center of the 2D pattern, measured for each measurement to account for possible beam moving. Thus, scattering along different directions of the scattering vector  $q$  is added to produce the one-dimensional raw scattering curve. It depends on the angle  $\theta$ , corrected by the sample-to-detector distance and rotation angle of the detector to avoid the deviation in the 1D raw data, or more physically can be expressed as a function of  $q = \frac{4\pi}{\lambda} \sin \theta$ . The intensity is corrected (divided) by the **transmission**:  $T = I_{transmitted \text{ by sample}} / I_{incident \text{ beam}}$ . It is then subtracted from empty cell, divided by the sample thickness, and normalized – i.e. re-scaled by the absolute intensity of **water**, which is measured with the same thickness as samples and equal to the absolute value  $\cong 0.0163 \text{ cm}^{-1}$  (Fan et al., 2010; Xie et al., 2018). The measured absolute intensity of a **Glassy carbon** sample as a function of  $q$ , which is more accurate, was also used. We obtain the absolute scattering intensity  $I(q)$  versus scattering vector  $q$ ,  $I(q)$ , in  $\text{cm}^{-1}$ .

**1D reduction:** To extract the structural information of cellulose chains in ionic liquids only, the **background** must be subtracted. Due to the low transmission and low scattering cross-section of cellulose/ionic liquid solutions at low concentrations, the contribution of empty cell and empty beam is a prominent (awfully!) part of the scattering signal, especially the huge intensity from empty cell at low  $q$ . Thus, the data processing (reduction, subtraction) needs to be carried out very accurately. We used capillaries made of quartz, borosilicate glass, or Kapton (polyimide, with chemical stability and heat resistant to avoid the beam damage of the container by the heating of X-ray with long time irradiation, which is majority frequently used in as the sample container in SAXS experiments) capillaries. We used low through capillaries (same capillary, where samples are changed by flow through) only for low cellulose concentration  $< 2$  wt% of in same measurements for comparison background subtraction effects. The solution intensity was obtained from the relationship:  $I_{solution}(q) = I_{raw\ solution}(q) - I_{empty\ cell}(q)$ , in which all  $I(q)$  were corrected by transmission. The scattering intensity of cellulose chain was extracted by  $I_{cellulose}(q) = I_{solution}(q) - f \times I_{solvent}(q)$ ,  $f$  being the volume fraction of solvent. We used the  $I_{cellulose}(q)$  measured in quartz capillary as the standard intensity to correct the scattering of samples contained in other capillaries.

For the samples in **Kapton** substrate, in the low  $q$ -limit the scattering of the Kapton is prevailing, while for other material like quartz, and borosilicate the low  $q$  scattering is very close, after correction by transmission, to the one of the empty beam (divergence, scattering from air). Thus importantly, in the low  $q$ -range the scattering of the Kapton is the limiting factor (Bauer et al., 2019; Lange et al., 2020). Another problem of Kapton is its mechanical properties: being flexible, it can lose its cylindrical shape and become more or less flat during the measurements. That can give changes in the thickness and a huge scattering intensity at low  $q$ , which cannot be used anymore for the capillary background subtraction. Therefore, an “adjusted Kapton”  $I_{adj\ kapton}(q)$  was used for the background subtraction.  $I_{adj\ kapton}(q) = I_{water}(q) - 0.0163\ \text{cm}^{-1}$ . The Kapton effect just described (shape changing, reflection from the capillary wall and uncertainty due to heterogeneity of Kapton) can be removed using such  $I_{adj\ kapton}(q)$ . For WAXS, the intensity of empty capillary was subtracted using  $I_{solution}(q) = I_{raw\ solution}(q) - f_1 \times I_{empty\ capillary}(q)$ . We adjusted the  $f_1$  parameter to remove the Kapton peak coming from the capillary (and sometimes from the spectrometer windows), and which should not be present in the final  $I_{solution}(q)$  data.

After the capillary subtraction, the solvent scattering also needs to be subtracted from the solution to extract the cellulose chain scattering in solution. The scattering contribution from solvent (e.g. Ionic Liquid) was subtracted using:

$$I(q) = I_{solution}(q) - f_2 \times I_{solvent}(q) \quad (2.6.8)$$

With  $f_2$  being the volume fraction of solvent in the solution.

The “Kapton effect” (change in shape/flattening, lower thickness) also influences for large- $q$  range, the solvent subtraction.

Arrived at this stage, a **generalized scattering intensity equation** (shape-structure coupling equation) is used to combine the shape dependent model with structure-dependent model, in the case of **centrosymmetric** assembly of scattering objects.

$$I(q) = N_p(\Delta\rho)^2V_p^2P(q)S(q) = \phi(\Delta\rho)^2V_p^2P(q)S(q) \quad (2.6.9)$$

where  $N_p$  is the number density of particles per  $cm^{-3}$ ;  $\Delta\rho$  is the scattering contrast - the difference between the Scattering Length Density of objects and surrounding media;  $V_p$  is the volume per particle ( $cm^3$ );  $P(q)$  and  $S(q)$  are the form factor – assumed independent of the concentration- and structure factor of the scattered particles. If these conditions, as well as centro - symmetry, are not filled, the factorization (2.6.9) does not apply.

### 2.6.5 Neutron scattering: SANS/WANS

**SANS:** Small Angle Neutron Scattering (SANS) measurements on cellulose solutions were performed on the D22 spectrometer of the Institut Laue-Langevin (ILL, Grenoble, France), which gives access to structural information at low resolution and permits to identify the chain conformation here. The data were acquired on the [D22](#) instrument. The wavelength was fixed at 6.0 Å (relative FWHM 10%), with two configurations combining different detector distances: the front detector was set to 1.4 m, and the rear detector was set to either 5.6 m or the 17.6 m to get the full  $q$  range 0.001-0.1 Å<sup>-1</sup>. The measurements were performed using a thermostatic sample changer allowing access to a constant temperature of 20 °C. Data were reduced with the program Grasp v10.17, normalizing with monitor, subtracting the contribution from empty cell. The transmission intensity was obtained using an attenuated direct beam. Samples were held in 1 mm optical path length flat quartz cuvettes, whatever the solvent was non deuteriated

(hydrogen atoms, no deuterium) or deuteriated (in that case 2 mm could be used but we had not sufficient quantities).

**WANS:** the Wide-angle structure information was investigated on the high-resolution diffractometer [D16](#) at ILL with neutron wavelength  $\lambda = 4.5 \text{ \AA}$  and a sample-to-detector distance at 0.95 m. leading to the scattering vector range ( $2.6 \times 10^{-1} < q < 5.3$ )  $\text{nm}^{-1}$ . The cell was specially and carefully designed. They are aluminium cylinders of 3mm diameter with thin walls, water-proof since water should not go inside the ionic liquid.

## References

- Bali, G., Foston, M.B., O'Neill, H.M., Evans, B.R., He, J., Ragauskas, A.J., **2013**. The effect of deuteration on the structure of bacterial cellulose. *Carbohydrate Research*. 374, 82–88. <https://doi.org/10.1016/j.carres.2013.04.009>
- Bauer, P.S., Amenitsch, H., Baumgartner, B., Köberl, G., Rentenberger, C., Winkler, P.M., **2019**. In-situ aerosol nanoparticle characterization by small angle X-ray scattering at ultra-low volume fraction. *Nat Commun*. 10, 1122. <https://doi.org/10.1038/s41467-019-09066-4>
- Bellisola, G., Sorio, C., **2011**. Infrared spectroscopy and microscopy in cancer research and diagnosis. *Am J Cancer Res*. 2(1), 1–21.
- Bonhôte, P., Dias, A.P., Papageorgiou, N., Kalyanasundaram, K., Grätzel, M., **1996**. Hydrophobic, Highly Conductive Ambient-Temperature Molten Salts. *Inorg. Chem*. 35(5), 1168–1178. <https://doi.org/10.1021/ic951325x>
- Cammarata, L., Kazarian, S.G., Salter, P.A., Welton, T., **2001**. Molecular states of water in room temperature ionic liquids. *Phys. Chem. Chem. Phys*. 3, 5192–5200. <https://doi.org/10.1039/B106900D>
- Chumpitazi-Hermoza, B.F., Gagnaire, D., Taravel, F.R., **1983**. Bacterial biosynthesis of cellulose from d-glucose or glycerol precursors labelled with deuterium. *Carbohydrate Polymers*. 3(1), 1–12. [https://doi.org/10.1016/0144-8617\(83\)90008-5](https://doi.org/10.1016/0144-8617(83)90008-5)
- Chumpitazi-Hermoza, B.F., Gagnaire, D., Taravel, F.R., **1978**. Biosynthèse de cellulose bactérienne à partir de glycérol sélectivement deutérié en position 1, 2, ou 3: Etude par résonance magnétique nucléaire. *Biopolymers*. 17(10), 2361–2372. <https://doi.org/10.1002/bip.1978.360171006>
- Clough, M., Griffith, J., Sulaiman, M.R., Corbett, P., **2014**. Alkylation of 1-Methylimidazole with 1-Chlorobutane. <https://doi.org/10.1039/SP747>
- Dharaskar, S.A., Varma, M.N., Shende, D.Z., Yoo, C.K., Wasewar, K.L., **2013a**. Synthesis, Characterization and Application of 1-Butyl-3 Methylimidazolium Chloride as Green Material for Extractive Desulfurization of Liquid Fuel. *The Scientific World Journal*. 2013, e395274. <https://doi.org/10.1155/2013/395274>
- Dharaskar, S.A., Wasewar, K.L., Varma, Mahesh.N., Shende, Diwakar.Z., Yoo, C.K., **2013b**. Deep Removal of Sulfur from Model Liquid Fuels using 1-Butyl-3-Methylimidazolium Chloride. *Procedia Engineering*. 51, 416–422. <https://doi.org/10.1016/j.proeng.2013.01.058>

- Fan, L., Degen, M., Bendle, S., Grupido, N., Ilavsky, J., **2010**. The Absolute Calibration of a Small-Angle Scattering Instrument with a Laboratory X-ray Source. *J. Phys.: Conf. Ser.* *247*, 012005. <https://doi.org/10.1088/1742-6596/247/1/012005>
- Halib, N., Mohd Amin, M.C.I., Ahmad, I., **2012**. Physicochemical Properties and Characterization of Nata de Coco from Local Food Industries as a Source of Cellulose. *Sains Malaysiana*. *41*(2), 205–211.
- Herawati, H., Kamsiati, E., Widyaputri, S., Sutanto, **2020**. Physic-chemical characteristic of nata de coco. *IOP Conf. Ser.: Earth Environ. Sci.* *458*, 012014. <https://doi.org/10.1088/1755-1315/458/1/012014>
- Kaszyńska, J., Rachocki, A., Bielejewski, M., Tritt-Goc, J., **2017**. Influence of cellulose gel matrix on BMIMCl ionic liquid dynamics and conductivity. *Cellulose*. *24*, 1641–1655. <https://doi.org/10.1007/s10570-017-1223-z>
- Lange, T., Charton, S., Bizien, T., Testard, F., Malloggi, F., **2020**. OSTE+ for in situ SAXS analysis with droplet microfluidic devices. *Lab Chip*. *20*, 2990–3000. <https://doi.org/10.1039/D0LC00454E>
- Lefroy, K.S., Murray, B.S., Ries, M.E., **2022**. Effect of Oil on Cellulose Dissolution in the Ionic Liquid 1-Butyl-3-methyl Imidazolium Acetate. *ACS Omega*. *7*(24), 37532–37545. <https://doi.org/10.1021/acsomega.2c04311>
- Nishikawa, K., Wang, S., Katayanagi, H., Hayashi, S., Hamaguchi, H., Koga, Y., Tozaki, K., **2007**. Melting and Freezing Behaviors of Prototype Ionic Liquids, 1-Butyl-3-methylimidazolium Bromide and Its Chloride, Studied by Using a Nano-Watt Differential Scanning Calorimeter. *J. Phys. Chem. B*. *111*(18), 4894–4900. <https://doi.org/10.1021/jp0671852>
- Raghuwanshi, V.S., Cohen, Y., Garnier, Guillaume, Garvey, C.J., Garnier, Gil, **2021**. Deuteriated Bacterial Cellulose Dissolution in Ionic Liquids. *Macromolecules*. *54*(14), 6982–6989. <https://doi.org/10.1021/acs.macromol.1c00833>
- Raghuwanshi, V.S., Cohen, Y., Garnier, Guillaume, Garvey, C.J., Russell, R.A., Darwish, T., Garnier, Gil, **2018**. Cellulose Dissolution in Ionic Liquid: Ion Binding Revealed by Neutron Scattering. *Macromolecules* *51*(19), 7649–7655. <https://doi.org/10.1021/acs.macromol.8b01425>
- Raghuwanshi, V.S., Su, J., Garvey, C.J., Holt, S.A., Holden, P.J., Batchelor, W.J., Garnier, G., **2017**. Visualization and Quantification of IgG Antibody Adsorbed at the Cellulose–Liquid Interface. *Biomacromolecules* *18*(8), 2439–2445. <https://doi.org/10.1021/acs.biomac.7b00593>
- Rusdi, R.A.A., Halim, N.A., Norizan, M.N., Abidin, Z.H.Z., Abdullah, N., Che Ros, F., Ahmad, N., Azmi, A.F.M., **2022**. Pre-treatment effect on the structure of bacterial cellulose from Nata de



- Coco (*Acetobacter xylinum*). *Polimery*. 67(3), 110–118.  
<https://doi.org/10.14314/polimery.2022.3.3>
- Safarov, J., Geppert-Rybczyńska, M., Kul, I., Hassel, E., **2014**. Thermophysical properties of 1-butyl-3-methylimidazolium acetate over a wide range of temperatures and pressures. *Fluid Phase Equilibria*. 383, 144–155. <https://doi.org/10.1016/j.fluid.2014.10.015>
- Su, J., Raghuwanshi, V.S., Raverty, W., Garvey, C.J., Holden, P.J., Gillon, M., Holt, S.A., Tabor, R., Batchelor, W., Garnier, G., **2016**. Smooth deuterated cellulose films for the visualisation of adsorbed bio-macromolecules. *Sci Rep*. 6, 36119. <https://doi.org/10.1038/srep36119>
- Sun, C. (Calvin), **2005**. True Density of Microcrystalline Cellulose. *Journal of Pharmaceutical Sciences*. 94(10), 2132–2134. <https://doi.org/10.1002/jps.20459>
- Xie, F., Li, Zhihong, Li, Zhenzhong, Li, D., Gao, Y., Wang, B., **2018**. Absolute intensity calibration and application at BSRF SAXS station. *Nuclear Instruments and Methods in Physics Research Section A: Accelerators, Spectrometers, Detectors and Associated Equipment*. 900, 64–68. <https://doi.org/10.1016/j.nima.2018.05.026>
- Xu, A., Zhang, Y., Li, Z., Wang, J., **2012**. Viscosities and Conductivities of 1-Butyl-3-methylimidazolium Carboxylates Ionic Liquids at Different Temperatures. *J. Chem. Eng. Data*. 57(11), 3102–3108. <https://doi.org/10.1021/je300507h>

<b>CHAPTER 3 X-RAY SCATTERING.....</b>	<b>85</b>
<b>3.1 From raw data to treated data: displaying the difficulties .....</b>	<b>86</b>
<b>3.2 Dilute solution .....</b>	<b>90</b>
3.2.1 Difficulties in data treatment.....	90
3.2.2 Description .....	91
3.2.3 Direct estimate of the chain parameters: unit length, cross-section.....	93
3.2.3.1 Unit length - cross-section.....	93
3.2.3.2 Unit cross-section area .....	96
3.2.4 Rod scattering: equations .....	97
3.2.5 Fit to a model form factor .....	99
3.2.5.1 Cylinder form factor in BmimAc .....	99
3.2.5.2 Core-shell cylinder form factor in BmimAc .....	100
3.2.5.3 Flexible cylinder model in BmimAc .....	101
3.2.5.4 Core-shell model in BmimAc and BmimCl discussion.....	102
<b>3.3 Higher cellulose concentration (semi-dilute regime).....</b>	<b>105</b>
3.3.1 Description .....	105
3.3.2 Effective structure factor .....	108
3.3.2.1 Principle .....	108
3.3.2.2 Calculations .....	110
3.3.3 Hard cylinder 2D structure factor: comparison with data .....	112
<b>3.4 Higher concentrations: biphasic state.....</b>	<b>115</b>
<b>3.5 Solutions in BmimCl: similarities and differences, a check.....</b>	<b>121</b>
3.5.1 BmimCl solutions at different concentrations.....	121
3.5.2 Comparison between BmimCl and BmimAc.....	122
<b>3.6 Effects of water and temperature in BmimAc and BmimCl .....</b>	<b>123</b>
3.6.1 Effect of water for BmimAc at large $q$ .....	123
3.6.2 Effect of water for BmimAc - cellulose solution at low $q$ .....	124
3.6.3 Effects of water: comparison with BmimCl solutions .....	125
3.6.4 Absence of temperature effect in BmimAc.....	127
3.6.5 Effect of temperature: case of BmimCl.....	128
<b>3.7 Influence of the cellulose origin .....</b>	<b>129</b>
3.7.1 Other microcrystalline cellulose.....	129
3.7.2 Bacterial cellulose .....	129
<b>3.8 Influence of co-solvent.....</b>	<b>131</b>
<b>3.9 Discussion and conclusion .....</b>	<b>133</b>
<b>References.....</b>	<b>135</b>

## Chapter 3 X-ray Scattering

**Abstract.** The nanostructure of cellulose chains in solutions was studied by the essential technique SAXS. At first, we show how to overpass two major challenges in analyzing scattering intensities of SAXS measurements at both low and high  $q$  values. Then, we focus on the cellulose chains dissolved in an ionic liquid BmimAc, specifically with concentration ranging from 0.05 wt% to 1 wt%. That concentration range is close to a dilute regime which avoids the effect of inter-chain interactions, and enabling us, within a reasonable accuracy, to present the form factor of individual cellulose chain. The analysis of these solutions has been performed with both cylindrical and core-shell models to extract detailed cellulose structure, including the monomer diameter and shell thickness.

At semi-dilute concentration of cellulose in BmimAc, ranging from 2 wt% to 15 wt%, the slope of the curve is decreasing with higher cellulose concentration, which suggests a nanostructure in the interpenetrated region, with the weak inter-chain interaction. As a result, the curves overlap in the plot (Fig 3.3.1  $I(q)/c$  vs  $q$  at large  $q$ , reflecting similar scattering behaviors at local scale. At larger  $q$  values, a characteristic shoulder appears at a certain  $q$  value  $3.5 \text{ \AA}^{-1}$  across all comparable cellulose concentration curves. However, above 1 wt% of cellulose, a significant upturn is measured at low  $q$  values, which suggests the presence of cellulose aggregation in solution. At intermediate  $q$  values, the slope gradually decreases from -1 to -0.5 as cellulose concentration rises from 1 wt% to 15 wt%, indicating structural changes between cellulose chains, which can be reproached from rheological experiments. To account for these interactions, a  $I(q)/P(q)$  vs  $q$  analysis has been achieved by introducing a hard-disk effective structure factor model.

At cellulose concentration higher than 15 wt%, the phase separation was observed and the scattering quantified. Cellulose crystal peaks were found in the 40 wt% cellulose sample, which indicates the non-dissolved state.

Effects of water were also monitored. For BmimAc they showed no effect at low water concentration only, while BmimCl solutions showed much more sensitive and showed extra-scattering due to aggregation or phase separation. No temperature effect was observed for dry BmimAc, while temperature reduced the extra-scattering of BmimCl solutions.

### 3.1 From raw data to treated data: displaying the difficulties

In order to illustrate the difficulties to obtain reliable scattering data of our IL/cellulose solutions, **Figure 3.1.1** presents the curves obtained for MCC cellulose concentration of 0.05-15 wt%. This figure shows the raw data (here from SWING beamline) as radially regrouped from the detector without any more treatment (arbitrary units, a.u.). We can distinguish three kinds of curves:

- **Part 1.** the empty beam and empty capillary: they show a pronounced bump at large  $q$ ,  $q = 4 \times 10^{-1} \text{ \AA}^{-1}$ , due to the windows of the spectrometer, a wide shoulder around  $q = 8 \times 10^{-2} \text{ \AA}^{-1}$ , and a fast increase below  $q = 3 \times 10^{-2} \text{ \AA}^{-1}$  from  $I(q) = 2 \times 10^0 \text{ a.u.}$  to  $6 \times 10^{+4} \text{ a.u.}$  .
- **Part 2.** the solutions of concentration between 0.1 % and 15 %: they show a rather flat signal, between 2 and 5 a.u., between  $q = 3 \times 10^{-2} \text{ \AA}^{-1}$  and  $q = 3 \times 10^{-1} \text{ \AA}^{-1}$ . In the other parts of the  $q$  range, obviously we will have to make some delicate subtractions. At large  $q$ , but particularly at low  $q$ , where the upturn reaches a value 10 000 larger at the lowest  $q$ , close to the beam-stop!
- **Part 3.** the solutions of concentration between 20 % and 40 % with much larger intensities for which the subtraction is no longer a problem in most of the  $q$  range.

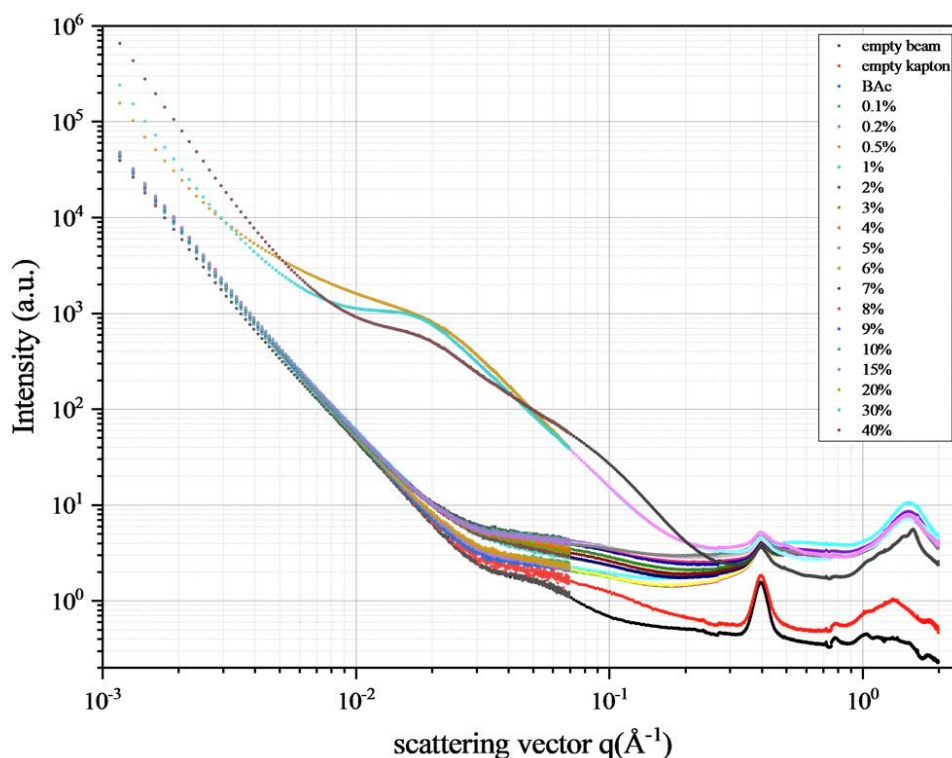


**Figure 3.1.1:** Raw scattering intensity (here from SWING) as radially regrouped from the detector without any treatment (arbitrary units) for MCC cellulose in BmimAc at concentrations of 0.05 to 40 wt%.

**Data correction.** We will first present the results for **part 2**, which we will divide in the dilute regime,  $c < c^*$ ,  $c^*$  being evaluated from rheology as close to 0.5 %, and semi-dilute for  $c > c^*$ . **Figure 3.1.2** shows the result of a simple data treatment by subtracting both the low  $q$  scattering and the large  $q$  scattering (“empty beam, empty capillary”, ionic liquid as described in Chapter 2. We observe a series of samples in BmimAc with different MCC concentrations, ranging from 2 wt% to 15 wt%. At low  $q$  ( $q < 10^{-2} \text{\AA}^{-1}$ ), the upturn of the scattering is due to the various degree of aggregation. In the middle  $q$  range ( $10^{-2} \text{\AA}^{-1} < q < 7 \times 10^{-1} \text{\AA}^{-1}$ ), the scattering intensity increases with increasing MCC concentration due to the cellulose volume increase. The curves exhibit the slope changing from  $q^{-1}$  to  $q^{-0.5}$  with increasing MCC concentration from 2 wt% to 15 wt%, which suggests the presence of structural features related to the MCC concentration (details in **section 3.3**). At large  $q$ , the peak exist at  $\sim 1.2 \text{\AA}^{-1}$ , which is difficult to understand as due to interpret the subtraction of capillaries (see below). The data provide insight into how the chain organization evolves as the concentration increases.

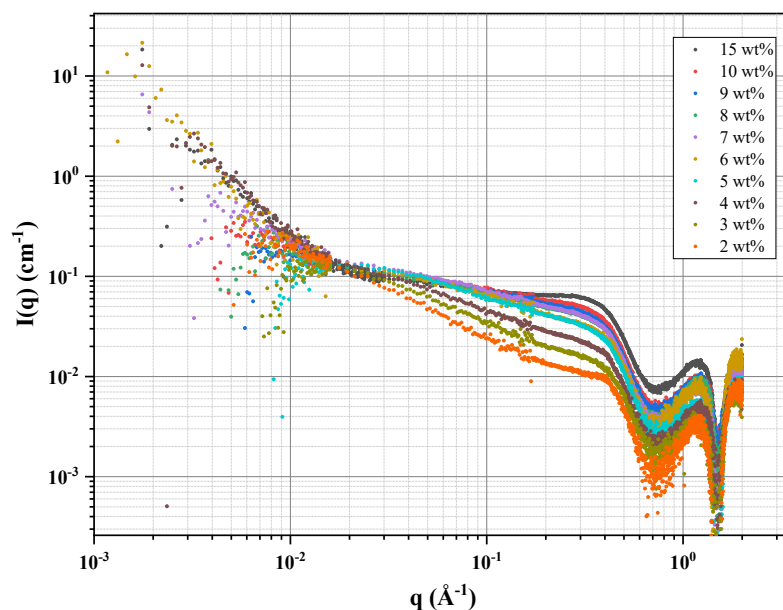


**Figure 3.1.2:** SAXS pattern for representative samples of various cellulose concentration in BmimAc ranging from 2 wt% to 15 wt%. All the samples were measured in Kapton capillaries in SWING beamline of Soleil Synchrotron.

We will now focus on the other extreme of the  $q$  range, at very large  $q > 8 \times 10^{-1} \text{ \AA}^{-1}$ . We see a series of two maxima, separated by a well. We propose the following explanation: the structure of the ionic liquid is altered in the presence of cellulose. The smooth peak, typically caused by small-scale local ordering in the IL, becomes broader due to a loss of order (also observed by Wide Angle Neutron Scattering, WANS, see Chapter 4). The difference only happens at large  $q$  when  $q > 0.5 \text{ \AA}^{-1}$ .

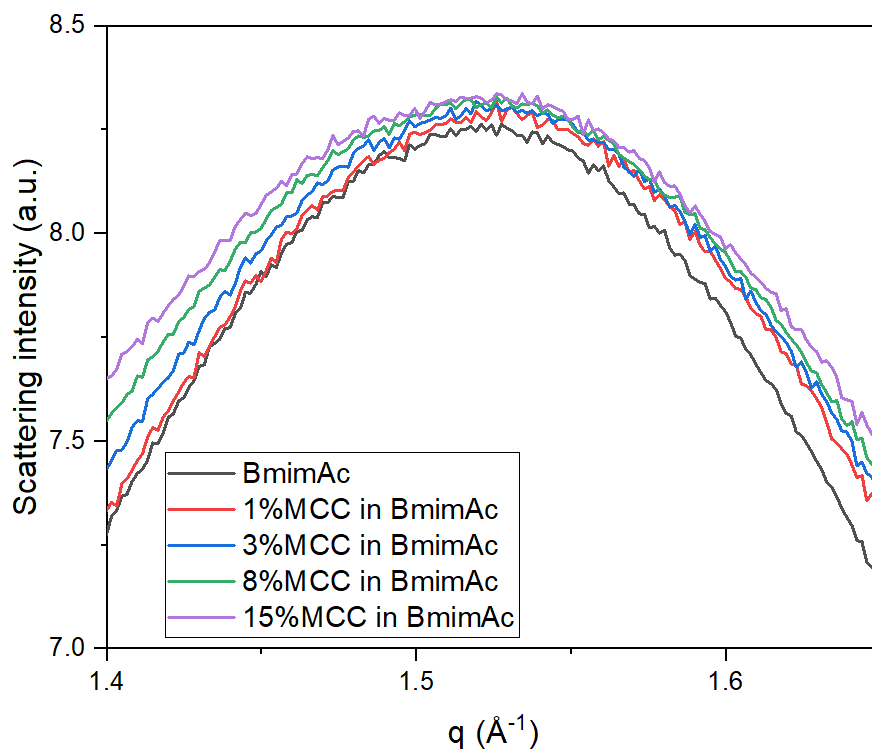


**Figure 3.1.3:** WAXS plot of scattering intensity of the BmimAc and cellulose solution with different cellulose concentration, without subtraction of ionic liquid BmimAc. Here we show the peak shift and the difficulty to subtract the solvent.

This peak at large  $q$  corresponds to local spatial correlation length, i.e. nano structuration in ionic liquids, as it was largely depicted in the literature (Boudie et al., 2023; Lo Celso et al., 2019; Lundin et al., 2021). As a consequence, the subtraction from each solution scattering, of the narrower peak of pure IL leads to two “artificial” peaks around 1.5 and 2  $\text{\AA}^{-1}$ . As the cellulose concentration increases, the peak also shifts to lower  $q$ . Such shift was already observed by (Endo et al., 2016) which is explained by expansion of the cellulose chain local separations in the presence of ionic liquid. The interaction between acetate ( $\text{Ac}^-$ ) anions and the OH groups of cellulose is believed to play a dominant role in this process, by many authors. Molecular dynamics (MD) simulations estimate the distance between cellulose chains to be  $1.21 \pm 0.004$  nm. For further reference, see the MD simulation study by (Gupta and Jiang, 2015).

## 3.2 Dilute solution

### 3.2.1 Difficulties in data treatment

Dilute solutions with a cellulose concentration of 0.05-1 wt% are studied in this section. In these solutions, the scattering of the solution and the contribution of the polymer are very low which means to have a robust procedure to extract the data.

Then, at a first step it was important to check data treatment for scattering curves obtained in different capillaries for dilute solution. Comparing the Kapton, borosilicate, and quartz capillaries and the square capillaries of dilute cellulose solution of 1 wt% (**Figure 3.2.1**), we observe quite good agreement for  $4 \times 10^{-3} \text{ \AA}^{-1} < q < 5 \times 10^{-1} \text{ \AA}^{-1}$  for all capillaries except the Kapton (for which agreement is found at higher  $c \geq 2\%$ ). The square cross-section capillaries present a shift in intensity. The old measurements with quartz capillaries suffer from a slight shift along  $q$ . Above  $7 \times 10^{-1} \text{ \AA}^{-1}$ , the intensity is very weak ( $0.005 \text{ cm}^{-1}$ ), so that the subtraction of the background (solvent, capillary) is not meaningful. The worst data are for the Kapton capillary, which unfortunately we used many times. However, as said above, the situation is better as soon as  $c$  is higher ( $\geq 2\%$ ).



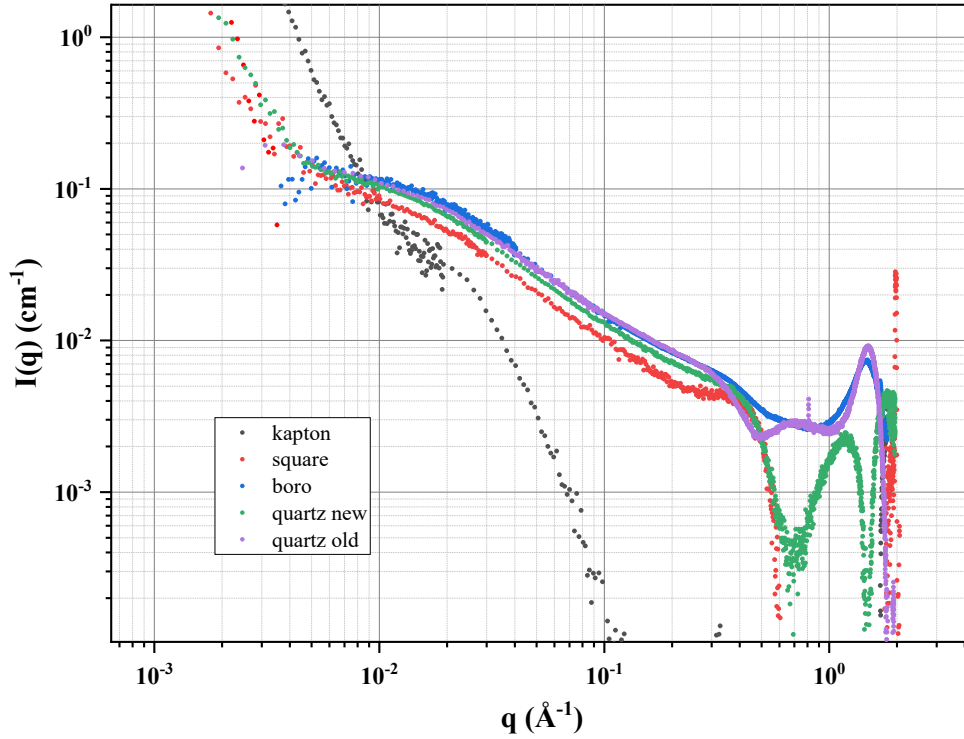


**Figure 3.2.1:** Comparison between measurements for solutions at  $c = 1$  wt% in Kapton, Boro silicate, Quartz capillaries and square Glass capillaries. The scattering intensity  $I(q)$  is from a MCC solution at a concentration  $c = 1$  wt% after subtraction of capillaries and solvent BmimAc. The scattering intensity  $I(q) = [I_{1wt\% \text{ solution}}(q) - I_{\text{capillary}}(q)] - (1 - \phi_{MCC})[I_{BmimAc}(q) - I_{\text{capillary}}(q)]$ .

### 3.2.2 Description

**Figure 3.2.2** presents three plots of scattering, after backgrounds subtractions, obtained for: low concentrations and very low concentrations, and divided by the nominal concentration.

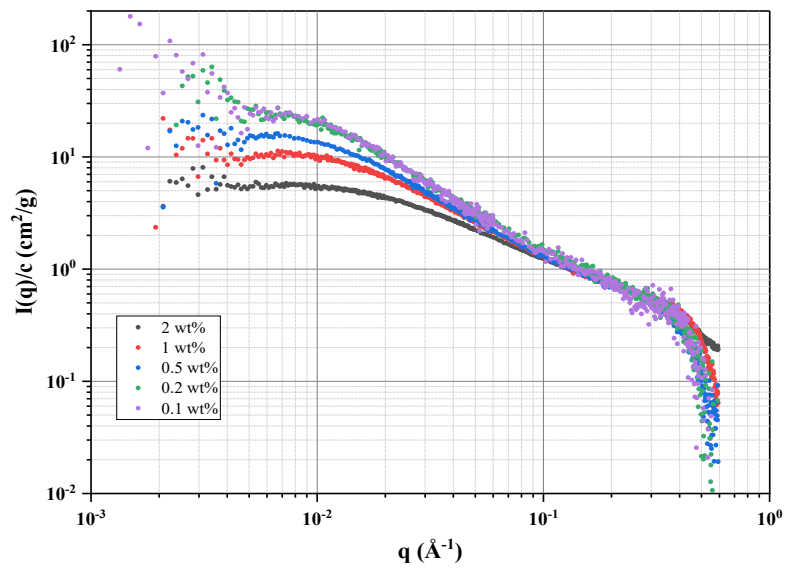
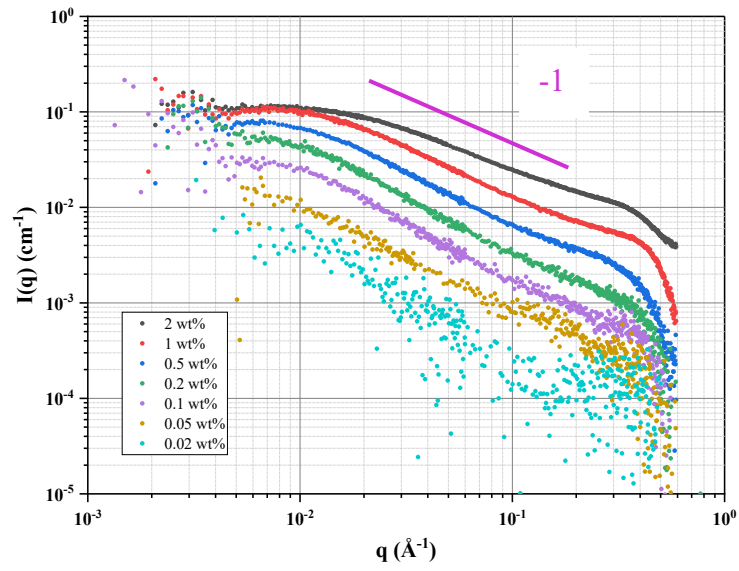
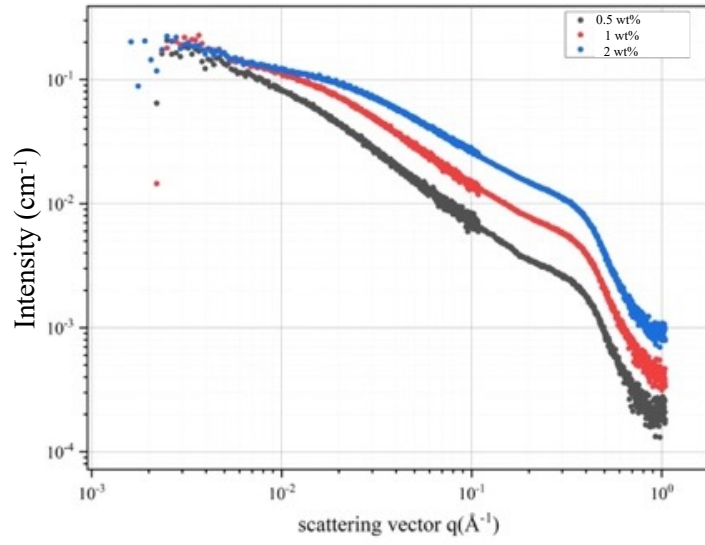


**Figure 3.2.2.** Scattering profile from MCC-Avicel solutions at room temperature for concentrations 0.5, 1 and 2 wt.%. a, upper plot: a solution in quartz capillaries for 0.5, 1 and 2%, b, lower left plot: a set of concentrations  $c$  starting from very dilute solutions, and c, lower, right: part of the same set after division by the nominal concentration.

One can see that we succeeded here to:

- avoid strong low  $q$  upturns: we could manage to obtain a close to flat signal, as expectable from the form factor of an object of size a few hundred Å, or from a semi-dilute polymer solution, with no aggregation at large scale.
- get shoulder-like shapes, quasi superposable, at large  $q$  for the three concentrations, as expectable from objects without interactions at these scales, suggesting no occurrence of a structure factor within this concentration range. At medium  $q$  the apparent slope is -1 at low concentration (e.g. 0.5 %). Such a value is well known for the scattering of a rod.
- For higher  $c$ , the slope decreases clearly. Going to lower  $q$ , we observe a bend towards a plateau.

These are the main features of the scattering which we will analyze below.

### 3.2.3 Direct estimate of the chain parameters: unit length, cross-section

We will use the signal recorded at the lowest concentration at which the counting statistics and the accuracy in backgrounds subtraction make exploitable. We will mainly work with a concentration of 0.5% (Remark: we could use 1%, except at the lowest  $q_s$ , which show a flat part extending at larger  $q$  compared to 0.5 %; the 0.2 % scattering shows the opposite effect, but the subtraction accuracy at low  $q$  is questionable).

The curve as a function of  $q$  is made, as already described phenomenologically, of different parts along successive  $q$  ranges, which we will use differently to obtain more information.

#### 3.2.3.1 Unit length - cross-section

In the medium  $q$  part ( $0.02 < q < 0.1 \text{ \AA}^{-1}$ ), it is very close to a straight line of slope  $q^{-1}$ , which is known as the form factor of a rod with random orientation. Using the formula for a rod:

$$\begin{aligned}
I(q) &= \frac{1}{V_{irr}} \frac{d\Sigma}{d\Omega} (cm^{-1}) = \Delta\rho^2 \phi V_{mono} P(q) \\
&= \frac{\Delta\rho^2 \phi N v_{mono} \pi}{qL} \\
&= \frac{\Delta\rho^2 \Phi v_{mono} \pi}{qa}
\end{aligned} \tag{3.2.1}$$

where  $V_{irr}$  is the irradiated volume of the sample;  $\frac{d\Sigma}{d\Omega}$  the differential scattering cross section;  $\Delta\rho = \rho_{rod} - \rho_{solvent}$  the contrast of the scattering length density, represents the density difference between the rods and solvent;  $\phi$  the rod's volume fraction.

For the rod,  $P(q)$ :

$$P(q) = \frac{2}{qL} \int_0^{qL} \frac{\sin t}{t^2} dt \tag{3.2.2}$$

where  $L$  represents the length of the rod;  $t = qL \cos \theta$ ,  $\theta$  is the angle of the rod orientation.

For the randomly oriented rods, for  $qL \gg 1$ , the form factor  $P(q)$  can be approximated as:

$$\begin{aligned}
P(q) &\approx \frac{2}{qL} \cdot \frac{\pi}{2} \\
&= \frac{\pi}{qL}
\end{aligned} \tag{3.2.3}$$

For the middle  $q$  range, the effect of the short axis diameter  $a$  becomes more important, combine the formula with volume fraction, the formula simplifies to:

$$I(q) = \frac{\Delta\rho^2 \Phi v_{mono} \pi}{qa} \tag{3.2.4}$$

where  $\Phi = N\phi$  represents the effective volume fraction per rod;  $a$  is the equivalent diameter of the rod.

For  $\phi \sim 0.0035$ , for 0.5 wt% (see **Table 1**). For Xray at 12 keV (Ref. [NIST](#)), Scattering Length Density (SLD) for Cellulose ( $C_6H_{10}O_5$ ) is  $13.530 (10^{-6}/\text{\AA}^2)$  and  $V_{monoCell} = 162.1406 \text{ g}/1.5 \text{ g/cm}^3 = 108.09 / N_{Avogadro} = 179.5 \text{ \AA}^3$ . For BmimAc ( $C_{10}H_{18}N_2O_2$ ),  $SLD = 9.721 \times 10^{-6}/\text{\AA}^2$ , hence  $\Delta\rho^2 = 14.51 \cdot 10^{-12} \text{ \AA}^{-4}$ .

Name	Formula	M <sub>w</sub> (g/mol)	Density (g/cm <sup>3</sup> )	SLD (10 <sup>-6</sup> /Å <sup>2</sup> )
Cellulose	C <sub>6</sub> H <sub>10</sub> O <sub>5</sub>	162.1406	1.5	13.530
BmimAc	C <sub>10</sub> H <sub>18</sub> N <sub>2</sub> O <sub>2</sub>	198.2621	1.05	9.721

**Table 3.2.1** Scattering Length Densities (SLD) of cellulose and BmimAc

We obtain:

$$\begin{aligned}
\frac{1}{V_{irr}} \frac{d\Sigma}{d\Omega} (cm^{-1}) &= \frac{\Delta\rho^2 \Phi v_{mono} \pi}{qa} \\
&= \frac{(14.51 \times 10^{-12} \text{ \AA}^{-4}) \times 0.0035 \times (179.5 \text{ \AA}^3) \times 3.14}{qa} \\
&\approx 2.86 \times 10^{-11} \times \frac{1}{qa} \text{ \AA}^{-1}
\end{aligned} \tag{3.2.5}$$

For  $q = 10^{-1} \text{ \AA}^{-1}$ , the intensity can be found from the curve:

$$\begin{aligned}
\frac{1}{V_{irr}} \frac{d\Sigma}{d\Omega} (cm^{-1}) &= 7 \times 10^{-3} \text{ cm}^{-1} \\
&= 7 \times 10^{-3} \times 10^{-8} \text{ \AA}^{-1} \\
&= 7 \times 10^{-11} \text{ \AA}^{-1}
\end{aligned} \tag{3.2.6}$$

combine the two equations, which gives the value of  $a$ :

$$2.86 \times 10^{-11} \times \frac{1}{(10^{-1} \text{ \AA}^{-1}) a} \text{ \AA}^{-1} = \frac{1}{V_{irr}} \frac{d\Sigma}{d\Omega} (cm^{-1}) = 7 \times 10^{-11} \text{ \AA}^{-1} \tag{3.2.7}$$

$$a = \frac{2.86 \times 10^{-11} \text{ \AA}^{-1}}{(10^{-1} \text{ \AA}^{-1}) \times (7 \times 10^{-11} \text{ \AA}^{-1})} = 4.1 \text{ \AA} \tag{3.2.8}$$

value of  $a$  smaller than expected from the geometry of the cellulose unit.

It depends on the calculation of the contrast. It is possible that the contrast is lower. This would lead to an even lower value of  $a$ , which is difficult to imagine. Another possibility is that a number  $n_{strands} > 1$  of cellulose chain strands are linked together, so that  $a = n_{strands} \cdot 4.1 \text{ \AA}$  would be larger.

### 3.2.3.2 Unit cross-section area

We can also rewrite in term of unit area  $A_{\text{mono}}$  calculation, where  $A_{\text{mono}}$  is the cross-section, usually taken as  $32 \text{ \AA}^2$  (Raghuwanshi 2018, Nishiyama, Y., 2022) from the crystal structure.

$$\begin{aligned}
 I(q)(\text{cm}^{-1}) &= \frac{\Delta\rho^2\Phi v_{\text{mono}}\pi}{qa} \\
 &= \frac{\Delta\rho^2\Phi A_{\text{mono}}\pi}{q} \\
 &= \frac{(14.51 \times 10^{-12} \text{ \AA}^{-4}) \times 0.0035 \times (32 \text{ \AA}^2) \times 3.14}{q} \\
 &= \frac{5.105 \times 10^{-12} \text{ \AA}^{-2}}{q}
 \end{aligned} \tag{3.2.9}$$

which for  $q = 10^{-1} \text{ \AA}^{-1}$ , gives  $I(q) = (5.1 \times 10^{-12} \text{ \AA}^{-2}) / (10^{-1} \text{ \AA}^{-1}) = 5.1 \times 10^{-11} \text{ \AA}^{-1} = 5.1 \times 10^{-3} \text{ cm}^{-1}$ . From the data at for  $q = 10^{-1} \text{ \AA}^{-1}$ , we find  $7 \times 10^{-3} \text{ cm}^{-1}$ , which corresponding therefore to  $A_{\text{mono-measured}} = 32 \times \frac{7 \times 10^{-3}}{5.1 \times 10^{-3}} \approx 44 \text{ \AA}^2$ .

Note that from the volume  $V_{\text{monoCell}} = 179.5 \text{ \AA}^3$ , we obtain a value of  $a$

$$a_{\text{theo}} = \frac{V_{\text{mono Cell}}}{A_{\text{mono-theoretical}}} = \frac{179.5 \text{ \AA}^3}{32 \text{ \AA}^2} = 5.6 \text{ \AA} \tag{3.2.10}$$

or

$$a_{\text{measured}} = \frac{V_{\text{mono Cell}}}{A_{\text{mono-measured}}} = \frac{179.5 \text{ \AA}^3}{44 \text{ \AA}^2} = 4.08 \text{ \AA} \tag{3.2.11}$$

The same calculations for 1%, using

$$\left( \frac{1}{V_{\text{irr}}} \frac{d\Sigma}{d\Omega}, \text{cm}^{-1} \right) = 10^{-1} \text{ cm}^{-1} = 10^{-9} \text{ \AA}^{-1}$$

give

$$a = 57.277 \times 10^{-10} / 10^{-9} \text{ \AA} = 57.277 \times 10^{-10+9} = 5.727 \text{ \AA}$$

**For solutions in BmimCl**, the values of intensities are very close. Knowing that the SLD of BmimCl, equal to  $9.98 \times 10^{-6}/\text{\AA}^2$ , is very close to the one of  $9.81 \times 10^{-6}/\text{\AA}^2$  for BmimAc, we can conclude that both parameters  $a$  and  $A$  are very close for acetate and chloride.

### 3.2.4 Rod scattering: equations

In agreement with the image of a long chain of cellulose, partially rigid (see **Chapter 1**), we decided to fit the curve using both the cylinder and core-shell cylinder models, the length per cellulose monomer was calculated, with the signal simplified using a rod model formula:

$$I(q)(cm^{-1}) = \frac{1}{V} \frac{d\Sigma}{d\Omega} = \frac{\Delta\rho^2 \Phi N V_{mono} \pi}{q N a} \quad (3.2.12)$$

where  $\Delta\rho$  is the scattering length density contrast;  $\Phi$  is the volume fraction of the sample;  $N$  is the number density of polymer chains;  $V_{mono}$  is the volume of a monomer unit;  $a$  refers to the length monomer unit.

The X-ray SLD of cellulose and ionic liquids were calculated by NIST database and shown below in the **Table 3.2.2**.

**Table 3.2.2** X-ray scattering length density of samples

Name	Formula	Density (g/cm <sup>3</sup> )	X-ray SLD (10 <sup>-6</sup> /\AA <sup>2</sup> )
Cellulose	C <sub>6</sub> H <sub>10</sub> O <sub>5</sub>	1.5	13.561
BmimAc	C <sub>10</sub> H <sub>18</sub> N <sub>2</sub> O <sub>2</sub>	1.05	9.739
BmimCl	C <sub>8</sub> H <sub>15</sub> ClN <sub>2</sub>	1.086	9.980

These low concentration scattering patterns have been modeled using the form factor  $P_{cylinder}(q)$  of a cylinder model, using the (Pedersen, 1997) and the form factor  $P_{core-shell\ cylinder}(q, \alpha)$  of a core-shell cylinder model (Kline, 2006) using:

$$P_{cylinder}(q) = \frac{scale}{V} \int_0^{\frac{\pi}{2}} F_{cylinder}^2(q, \alpha) \sin(\alpha) d\alpha + background \quad (3.2.13)$$

where

$$F_{cylinder}(q, \alpha) = 2(\Delta\rho)V \frac{\sin\left(\frac{1}{2}qL \cos \alpha\right) J_1(qR \sin \alpha)}{\frac{1}{2}qL \cos \alpha \quad qR \sin \alpha} \quad (3.2.14)$$

where  $\alpha$  is the angle between the axis of cylinder; L, R are the length and radius of the cylinder;  $V = \pi R^2 L$  is the volume of the cylinder;  $\Delta\rho = \rho_c - \rho_s$  is the scattering length density difference (contrast) between the scatter and the solvent;  $J_1$  is the first order Bessel function.

$$P_{core-shell\ cylinder}(q, \alpha) = \frac{scale}{V_s} F_{core-shell\ cylinder}^2(q, \alpha) \cdot \sin(\alpha) + background \quad (3.2.15)$$

where

$$F_{core-shell\ cylinder}(q, \alpha) = \frac{(\rho_c - \rho_s)V_c \sin\left(q \frac{1}{2}L \cos \alpha\right) 2J_1(qR \sin \alpha)}{q \frac{1}{2}L \cos \alpha \quad qR \sin \alpha} + \frac{(\rho_c - \rho_{solv})V_s \sin\left(q \left(\frac{1}{2}L + T\right) \cos \alpha\right) 2J_1(q(R + T) \sin \alpha)}{q \left(\frac{1}{2}L + T\right) \cos \alpha \quad q(R + T) \sin \alpha} \quad (3.2.16)$$

$$V_s = \pi(R + T)^2(L + 2T) \quad (3.2.17)$$

where  $\alpha$  is the angle between the axis of the cylinder;  $V_s$  is the total volume (including both the core and the outer shell);  $V_c$ ,  $L$ ,  $R$  are the volume, length and radius of the core;  $T$  is the thickness of the shell;  $\rho_c$ ,  $\rho_s$ ,  $\rho_{solv}$  are the scattering length density of the core, shell and solvent respectively; The outer radius of the shell is given by  $R + T$ ; the total length of the outer shell is given by  $L + 2T$ .



### 3.2.5 Fit to a model form factor

In the large  $q$  part, we observe, as remarked above, a shoulder, characteristic of the finite radius of the cylinder. Finally, in the low  $q$  part, we observe a slight plateau. This can be attributed to a finite length of the chains, or to a beginning of repulsive interaction between the elementary objects.

On the very large  $q$  part, we observe, as described before, strong oscillations, which are mostly due to the inner correlations in the very local structure of the ionic liquid and will not be discussed here. They are shown in the plots for the reader to appreciate the conditions of data treatment nature of the scattering in this range.

We have used SASview to get more insight on the geometry of the chain.

#### 3.2.5.1 Cylinder form factor in *BmimAc*

Figure 3.2.3 below shows the fit for a cylinder. The fit parameters are indicated in the Table 3.2.3.

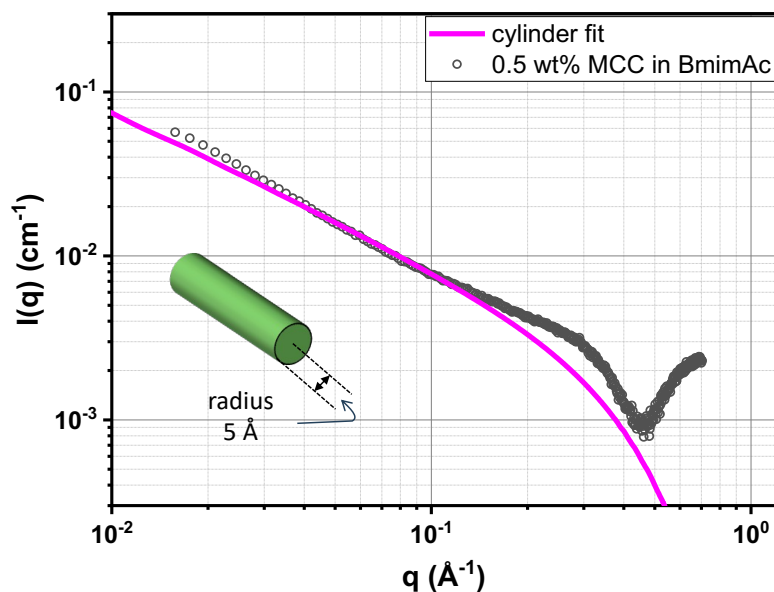


**Figure 3.2.3:** Fit of the 0.5 % scattering with the form factor of a cylinder model, The inset shows the cylindrical shape with radius  $5 \text{ \AA}$  used in the cylinder model.

Model	Cylinder	Core-shell cylinder	Flexible cylinder
scale	0.003	0.014	0.0021
background	0	0	0
SLD cylinder (core) $\times 10^{-6}/\text{\AA}^2$	13.561	13.561	13.561
SLD shell $\times 10^{-6}/\text{\AA}^2$		9	
SLD solvent $\times 10^{-6}/\text{\AA}^2$	9.739	9.739	9.739
Radius $\text{\AA}$	4	5.2	5
			0.2
Radius polydispersity	0.2	0.3	
Shell thickness $\text{\AA}$		5	
Length $\text{\AA}$	617.81	617.81	617.81
Kuhn length $\text{\AA}$			200

**Table 3.2.3:** Parameters of the fits of the 0.5 % scattering with the form factor of a cylinder, a core-shell cylinder, and a flexible cylinder models using SASView.

The fit is satisfactory in the middle  $q$  range, both in shape and in absolute value. The parameter “scale” in SASView which should here be equal to the volume fraction (SASView user manual) is taken equal to 0.003 for  $c = 0.5\%$ . At larger  $q$  ( $0.2$  up to  $0.4 \text{\AA}^{-1}$ ; we do not wish to fit above), on the contrary, the fit of the shoulder is unsatisfactory: the experimental shape of the shoulder is in practice more pronounced than what can be expected from a simple cylinder shape.

### 3.2.5.2 Core-shell cylinder form factor in *BmimAc*

The shoulder shape led us to test a core-shell cylinder model. The **Figure 3.2.4** shows a much better agreement both at medium  $q$  and high  $q$  in the shoulder region. The SLD taken for the core is the one for cellulose, and for the outside the one of *BmimAcetate*. The SLD of the shell is taken equal to  $9 (10^{-6}/\text{\AA}^2)$ , i.e. slightly lower than the solvent.

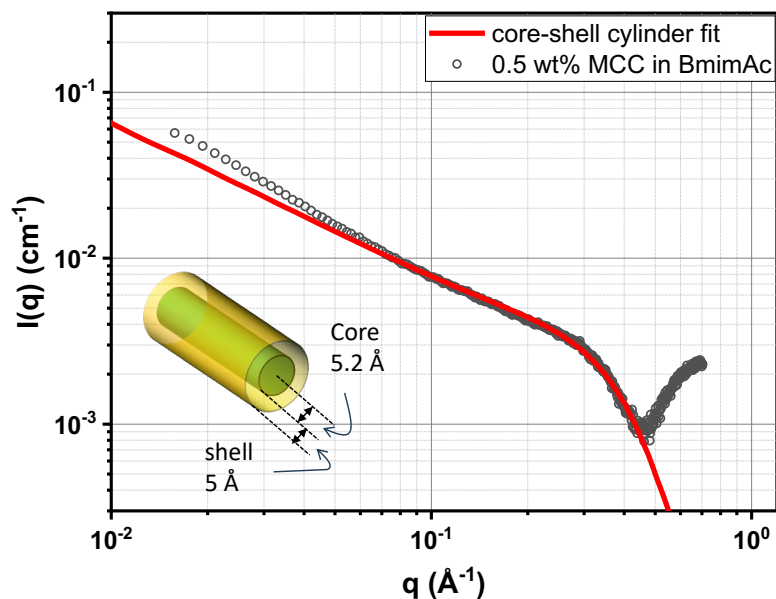


**Figure 3.2.4:** Fit of the 0.5 % scattering with the form factor of a core-shell cylinder model, the inset shows the core-shell cylinder shape with core radius 5.2 Å and shell 5 Å.

The core-shell model is therefore satisfactory.

However, in the lowest  $q$  part, the intensity appears somewhat larger than the fit: it shows a smooth upturn. We attempted a last test to account this trend.

### 3.2.5.3 Flexible cylinder model in BmimAc

The flexible cylinder model accounts for a moderate flexibility at large size. It involves a cross-over to a  $q^{-2}$  law characteristic of a Gaussian, random, chain. The model is not designed to fit the large  $q$  region of the shoulder at  $0.3 \text{ \AA}^{-1}$ , while at low  $q$ , we obtain a good fit with  $L_K = 200 \text{ \AA}$  ( $L_p = 100 \text{ \AA}$ ). Note also that using a Holtzer plot,  $q \times I(q)$  versus  $q$ , our data appear extremely close to the one published by Jiang and Terao (Jiang 2017), who proposed a fit with  $L_K = 70 \text{ \AA}$ . We must keep in mind that this  $q$  range is extremely sensitive to the subtraction of the direct beam signal, as well as to the presence of some slight aggregation (the problem was encountered at a higher degree with aqueous solvents and Static Light Scattering, see Chapter 1, but the obtained values of  $L_K$  lie in the same range).

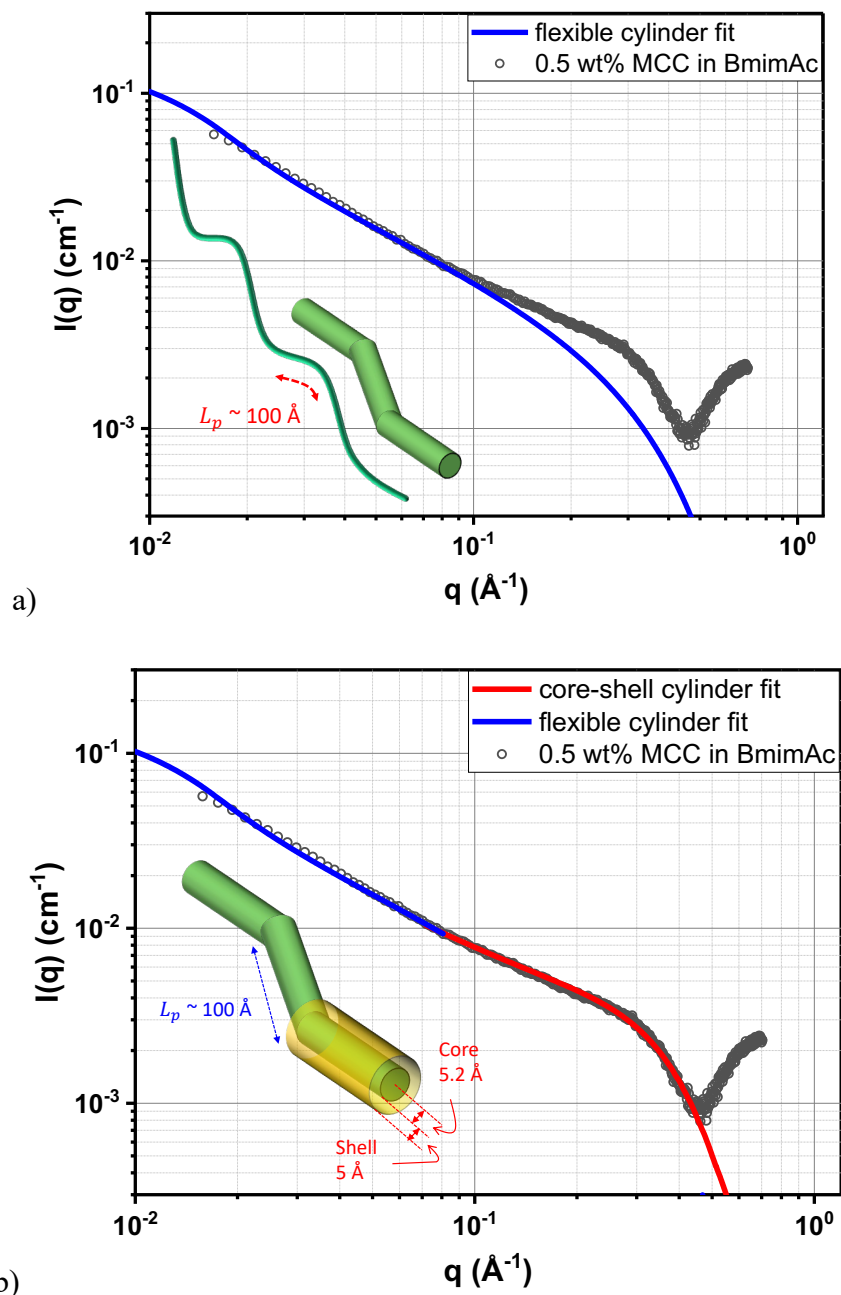


**Figure 3.2.5:** a) Fit of the 0.5 % scattering with the form factor of a flexible cylinder model, the inset shows the flexible cylinder with  $L_p \sim 100 \text{ \AA}$ ; b) Fit of the 0.5 % scattering with the form factor with stitched flexible cylinder and core-shell cylinder model, the inset shows the flexible core-shell cylinder shape with core radius  $5.2 \text{ \AA}$ , shell  $5 \text{ \AA}$  and  $L_p \sim 100 \text{ \AA}$ .

### 3.2.5.4 Core-shell model in BmimAc

A fit with a core-shell is possible for the scattering of 0.5 % MCC in BmimAc. Rather close parameters can be obtained – knowing that there is no unicity of the result. Although the profile

of the shoulder looks slightly different as commented above, it is difficult to account for it in the fit.

The volume of the rod unit for the fit (important at intermediate  $q$ ) is therefore the one corresponding to the diameter of the rod, with no other adjustable parameters. For the 1 wt% sample, at  $0.01 \text{ \AA}^{-1}$ , the scattering intensity reaches  $10^{-1} \text{ cm}^{-1}$ , yielding a length per cellulose monomer of approximately  $5.727 \text{ \AA}$ . The core-shell model fitting, as shown in the **Figure 3.2.6**, reveals a radial SLD profile with a  $\sim 5 \text{ \AA}$  thick shell surrounding a cellulose core of  $\sim 5 \text{ \AA}$ . This results in a shell SLD of approximately  $9 \times 10^{-6} \text{ \AA}^{-2}$ , which is lower than the SLDs of both cellulose and BmimAc. The SLD difference is depicted in the figure, using the SLD given through the cellulose and solvent densities. The core-shell structure has been introduced to describe the pronounced shoulder feature at high  $q$  value at  $0.35 \text{ \AA}^{-1}$ , which is due to the existence of a solvent shell around the core cellulose chain, with a specific chemical composition, inducing a different scattering length density respect to the bulk solvent. However, the shape is very sensitive to the different distances, polydispersity, and SLDs chosen; it corresponds to a narrow set of values, which is surprising.

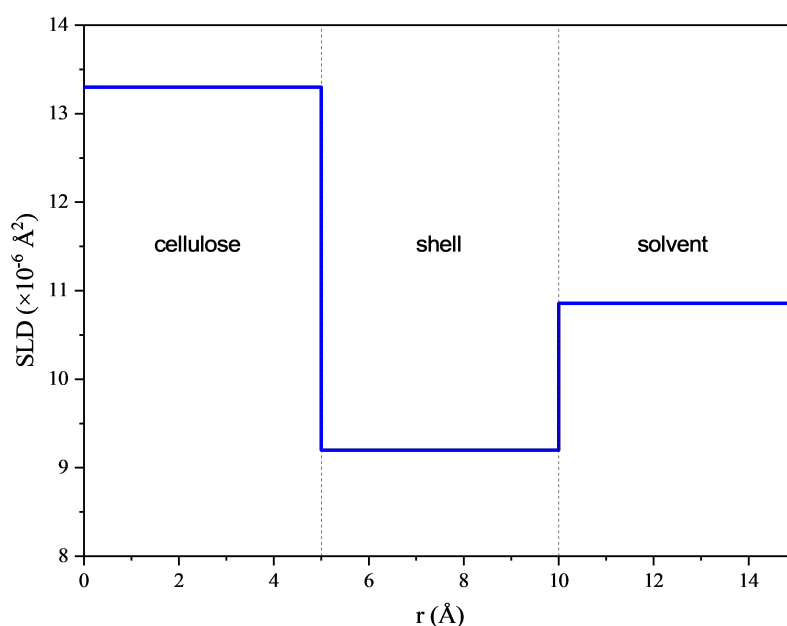


**Figure 3.2.6:** SLD radial profile used for fitting of the form factor of the single chain, refer the paper (Idström et al., 2017). Depiction of the SLD distribution along the radius of a cellulose and solvent shell.  $\rho_0$  is the SLD contrast, the SLD difference between the scattering particle and the solvent.  $r$  is the radius of the object axis.

The shell SLD suggests the presence of a solvation shell enriched with the bulk BmimAc solvent. A core-shell cross section model was introduced with the shell electron density being about 90% of the bulk solvent, as described in **Figure 3.1.6**. This SLD corresponds to that of the acetate anions, emphasizing the critical role of anions in the cellulose dissolution process, as many papers have claimed - sometimes on not always convincing grounds. For example, the association between acetate anions and cellulose (i.e., the number of anions per glucose unit) has been depicted from NMR analysis by Zhang et al (Zhang, J., 2010), the variation of  $^1\text{H}$  chemical shifts being interpreted as H-bonding variations. However, Remning et al, Remsing et al 2010) and Youngs et al claim it is wrong. This is also proposed by Garvey, Garnier et al (Raghuwanshi et al, 2018) from the estimate of the experimental value of contrast in neutron scattering studies. We propose to look for other explanations resulting in variable SLD around the cellulose chains:

- that the non-helical cellulose chains results in a plate-like elongate structure, which would make the solvent distribution around the cellulose inhomogeneous;
- or simply that the Bmim counterions lie further from the chains due to a steric effect.

### 3.3 Higher cellulose concentration (semi-dilute regime)

#### 3.3.1 Description

In a dilute, disordered system, what the randomly distributed cellulose chains in the solution exhibit a minimal structure factor, with the scattering predominantly representing the form factor of the individual cellulose chains. At higher cellulose concentrations, we expect that chain correlations become significant due to the interactions between cellulose chains. The scattering curves  $\log I(q)$  vs  $\log q$ , for cellulose solutions in BmimAc, are presented on **Figure 3.1.2**, each spectrum corresponding to a different cellulose concentration ranging from 2 wt% to 15 wt%. **Figure 3.3.1a** shows also the corresponding scattering curves shifted for better clarity, and **Figure 3.3.1b** shows them divided by the concentration,  $\log I(q)/c$  vs  $\log q$ .

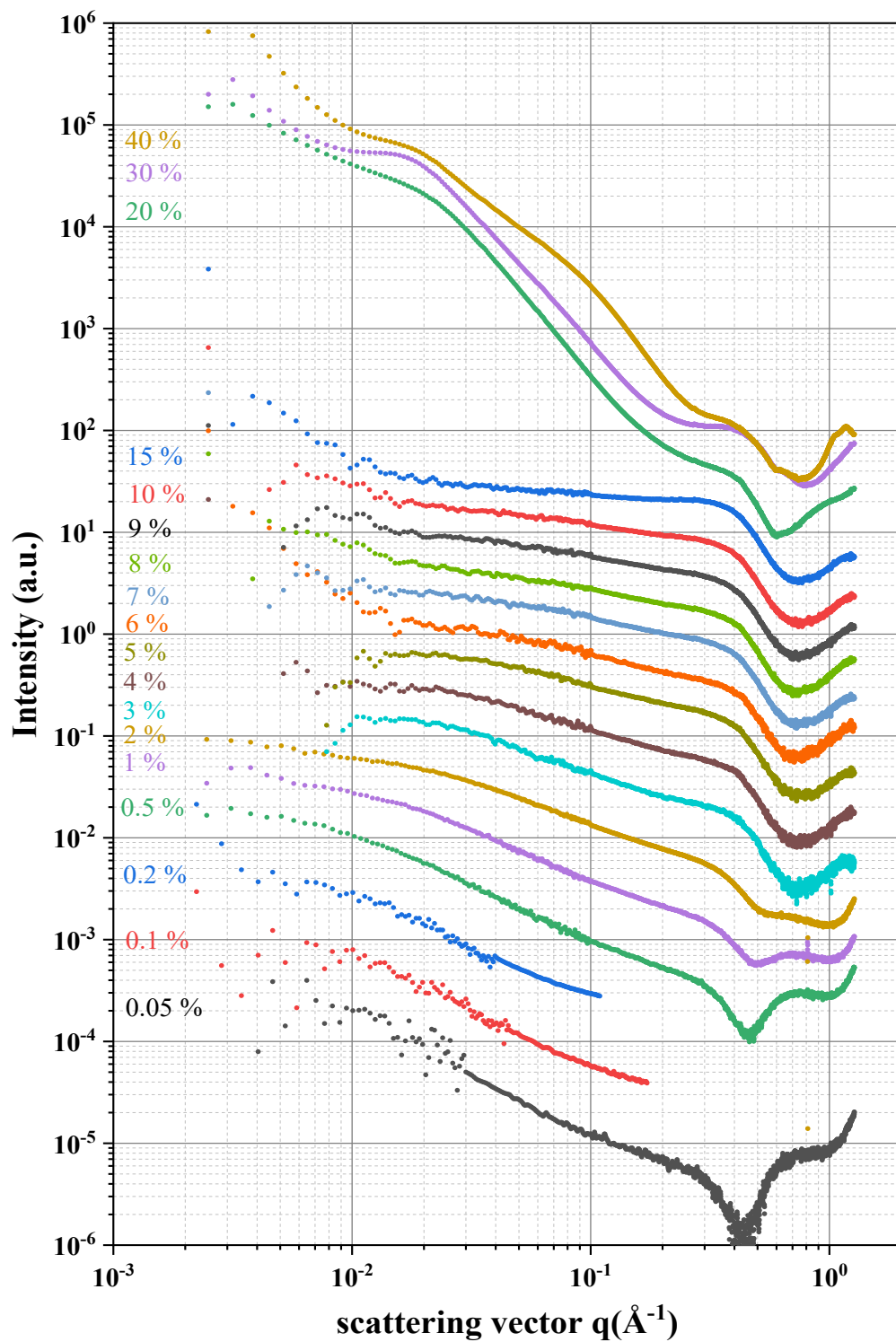


**Figure 3.3.1 a:** Scattering intensity, for concentration between 0.05 % and 40%, shifted for better clarity by a factor 5 (2 % sample as the reference).



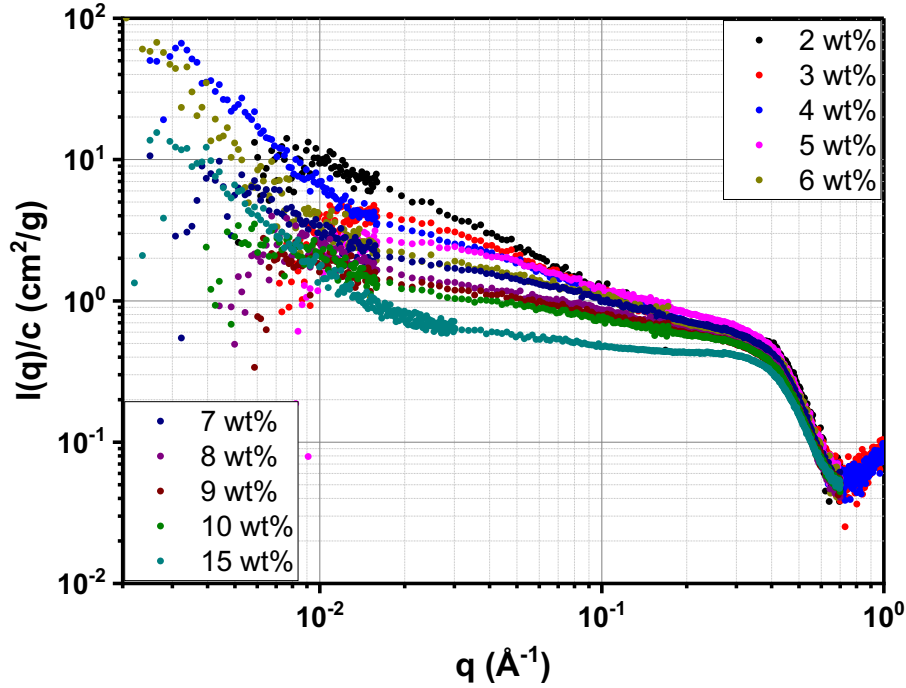


**Figure 3.3.1 b:** SAXS  $I(q)/c$  vs  $q$  pattern for representative samples of various cellulose concentration in BmimAc ranging from 2 wt% to 15 wt%.

### Different features appear with the change/increase of cellulose concentration

Let us start with the large  $q$  domain: all curves indicate a shoulder of same shape than for the dilute solution. The curves  $I(q)/c$  practically overlap up to 10% suggesting no occurrence of a structure factor within this concentration range. Hence, we see here the local shape of the cellulose chains. For 15%, there is a slight reinforcement of the shoulder which could correspond to a chain-chain correlation (better seen in **Figure 3.1.2**).

In the middle  $q$  range lies the most interesting behavior. The intensity increases due to the cellulose concentrations, and at the same time, the slope decreases with concentration from 2 wt% to 15 wt%, from  $q^{-1}$  to  $q^{-0.25}$  or even less for 15 wt%. The interaction between chains with dependence of cellulose concentration reduces the scattering, which resembles the one of a molecular liquid, while the large  $q$  part still fit to the form factor  $P(q)$  of the dilute solution without interaction. This indicates that the conformation of the semi-flexible chain with the core-shell rod at small scale is kept. The 1 wt% samples were used as the form factor  $P(q) = I_{1wt\%}(q)/c_{1wt\%}$  for studying the chain interaction in the semidilute region.

At low  $q$ , upturns can be found. For low concentration, they are moderate, so that the curve seems to be in continuity with the increasing at middle  $q$ ,  $q^{-1}$  behavior. In high cellulose

concentration samples, as commented above, the upturns are larger, and all the more visible since the curve at middle  $q$  variation is very flat.

### 3.3.2 Effective structure factor

#### 3.3.2.1 Principle

For high cellulose concentration, we propose an analysis based on an effective structure factor  $S(q, c)$ , by applying the equation:

$$I(q) = n(c)P(q)S(q) \quad (3.3.1)$$

where the number density  $n = N/V$ , is directly proportional to the experimental mass density  $c$  (here we need to calculate the volume fraction as follows:

$$\phi = c(\text{vol}\%) = \frac{\frac{m_{\text{cellulose}}}{\rho_{\text{cellulose}}}}{\frac{m_{\text{cellulose}}}{\rho_{\text{cellulose}}} + \frac{m_{\text{BmimAc}}}{\rho_{\text{BmimAc}}}} \quad (3.3.2)$$

Values of  $\phi$  are listed in the **Table 3.3.1**.

**Table 3.3.1:** Values of the volume fraction  $\phi$  as a function of the weight concentration  $c$ .  $M_{\text{cell}}$  is the mass of cellulose powder, of density  $\rho_{\text{cellulose}}$  introduced in the solvent,  $M_{\text{sol}}$  is the mass of solvent of density  $\rho_{\text{solvent}}$  weighed in the vial.

$M_{\text{cell}}$	$\rho_{\text{cellulose}}$	$M_{\text{sol}}$	$\rho_{\text{ionic liquid}}$	$c$ (% w/w%)	$\phi$
0.00525	1.5	1.05	1.05	0.5	0.00349
0.0105		1.05		1	0.00695
0.021		1.05		2	0.01381
0.0315		1.05		3	0.0206
0.042		1.05		4	0.0272
0.0525		1.05		5	0.0338
0.063		1.05		6	0.0403
0.0735		1.05		7	0.0467
0.084		1.05		8	0.0530
0.0945		1.05		9	0.0593
0.105		1.05		10	0.06542
0.1575		1.05		15	0.09502
0.21		1.05		20	0.1228
0.315		1.05		30	0.1735
0.42		1.05		40	0.2187

$P(q)$  is the form factor. In principle this equation applies for undeformable, impenetrable, isotropic objects such as hard spheres (silica nanoparticles for example). This assumes that  $P(q)$  is independent of the concentration, which is plausible for rigid chains (at variance with flexible Gaussian or Self-Avoiding polymer chains which interpenetrate each other).

All curves were standardized with the intensity  $I = (I_{solution} - I_{solvent})/\phi_{cellulose}$  at  $2 \text{ cm}^{-1}$  for  $q = 0.69 \text{ \AA}^{-1}$ .

Here we extend this model to a set of hard cylinders, assuming that they are parallel at the scale of their length. Considering then a planar section perpendicular to the axis of the chains, which appear as disks, the model is equivalent for disks in 2D to a 3D model for spheres. This is an approximation, but we think it may describe local chain-to-chain interactions. Those are parametrised by:

- an infinite wall, at a distance  $R_{HD}$  from the chain axis in the “perpendicular” plane, representing the hard cylinder wall
- a soft interaction potential, measured in  $k_B T$  units, with a range, noted *range*.
- a 2D density of chains (in the transverse plane),  $n_{2D} = \phi \cdot A$ , where  $\phi$  is the volume fraction of chains,  $A$  is the surface of the disks.

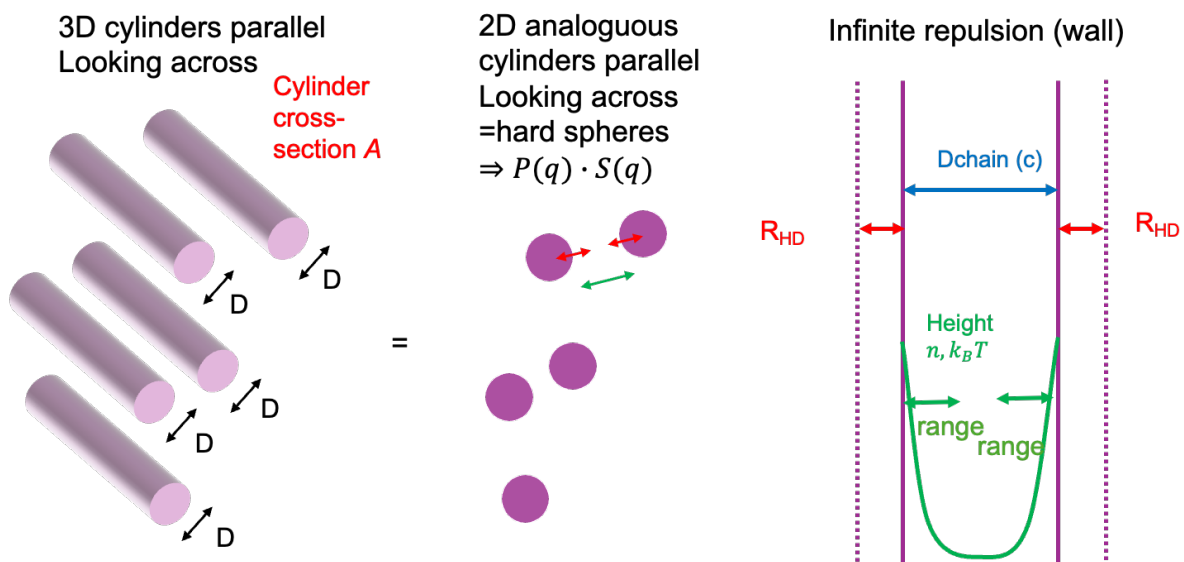


**Figure 3.3.2a:** 2D model of interacting parallel cylinders.  $D$  is the diameter of the rods,  $A$  their section area,  $R_{HD}$  is the radius of the hard-disk, *range* is the range of the soft potential

$V(r) = u \cdot \exp\left(-\frac{1}{2}\left(\frac{r}{range}\right)^2\right)$ .  $D_{chain}(c)$  is the average distance between chains, which depends on concentration  $c$ .

### 3.3.2.2 Calculations

For the cellulose solution, we used the structure factor of hard disk ( $u = 0$ ), which has a simple analytical expression and yields two parameters: the hard disk radius  $R_{HD}$  and the in-plane number concentration  $n_{2D}$  (**Figure 3.3.2a**). The structure factor  $S(q \rightarrow 0)$  reflects the long-range behavior, for semidilute solutions.  $S(0)$  is related to the (two-dimensional) osmotic pressure  $\Pi_{2D}$  which results from particle interactions,

$$\Pi_{2D} = \frac{n_{2D}k_B T}{S(0)} \quad (3.3.3)$$

which  $n_{2D}$  is the in-plane number concentration of the objects;  $k_B$  is the Boltzmann constant;  $T$  is the temperature /K;  $S(0)$  refers the structure factor as  $q \rightarrow 0$ .

$$S(0) = 1 - \frac{n_{2D}}{2} \int_0^\infty [S(q) - 1] dq \quad (3.3.4)$$

The structure factor  $S(q)$  is calculated using the hard disk model with the Percus-Yevick approximation and is obtained through a numerical solution. The structure factor for a hard disk mixtures, it is derived by Y. Rosenfeld (Rosenfeld, 1990), which is using the one-component simplified form given in equation:

$$S(q) = \frac{1}{1 + 4\eta c(q)} \quad (3.3.5)$$

Where  $\eta = \phi\pi r^2$  is the area fraction; the intermediate function  $c(q)$  is computed using the Bessel functions  $J_1(qR)$  and  $J_0(qR)$

$$c(q) = a \left( \frac{J_1(qR)}{qR} \right)^2 + b \frac{J_0(qR)J_0(qR)}{qR} + g \frac{J_1(2qR)}{qR} \quad (3.3.6)$$

The relationship between the area fraction  $\eta$ , parameter  $g$  and compression parameter  $\chi$  is:

$$g = (1 - \eta)^{-1.5} \quad (3.3.7)$$

$$\chi = \frac{1 + \eta}{(1 - \eta)^3} \quad (3.3.8)$$

where  $a$  and  $b$  are the functions of  $\eta$ , representing short-range repulsive interactions and mid-range interactions,  $a$  describing the direct effect of the repulsive makes the object cannot overlap, and  $b$  reflecting the arrangement and geometric effects of the objects at intermediate distances respectively:

$$a = \frac{1 + (2\eta - 1)\chi + 2\eta g}{\eta} \quad (3.3.9)$$

$$b = \frac{(1 - \eta)\chi - 1 - 3\eta g}{\eta} \quad (3.3.10)$$

The total function can be re-written below:

$$S(q) = \frac{1}{1 + 4\eta \left[ a \left( \frac{J_1(qR)}{qR} \right)^2 + b \frac{J_0(qR)J_0'(qR)}{qR} + g \frac{J_1(2qR)}{qR} \right]} \quad (3.3.11)$$

Where  $R$  is the radius of the rod;  $\eta$  is the volume fraction, representing the density of the model in the system;  $J_0$  and  $J_1$  are the Bessel function, which is for the cylindrical symmetry problem.

In the case of an additional soft potential ( $u \neq 0$ ), the calculation can be done only numerically. We used a software kindly provided by Doru Constantin, see **Figure 3.3.3**.

At low  $q$ , we observed oscillation, they are due to the edge effect in the calculation, as also observed from the numerical calculation for ( $u = 0$ ). In this case, the curve oscillates around the analytical calculation of Rosenfeld. It demonstrates that they are artefacts; for they don't reduce the validity of the numerical calculation, see **Figure 3.3.2b** for comparison between analytical and numerical calculation for hard-disks.

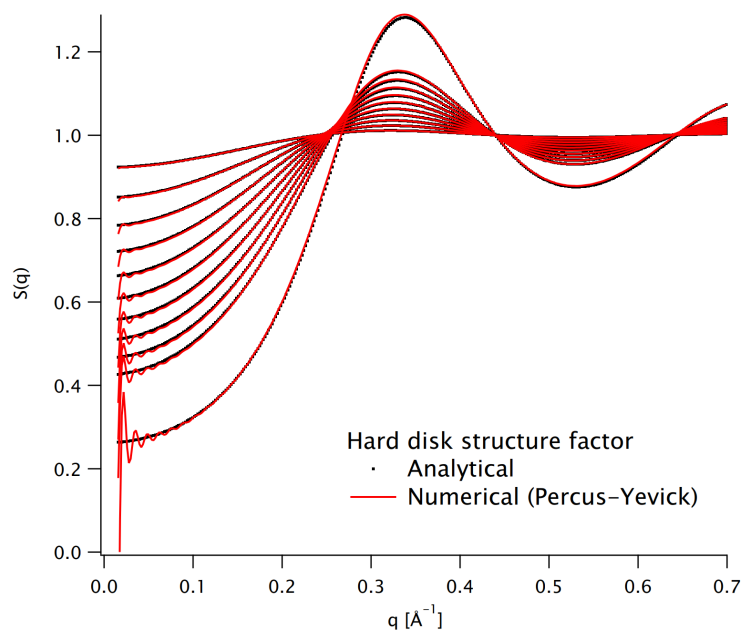


**Figure 3.3.2b:** The analytical and numerical structure factor  $S(q)$  with cellulose concentration from ranging from 1 wt% - 15 wt%

### 3.3.3 Hard cylinder 2D structure factor: comparison with data

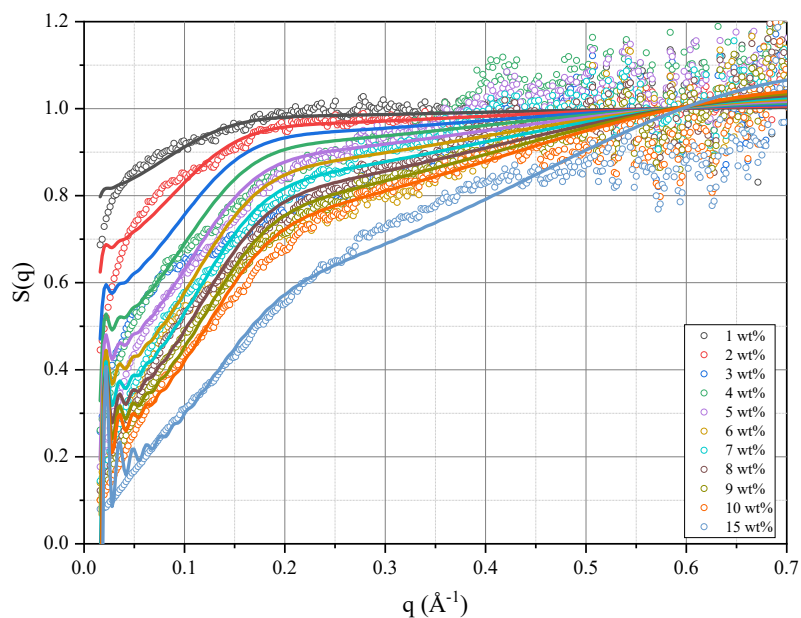


**Figure 3.3.3:** Fitting (the lines) of numerical structure factor  $S(q)$  of MCC/BmimAc solution with cellulose concentration ranging from 1 wt% - 15 wt%

Radius (Å)	Potential strength (V(r)/k <sub>B</sub> T)	Potential range (Å)	2D number density (Å <sup>-2</sup> )
3.3	0.65	14	0.0045

**Table 3.3.2:** Parameters for the fit of Figure 3.3.2 (structure factor  $S(q)$  of MCC/BmimAc solution with cellulose concentration ranging from 1 wt% - 15 wt%)

The structure factor  $S(q)$  obtained using SAXS for several cellulose concentration samples in ionic liquid BmimAc have been fitted using the hard-disk scheme using an *IgorPro* software written by Doru Constantin, ICS, Strasbourg. The only adjustable parameters are the  $R_{HD}$  and the range (*range*) respectively (in principle  $n_{2D} = \phi \times A$ , where the chain cross-section  $A$  is known), determined from a fit to the SAXS structure factor. The parameters characterizing the several samples are list in **Table 3.3.2**. The SAXS data for  $S(q)$  are shown in **Figure 3.3.3**, shows the fits to the experimental scattering data of  $S(q)$  and the variations across different cellulose concentrations. In all cases, the agreement between the calculated and experimental values provides confidence in using the configuration files to gain further insights into the chain interactions under investigation. The input function used is the structure factor, as previously noted, based on the hard-disk model. At low concentrations, there is a noticeable deviation, as the structure factor does not decay as quickly toward the uncorrelated value  $S(q) = 1$  compared to the experimental data.

According to the Gaussian repulsive potential (Hansen and McDonald, 2007), the potential function  $V(r)$  describes the interaction potential between objects as a function of their separation distance,

$$V(r) = u \cdot \exp\left(-\frac{1}{2}\left(\frac{r}{range}\right)^2\right) \quad (3.3.12)$$

where  $u$  is the amplitude or strength of the potential (k<sub>B</sub>T);  $r$  is the distance between two objects; *range* is the interaction range, which determines the spatial extent of the potential; it controls how quickly the potential decays as the distance increases.

In **Figure 3.3.4**, for small values of  $r < 2r_0$ ,  $r_0$  being the radius of the hard object, the potential  $V(r)$  is very large, indicating a strong repulsive interaction between particles at short distances.

As  $r$  increases, for ( $r > 2r_0$ ), the potential decays exponentially due to the Gaussian function, indicating that the repulsive interaction weakens with increasing distance.

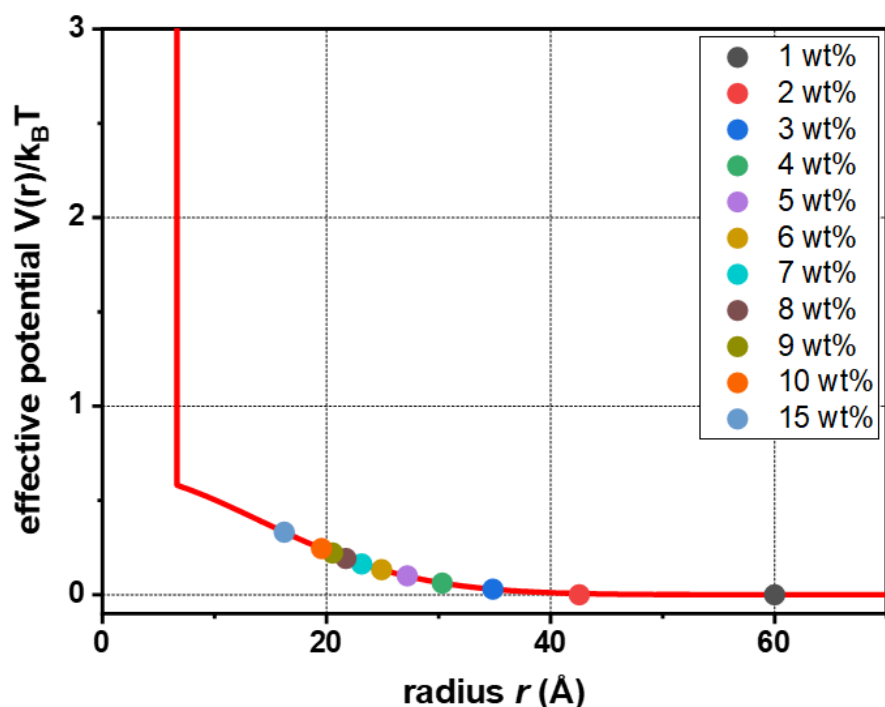


**Figure 3.3.4:** Interaction potential  $V(r)$  as a function of the radius  $r$ , derived from the fitting of the structure factor. The sharp wall at small  $r$  indicates short-range interactions, while the smooth decay to zero as  $r$  increases, suggests weak long-range interactions. The *range* of the soft potential  $V(r)$  – eq. 3.16 - is 14 Å.

In the **Figure 3.3.4**,  $V(r)$  the effective potential, describes the averaged effects of multiple interactions within a system, to describe an effective or mean-field potential derived from the interactions between multiple particles. For  $V(r)/k_B T < 1$ , the interaction energy domain in the system, form ordered structures with minimal thermal fluctuations,  $V(r)/k_B T > 0$ , which means a weak repulsion between cellulose chains

In the **Figure 3.3.4**  $V(r)$  vs  $r$ , for  $r < 10$  Å, the high potential indicates the strong repulsive between the cellulose chains, where 10 Å is the chain core-shell diameter. For  $10$  Å  $< r < 40$  Å, the weak repulsive interaction between the cellulose chain indicates that the chains are weakly aligned with each other. This corresponds to a decrease of the scattering (weaker fluctuations), in such a way that the SAXS slope decreases in the middle  $q$  range. For  $r > 40$  Å, the low potential approaches zero: the chain-to-chain interactions at such large distance are screened, due to the high concentration.



### 3.4 Higher concentrations: biphasic state

Scattering curves for solution with  $c$  higher than 15 wt%, equal to 20%, 30%, and 40% are shown in **Figure 3.4.1**, (other concentrations are also presented for comparison). As commented at the beginning of the Chapter, the scattering is much higher for larger concentrations. The curves are also shown separately for better visibility, both in the SAXS and the WAXS  $q$  ranges. For 40%, we notice some crystal peaks in the WAXS range **Figure 3.4.1** and **Figure 3.4.2 b**). This means that a part of the cellulose is not dissolved. However, the scattering at lower  $q$  is not very different from the 20 and 30%, suggesting coexistence of the same kind of biphasic structure, with the crystals.

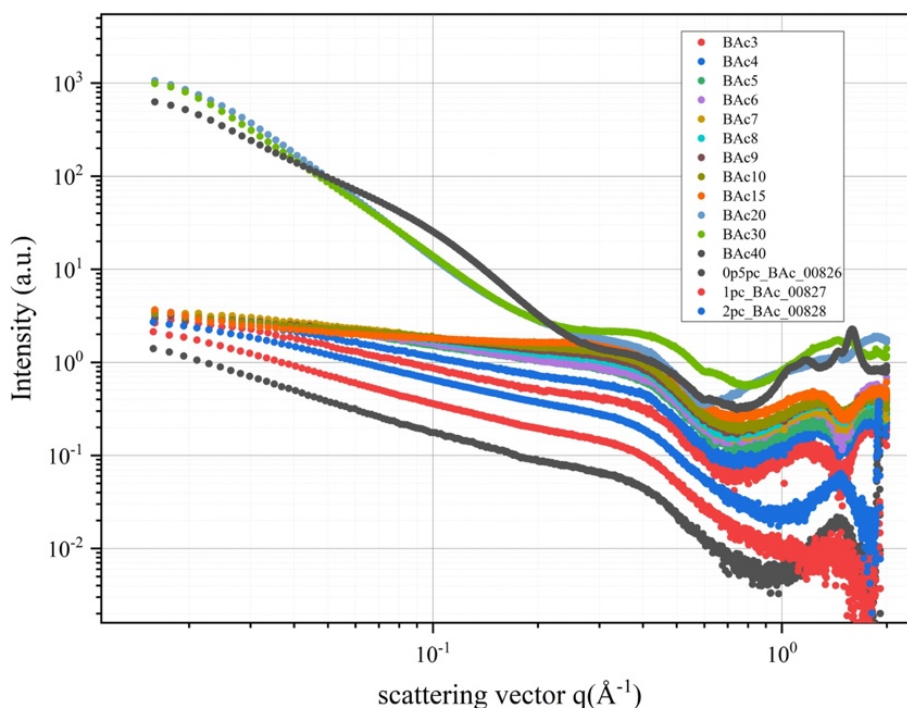


**Figure 3.4.1:** Scattering from MCC solutions in BmimAcetate at increasing concentrations from 3 to 40%. Only the black curve for 40% displays crystal peaks at the largest  $q_s$ .

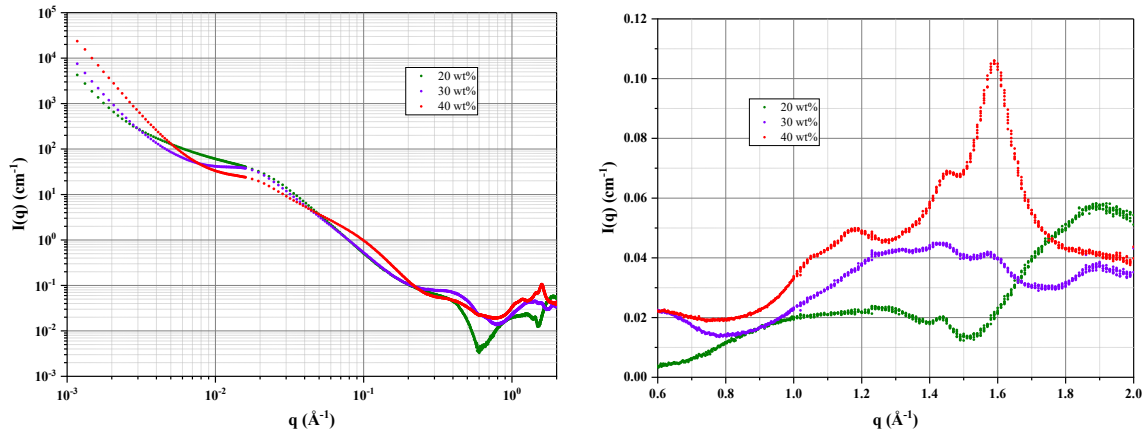
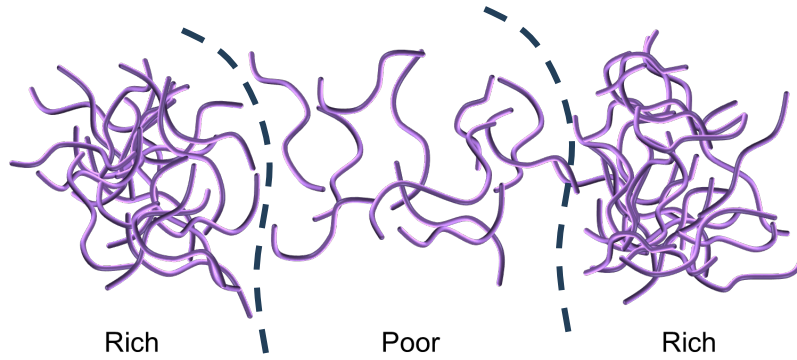


**Figure 3.4.2:** a) Strong low  $q$  scattering from MCC solutions in BmimAcetate at high concentrations 20, 30 and to 40%. Only the black curve for 40% displays crystal peaks at the largest  $q_s$ ; b) Same spectra at large  $q$ . The red curve shows crystalline peaks from cellulose crystals.



**Scheme 3.4.1:** Spatial coexistence of cellulose rich and cellulose poor phases.

### Analysis.

We can analyze the scattering for the 20 and 30% as the sum of two contributions (**Figure 3.4.3**):

- the scattering of a rod, which is visible at larger  $q$ , in the region of the rod diameter
- a biphasic system, as described by the Debye - Anderson - Braumberger expression (otherwise called Debye-Bueche) (Debye et al., 1957; Debye and Bueche, 1949).

$$S_{DAB}(q) = \frac{8\pi\Phi_{phase\ rich}(1 - \Phi_{phase\ rich})\Delta\rho^2\Xi^3}{(1 + q^2\Xi^2)^2} \quad (3.4.1)$$

The principle of the analysis is illustrated on **Figure 3.4.3**, and the result using SASView combined with a “Plugin model” consisting of such sum in **Figure 3.4.4**.  $\Phi_{phase\ rich}$  is the

volume fraction of the phase rich in cellulose, of cellulose volume fraction  $\phi_{rich}$ , and  $1 - \Phi_{phase\ rich}$  the one of the other (poor in cellulose), of cellulose volume fraction  $\phi_{poor}$ . We can assume either that most of the dissolved cellulose is contained in one of the phases – in this case  $\phi_{rich} \sim \phi_{nominal}$  or that some cellulose is contained in both phases. The variable  $\Xi$  is the characteristic correlation size of the biphasic medium (the correlations vary as  $C(r) \times C(0) \sim \exp(-\Xi/r)$ ).

Knowing  $\Xi$  from the dependence on  $q$  (variation along the  $q$  axis), we can extract from the front factor the quantity  $\Phi_{phase\ rich}(1 - \Phi_{phase\ rich})\Delta\rho_{eff}^2$ , where  $\Delta\rho_{eff}^2$  is the contrast between the two phases (Lal et al., 1994). It is easy to show that

$$\Delta\rho_{eff}^2 = \Delta\rho_{max}^2 \cdot (\phi_{poor} - \phi_{rich})^2 \quad (3.4.2)$$

where  $\Delta\rho_{max}^2$  is the contrast between cellulose and the solvent, while conservation of cellulose implies that

$$\Phi_{phase\ rich} \cdot \phi_{rich} + (1 - \Phi_{phase\ rich})\phi_{poor} = \phi_{nominal} \quad (3.4.3)$$

And introducing  $\delta\Phi_{rich} = \phi_{rich} - \phi_{nominal}$  and  $\delta\Phi_{poor} = \phi_{poor} - \phi_{nominal}$ , we have

$$\Phi_{phase\ rich}(1 - \Phi_{phase\ rich})(\phi_{rich} - \phi_{poor})^2 = \delta\Phi_{rich}\delta\Phi_{poor} \quad (3.4.4)$$

Thus

$$\begin{aligned} \Delta\rho_{eff}^2\Phi_{phase\ rich}(1 - \Phi_{phase\ rich}) \\ &= \Delta\rho_{max}^2(\phi_{rich} - \phi_{poor})^2\Phi_{phase\ rich}(1 - \Phi_{phase\ rich}) \\ &= -\Delta\rho_{max}^2\delta\Phi_{rich}\delta\Phi_{poor} \end{aligned} \quad (3.4.5)$$

From another point of view,

$$\Delta\rho_{eff}^2\Phi_{phase\ rich}(1 - \Phi_{phase\ rich}) < \Delta\rho_{max}^2\phi_{nominal}(1 - \phi_{nominal}) \quad (3.4.6)$$

The SASView – DAB fit gives a front parameter “scale” which must be equal to:

$$\begin{aligned}
scale &= 8\pi\Phi_{phase\ rich}(1 - \Phi_{phase\ rich})\Delta\rho_{eff}^2\Xi^3 \\
&= 55\ cm^{-1}
\end{aligned}
\tag{3.4.7}$$

which, for  $\Xi = 35\ \text{\AA}$ , gives

$$\begin{aligned}
\Delta\rho_{eff}^2\Phi_{phase\ rich}(1 - \Phi_{phase\ rich}) &= \frac{scale}{8\pi\Xi^3} \\
&= \frac{55\ cm^{-1}}{8\pi \times 35^3 \times 10^{-24}\ cm^3} \\
&= 4 \times 10^{-5+24-32=-13}\ \text{\AA}^{-4} \\
&= 0.4 \times 10^{-12}\ \text{\AA}^{-4}
\end{aligned}
\tag{3.4.8}$$

to compare to  $(0.173 \times 0.826 = 0.1434) \times 14.7 \times 10^{-12}\ \text{\AA}^{-4} = 2.1 \times 10^{-12}\ \text{\AA}^{-4}$ , It is 5 times lower than  $\Delta\rho_{max}^2$ , in other words  $\delta\Phi_{rich}\delta\Phi_{poor} = 0.2$ , suggesting that we have two phases containing both cellulose.

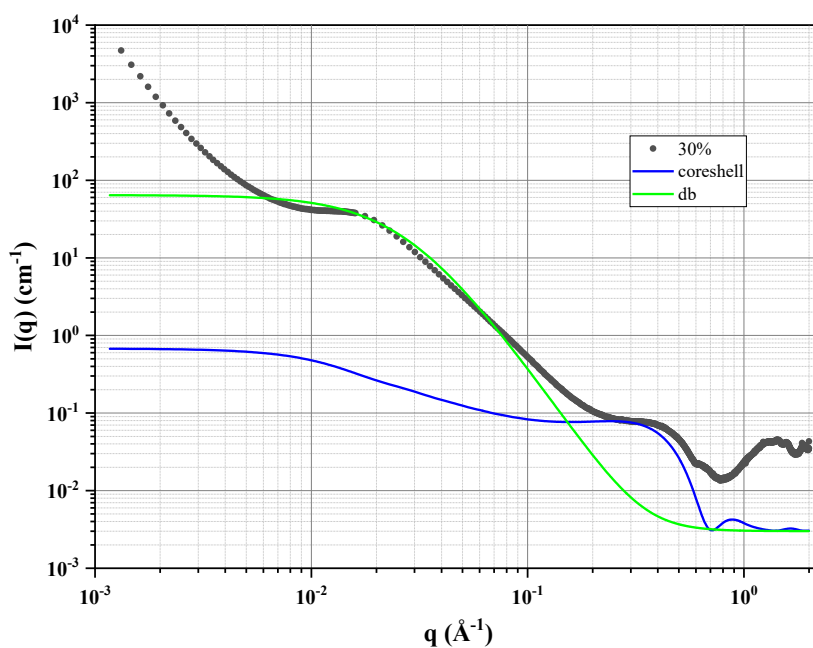
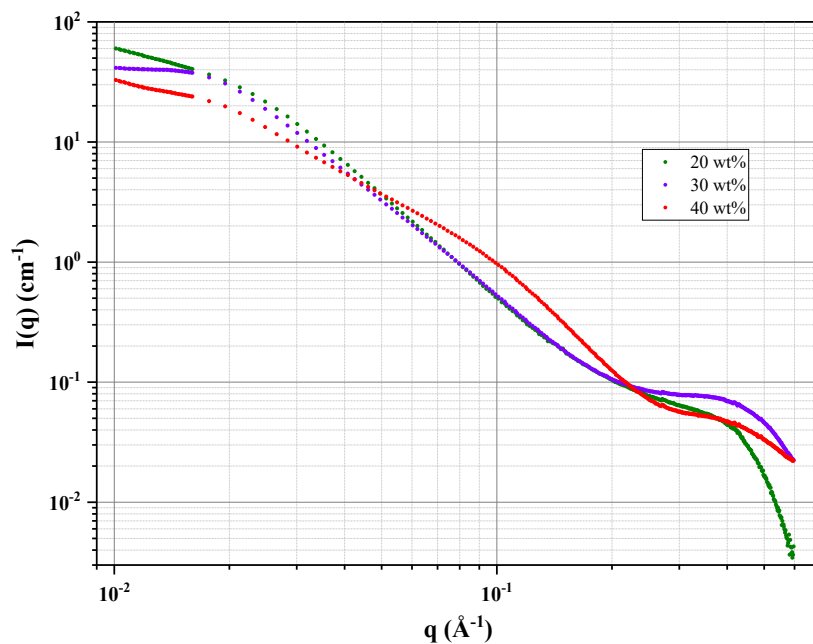


**Figure 3.4.3:** Scheme of the principle of a fit of the plot (curves above) using the sum of a scattering from a biphasic system (green) and a core-shell rod (blue).

Below is an example of SASview fit for 30%. Note that a slight maximum is observed on the experimental curve. This is often observed as a consequence of local polymer phase separation, at different stages of spinodal or binodal decomposition.

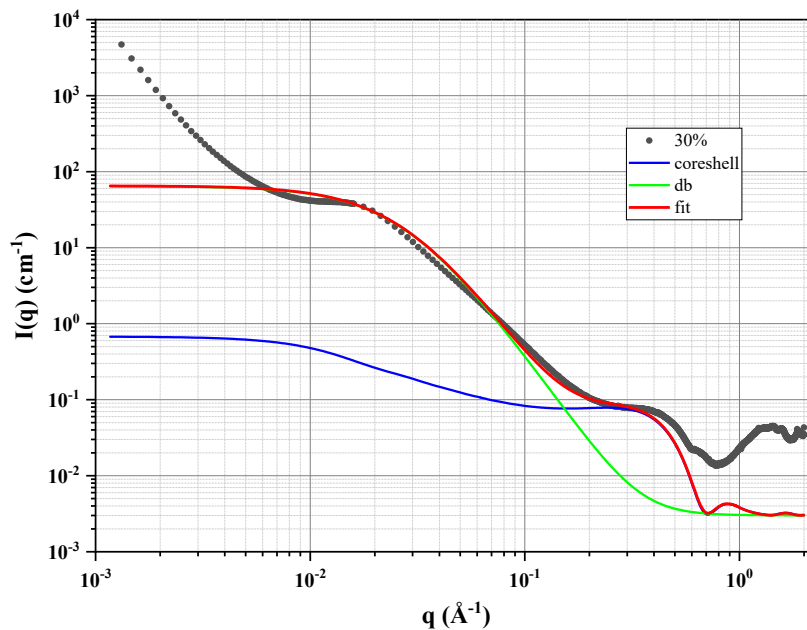


**Figure 3.4.4:** Example of SASview fit (red curve) for 30 wt% MCC in BmimAc. Note that a slight maximum is observed on the experimental curve

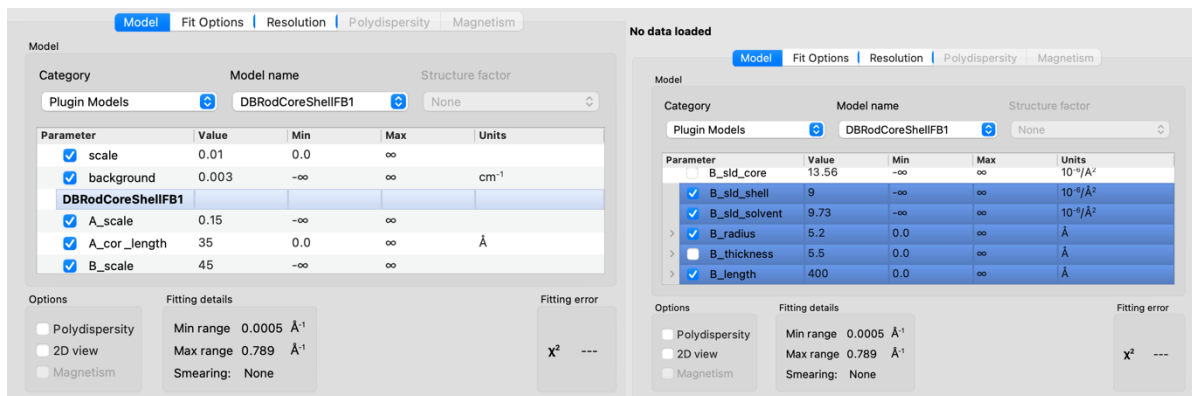


**Figure 3.4.5:** Screenshot of SASview fit for 30 wt% MCC in BmimAc

## 3.5 Solutions in BmimCl: similarities and differences, a check

### 3.5.1 BmimCl solutions at different concentrations

Preparation of solution is slightly different since pure BmimCl at room temperature should be a crystalline powder. However, it melts above 90 °C, and remains liquid at room temperature, because the crystallization is hindered (over cooling). It is thus necessary to have a careful check on the presence of BmimCl crystals. In cellulose solutions, there is a crystallization behavior of BmimCl in presence of cellulose at -25°C, BmimCl crystallization also induce partial cellulose self-organization (Kotov et al., 2020, 2016) as it was observed from NMR. It is important to keep that in mind. In our experiments, we never detected any crystals which should be observed by diffraction peaks in the WAXS/SAXS curves.

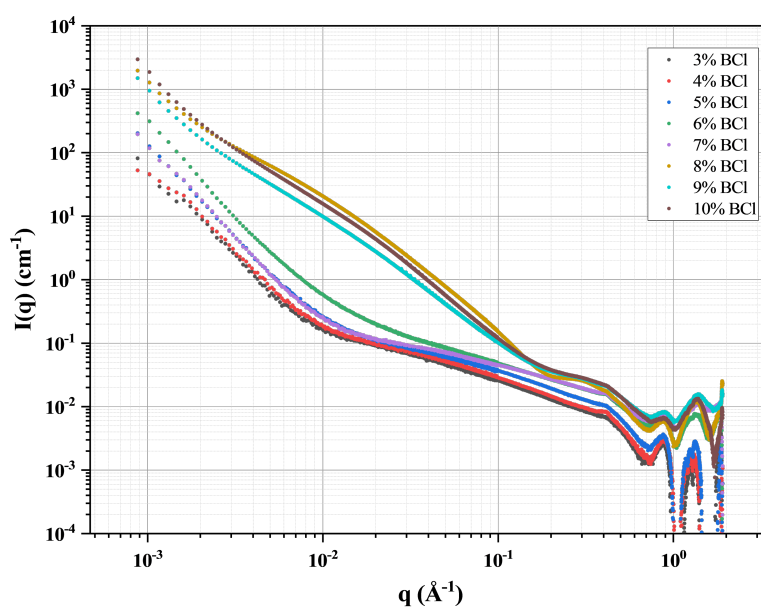


**Figure 3.5.1:** SAXS and WAXS plots for MCC in BmimCl at increasing concentration.

**Figure 3.5.1** shows the effect of concentration on the scattering of MCC in BmimCl. For concentrations below 7 %, the scattering curves present a progressive decrease of the slope when cellulose concentration increases, as for BmimAc, for  $q > 10^{-2} \text{\AA}^{-1}$ . For concentration larger than 7%, we observe a  $q^{-3}$  dependence evidencing compact aggregates resulting from strong aggregation.

Completely differently, large concentrations above 7 % show a large additional contribution

as soon as  $q < 10^{-1} \text{ \AA}^{-1}$ . If one subtracts the low  $q$  contribution in  $q^{-3}$ , we obtain a plateau, with a characteristic size of order 100  $\text{\AA}$ . This is similar to the highest concentrations of BmimAc, and very similar to the effect of water for BmimAc. No scattering from crystals at larger  $q$  (WAXS) is detectable.

### 3.5.2 Comparison between BmimCl and BmimAc

Comparison with the scattering from BmimAc is shown in **Figure 3.5.2**, for the same concentration, 1 %. The levels of intensity are very close, being slightly higher for BmimAc. This agrees with the higher contrast for BmimAc – by a ratio 10.4 %, in part only. The shape (profile) is very similar, except at large  $q$  in the shoulder region which is less pronounced for BmimCl. This could be due to insufficient solvent subtraction, but this more pronounced shape is seen through all concentration, including the largest ones where this should not be as important.

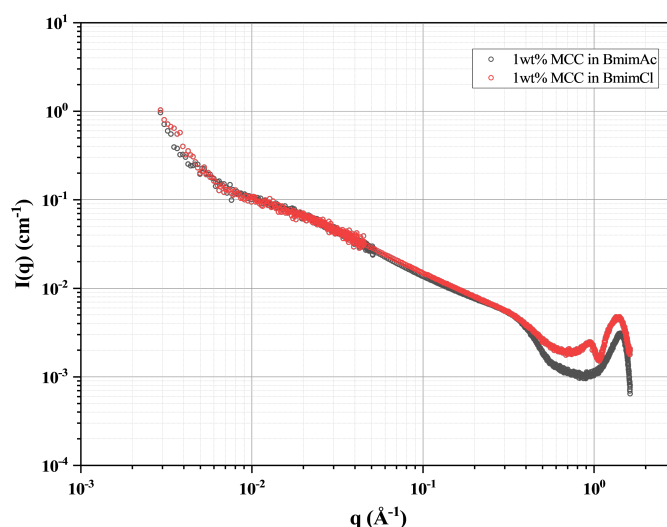


**Figure 3.5.2:** Comparison between scattering from BmimCl (red circle) and BmimAc (black circle) at the same concentration 1 wt% of MCC cellulose (no water added).



## 3.6 Effects of water and temperature in BmimAc and BmimCl

### 3.6.1 Effect of water for BmimAc at large $q$

It is reported in literature that room temperature ionic liquids based on 1-butyl-3-methylimidazolium are hygroscopic and quickly absorb water when they are exposed to environmental air, the higher amounts of water can be absorbed when anion of the ionic liquid can strongly interact and stabilize absorbed water molecules by forming hydrogen bonds with them, or inducing hydrogen bonds among water molecules (Tran et al., 2003) as well as chloride and acetate. In ionic liquid/cellulose system, water content can change the performance of the solution (Zhao et al., 2022). So, what effect will have the water concentration variation in cellulose/IL system, on the cellulose dissolution and chain conformation? We want to know the chain state with the IL/water mixture, to give better advice for application.

The WAXS scattering curve of BmimAc (Figure 3.6.1) shows the ionic liquid peaks at  $\sim 1.55 \text{ \AA}^{-1}$  and  $0.64 \text{ \AA}^{-1}$ , which is indicating the short-range order or distance of cation  $\text{Bmim}^+$  and  $\text{Ac}^-$ , and the nanostructure between the polar ( $\text{Bmim}^+$  and  $\text{Ac}^-$ ) and non-polar (hydrophobic butyl side chain) regions. The scattering from water (purple curve) shows an absolute intensity of  $0.0163 \text{ cm}^{-1}$  in the flat part. It shows an increase at large  $q$ , ( $q > 1 \text{ \AA}^{-1}$ ), due to the short-range order of the water oxygen-oxygen distance ( $\sim 2.8 \text{ \AA}$ ), corresponding to an onset of the peak at  $2.2 \text{ \AA}^{-1}$  of water, which cannot be detected in this configuration. The intensity of BmimAc/ $\text{H}_2\text{O}$  mixtures shows, with adding  $\text{H}_2\text{O}$  in BmimAc:

- a decrease and a shift of the first peak to lower  $q$ , due to the segregation of the non-polar butyl side chain with water.
- a shift of the second peak to larger  $q$  with peak broadening, indicating the perturbation by the water of the short-range order of the ionic liquid BmimAc.

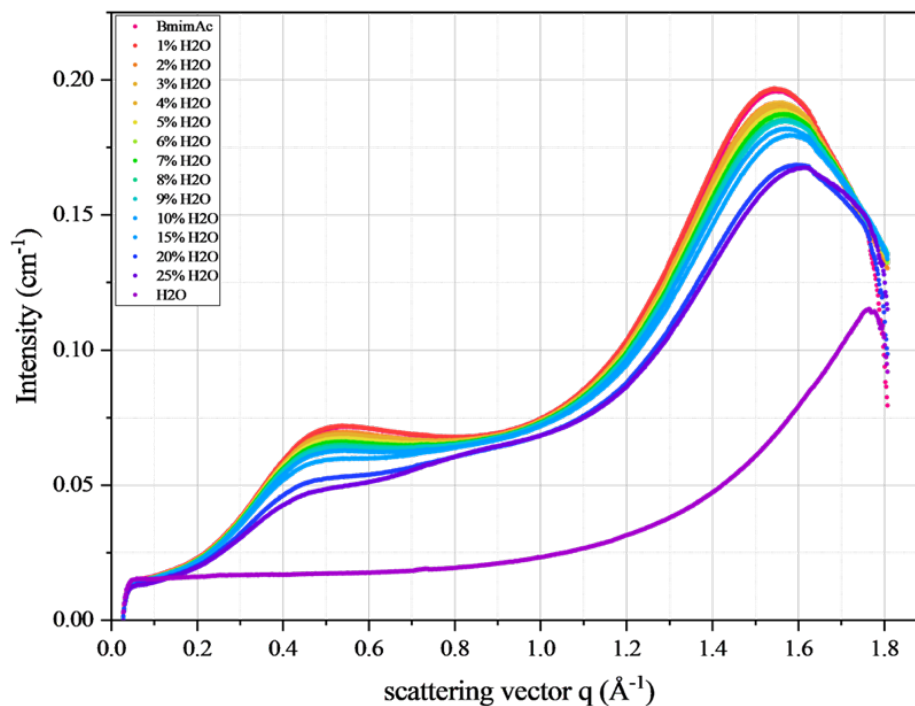


**Figure 3.6.1:** WAXS patterns of [Bmim][Ac], H<sub>2</sub>O and [Bmim][Ac]/H<sub>2</sub>O mixtures with various H<sub>2</sub>O concentrations (no cellulose).

### 3.6.2 Effect of water for BmimAc - cellulose solution at low $q$

On top of checking water effect on the solubility, it is interesting to monitor water effects since water is used as an anti-solvent to facilitate the "regeneration" of cellulose crystals from solutions. Therefore, we conducted SAXS experiments on cellulose solutions within a H<sub>2</sub>O/ILs mixture solvent systems. Our aim was to investigate possible aggregation, or phase separation, between cellulose and the solvent. The **Figure 3.6.2** shows the SAXS measurements, it evidences that water addition leads to a significant increase of scattering, with a power-law behavior characterized by  $q^{-4}$  at middle  $q$  values, corresponding to the formation of compact objects. This phenomenon is likely attributed to the growth of cellulose aggregates, or solvent rich phases – solvent poor phases separated by thin interfaces, or crystals.

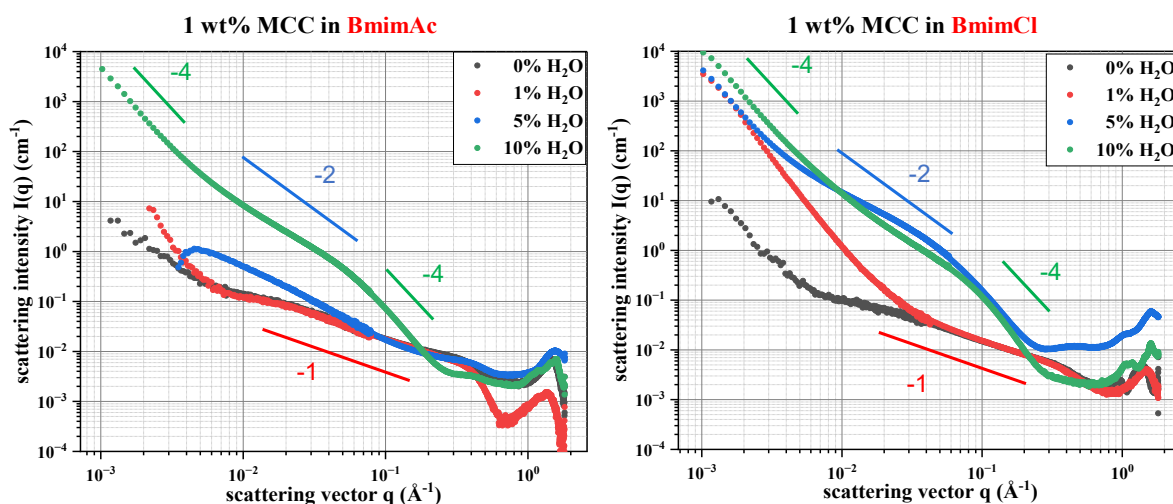


**Figure 3.6.2:** SAXS patterns of 1 wt% MCC solution in BmimAc/H<sub>2</sub>O mixtures (left) and BmimCl/H<sub>2</sub>O mixtures (right).

The solutions of cellulose at same concentration 1 wt% were prepared in various water/BmimAc ratio mixtures at 70 °C, from 0 wt% to 10 wt% water. Restraining ourselves to the right side of **Figure 3.6.2**, we observe the evolution of SAXS patterns with the incremental addition of water. The alterations in the scattering patterns become evident within the intermediate  $q$  range (0.01 to 0.1  $\text{\AA}^{-1}$ ). When the water ratio is below 1 wt%, for BmimAc, we observe a  $q^{-1}$  characteristic, both in the low  $q$  and middle  $q$  regions, indicative of rod-like scattering behavior, likely arising from the semi-flexibility of the polymer chains. As the water ratio increases to 5 wt%, the slope at low  $q$  and intermediate  $q$  increases suggesting the initiation of aggregation. In the case of a higher water ratio, specifically 10 wt%, we observe a distinct shoulder located at 0.04  $\text{\AA}^{-1}$ , positioned between a  $q^{-2}$  behavior at low  $q$  and a  $q^{-4}$  slope at larger  $q$ . This transformation indicates a transition in the interface between the cellulose chains and BmimAc, shifting from a softer interface to a sharper one ( $q^{-4}$ , indicative of Porod's limit) for compact aggregates, possibly in the form of fibers or disks, or separated phases. It is plausible to assume that within these aggregates or phases, the polymer chains are intermixed with water.

### 3.6.3 Effects of water: comparison with BmimCl solutions

For comparing, cellulose solutions in various water/BmimCl ratio from 0 wt% to 10 wt% of H<sub>2</sub>O were prepared with similar method. In **Figure 3.6.2**, BmimCl shows more sensitivity to water than BmimAc, and the effect is visible as soon as  $c_{water} = 1\%$ . At low  $q$  the significant

upturn indicates that the aggregation appears in the big scale with 1 wt% addition water. In the middle  $q$  range, the curve is overlapped with the curve of non-water solution. For 5 wt% addition, the spectrum shows phase separation already at middle  $q$ , meaning that the cellulose is not dissolved homogeneously, and peaks are observed at large  $q$ , evidencing the presence of cellulose crystals. The crystalline peaks clearly remain detectable when 10 wt% water is introduced into the solvent. This suggests that cellulose did not completely dissolve (or reformed). To gain deeper insights, it is essential to compare cellulose solutions in pure ionic liquids with cases where water is added after cellulose dissolution in ionic liquids.

In conclusion, the size of cellulose aggregates in BmimAc solutions experiences significant growth with increasing water content and cellulose concentration within the solution. This phenomenon can be attributed to the deteriorating effect of the solvent, which results in aggregation in the presence of water.

### 3.6.4 Absence of temperature effect in BmimAc

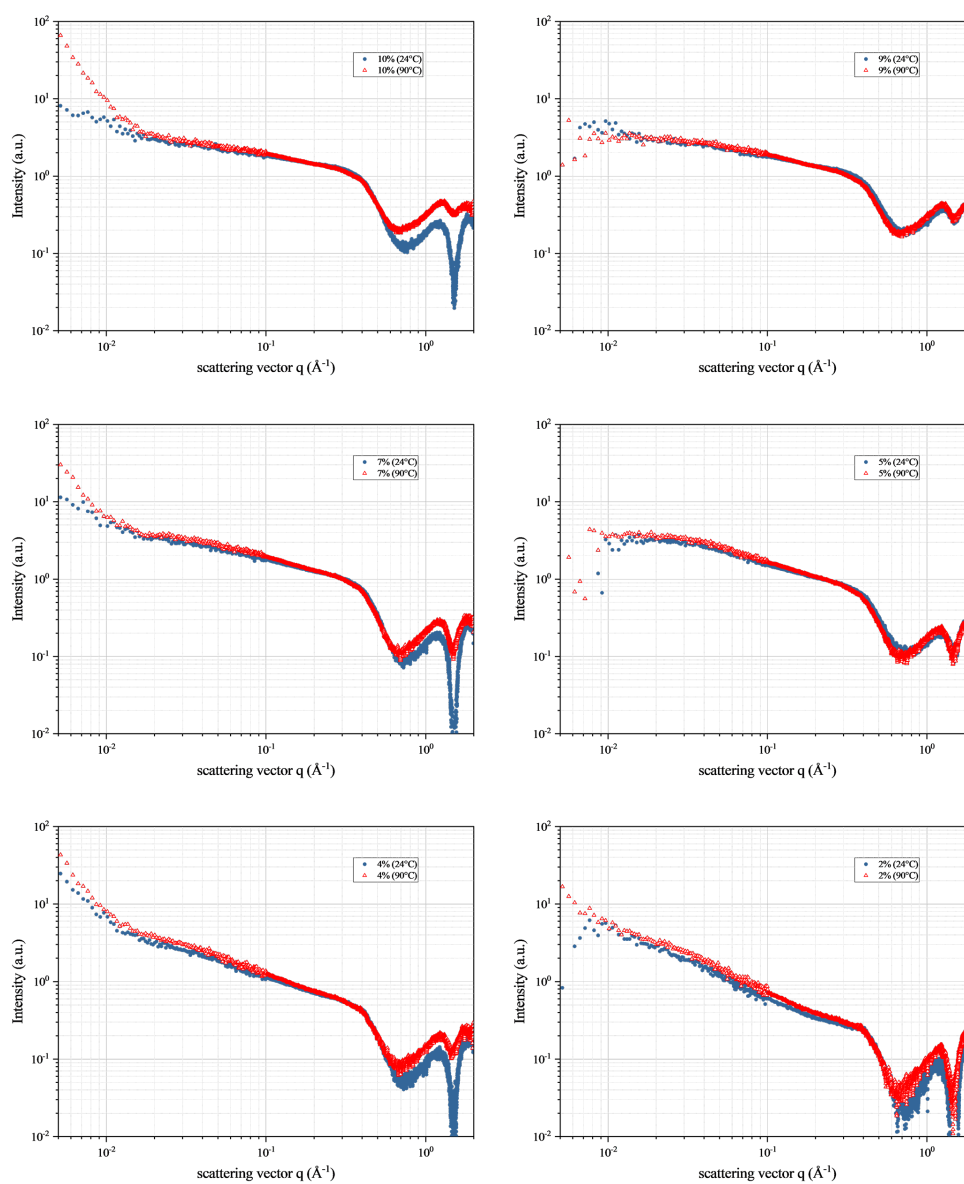


**Figure 3.6.3:** Effect of temperature on cellulose solutions: SAXS profiles at 24 °C and 90 °C for various cellulose concentrations in BmimAc with concentration 2%, 4%, 5%, 7%, 9% 10%. Curves for the two temperatures superimpose.

### 3.6.5 Effect of temperature: case of BmimCl

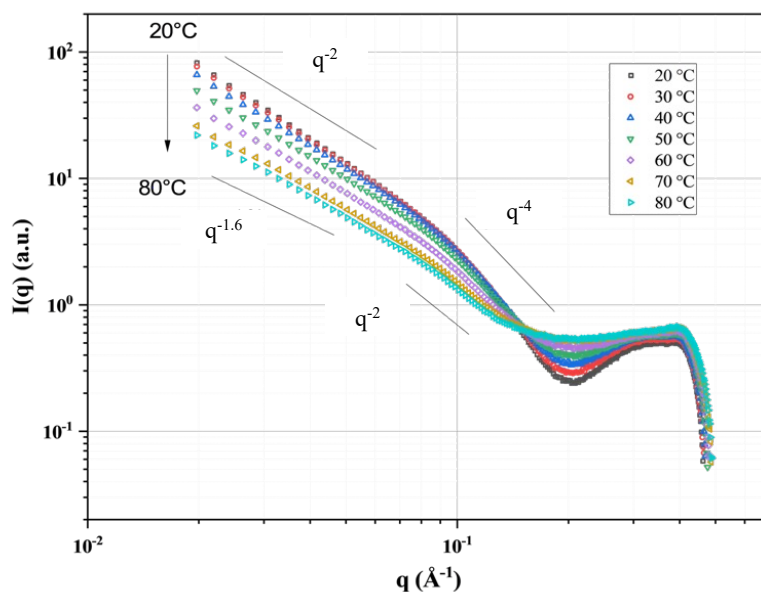


**Figure 3.6.4:** Variation of the scattering  $I(q)$  versus  $q$  during a temperature scan ( $0.5\text{ }^{\circ}\text{C/s}$  in a Linkam temperature stage) of a 2 wt% MCC solution in BmimCl containing water initially.

**Figure 3.6.4** shows the variation of the scattering curve of a 2 wt% MCC solution in BmimCl containing water initially during a temperature scan ( $0.5\text{ }^{\circ}\text{C/s}$ ) in a Linkam temperature stage. The evaporation of most of the water through the Kapton wall is probably too slow to occur during the measurement. The variation of the scattering is minimal from 20 to 30  $^{\circ}\text{C}$ , and then faster when above, until 80  $^{\circ}\text{C}$ . The apparent slope passes from -2, a value often obtained with aqueous solvents, down to -1.6. The  $q^{-1}$  power-law is not reached here, which may necessitate a longer time before observation. The reaction time for restructuring appears here, nevertheless, short. Obviously, under the presence of water, a structure has built up which is partly reversible. In the case of aqueous solvents, many observations have concluded in favour of the formation of a gel. We have also observed, through handling (i.e. macroscopically), gel-like behaviour. It also can depend on the kinetics of formation of the gel, which may be different. More studies would obviously be interesting, since these properties are at work during final steps of regeneration of cellulose.

## 3.7 Influence of the cellulose origin

### 3.7.1 Other microcrystalline cellulose

We compared scattering from solutions of microcrystalline cellulose (MCC) Avicel (degree of polymerization DP~220) and also another source, viscose cellulose (VC) (DP~250-350) in regard to the SAXS experiments. From the SAXS plot (**Figure 3.7.1**), MCC, and VC, present a nice overlapping. Cellulose from CNC films were also studied, with very good overlapping.

### 3.7.2 Bacterial cellulose

For the purpose of neutron scattering experiments, we also studied bacterial cellulose, BC (DP~2000-8000), as it is the only cellulose that can be obtained with deuterium substitution.

As a model for non-deuteriated BC, we choose the so-called “Nata de Coco”, a preparation from which cellulose can be extracted by vigorous and extended washing in water.

We see, also in **Figure 3.7.1**, that in the case of the BC sample, a substantial increase in signal at low  $q$  is evident, very differently from MCC and VC. At large  $q$ , presence of a very small crystal peak is also depicted in BC sample. We hypothesize that this increase is attributable to the aggregation of long chains within the BC sample for cellulose concentration of 2 wt%.

In the same **Figure 3.7.1**, the scattering bacterial cellulose is also plotted. It perfectly superimposes at large  $q$  on the other curves, showing that at local scale the BC chains have the same backbone. For low  $q$  range, the upturn increasing slope and intensity approximately 500 times higher than the MCC and viscose cellulose. For  $q < 3 \times 10^{-2}$  the BC presents a slope of  $q^{-4}$ , while MCC and VC keep a slope  $q^{-1}$ . It therefore shows some aggregation of BC. Here, we attempted to mitigate the impact of aggregation by subtracting the  $q^{-4}$  slope contribution, which is illustrated in the right part of the figure. Indeed, the agreement is satisfying. It therefore seems that the aggregates are compact, although it has been proposed that the chains would form a network as a consequence of the synthesis by several cells closely mingled.

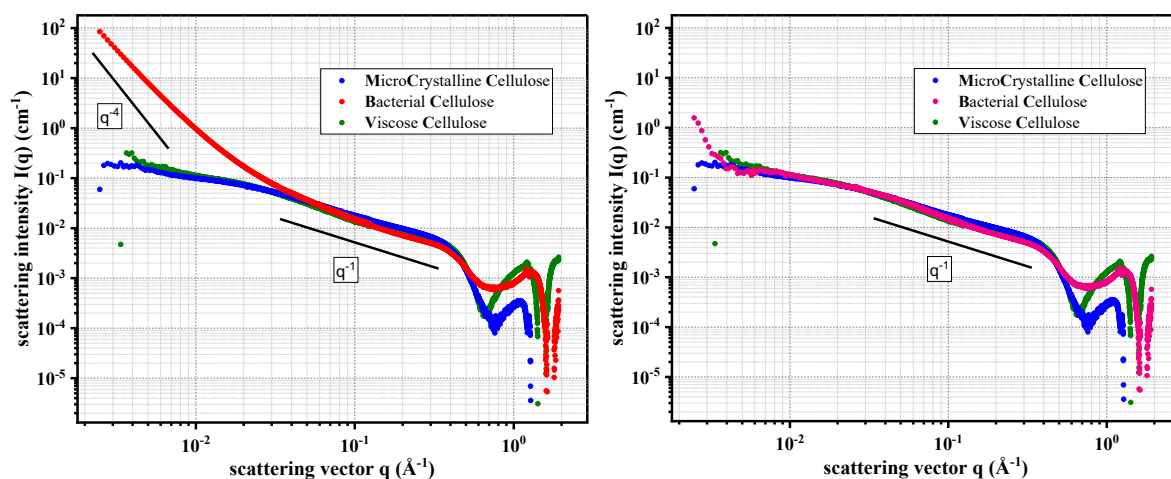


**Figure 3.7.1:** SAXS patterns of 2wt% MCC, VC and BC solutions in BmimAc; left: after background subtraction; right: subtract the large objects contribution of bacterial cellulose.

Very similar scattering has been observed on the deuteriated cellulose dBC (donated by Yoshiharu Nishiyama and Howard Wang). In the context of our SANS experiment, we are actively exploring methods to diminish the low  $q$  contribution. We have subjected bacterial cellulose (BC) from Nata de Coco to sonication of increasing duration until a total of 2 hours (so a total duration including the duration of rest periods – for cooling down - of 3 days). The decrease of aggregates is visible but insufficient. Acid hydrolysis processes to reduce the chain length effectively should be achieved. More work will be here necessary to control at the same time, the mass distribution.



### 3.8 Influence of co-solvent

Due to the high viscosity, in industry production, usually adding co-solvent to make the production. We studied the effect of one cosolvent dimethylformamide (DMF) effect on the different cellulose concentration. Various cellulose concentration with 2 wt%, 5 wt% and 10 wt% were dissolved in the different BmimAc/DMF mixtures with DMF content of 0%, 20%, 40% and 60%. The SAXS profiles are shown in **Figure 3.8.1**.

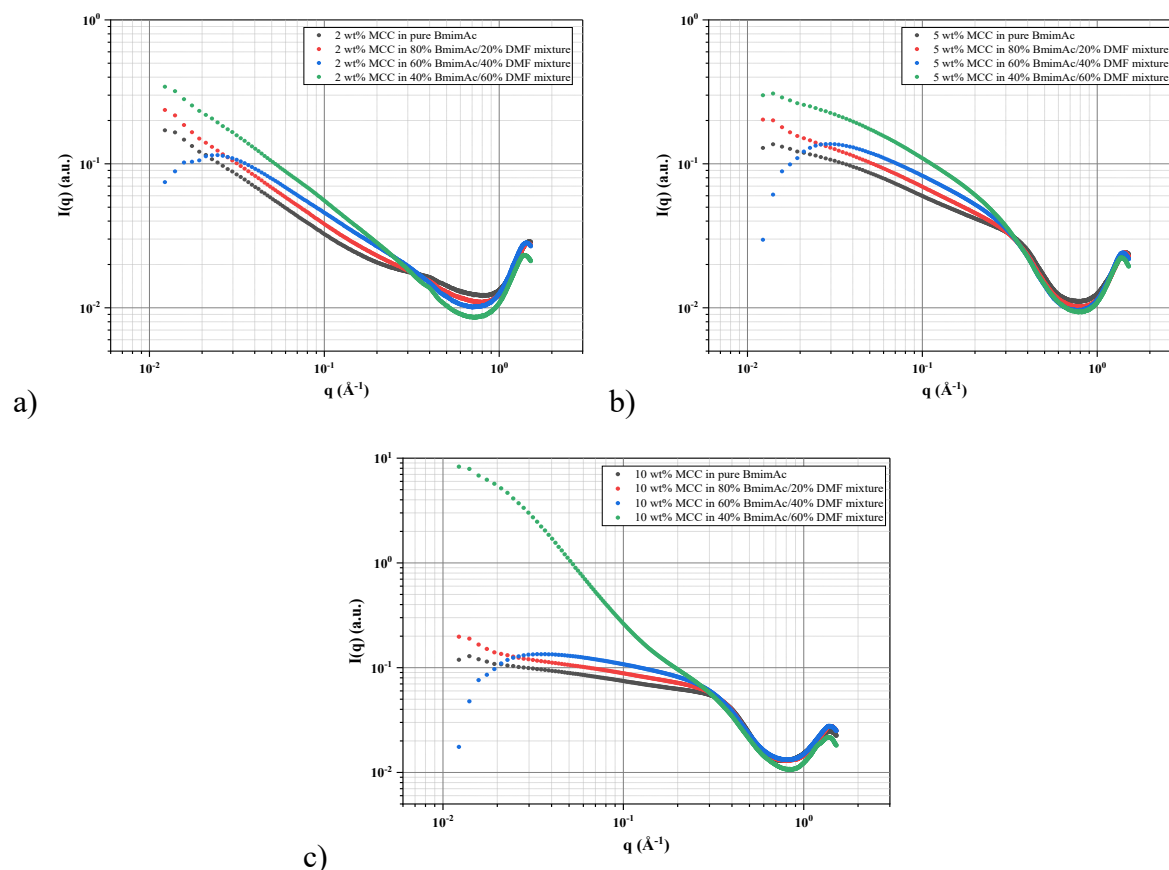


**Figure 3.8.1:** SAXS profiles of MCC solution in BmimAc/DMF mixtures with DMF content of 0%, 20%, 40% and 60% measured at 70 °C. Cellulose concentration are: a) 2 wt%; b) 5 wt%; c) 10 wt% respectively. highlighting the effect of so-solvent effect on the cellulose concentration.

For the 2 wt% and 5 wt% MCC solution, DMF have no effect on the cellulose structure of the form factor and structure factor, the intensity differences at low  $q$  are due to the volume fraction difference. The shoulder dismisses with increasing DMF content, indicates changes of the core-shell structure at cellulose local scale towards a cylinder structure.

For the 10 wt% MCC solution, when increasing the DMF content to 60%, the obvious phase separation shown in the profile indicates that the DMF reduced the BmimAc solubility at a certain DMF fraction with high cellulose concentration (e.g. 10 wt%).

### 3.9 Discussion and conclusion

We succeeded to make solutions in BmimAc sufficiently well controlled, without noticeable influence of water and temperature, to get strong insights on their scattering in close to dilute, semi-dilute, and concentrated biphasic regime.

In close to dilute regime, the scattering could be described as the one of a single cylinder, with a core-shell radial structure where the shell corresponds to a slightly different (around 10%) scattering length density (SLD). The lineic density, or equivalently the cross area of one unit, are in good agreement with the one of a cellulose chain inferred from crystallographic studies. It is possible to account for a persistence length of order 8 nm using information at the lowest  $q$  accessible, which is unfortunately limited by the subtraction of the spectrometer empty beam, and maybe by a small degree of aggregation. However, because of our careful procedures, these limitations are quite milder compared to other measurements reported in the literature, in other words the quality of our data is satisfying compared with the literature in ionic liquid, or in other solvents (aqueous solvent). To go further, it would be interesting to use techniques giving information at largest distances, like light scattering, which is however delicate.

In semidilute regime, we could describe the scattering owing to a model of aligned cylinders (D. Constantin). The chains appear through this model in weakly repulsive interaction, hence weakly aligned. From this result we can propose the picture of a very simple model system in BmimAcetate:

- cellulose chains are dissolved up to a concentration of 15%, without coexistence of crystals. They stay individual, forming no fibers and very limited aggregates, keeping their shape.
- At larger concentration, the system is not anymore monophasic, new objects appear, probably due to phase separation with microphases of size of order 35 Å. This can occur with or without coexistence with crystals.

We also noticed a clear absence of temperature effect in the BmimAc solutions we prepared. This agrees with the fact that the solution keeps the same structure in presence of 1% water, and probably even for a slightly larger ratio. It aggregates above 5%, and even phase separate at larger concentrations.

These conclusions are strengthened by comparison with solutions in BmimCl, which is more hygroscopic. At low cellulose concentration ( $c \leq 6\%$ ), the scattering is very close and confirm

the data for Acetate. The core-shell parameters are very close. Above 7% of cellulose, we observe an onset of aggregation, or a phase separation, while the chain conformation seems to be preserved. The behavior maps the one of Acetate, within a shift of a few percent in water content. The reaction to water or moisture seems to display a saturation (blocked, or “arrested” separation?). It seems that we rejoin the behaviors in aqueous solvents of the gelation type, as suggested by the clear effect of temperature on BmimCl. Conformation in aqueous solvents is similar at the lowest concentration but shows aggregation much sooner when  $c$  is increased. Hence the two ILs chosen to appear as very good solvent to study the chain conformation and interactions.

## References

- Boudie, C., Maréchal, M., Ah-Lung, G., Jacquemin, J., Nockemann, P., **2023**. Tuneable-by-design copper oxide nanoparticles in ionic liquid nanofluids. *Nanoscale*. *15*, 18423–18434. <https://doi.org/10.1039/D3NR04159J>
- Debye, P., Anderson, H.R., Jr., Brumberger, H., **1957**. Scattering by an Inhomogeneous Solid. II. The Correlation Function and Its Application. *Journal of Applied Physics*. *28*, 679–683. <https://doi.org/10.1063/1.1722830>
- Debye, P., Bueche, A.M., **1949**. Scattering by an Inhomogeneous Solid. *Journal of Applied Physics*. *20*, 518–525. <https://doi.org/10.1063/1.1698419>
- Endo, T., Hosomi, S., Fujii, S., Ninomiya, K., Takahashi, K., **2016**. Anion Bridging-Induced Structural Transformation of Cellulose Dissolved in Ionic Liquid. *J. Phys. Chem. Lett.* *7*(24), 5156–5161. <https://doi.org/10.1021/acs.jpcclett.6b02504>
- Gupta, K.M., Jiang, J., **2015**. Cellulose dissolution and regeneration in ionic liquids: A computational perspective. *Chemical Engineering Science*. *121*, 180–189. <https://doi.org/10.1016/j.ces.2014.07.025>
- Hansen, J.-P., McDonald, I.R., **2007**. Theory of simple liquids. *3rd ed. Elsevier/Academic Press, Amsterdam Boston*.
- Idström, A., Gentile, L., Gubitosi, M., Olsson, C., Stenqvist, B., Lund, M., Bergquist, K.-E., Olsson, U., Köhnke, T., Bialik, E., **2017**. On the dissolution of cellulose in tetrabutylammonium acetate/dimethyl sulfoxide: a frustrated solvent. *Cellulose*. *24*, 3645–3657. <https://doi.org/10.1007/s10570-017-1370-2>
- Kline, S.R., **2006**. Reduction and analysis of SANS and USANS data using IGOR Pro. *J Appl Cryst*. *39*(6), 895–900. <https://doi.org/10.1107/S0021889806035059>
- Kotov, N., Raus, V., Urbanová, M., Zhigunov, A., Dybal, J., Brus, J., **2020**. Impact of Cellulose Dissolution on 1-Butyl-3-Methylimidazolium Chloride Crystallization Studied by Raman Spectroscopy, Wide-Angle X-ray Scattering, and Solid-State NMR. *Cryst. Growth Des.* *20*(3), 1706–1715. <https://doi.org/10.1021/acs.cgd.9b01458>
- Kotov, N., Šturcová, A., Zhigunov, A., Raus, V., Dybal, J., **2016**. Structural Transitions of 1-Butyl-3-methylimidazolium Chloride/Water Mixtures Studied by Raman and FTIR Spectroscopy and WAXS. *Cryst. Growth Des.* *16*(4), 1958–1967. <https://doi.org/10.1021/acs.cgd.5b01551>
- Lo Celso, F., Appetecchi, G.B., Simonetti, E., Zhao, M., Castner, E.W., Keiderling, U., Gontrani, L., Triolo, A., Russina, O., **2019**. Microscopic Structural and Dynamic Features in Triphilic

- Room Temperature Ionic Liquids. *Front. Chem.* 7, 285.  
<https://doi.org/10.3389/fchem.2019.00285>.
- Lundin, F., Hansen, H.W., Adrjanowicz, K., Frick, B., Rauber, D., Hempelmann, R., Shebanova, O., Niss, K., Matic, A., **2021**. Pressure and Temperature Dependence of Local Structure and Dynamics in an Ionic Liquid. *J. Phys. Chem. B.* 125(10), 2719–2728.  
<https://doi.org/10.1021/acs.jpcc.1c00147>
- Pedersen, J.S., **1997**. Analysis of small-angle scattering data from colloids and polymer solutions: modeling and least-squares fitting. *Advances in Colloid and Interface Science.* 70, 171–210.  
[https://doi.org/10.1016/S0001-8686\(97\)00312-6](https://doi.org/10.1016/S0001-8686(97)00312-6)
- Rosenfeld, Y., **1990**. Free-energy model for the inhomogeneous hard-sphere fluid in  $D$  dimensions: Structure factors for the hard-disk ( $D=2$ ) mixtures in simple explicit form. *Phys. Rev. A.* 42(10), 5978–5989. <https://doi.org/10.1103/PhysRevA.42.5978>
- Tran, C.D., De Paoli Lacerda, S.H., Oliveira, D., **2003**. Absorption of water by room-temperature ionic liquids: effect of anions on concentration and state of water. *Appl Spectrosc.* 57(2), 152–157. <https://doi.org/10.1366/000370203321535051>
- Zhao, D., Sultana, A., Edberg, J., Chaharsoughi, M.S., Elmahmoudy, M., Ail, U., Tybrandt, K., Crispin, X., **2022**. The role of absorbed water in ionic liquid cellulosic electrolytes for ionic thermoelectrics. *J. Mater. Chem. C.* 10, 2732–2741. <https://doi.org/10.1039/D1TC04466D>

<b>Chapter 4 NEUTRON SCATTERING .....</b>	<b>138</b>
<b>4.1 Small angle scattering .....</b>	<b>138</b>
4.1.1 Introduction.....	138
4.1.2 Solutions scattering in different solvents. Effect of deuteration on the contrast ..	140
4.1.2.1 Values of Scattering Length Densities .....	140
4.1.2.2 In [d-Bmim][Cl] .....	141
4.1.2.3 In [d-Bmim][d-Ac] .....	142
4.1.2.4 In [d-Bmim][h-Ac] .....	143
4.1.2.5 In [h-Bmim][d-Ac] .....	144
4.1.2.6 Ionic liquids with few water added: H <sub>2</sub> O – D <sub>2</sub> O mixtures .....	145
4.1.2.7 Phase separation due to moisture effects.....	146
4.1.2.8 Aqueous solutions: NaOH/urea mixture solvent.....	147
4.1.2.9 Summary.....	147
4.1.3 Extrapolation at zero fraction of deuteriated chains by matching H chains: getting the intrachain scattering function $S_1(q)$ and the interchain scattering function $S_2(q)$ ...	149
4.1.3.1 Principle.....	149
4.1.3.2 Determination of the contrast conditions.....	150
4.1.3.3 Zero $\phi_D$ extrapolation: results .....	151
4.1.4 Zero Average contrast.....	155
4.1.4.1 Principle.....	155
4.1.4.2 ZAC matching conditions.....	156
4.1.4.3 Results .....	157
4.1.5 Conclusion on SANS .....	161
<b>4.2 Wide Angle Neutron Scattering .....</b>	<b>162</b>
4.2.1 Results.....	162
4.2.1.1 All samples with 5mm beam .....	162
4.2.1.2 All samples with 10 mm beam .....	164
4.2.1.3 Focus on [d-Bmim][h-Ac] series .....	165
4.2.2 Summary .....	167
<b>4.3 Conclusion .....</b>	<b>168</b>
<b>References .....</b>	<b>169</b>

## Chapter 4 Neutron Scattering

### 4.1 Small angle scattering

#### 4.1.1 Introduction

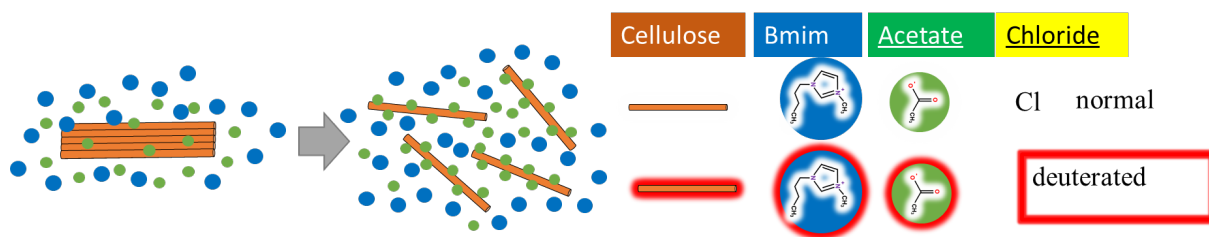
The two main questions we address here are the question of the solvent localization with respect to the chain, and a direct measurement of the cellulose chain conformation. The first one has to be addressed first because it governs the contrast, which we must bring to a given value to address the second question.

It has been proposed that the acetate ions bind with cellulose chains, based on the unexpectedly low SANS contrast, in Garnier, Garvey et al paper (Raghuwanshi et al., 2018). They assume that the SLD (scattering length density) difference is reduced due to the tight binding of acetate ions of EmimAc (1-Ethyl-3-methylimidazolium acetate) to the cellulose chains. According to the contrast reduction, the calculation indicates at least one acetate ion binding per anhydroglucose unit (AGU). However, it can be argued (Y. Nishiyama, private communication) that it may not be a tight ion binding, but rather only the association between acetate ions and cellulose chain. The binding problem is not clear actually. Using Nuclear Magnetic Resonance (NMR), the strong hydrogen bonding between protons of cellulose and anions of BmimCl (Remsing et al., 2006) and Emim Acetate (1-Ethyl-3-methylimidazolium Acetate) was proposed without strong final evidence, based not in a chemical shift (Remsing et al., 2010) (Zhang et al., 2010a, 2010b) but on some kind of association/reduction of mobility of the anions, suggesting “some proximity” (Remsing et al., 2010;), see Chapter 1. We will discuss the acetate and chloride binding with cellulose chain, and the hydrogen bonding later.

Studies of solvent localization at more local scale (large  $q$  part of SANS  $q$ -range), using in particular available combinations of [h-Bmim] or [d-Bmim] with [h-Ac] or [d-Ac], have been attempted.

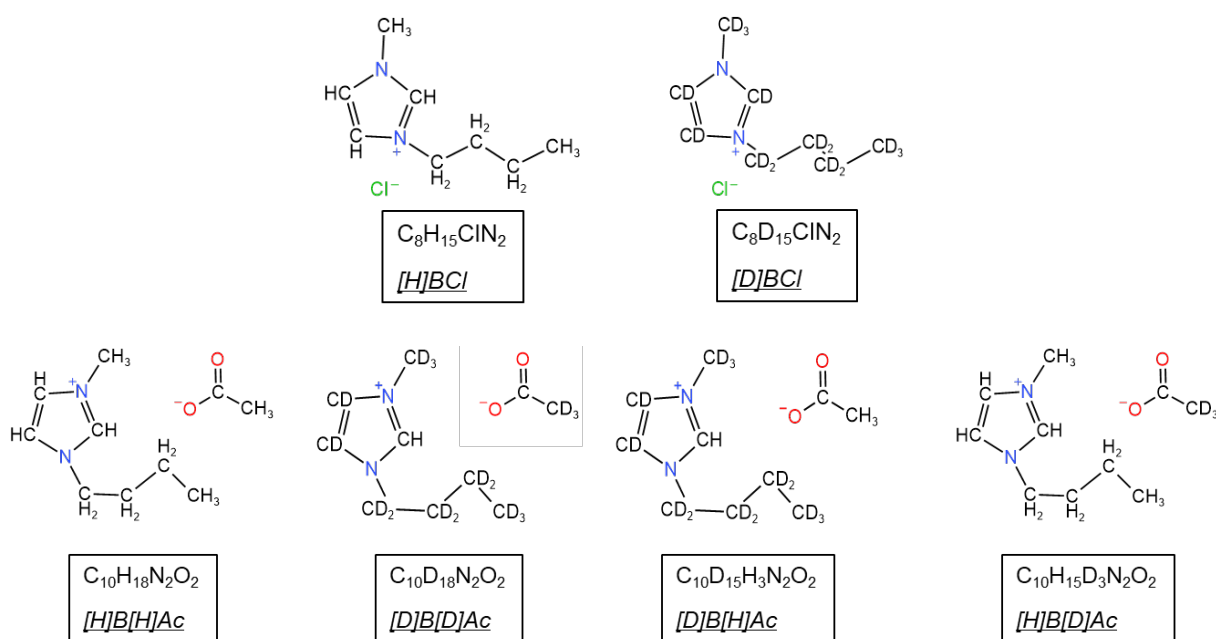
Technical problems are moisture absorption for BmimAc and for BmimCl the supercooled state. In practice, after BmimCl contacts air, it changes from solid to liquid. Another problem is that the high cellulose concentration solutions in BmimCl may undergo cellulose crystallization (from our experience), which has not been examined.





**Scheme 4.1:** a) above: localization of the ions (above), and possible situations of labeling (schematized by a surrounding red line, see below the exact formulae), for SANS and for WAXS (after Raguwanshi et al).

b) below: semi-developed formula showing the different deuterium labeling.



The deuteration of solvents has been described in the Materials and Methods section. The deuterated bacterial cellulose (“d cellulose”, dBC – **sometimes noted DBC**) donated by Yoshihiro Nishiyama and Howard Wang, was used for the SANS experiment.

The measurements were done on D22 beamline of ILL (see Materials and Methods). The instrument configurations used  $\lambda = 6 \text{ \AA}$ , sample-to-detector distance  $D = 17.6 \text{ m}$  and  $D = 5.6 \text{ m}$ , with exposure times ranging from 600s to 900s. The experiments were initially run at  $25 \text{ }^\circ\text{C}$ .

## 4.1.2 Solutions scattering in different solvents. Effect of deuteration on the contrast

### 4.1.2.1 Values of Scattering Length Densities

The SLD, calculated from [NIST](#) , are listed in **Table 4.1**.

Name	Formula	Density (g/cm <sup>3</sup> )	SLD (10 <sup>-6</sup> /Å <sup>2</sup> )	Scattering cross section (cm <sup>-1</sup> )	
				Coherent	Incoherent
NaOH	NaOH	2.13	1.826	0.044	2.828
H <sub>2</sub> O	H <sub>2</sub> O	1	-0.561	0.004	5.621
urea	CH <sub>4</sub> N <sub>2</sub> O	1.32	2.146	0.055	4.722
5%NaOH7%urea H <sub>2</sub> O	—	—	6.082	—	—
NaOD	NaOD	2.18	5.158	0.348	0.137
D <sub>2</sub> O	D <sub>2</sub> O	1.1	6.335	0.508	0.137
5%NaOD7%urea D <sub>2</sub> O	—	—	6.082	—	—
MCC	C <sub>6</sub> H <sub>10</sub> O <sub>5</sub>	1.5	1.755	0.033	4.840
dBC	C <sub>6</sub> D <sub>10</sub> O <sub>5</sub>	1.59	7.543	0.612	0.115
BmimAc	C <sub>10</sub> H <sub>18</sub> N <sub>2</sub> O <sub>2</sub>	1.05	0.940	0.011	4.975
BmimCl	C <sub>8</sub> H <sub>15</sub> ClN <sub>2</sub>	1.086	0.950	0.012	4.910
[d-Bmim][d-Ac]	C <sub>10</sub> D <sub>18</sub> N <sub>2</sub> O <sub>2</sub>	1.146	6.920	0.590	0.127
[d-Bmim][Cl]	C <sub>8</sub> D <sub>15</sub> ClN <sub>2</sub>	1.180	6.800	0.597	0.148
[d-Bmim][h-Ac]	C <sub>10</sub> D <sub>15</sub> H <sub>3</sub> N <sub>2</sub> O <sub>2</sub>	1.130	5.923	0.432	0.996
[h-Bmim][d-Ac]	C <sub>10</sub> H <sub>15</sub> D <sub>3</sub> N <sub>2</sub> O <sub>2</sub>	1.066	1.937	0.046	4.228
mixed solvent for 0% extrapolation	17%-[d-Bmim][h-Ac]/ 83%-[h-Bmim][h-Ac]	—	1.787	0.0826	4.299

**Table 4.1:** Scattering Length Densities of different solvents and cellulose monomers.

### 4.1.2.2 In [d-Bmim][Cl]

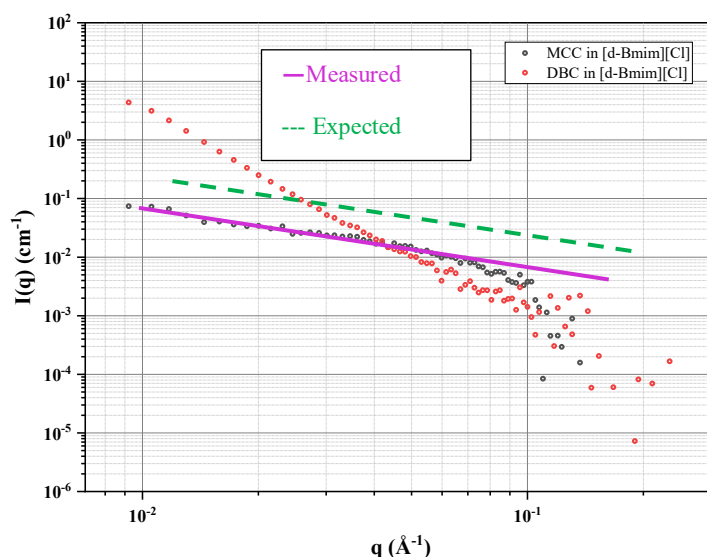


**Figure 4.1:** SANS from 2 wt% MCC and dBC in [d-Bmim][Cl].

**Comment:** dBC shows a straight line which can be interpreted as due at low  $q$  to aggregates and at large  $q$  to background subtraction (the contrast is very low) MCC benefits from a good contrast, however the obtained scattering is  $0.008 \text{ cm}^{-1}$  instead of  $0.05 \text{ cm}^{-1}$ .

name	Neutron contrast, $10^{-12}/\text{\AA}^4$	X ray contrast (in [h-Bmim][Cl]), $10^{-12}/\text{\AA}^4$
MCC/[d-Bmim][Cl]	25.44	12.82
dBC/[d-Bmim][Cl]	0.55	12.63
Scattering intensity at $q = 0.1 \text{ \AA}^{-1}$	MCC Expected $0.05 \text{ cm}^{-1}$ Measured $0.008 \text{ cm}^{-1}$	Measured $0.025 \text{ cm}^{-1}$

**Table 4.2:** SANS from MCC and dBC in [d-Bmim][Cl] (fully deuteriated). Comparison between the  $q^{-1}$  slope height at  $q = 0.1 \text{ \AA}^{-1}$ , (i) measured, and (ii) expected from the level in SAXS normalised to the SANS contrast.

**In summary, the measured contrast for BmimCl is much weaker than expected. dBC appears that more aggregated than hBC (Nata de Coco) (scattering 10 times higher at  $10^{-2} \text{ \AA}^{-1}$ ).**

### 4.1.2.3 In [d-Bmim][d-Ac]

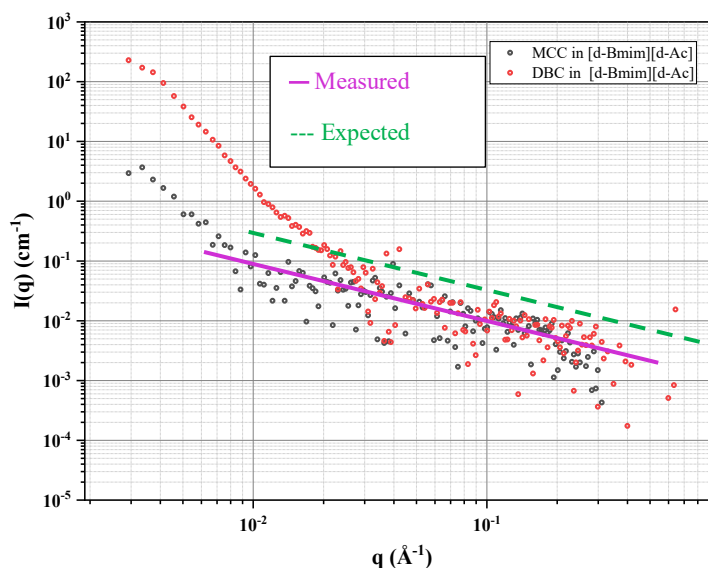


**Figure 4.2:** SANS from MCC and dBC in [d-Bmim][d-Ac] (fully deuteriated)

name	Neutron contrast, $10^{-12}/\text{\AA}^4$	X ray contrast, $10^{-12}/\text{\AA}^4$
MCC/[d-Bmim][d-Ac]	26.67	14.61
dBC/[d-Bmim][d-Ac]	0.39	14.40
Scattering intensity at $q = 0.1$ $\text{\AA}^{-1}$	MCC: Expected $0.05 \text{ cm}^{-1}$ Measured $0.01 \text{ cm}^{-1}$	Measured $0.025 \text{ cm}^{-1}$
	dBC: Expected $0.0007 \text{ cm}^{-1}$ Measured $0.01 \text{ cm}^{-1}$	

**Table 4.3:** SANS from MCC and dBC in [d-Bmim][d-Ac] (fully deuteriated). Comparison between the  $q^{-1}$  slope height at  $q = 0.1 \text{ \AA}^{-1}$ , (i) measured, and (ii) expected from the level in SAXS normalised to the SANS contrast.

The contrast with MCC of the deuteriated solvent should give much **higher** values than measured.

The contrast with dBC of the deuteriated solvent should give much **lower** values than measured!

#### 4.1.2.4 In [d-Bmim][h-Ac]

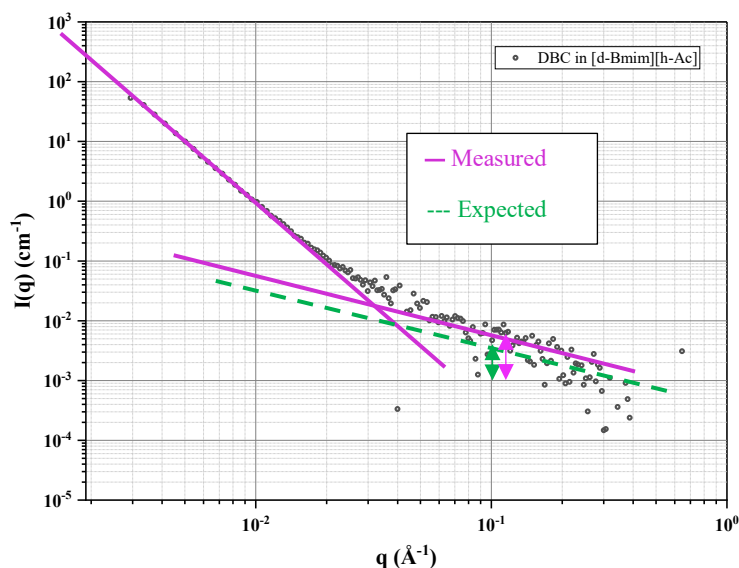


**Figure 4.3:** SANS from dBC in [d-Bmim][h-Ac] (partially deuteriated)

We observe a stronger upturn from dBC.

name	Neutron contrast, $10^{-12}/\text{\AA}^4$	X ray contrast, $10^{-12}/\text{\AA}^4$
dBC/[d-Bmim][h-Ac]	2.62	14.40
Scattering intensity at $q = 0.1 \text{\AA}^{-1}$	Expected $0.0045 \text{ cm}^{-1}$ Measured $0.006 \text{ cm}^{-1}$	Assuming no influence of deuteriation for X rays, we use the value for Nata de coco, very close to the MCC one, $0.025 \text{ cm}^{-1}$

**Table 4.4:** SANS from MCC and dBC in [d-Bmim][h-Ac] (partial deuteriated). Comparison between the  $q^{-1}$  slope height at  $q = 0.1 \text{\AA}^{-1}$ , (i) measured, and (ii) expected from the level in SAXS normalised to the SANS contrast.

dBC in [d-Bmim][h-Ac] is expected to give weak scattering; the measured values are close indeed to indeed, estimate. However, one must be cautious about the level of these curves when the signal is very low.

#### 4.1.2.5 In [h-Bmim][d-Ac]

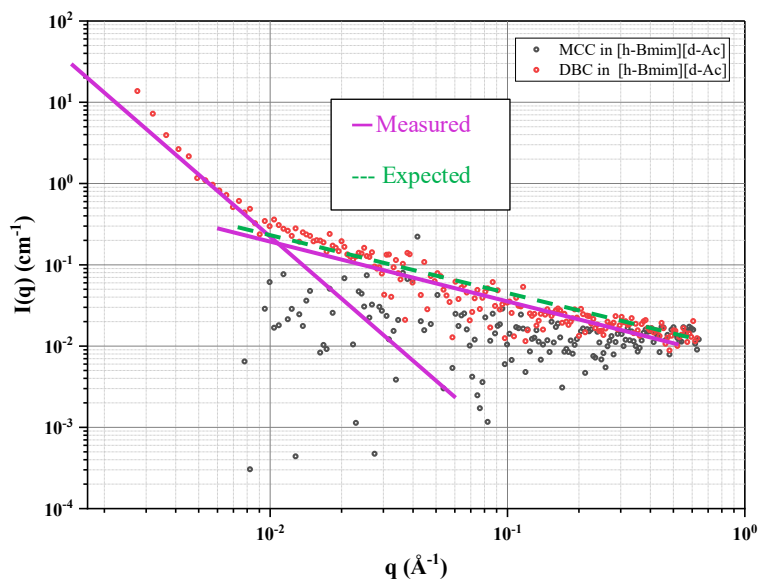


**Figure 4.4:** SANS from dBC and MCC in [h-Bmim][d-Ac] (partial deuteration)

name	Neutron contrast, $10^{-12}/\text{\AA}^4$	X ray contrast, $10^{-12}/\text{\AA}^4$
MCC/[h-Bmim][d-Ac]	0.03	14.61
dBC/[h-Bmim][d-Ac]	31.43	14.40
Scattering intensity at $q = 0.1 \text{ \AA}^{-1}$	dBC/hBdAc measured $0.05 \text{ cm}^{-1}$ Expected $0.065 \text{ cm}^{-1}$	$0.03 \text{ cm}^{-1}$

**Table 4.5:** SANS from MCC and dBC in [d-Bmim][d-Ac] (partial deuteriated). Comparison between the  $q^{-1}$  slope height at  $q = 0.1 \text{ \AA}^{-1}$ , (i) measured, and (ii) expected from the level in SAXS normalised to the SANS contrast.

The  $q^{-1}$  value for dBC/[h-Bmim][d-Ac] is  $0.05 \text{ cm}^{-1}$  at  $q = 0.1 \text{ \AA}^{-1}$ , close to what expected.

For dBC, we surprisingly observe a lower upturn at low  $q$  in [h-Bmim][d-Ac] than in [d-Bmim][h-Ac].

These observations will be summarised below in **section 4.1.2.9** Summary.

#### 4.1.2.6 Ionic liquids with few water added: $H_2O - D_2O$ mixtures

##### BmimAc/ $D_2O$ mixture

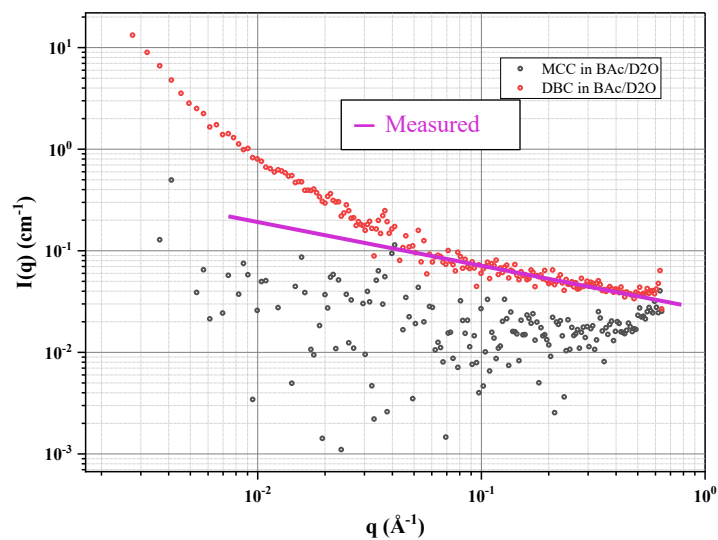


**Figure 4.5:** SANS from dBC and MCC in BmimAc /  $D_2O$  mixture with 5% of  $D_2O$

We observe that dBC shows here a stronger upturn in presence of  $D_2O$ . Is it due to a different solubility? Or a stronger contrast?

##### BmimCl / $D_2O$ mixtures.

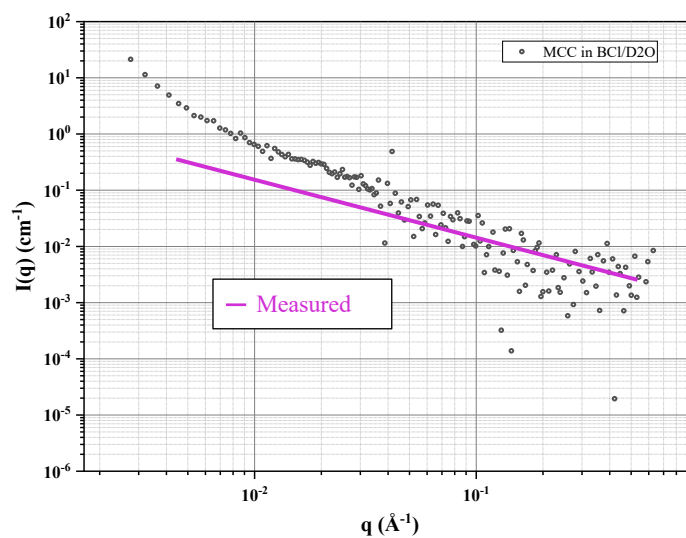


**Figure 4.6:** SANS from MCC in BmimCl/  $D_2O$  mixture with 5% of  $D_2O$

We observe a gentle upturn at low  $q$ , probably due a slight aggregation, but  $q^{-1}$  nevertheless observed at high  $q$ .

#### 4.1.2.7 Phase separation due to moisture effects

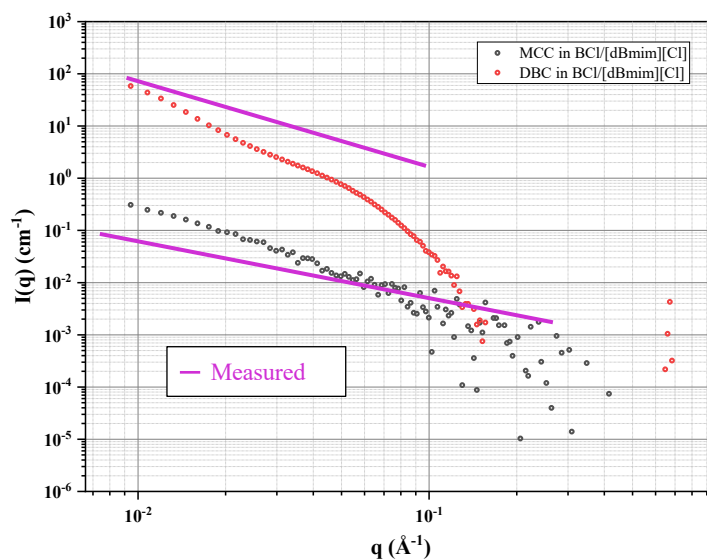


**Figure 4.7:** SANS from MCC in BmimCl/  $\text{D}_2\text{O}$  mixture with 5% of  $\text{D}_2\text{O}$

DBC has phase separated in this mixture. The observed shape (including the slope at medium  $q$ , close to 1.6) is reminiscent from water effect in BmimCl, seen by SAXS. The MCC displays a slope  $> 1$  at low  $q$ , also due probably to some presence of water.



#### 4.1.2.8 Aqueous solutions: NaOH/urea mixture solvent

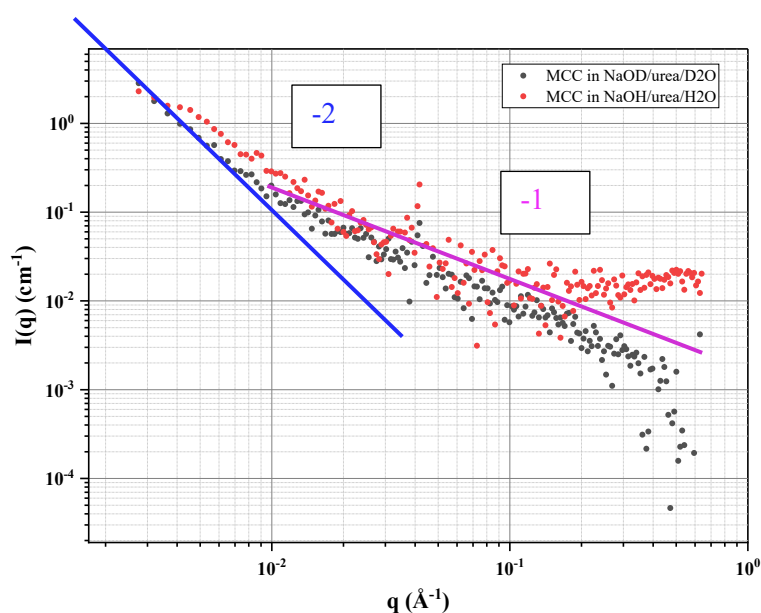


**Figure 4.8:** SANS from MCC in 5% NaOH/7% urea/H<sub>2</sub>O mixture and MCC in 5% NaOD/7% urea/D<sub>2</sub>O mixture

We observe not such a big difference between h and d solvent in contrast, but the easier background subtraction for deuteriated solvent leads to a well-defined  $q^{-1}$  decrease (black curve). Note: a different slope of  $q^{-2}$  was observed all over the  $q$  range for solutions in pure NaOH. The system was gelled. Urea is known to slow down such gelification, as observed here, but does not block it.

#### 4.1.2.9 Summary

**Comparison at different contrasts.** Table below summarizes the results. There is:

- disagreement between expected and measured for [d-Bmim][d-Ac], and partly for [d-Bmim][Cl] (for MCC).

Comparing with the results of Garvey-Garnier (Raghuwanshi et al) for [d-Emim][d-Ac], we find also like them disagreements for MCC in [d-Bmim][h-Ac], but also for [d-Bmim][Cl], which does not involve Acetate anion.

- slight disagreement for [d-Bmim][h-Ac].

Fortunately:

- this solvent will be used as the deuterated solvent for the zero  $\phi_D$  extrapolation, the non deuterated one being simply [h-Bmim][h-Ac].
- the mixture [d-Bmim][h-Ac]/[h-Bmim][h-Ac] will also be used for the ZAC measurements.
- agreement for [h-Bmim][d-Ac].

In summary, we have satisfied preliminary performances for our two ways of extrapolating the intrachain function. The difficulties detected by Garnier and Garvey seems present here. However, until now, altogether, it is difficult to find a rationale for the ensemble of cases.

sample	solvent		measured/ expected	Agree ment	Values Measured	Values Expected
MCC	[d-Bmim][Cl]	25.44	much lower	NO	0.008 cm <sup>-1</sup>	expected 0.05 cm <sup>-1</sup>
dBC		0.553536	very low	High		
MCC	[d-Bmim][d-Ac]	26.67	much lower	NO	0.01 cm <sup>-1</sup>	expected 0.05 cm <sup>-1</sup>
dBC	[d-Bmim][d-Ac]	0.389	much higher	NO	0.01 cm <sup>-1</sup>	expected 0.0007 cm <sup>-1</sup>
MCC	[d-Bmim][h-Ac]		no data			
dBC	[d-Bmim][h-Ac]	2.62	higher	OK	0.006 cm <sup>-1</sup>	expected 0.0045 cm <sup>-1</sup>
MCC	[h-Bmim][d-Ac]	0.0331	Very low, agreement	High		
dBC	[h-Bmim][d-Ac]	31.43	Agreement	High	0.05 cm <sup>-1</sup>	expected 0.065 cm <sup>-1</sup>
MCC	NaOH/urea/H <sub>2</sub> O		Idem H <sub>2</sub> O and D <sub>2</sub> O		0.01 cm <sup>-1</sup>	
MCC	NaOH/urea/D <sub>2</sub> O				0.01 cm <sup>-1</sup>	

**Table 4.6: Comparison at different labelings.** Summary of comparison between the  $q^{-1}$  slope height at  $q = 0.1 \text{ \AA}^{-1}$ , (i) measured, and (ii) expected from the level in SAXS normalised to the SANS contrast.

### 4.1.3 Extrapolation at zero fraction of deuterated chains by matching H chains: getting the intrachain scattering function $S_1(q)$ and the interchain scattering function $S_2(q)$

To extract the chain form factor, we aimed at contrast matching h-cellulose (Microcrystalline cellulose) to extrapolate at zero d-cellulose fraction. The matching solvent was made of h/d-ionic liquid ([h-Bmim][h-Ac] and [h-Bmim][d-Ac]). 2 vol% was the total cellulose concentration, with h/d cellulose volume ratio 0/10, 2/8, 5/6, 6/5, 8/2, 10/0 for small angle scattering.

#### 4.1.3.1 Principle

In the general equation of coherent scattering in SANS for  $q < q^*$

$$\Sigma(q) = \sum_{\alpha, \beta=2}^m k_\alpha k_\beta S_{\alpha\beta}(q) + \frac{b_1}{v_1} \sum_{\alpha=1}^m \langle n_\alpha \rangle (k_\alpha + b_\alpha) k T \chi_T \quad (4.1)$$

$$I(q)(cm^{-1}) = \frac{1}{V} \frac{d\Sigma}{d\Omega} = k_H^2 S_{HH}(q) + 2k_H k_D S_{HD}(q) + k_D^2 S_{DD}(q) \quad (4.2)$$

$k_i$  (cm or Å) =  $b_i - b_s(V_{mol\{i\}}/V_{mol\{S\}})$  is the “contrast length” between the scattering length  $b$  of cellulose and solvent ( $k_i/V_{mol\{i\}} = \Delta\rho_i$ );  $S_{HH}(q)$ ,  $S_{DD}$  are the scattering of the hydrogenated chains and deuterated chains separately, and  $S_{HD}(q)$  is the cross-term. With the SLD of hydrogenated chain matched by the solvent,  $k_H = 0$ ; hence:

$$I(q)(cm^{-1}) = \frac{1}{V} \frac{d\Sigma}{d\Omega} = k_D^2 S_{DD}(q) \quad (4.3)$$

The total volume fraction of chains in solution:  $\phi_T = \phi_H + \phi_D$ , assuming the  $V_{molH} = V_{molD} = V_{mol}$ , then,

$$S_{DD}(q) = \phi_D S_1(q) + \phi_D^2 S_2(q) \quad (4.4)$$

where both  $S_1(q)$  the intrachain scattering function, and  $S_2(q)$  the interchain function does not depend on  $\phi_D$ .

$$\frac{I(q)(cm^{-1})}{\phi_D} = k_D^2 (S_1(q) + \phi_D S_2(q)) \quad (4.5)$$

In other words, we can also write,

$$S_1(q) * S(q) = S_1(q) * \left(1 + \phi_D \frac{S_2}{S_1}\right) \quad (4.6)$$

hence, if we plot  $\frac{I(q)}{\phi_D k_D^2}$ , the concept

$$\lim_{\phi_D \rightarrow 0} \frac{I(q)}{\phi_D k_D^2} = S_1(q) (\text{\AA}^{-3}) = \frac{1}{V_{mol}} N_w P(q) \quad (4.9)$$

and the slope is  $S_2(q) (\text{\AA}^{-3})$ .

$N_w$  the weight average number of units.

#### 4.1.3.2 Determination of the contrast conditions

Using the values given in **Table 4.7**, we applied the principle of matching as show in **Figure 4.9**.

name	sample	Density (g/cm <sup>3</sup> )	SLD (10 <sup>-6</sup> \AA <sup>-2</sup> )	vol%	SLD (10 <sup>-6</sup> \AA <sup>-2</sup> )
dBhAc/hBhAc mixture	[d-Bmim][h-Ac]	1.13	5.923	17.01%	1.7876
	[h-Bmim][h-Ac]	1.05	0.940	82.99%	
dBC		1.59	7.543		
MCC		1.5	1.755		

**Table 4.7:** Values of d and h fraction for matching of non-deuteriated cellulose.

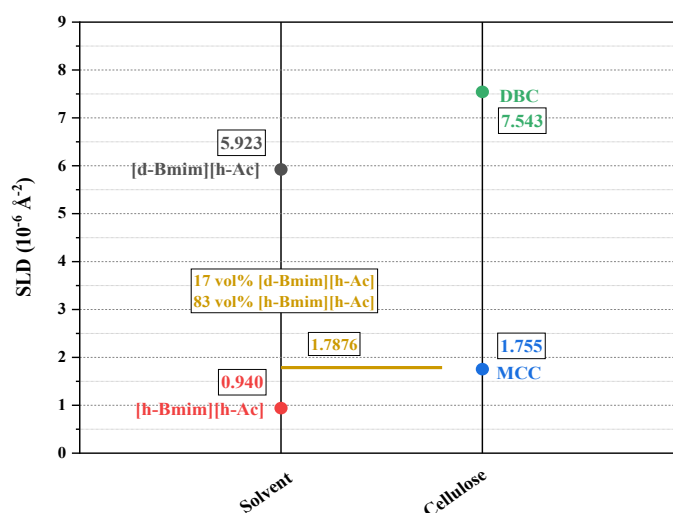


**Figure 4.9:** Comparison of neutron SLD of mixed solvent of [d-Bmim][h-Ac] and [h-Bmim][h-Ac] with cellulose to match the hydrogenated MCC (here dBC is noted DBC).

### 4.1.3.3 Zero $\phi_D$ extrapolation: results

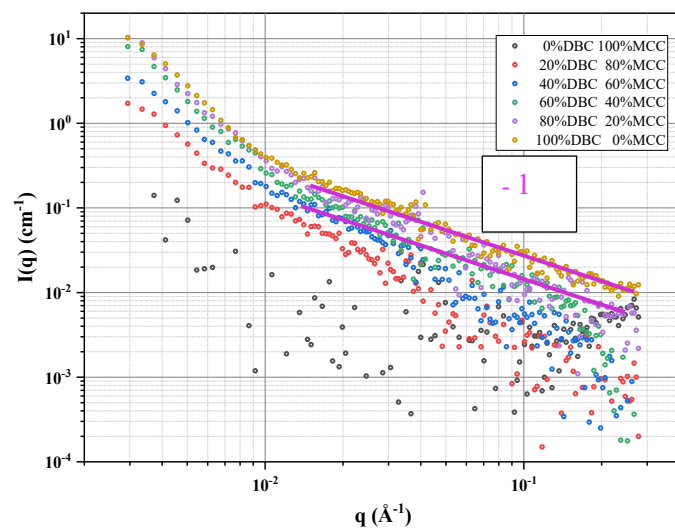


**Figure 4.10:** Extrapolation at zero deuterated fraction. SANS profiles measured for d-cellulose/h-cellulose (0, 20, 50, 60, 80, 100 vol% d-cellulose with total h-cellulose and d-cellulose 2 vol% in [h-Bmim] [h-Ac] and [h-Bmim][d-Ac] mixture at 25°C)

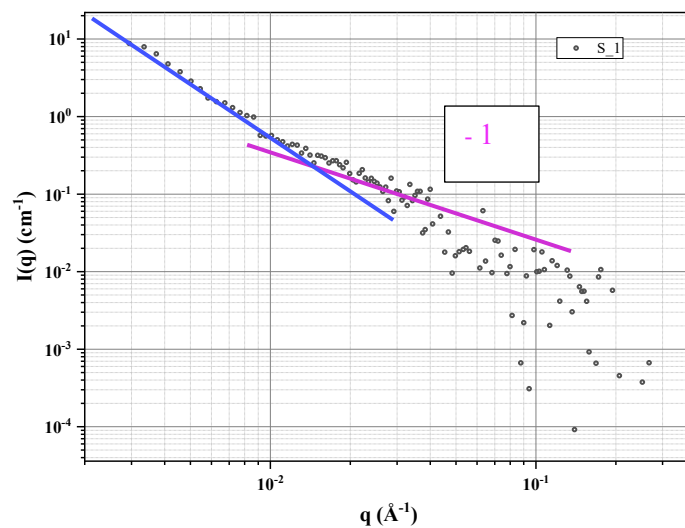


**Figure 4.11:** Extrapolated function  $S_1(q)$

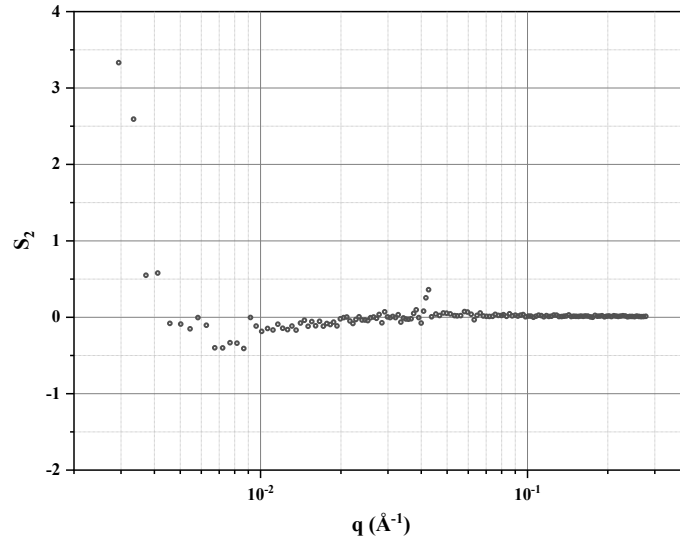


**Figure 4.12** Extrapolated function  $S_2(q)$

**Discussion:** The SANS data are, as above, very scattered because of the weak signal, in spite of long counting on a powerful spectrometer, D22.

The scattering at different  $\phi_D$  appear parallel (in log-log, i.e. proportional) at intermediate  $q$ . That corresponds to a zone where  $S_1(q)$  is close to  $q^{-1}$ , although a little more slopy. It is due to the effect of decrease at larger  $q$  for the intermediate values of  $\phi_D$ . The uncertainty is very high in this  $q$  range because very sensitive to the subtraction of the background. We cannot affirm that this is relevant.

On the lower  $q$ , the scattering shows a stronger slope, due to the aggregates present in the dBC. An interesting point here is that the zero extrapolation works in the  $q$  range where no aggregates are present, even if their scattering is strong at low  $q$ . The **different domains are independent**.

Therefore, we propose to subtract the scattering of aggregates as was done for X Rays, with success. We obtain the following in **Figure 4.13** (red points), which can be fitted using SASview.

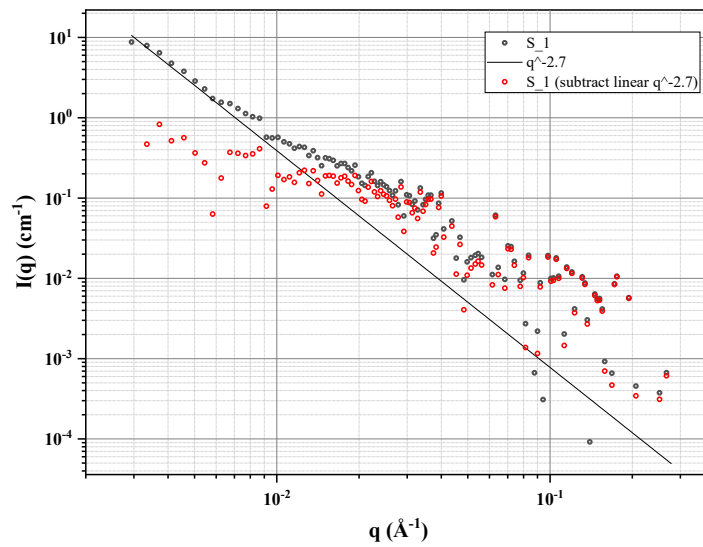


**Figure 4.13** Extrapolated function  $S_1(q)$ : effect of the subtraction of the low  $q$  upturn.

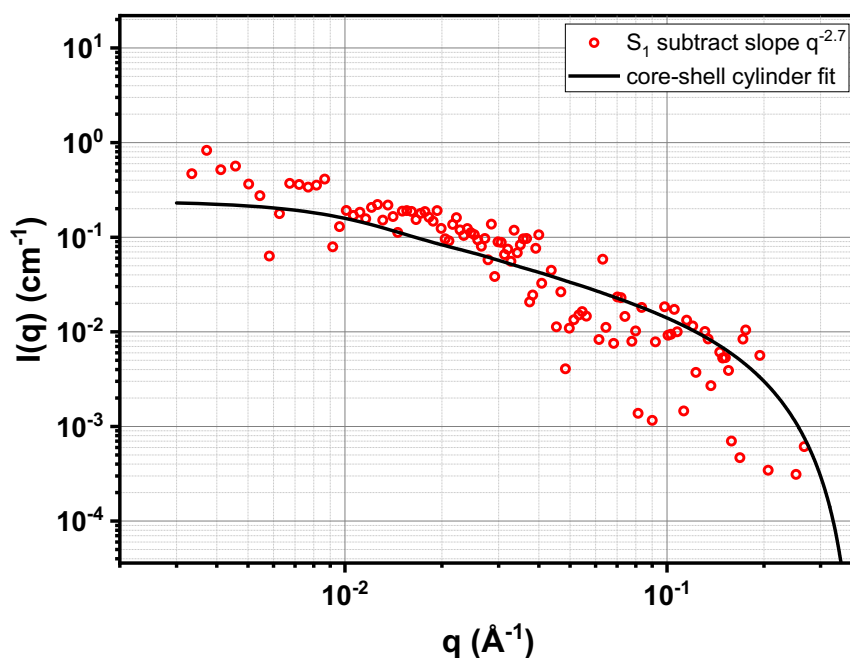
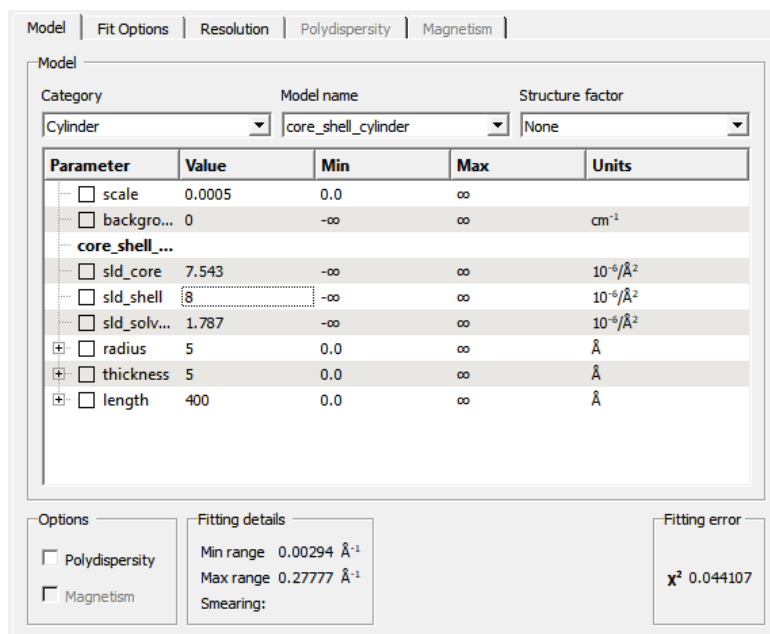


**Figure 4.14** Fit by SASView of the extrapolated function  $S_1(q)$  after subtraction of the low  $q$  upturn.

This gives the SLD of the shell equal to  $8 \times 10^{-6} \text{\AA}^{-2}$ .

Concerning the **function**  $S_2(q)$ , we see on Figure 4.9 a value equal to zero at large  $q$ , in agreement with the value 1 for the effective structure factor in SAXS. At medium  $q$ , we observe a slight decrease, again in agreement with the X rays effective structure factor discussed in Chapter 3. At very low  $q$ ,  $S_2(q)$  increases strongly, due to the dBC aggregates. We could have also subtracted it.



## 4.1.4 Zero Average contrast

### 4.1.4.1 Principle

From the fundamentals of the form factor of the chain among others (Benmouna and Hammouda, 1997; Nöjd et al., 2019, 2019), the general expression of the scattering intensity:

$$I(q)(cm^{-1}) = \frac{1}{V} \frac{d\Sigma}{d\omega} = I(\vec{q}) = \frac{1}{V} \left\langle \sum_{i,j} k_i k_j \exp(i\vec{q}(\vec{r}_i - \vec{r}_j)) \right\rangle \quad (4.10)$$

$$I(q)(cm^{-1}) = \frac{1}{V} \frac{d\Sigma}{d\omega} = k_H^2 S_T(q) \quad (4.11)$$

$$S_T(q) = S_1(q) + S_2(q), \text{\AA}^{-3} \quad (4.12)$$

$$S_1(q)(\text{\AA}^{-3}) = \frac{1}{V} \left\langle \sum_{\alpha, \beta=\alpha} \sum_{i,j} \exp(i\vec{q}(\vec{r}_i^\alpha - \vec{r}_j^\beta)) \right\rangle \quad (4.13)$$

$$S_2(q)(\text{\AA}^{-3}) = \frac{1}{V} \left\langle \sum_{\alpha, \beta \neq \alpha} \sum_{i,j} \exp(i\vec{q}(\vec{r}_i^\alpha - \vec{r}_j^\beta)) \right\rangle \quad (4.14)$$

If a fraction  $x_D$  of the cellulose is deuterated with contrast length  $k_D$

$$I(q)(cm^{-1}) = \frac{1}{V} \frac{d\Sigma}{d\omega} = \{[(1 - x_D)k_H^2 + x_D k_D^2] S_1(q)\} + \{[(1 - x_D)k_H + x_D k_D]^2 S_2(q)\} \quad (4.15)$$

In ZAC conditions, we must have

$$(1 - x_D)k_H + x_D k_D = 0 \quad (4.16)$$

Hence,

$$k_D = -k_H = k_{ZAC} \quad (4.17)$$

$$k_D^2 = k_H^2 = k_{ZAC}^2$$

and

$$I(q) = k_{ZAC}^2 S_1(q) \quad (4.18)$$

with, if  $c_p$  is the number of moles per L (or per  $\text{\AA}^3$ ),

$$S_1(q) = c_p N_{AV} N_W P(q) \quad (4.19)$$

and in particular,

$$\lim_{q \rightarrow 0} S_1(q) (\text{\AA}^{-3}) = c_p \left( \frac{\text{mol}}{\text{\AA}^{-3}} \right) N_{AV} N_W. \quad (4.20)$$

Similar to expression 4.9, since  $c_p N_{AV} = 1/V_{\text{molecular}}$ .

#### 4.1.4.2 ZAC matching conditions

To measure the ZAC (zero average contrast) sample, the dBC and MCC were dissolved in the [d-Bmim][h-Ac]/[h-Bmim][h-Ac] mixture solvent. The **Figure 4.15** shows the principle of determination of the appropriate fraction, the celluloses and solvent SLD for ZAC are shown in the **Table 4.8**:

name	sample	Density (g/cm <sup>3</sup> )	SLD (10 <sup>-6</sup> $\text{\AA}^{-2}$ )	vol%	SLD (10 <sup>-6</sup> $\text{\AA}^{-2}$ )
dBhAc/hBhAc mixture	[dBmim][hAc]	1.13	5.923	74.01%	4.6279
	[hBmim][hAc]	1.05	0.940	25.99%	
dBC/MCC mixture	dBC	1.59	7.543	46.98%	4.4742
	MCC	1.5	1.755	53.02%	

**Table 4.8:** Values of d and h fraction for Zero Average Contrast conditions.

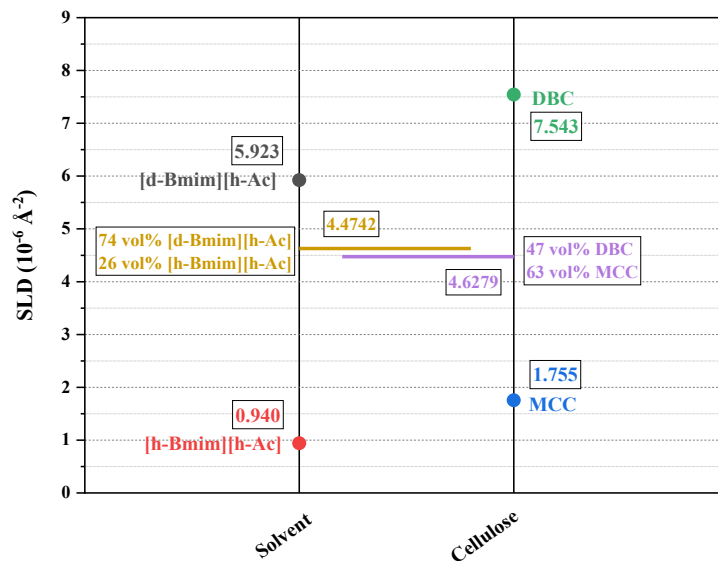


**Figure 4.15:** Comparison of SLD of Solvents and Cellulose in Neutron Scattering Studies for contrast matching of neutron scattering. It shows the difference between the deuterated and hydrogenated forms of solvents and highlights the mixture compositions, with SLD values for 74 vol% [d-Bmim][h-Ac] and 26 vol% [h-Bmim][h-Ac] mixture, as well as for cellulose MCC and dBC (noted DBC in the Figure)

For the measurement, the total cellulose concentration (dBC + MCC) was 1.75 vol% in dBhAc/hBhAc mixture.

#### 4.1.4.3 Results

In the raw data, the scattering intensity of solvent is higher than the one of solution, we assume that is due to the bubble of the high-viscosity of cellulose solution.

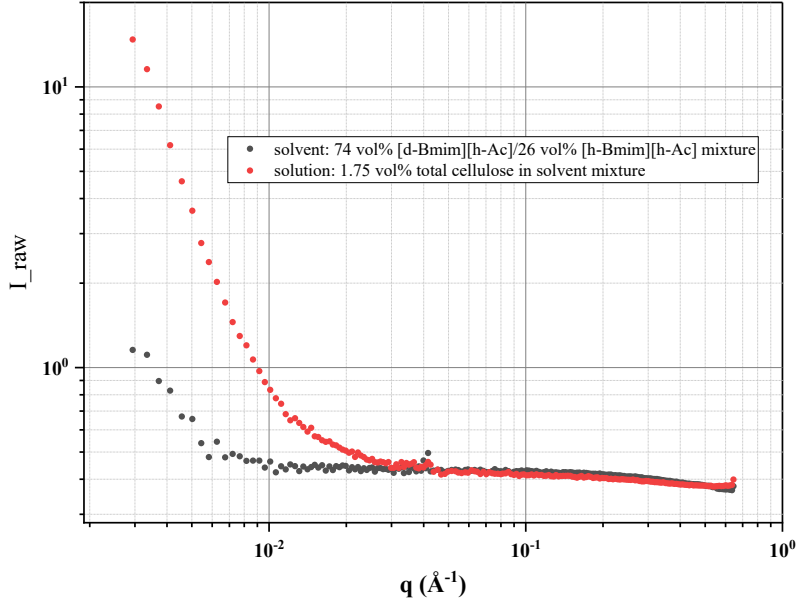


**Figure 4.16:** Raw SANS Data for ZAC samples before solvent subtraction. The plot shows the scattering intensity  $I_{raw}(q)$  for both the solvent and the cellulose solution. In the unprocessed data, the scattering intensity of the solvent is higher than that of the cellulose solution in the  $q$  range  $4 \times 10^{-2} \text{ \AA}^{-1}$  to  $5 \times 10^{-1} \text{ \AA}^{-1}$ .

To account for the potential transmission errors caused by bubbles in high-viscosity cellulose solutions, we have allowed a transmission error margin of 3.8% in our data analysis. This adjustment ensures that the transmission inaccuracies resulting from the presence of bubbles are minimized, improving the reliability of our scattering data. The resulting curve is calculated using the following function:

$$I(q) = f_{error} \times I_{solution}(q) - I_{solvent}(q) - I_{incoh}(q)$$

where  $f_{error}=1.038$  for getting the full curve.

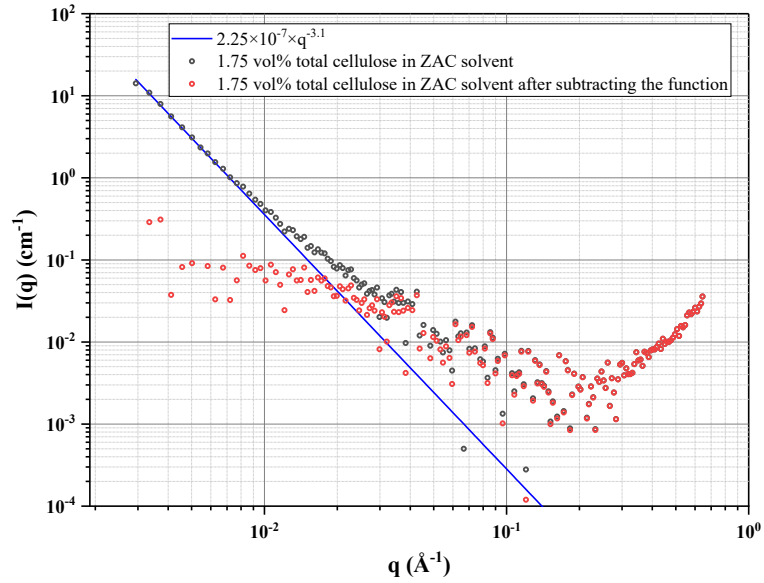


**Figure 4.17:** SANS data analysis of 1.75 vol% total cellulose in ZAC solvent. The black circles represent the data after solvent and incoherent scattering subtraction. The blue line shows the fitted function with slope  $q^{-3.1}$ , which models the background (aggregation of bacterial cellulose) scattering.

In **Figure 4.17**, after subtracting the upturn, the red circles depict the total background-subtracted scattering profile, allowing for a clearer observation of the cellulose structure without solvent interference. On the contrary, we have no explanation of the increase at large  $q$  ( $> 0.2 \text{ \AA}^{-1}$ ). It is extremely sensitive, due to the uncertainty in subtraction of the large angle shadow on the detector, which may be different for the sample and the solvent. We cannot correct it due the variation of the scattering of the ionic liquid with added cellulose.

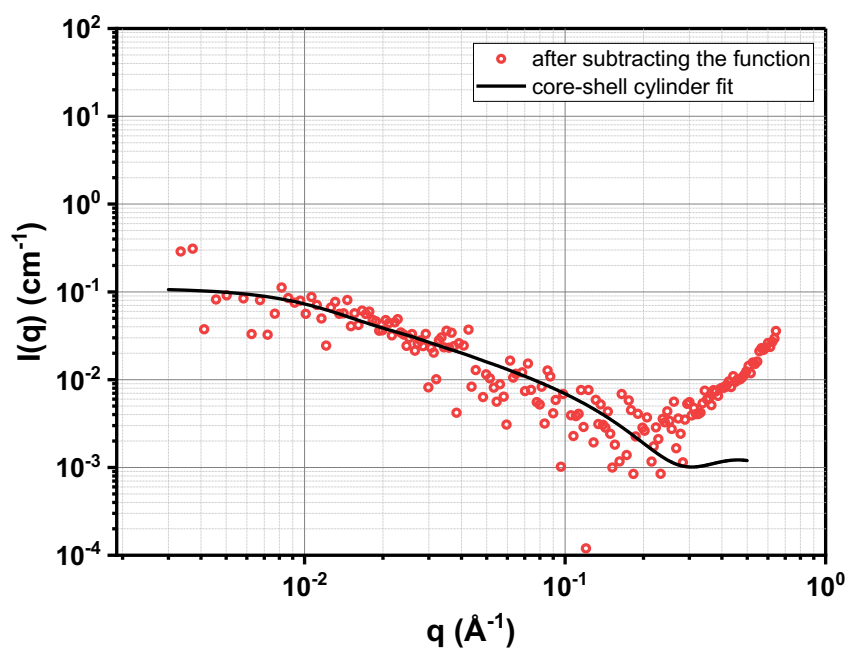
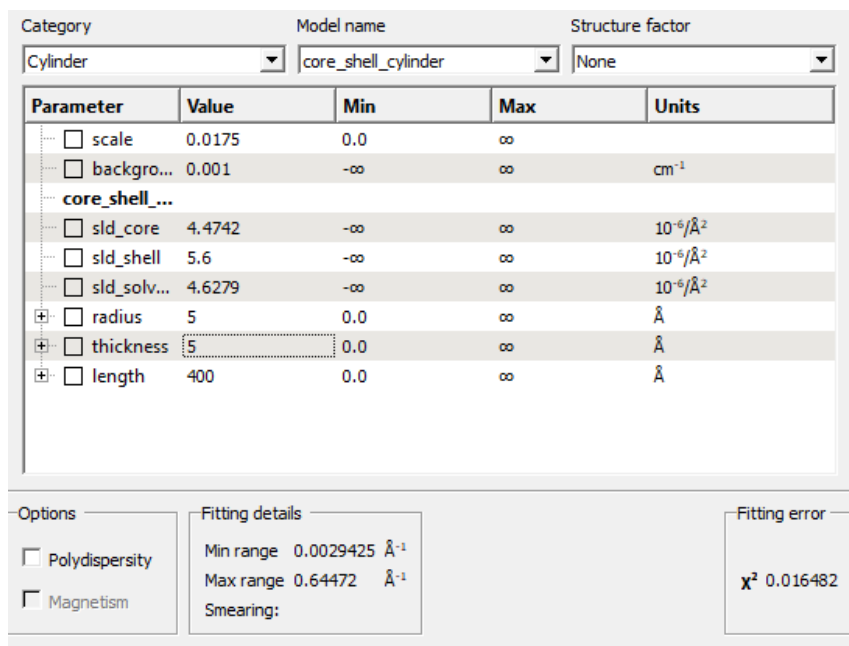


**Figure 4.18:** Fitting with SASView of form factor obtained from SANS-ZAC, for 1.75 vol% total cellulose in ZAC solvent, after subtraction of the low  $q$  upturn. Fitting gives here the SLD shell with  $5.6 \times 10^{-6} \text{\AA}^{-2}$ , which is higher than the SLD of solvent and mixture of cellulose. This has to be clarified accounting for the fact that the core-shell cylinder model leads to a SLD profile different for hMCC chains and dBC chains.

**Conclusion:** Zero Average Contrast method is subject to contrast problems because it uses an intermediate value of SLD between h and d chains. The conditions are therefore not favorable. Some data can however be extracted. Satisfyingly, it is possible to subtract the low  $q$  upturn

from bacterial cellulose. Data are not contradictory with other results. In conclusion, it seems possible to use ZAC for higher cellulose concentrations (if solubilisation of dBC can be improved).

#### **4.1.5 Conclusion on SANS**

The SANS data show a very weak scattering, difficult to approach in spite of the high flux of D22.

The measurements in different solvents, with one ion deuteriated, or both, agree only in some cases, within the uncertainty, while in some other cases, disagreement needs to be understood. The reasoning of Garvey and Garnier of adsorption of Acetate ions should be discussed in detail for the different cases. For chloride ions in BmimCl, it is not applying while we observe disagreement with the contrast estimates.

Our estimate of the h and d fractions of solvent for the matching of non-deuteriated (“h”) cellulose, is quite satisfying: indeed, the signal is close to zero.

Hence the zero  $\phi_D$  extrapolation is functioning. However, the signal is very weak.

These experiments are very difficult. However, it is obvious they would function better – and actually give more information, at larger concentration. For that dBC should be refined to stay soluble at high concentration. This would require higher amounts of dBC, not available at the moment, and reduction of the chain length far more efficient than sonication, which we tried with little success.

## 4.2 Wide Angle Neutron Scattering

In this section we would like to describe short scale correlations between the cations, anions and cellulose units owing to the selective deuteration. This could enable us to identify some specific localization of the Acetate units, as often claimed, on the chain.

### 4.2.1 Results

#### 4.2.1.1 All samples with 5mm beam

##### Description of results.

Concerning:

- [d-Bmim][Cl]: the double peak is not much modified by 8% MCC (two samples)
- [d-Bmim][d-Ac]: the single peak is not much modified by 8% MCC, **but surprisingly by dBC** (deuteriated bacterial cellulose, also noted DBC), which adds a strong foot at lower  $q$  to the peak
- [d-Bmim][h-Ac]: the double peak is not affected by MCC (see below a closer comparison, **Figure 4.20 b**)
- BmimCl (non deuteriated) peak is not modified by adding dBC.
- similarly, BmimAc (non deuteriated) peak is not modified by adding dBC.



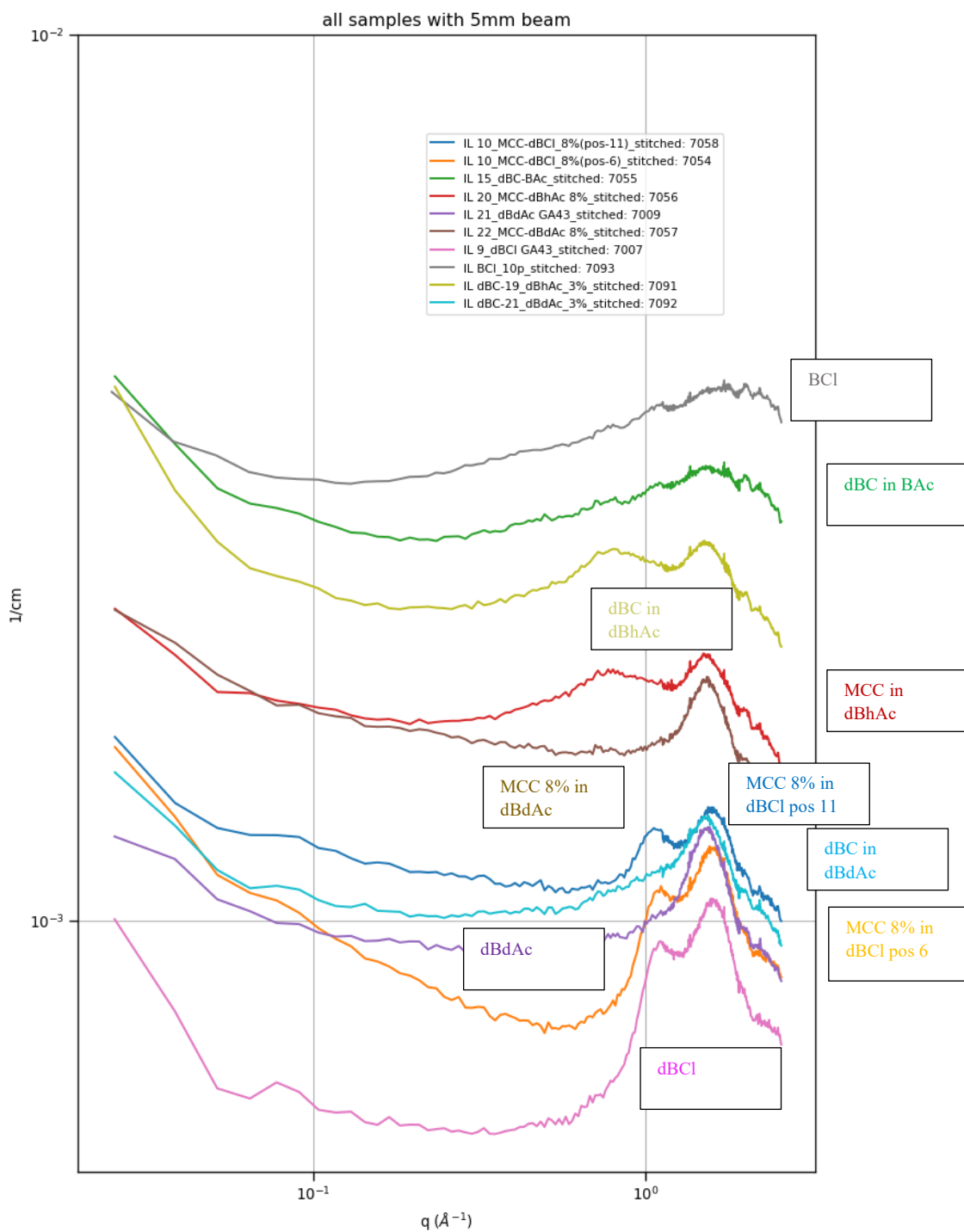


**Figure 4.19:** WANS spectra of solution of MCC and dBC (DBC) cellulose in differently labeled solvents

### 4.2.1.2 All samples with 10 mm beam

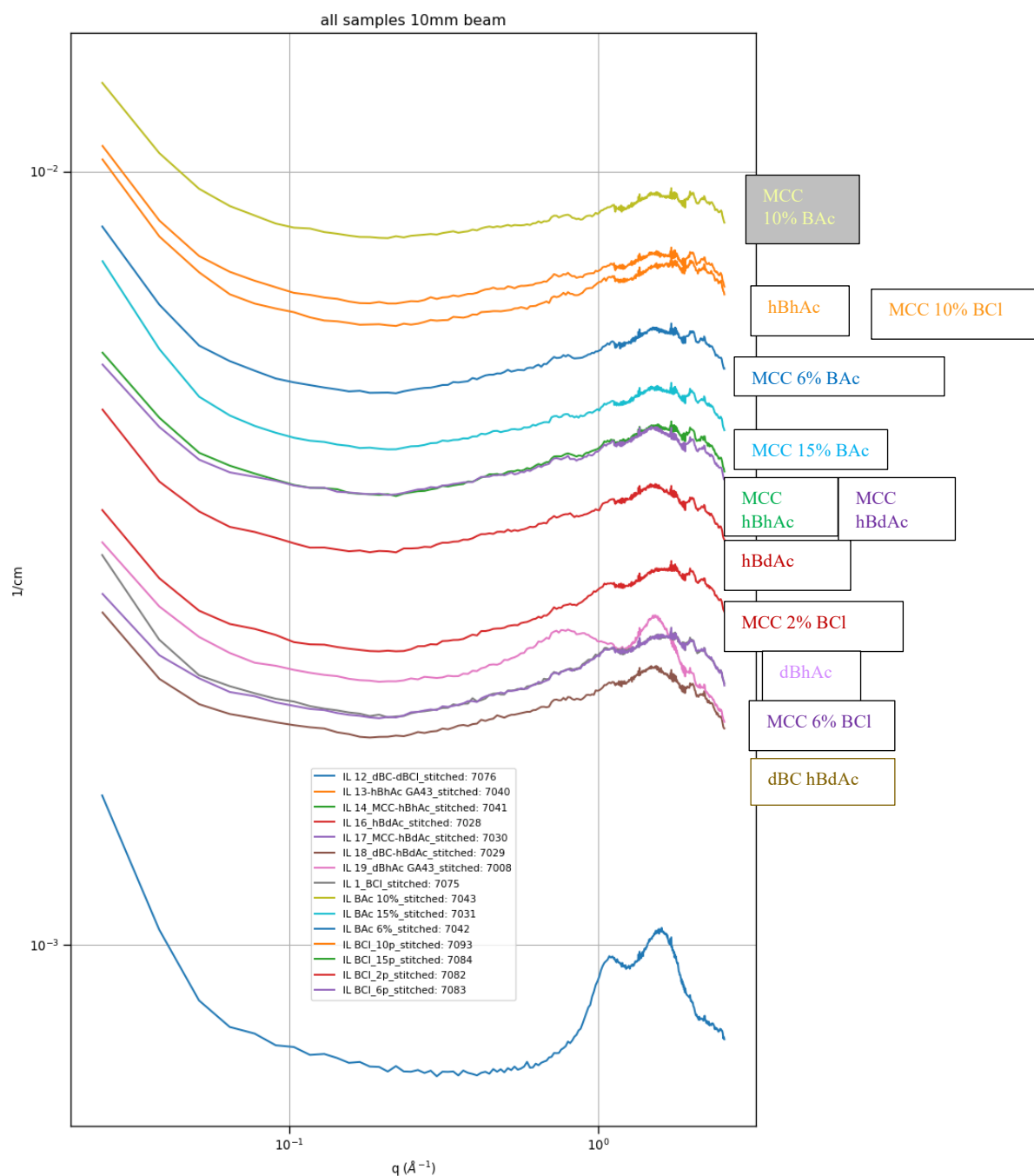


**Figure 4.20:** WANS spectra of solution of MCC and dBC cellulose in differently labeled solvents

**Description.** Here also are few differences between the solvent scattering and the one in presence of MCC. Even for higher concentration, from 2 to 15% of MCC, at least in non-deuteriated solvents, there are no widening.

### 4.2.1.3 Focus on [d-Bmim][h-Ac] series

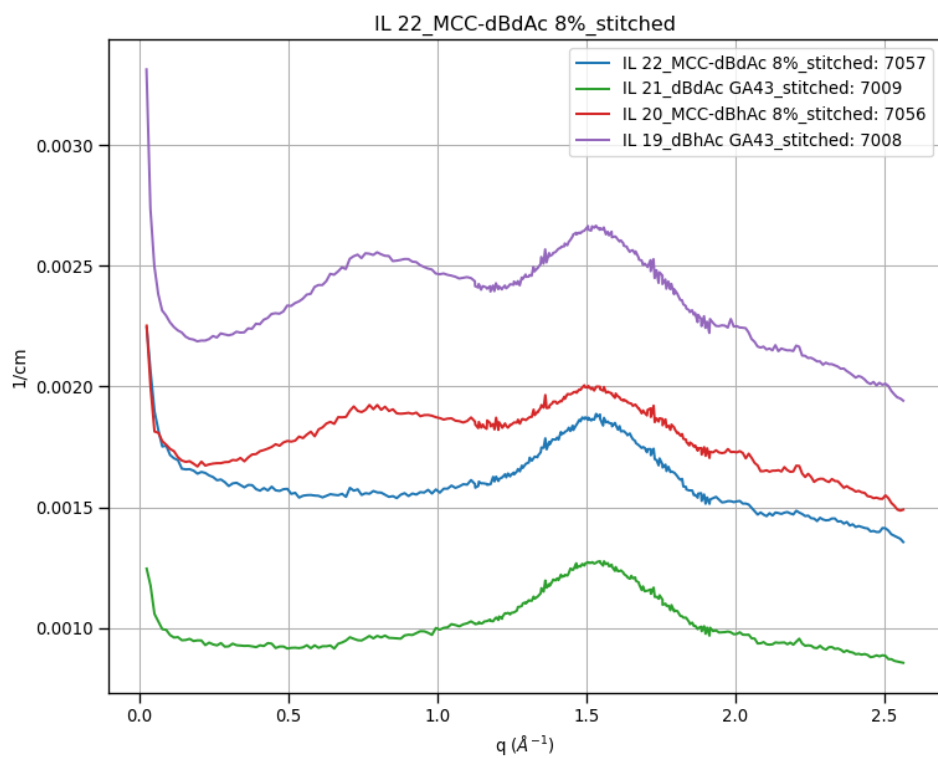


**Figure 4.21 a:** Detail of WANS spectra of solution of MCC 8% in two solvents, [d-Bmim][d-Ac] and [d-Bmim][h-Ac].

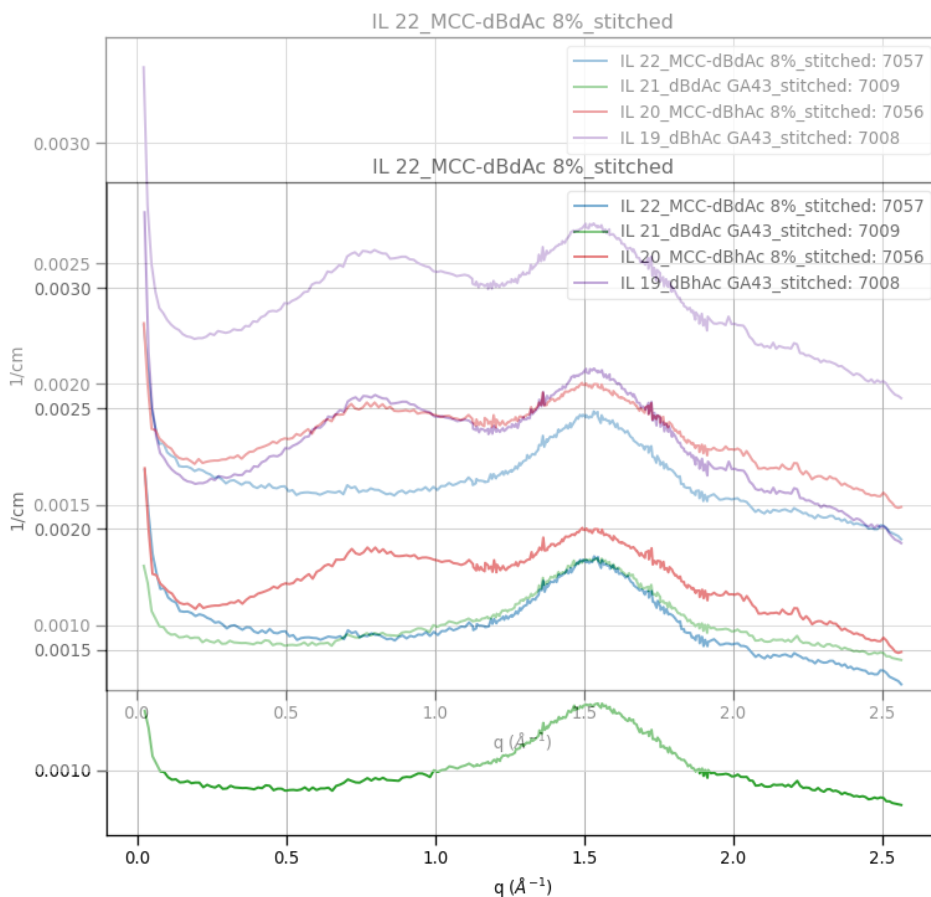


**Figure 4.21 b:** Superposition of WANS spectra of solution of MCC 8% in two solvents, [d-Bmim][d-Ac] and [d-Bmim][h-Ac], enabling us to evaluate the widening of the peaks by the presence of cellulose.

The [d-Bmim][h-Ac] shows two peaks. The large  $q$  peak can be attributed, crudely speaking, to anion-anion, or cation-cation correlations, while the low  $q$  one could be attributed to anion-cation correlations, inside a particular structuration. Such structures have been widely discussed in the literature and are beyond the scope of this work. We simply observe that the peaks are not modified by the presence of MCC cellulose at a concentration of 8%, a part of the fact that the peaks are, clearly, widened (see Figure b, where the plots are supposed).

This widening is reminiscent of WAXS observations of the peak widening, see Chapter 3.

This is the same for [d-Bmim][d-Ac], where there is only one peak visible at the largest  $q$ . At low  $q$ , one must take care of the increase of intensity due to the SANS of cellulose.

### 4.2.2 Summary

The main results are:

- the different labeling of the solvent induces clearly different profiles: one or two peaks, more or less narrow.
- the changes induced by cellulose are small, except for a progressive widening of the peaks.
- Thus the correlations between ions are modified very mildly.
- **before further detailed analysis, we cannot conclude on the existence of any important association between cellulose and the ions of the ionic liquids.**

### 4.3 Conclusion

SANS measurements in differently labeled ionic liquids appear as an interesting use of deuteration. However, they suffer of a very weak contrast and scattering. The different extrapolations could be achieved within great uncertainty. Altogether, the general picture is however consistent: SANS supports our work with SAXS, in particular the extraction of  $P(q)$  from very low scattering as well. Higher concentrations should be used with SANS to prove that  $P(q)$  remains the same. This requires higher concentrations of deuterated bacterial cellulose, dBC, difficult to attain, and needing supplementary chemical treatment.

WANS also in the same labeled ionic liquids appear useful here. The results appear as of good quality. After a first crude analysis, they do not show any strong enough contribution of an additional correlation in presence of cellulose chains, except for only a widening of the peaks. The latter can be interpreted as a partial disorganization of the structure around the chains. More refined analysis could be attempted.

## References

- Benmouna, M., Hammouda, B., **1997**. The zero average contrast condition: Theoretical predictions and experimental examples. *Progress in Polymer Science*. 22(1), 49–92.  
[https://doi.org/10.1016/S0079-6700\(96\)00004-4](https://doi.org/10.1016/S0079-6700(96)00004-4)
- Essafi, W., Spiteri, M.-N., Williams, C., Boué, F., **2009**. Hydrophobic Polyelectrolytes in Better Polar Solvent. Structure and Chain Conformation As Seen by SAXS and SANS. *Macromolecules*. 42(24), 9568–9580. <https://doi.org/10.1021/ma9003874>
- Gummel, J., Cousin, F., Boué, F., **2008**. Structure Transition in PSS/Lysozyme Complexes: A Chain-Conformation-Driven Process, as Directly Seen by Small Angle Neutron Scattering. *Macromolecules*. 41(8), 2898–2907. <https://doi.org/10.1021/ma702242d>
- Nöjd, S., Hirst, C., Obiols-Rabasa, M., Schmitt, J., Radulescu, A., Mohanty, P.S., Schurtenberger, P., **2019**. Soft particles in an electric field – a zero average contrast study. *Soft Matter*. 15, 6369–6374. <https://doi.org/10.1039/C9SM01208G>
- Raghuwanshi, V.S., Cohen, Y., Garnier, Guillaume, Garvey, C.J., Russell, R.A., Darwish, T., Garnier, Gil, **2018**. Cellulose Dissolution in Ionic Liquid: Ion Binding Revealed by Neutron Scattering. *Macromolecules*. 51(19), 7649–7655. <https://doi.org/10.1021/acs.macromol.8b01425>
- Remsing, R.C., Petrik, I.D., Liu, Z., Moyna, G., **2010**. Comment on “NMR spectroscopic studies of cellobiose solvation in EmimAc aimed to understand the dissolution mechanism of cellulose in ionic liquids” by J. Zhang, H. Zhang, J. Wu, J. Zhang, J. He and J. Xiang, *Phys. Chem. Chem. Phys.*, **2010**, 12, 1941. *Phys. Chem. Chem. Phys.* 12, 14827.  
<https://doi.org/10.1039/c004203j>
- Remsing, R.C., Swatloski, R.P., Rogers, R.D., Moyna, G., **2006**. Mechanism of cellulose dissolution in the ionic liquid 1-n-butyl-3-methylimidazolium chloride: a  $^{13}\text{C}$  and  $^{35/37}\text{Cl}$  NMR relaxation study on model systems. *Chem. Commun.* 1271–1273. <https://doi.org/10.1039/B600586C>
- Zhang, Jinming, Zhang, H., Wu, J., Zhang, Jun, He, J., Xiang, J., **2010a**. NMR spectroscopic studies of cellobiose solvation in EmimAc aimed to understand the dissolution mechanism of cellulose in ionic liquids. *Phys. Chem. Chem. Phys.* 12, 1941-1947.  
<https://doi.org/10.1039/b920446f>
- Zhang, Jinming, Zhang, H., Wu, J., Zhang, Jun, He, J., Xiang, J., **2010b**. Reply to “Comment on ‘NMR spectroscopic studies of cellobiose solvation in EmimAc aimed to understand the dissolution mechanism of cellulose in ionic liquids’” by R. C. Remsing, I. D. Petrik, Z. Liu and G. Moyna, *Phys. Chem. Chem. Phys.*, **2010**, 12, DOI: 10.1039/c004203j. *Phys. Chem. Chem. Phys.* 12, 14829. <https://doi.org/10.1039/c005453b>

<b>Chapter 5: DIFFERENT SITUATION OF DISSOLUTION ....</b>	<b>171</b>
<b>5. 1 Swelling gradient measurements using SAXS (SWING) .....</b>	<b>171</b>
5.1.1 Method .....	171
5.1.2 Results .....	172
<b>5.2 Conclusion .....</b>	<b>177</b>
<b>Supporting information.....</b>	<b>178</b>



## Chapter 5: Different situations of dissolution

### 5. 1 Swelling gradient measurements using SAXS (SWING)

#### 5.1.1 Method

We undertook a series of measurements in which a particular type of cellulose film was subject to dissolution owing to a particular type of process. The cellulose film was evaporated from a suspension of nanocrystals, showing a cholesteric order, such that the film was iridescent (see **Figure 5.1**). It was kindly provided by Benoit Duchemin, Université Le Havre, with whom we imagined this experiment. It was suspended and dipped in the solvent – either BmimAc or BmimCl, by its bottom end, as shown in **Figure 5.1**. We waited long enough - under heating in an oven at T around 70 °C, to let the ionic liquid diffuse and create a spatial gradient of swelling over a few mm. The wet part was transparent until the limit with the dry part.

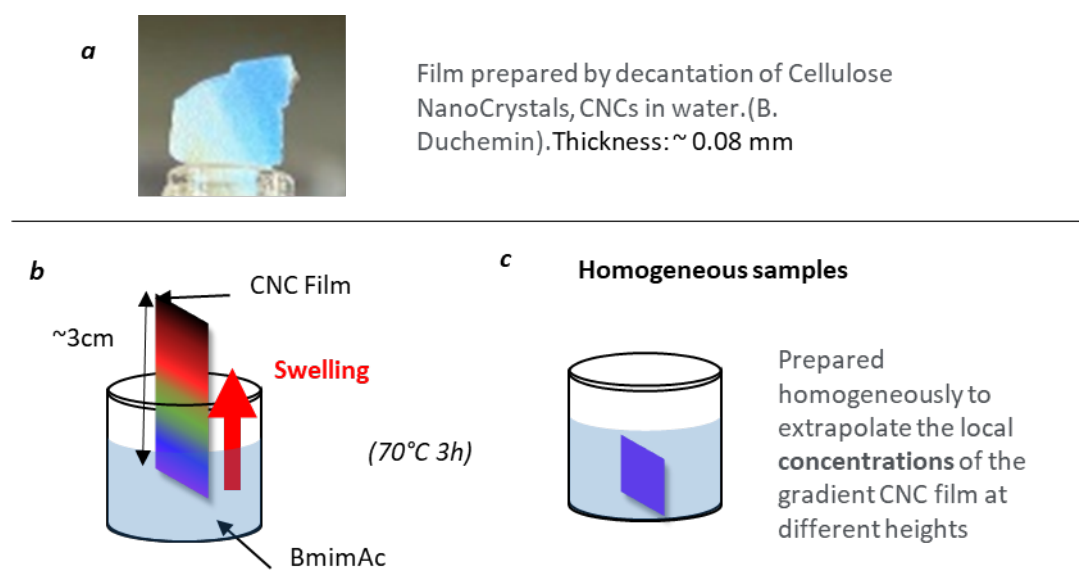


**Figure 5.1:** a) Photo of the piece of film, showing iridescence. b) Dipping experiment. c) Comparison with normal swelling.

The film was then suspended on a support and placed in front of the beam, of height between 100 and 200  $\mu\text{m}$ , depending on the session, and 100  $\mu\text{m}$  wide. It was then moved vertically

enabling a measurement each 200  $\mu\text{m}$  along the sample (see **Figure 5.2**). We must keep in mind that it could absorb water, before and during the measurement.

### 5.1.2 Results

**Figure 5.2** a, b, c, d, shows, for swelling in BmimAc (the ionic liquid the least sensitive to moisture) the SAXS and WAXS. We will see that it is very useful to be able to get information from the two  $q$  ranges together.

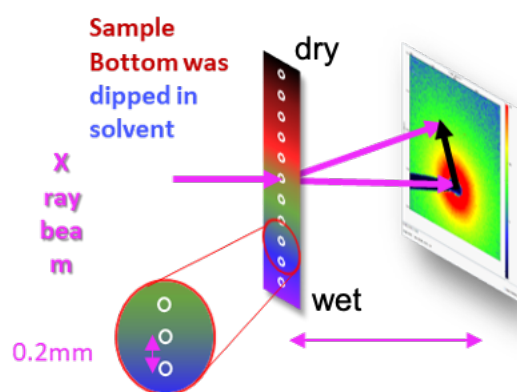
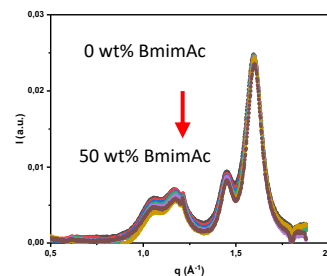
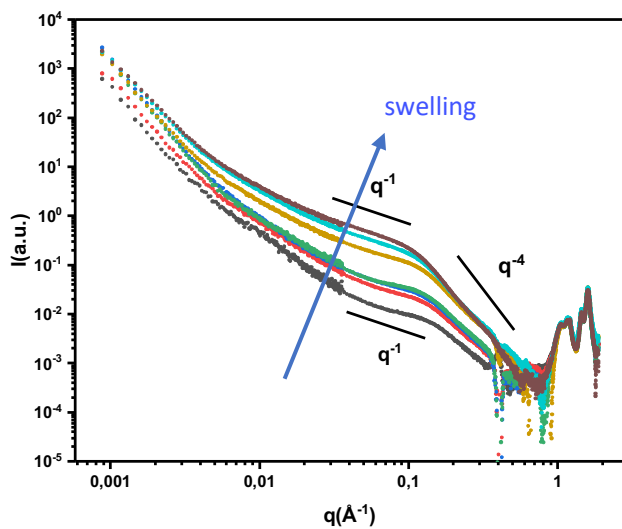
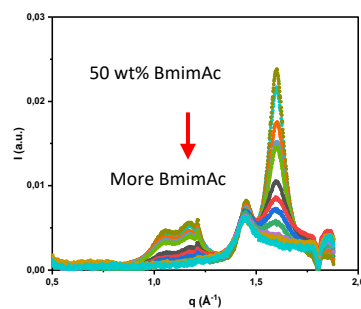
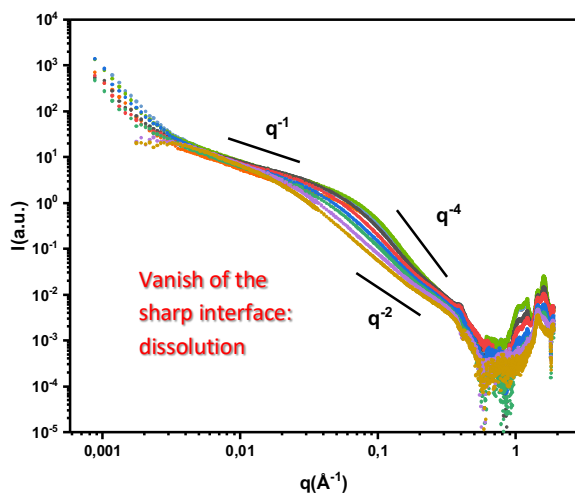


**Figure 5.2** Setup of the SAXS scanning measurement.



a)

b)



c)

d)

**Figure 5.3** SAXS from scanned film. (i) swelling region,  $c < 50\%$ : a) SAXS; b) WAXS shows very little changes. (ii) dissolving region,  $c > 50\%$ . c) SAXS; d) WAXS shows the dissolution of crystals.

## Description

In dry state, the black curve shows a low  $q$  upturn due to heterogeneity of the sample, and at larger  $q$ , a  $q^{-1}$  and a shoulder probably linked to the rod shape of the nanocrystal, with a radius  $\sim 10 \text{ \AA}$  (this is not the chain radius).

During swelling, two stages can be distinguished:

- In a first step, the WAXS stays constant
- Meanwhile, at the same time, the SAXS signal increases strongly during dilution. This is counterintuitive if we think of dilute solutions, but here we start from a fully concentrated solution (100%) in the dry state: the growing regions, at the origin of the scattering, are the one which contain mainly solvent. They probably contain individual chains, since the characteristic shoulder appears around  $q = 0.04 \text{ \AA}^{-1}$ . The curves have the same profile than the ones for the biphasic system analyzed for cellulose solutions above 20% concentration in BmimAc (and 7% in our measurements in BmimCl). They could be fitted similarly to a Debye-Bueche (or Debye-Anderson-Braumberger) profile for  $10^{-2} \text{ \AA}^{-1} < q < 10^{-1} \text{ \AA}^{-1}$  plus a rod scattering at large  $q$  ( $q > 10^{-1} \text{ \AA}^{-1}$ ). At the lowest  $q$  a power law is observed, close here to -1. It corresponds to the shape of the microphase.
- In a second step, above a degree of swelling corresponding to a concentration of 50%:
  - o the WAXS decreases: more and more crystals are dissolved; the width of the peaks should be better analyzed to see whether the crystal width decreases.
  - o meanwhile the SAXS still increases. The medium still display separated phases, while it contains both some crystals, but chain dissolution has started. Remember a similar situation was observed in BmimAc at 40% concentration.
  - o then, the evolution of the SAXS is reversed: it decreases. The crystal vanishes completely on the WAXS curve. Our interpretation is that the dilution goes on and the volume fraction of the rich phase annihilates. We return towards a monophasic system, which is progressively dissolved. However, we do not observe the scattering from a solution of individual chains, because the concentration is still too high.

The data can be compared with homogeneously swollen samples, made by letting small pieces of films in contact with the solvent on all their surface for a long time. We observed that the scattering is very similar, so that we propose to use them for calibration. However homogeneous swelling is only possible for low enough concentrations,  $c < 40\%$  - rejoining the former measurements in capillaries. Large concentrations are accessible only with the gradient experiment.

In our opinion, these systems are very dependent on the conditions of their formation, which involve kinetics, and sensitivity to moisture and water content.

This is why we display below other measurements which turn out to show different trends. They concern gradient swelling of the same CNC films by BmimAc and BmimCl.

In Figure 5.4, the scattering is continuously increasing, there is no dissolution of the phases. Moreover, we observe a  $q^{-1}$  only at intermediate degree of swelling, not for the final one, but only at intermediate swelling.

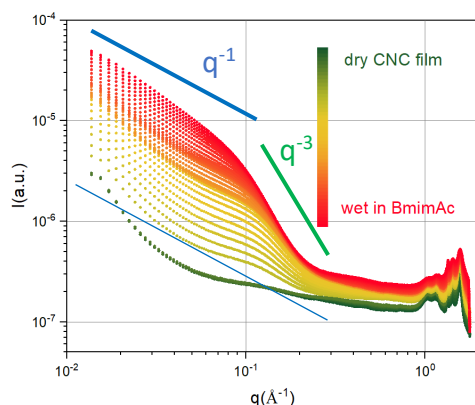


**Figure 5.4:** Scattering of cellulose nanocrystal film swollen in BmimAc (no Kapton wall). Slopes are indicative only.

Such apparent power laws have been observed formerly, for BmimCl solutions for example (with temperature dependence, see Chapter 3, Effect of temperature). Note that crystals are present in this case.

Two other cases are shown below. In **Figure 5.5**, for BmimAc, again no “re-decrease” of the scattering is observed in the small  $q$  range. The crystal peaks progressively vanish in WAXS. The sizes obtained for the biphasic medium are even larger, reaching more than 100 Å.

Using BmimCl as a solvent (**Figure 5.5 b**), we see a similar evolution, but the final shape shows two oscillations (as observed in SI 2).

We propose that water content is preventing dissolution towards a monophasic state, the system being arrested due to gelation.

Further analysis is required to understand the implications of these findings.

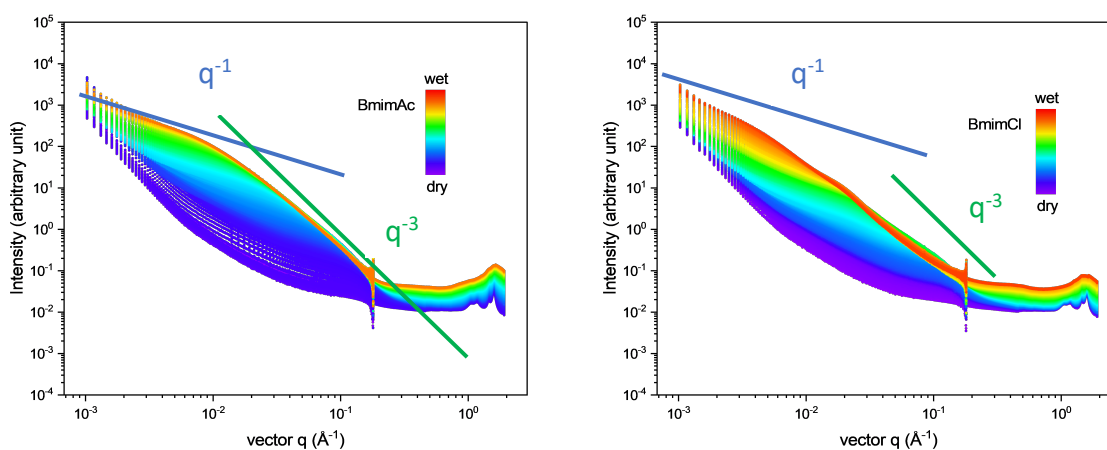


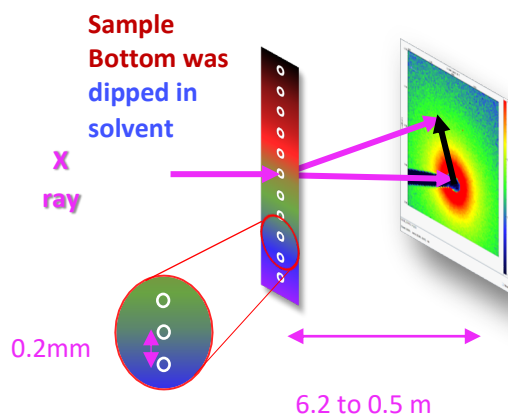
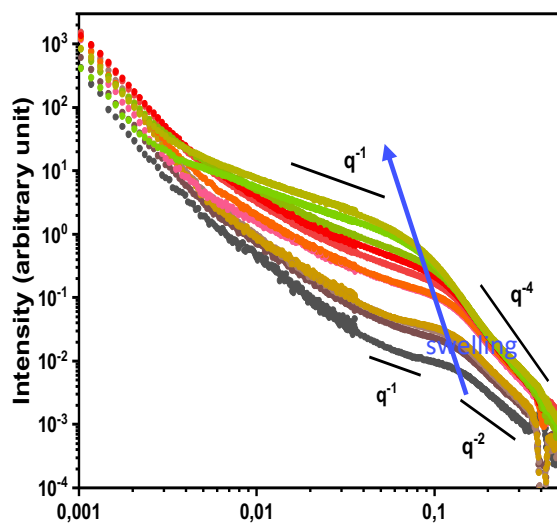
**Figure 5.5:** Scattering of swollen cellulose nanocrystal film: a) left, using BmimAc (no Kapton wall, no solvent ionic liquid subtraction), Slopes are indicative only; b) right, using BmimCl, shoulders in the profile can be seen for most wet area.

## 5.2 Conclusion

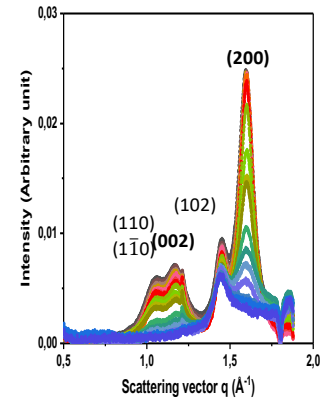
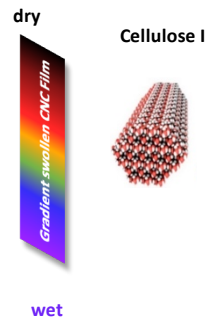
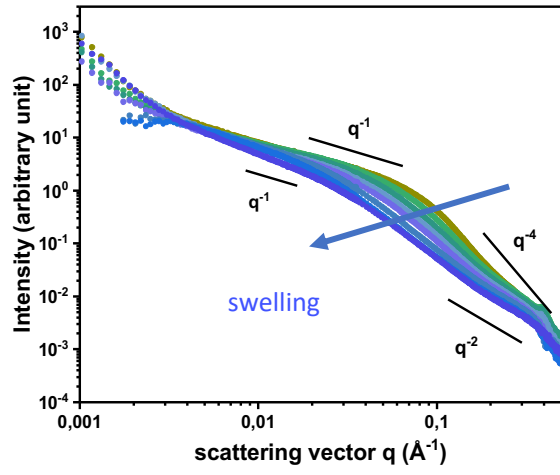
These measurements enabled us to approach the problematics of dissolution of cellulose in a particular case of a film of nanocrystals. It shows the potential of SAXS to monitor these behaviors, which can be interesting from a material science point of view, showing the large variety of structures which cellulose can lead to. They, however, present often the biphasic behavior, with a low  $q$  profile, linked to the organization at larger scale, which varies. One of the questions to solve is the coexistence of crystals and concentrated phase, seen also in capillaries ( $c = 40\%$ ), which confirms our results.

## Supporting information

5. **Figure SI 1:** BmimAc swelling gradient of a CNC film. Supplementary plots for case 1: same sample as in Figure 5.3.







## SI 2: Acoustic levitation

Using levitation, a droplet of MCC in BmimAc was kept in the beam. Soon it appeared that this droplet was absorbing the water from atmosphere. The final state of the droplet was gel-like (elasticity at the 10 sec scale). Intriguingly, we obtain a scattering characteristic of spherical objects of well-defined size, or of lamellar structure.

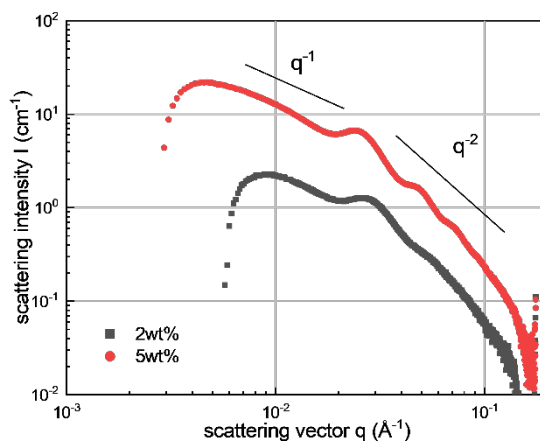


**Figure SI 2:** Scattering from droplet of cellulose concentration 2 and 5 wt%, after exposure to atmosphere in a levitation device (typical duration of 10 min).

## Conclusion

Cellulose chains solutions are not yet fully understood. In particular, while there have been many studies in aqueous solvents, by scattering of light, and a few small angle X rays and neutron scattering, there are few in Ionic Liquids (IL), although these solvents are industrially promising, and as we saw, less subjected to aggregation/gelation problems than in aqueous solvents. In this thesis, we have focused on the single chain and inter-chain scattering of cellulose to understand its conformation and spatial distribution in ionic liquids.

### Difficulties

Let us first summarize the **different choices and difficulties** in this work.

We chose Butyl-methyl-Imidazolium Acetate and Chloride (BmimAc and BmimCl); they appear the most suitable IL from our literature search, in particular in terms of maximum concentration ( $c > 10\%$ , in weight of cellulose / weight of solvent) attainable in clear solutions. We mostly used MicroCrystalline Cellulose (“MCC”, Avicel PH101), but could undoubtedly confirm results with very similar ones from Rayon, dissolved Cellulose NanoCrystals (CNC), and Bacterial Cellulose (Nata de Coco) at large  $q$  (short distance).

After rheometric detection of the overlapping concentration  $c^*$ , we used Small-Angle Scattering (SAS) techniques (SANS and mostly SAXS in capillary cells). That allowed to construct, through great effort to treat the very low scattering intensity (choice of spectrometers configuration, type of container, care of moisture and water content...), a reproducible description of chain structure in the solution. The observations included the single chain form factor in dilute solution, the structure factor in the semidilute solution and biphasic cellulose dissolution at higher concentration in ionic liquids, BmimAc and BmimCl.

We also used Wide Angle X-ray Scattering (WAXS) to detect the cellulose crystals in ionic liquids. The very frequent observation that the crystal scattering is absent proves that the cellulose can be completely dispersed in ionic liquids solvent below a certain concentration (e.g. until 15 wt% MCC in BmimAc).

To avoid the effect of water in the cellulose chain conformation studies, effect of the different water contents was studied to check chain conformation changes at a different cellulose concentration. For BmimAc, adding 1 wt% of water has no effect for the 1 wt% cellulose dissolution. Moreover, temperature had no effect. For BmimCl, the cellulose solution is more

sensitive to water: even for 1 wt% of water, we observed, together with a high aggregation at low  $q$ , a clear effect in the middle of the  $q$  range even for the lowest cellulose concentration (1 wt%). Such phase separation, for BmimCl, was very sensitive to temperature. In all cases, sensitivity to water increases with concentration.

However, under the conditions of preparation (heating at 70 °C for BmimAc and 90 °C for BmimCl) the scattering could be made reproducible, using many successive measurements at different dates and using different spectrometers in different facilities, with a majority at SWING (SOLEIL).

## Main results

Let us now **summarize the main results, namely about the chain spatial distribution** of cellulose using small and wide angle X-Ray and neutron scattering:

- for the dilute concentration ( $c < c^*$ ), in BmimAc, we showed that the single chain cellulose scattering agrees with the one of a long and thin chain, which **form factor** is considered as the one of a cylinder: more precisely, a core-shell cylinder, with a 5 Å diameter and 5 Å shell at local scale accounting for the “shoulder” of the SAXS curve. For the large scale, at low  $q$ , it is close to a semiflexible chain, which gives a Kuhn length  $L_K$  shorter than 200 Å, hence a persistence length  $L_p = L_K/2$  shorter than 100 Å. This value lies in the range of values formerly proposed for aqueous solvents and one IL. This determination is perturbed by a slight aggregation (which strength however lies within the lowest range of the ones of former measurements) by other groups (mostly in aqueous solvents).
- for  $c > c^*$ , in BmimAc, the more numerous cellulose chains start to interpenetrate with each other. The SAXS scattering slope decreases strongly at low  $q$ . We could describe this by the moderate inter-alignment of the cellulose chains with increasing concentrations, using a **2D structure factor model** (D. Constantin) of soft repulsion. This is a **new contribution in the field**.
- for higher cellulose concentration (20 wt%  $< c < 30$  wt%), a more complex situation can be analyzed, starting with concentrations where no cellulose crystals can be found in the dissolutions. The upturn of the SAXS curve at low  $q$ , suggests that the cellulose solution exists in two phases of different local chain concentrations, which shows the liquid-liquid phase separation phenomenon.

- with increasing cellulose higher than 30 wt%, in coexistence with the diphasic structure, the cellulose crystals can be found in the cellulose dissolution, which indicate that cellulose does not completely dissolve above a certain cellulose concentration.
- this was confirmed with studies of CNC films presenting a swelling gradient, allowing to reach very high concentrations, and follow dissolution kinetics.

For solutions in BmimChloride, the scattering is very similar at low concentration, which very satisfyingly confirms our results, whilst higher concentrations show phase separation, and even presence of remaining crystals. This is probably due to the high hygroscopy of BmimCl (high affinity of chloride ion for water, and maybe to H bond basicity). Mixtures of IL and DMF were briefly studied and showed the same chain scattering at medium  $q$ .

To establish our geometrical model, we employed Small Angle Neutron Scattering applying the zero **deuterated fraction extrapolation and the Zero Average Contrast (ZAC methods** to study the single cellulose chain at 2 wt% cellulose solution (i.e. in semidilute), in [d-Bmim][h-Ac]/[h-Bmim][h-Ac] mixtures. This involved **synthesis of deuteriated solvents**, with deuteration of either the cation or the anion, and the use of deuteriated cellulose, dBC (also noted DBC).

For the single chain of 2 wt% (semidilute solution), that gives the similar result with 5 Å core and 5 Å shell cylinder, while the scattering is even lower than SAXS. Within the possible (low) accuracy, by comparing the SAXS/SANS curves, and through the effort in getting  $S_1(q)$ , our claims are confirmed.

Finally, we used the deuteration of either the cation or the anion to track short scale spatial correlations in some cellulose solutions, using **Wide Angle Neutron Scattering, without visible effect except enlargement of the WANS peaks**, showing the increase of disorder in the Ionic Liquid structure. Hence, we do not detect strong adsorption of any ions on the chain, except through the assumption of sheath of lower Scattering Length Density prompted by the SAXS analysis in the shoulder  $q$  region.

## Perspectives

Concerning the **perspectives** of this work:

1. About the **core shell** model, more should be done applied to several different solvent in WAXS and SAXS. In our case, better subtraction by understanding the **ionic liquid peak variation** with different cellulose concentrations or by using a solvent with no such strong peaks at large  $q$ . As said above, the assumption of a sheath of lower SLD meets all controversies about the close presence of some of the solvent moieties. One could also think of more evolved shape models.

2. In the same line of thoughts, measurements with **short chains** would be useful to confirm the cylinder model, if we can fit the whole form factor including the Guinier range.

3. More studies on separated phases at high cellulose concentration are promising:

-3a: **coexistence** of crystals with phase separation should be given more attention. How do chains and crystals interact? How does dissolution proceed?

-3b: **dynamics/kinetics** of evolution with time should shed more light to know how the system evolves towards dissolution (maybe work with high temperature).

-3c: this hits the studies of regeneration processing by strong addition of water (attempted on ID02, data to treat) with relation with the industrial processing, to connect structure and performance of the final cellulose product. As seen in end of the chapter 3, interesting **fractal-like structures** appears in different temperature and moisture conditions.

-3d: this is also linked with **gelation**, under atmospheric moisture. Are these structures jammed, or kinetically blocked (“arrested”), how can they evolve? For example, measurements of droplets in levitation on SWING showed interesting - completely different, signals.

4. **Rheology**, to know whether the chains **align** or not - as suggested by rheo-softening at large shear rate, should be developed, more precisely rheo-SAXS. First tests at SWING were handicapped by atmospheric moisture. Rheological properties are interesting, in particular for spinning of textile fibers.

5. **Other scattering techniques** should be explored. **Static Light Scattering** could access the persistence length ranges; it was partially perturbed by the aggregation in many former experiments, but BmimAc may be more favorable in view of the medium  $q$  scattering (low  $q$  shows more or less strong upturns). If this is satisfying, one could monitor  $L_p$  as a function of the solvent structure. **Dynamic Light Scattering - DLS** maybe easier, since acquisition is relatively simple.

**Small Angle Neutron Scattering** gave very weak scattering intensities, due to contrast problems. Increasing the concentration is very difficult for the **deuteriated cellulose**, the solutions of which are extremely viscous (long chains, aggregation). To reduce their length, sonication showed inefficient, up to completion of a total of 2 hours of actual sonication. Ball milling is impossible in view of the small quantities available, or expectable from new syntheses. Acid hydrolysis seems an easier way to be attempted, but this must be discussed with experts.

To **conclude**, by the structural knowledge of cellulose solution in ionic liquids, the research work of this thesis aids in paving the way towards innovative applications of cellulose, contributing to the field of sustainable material science and technology, supporting the transition towards more environmentally friendly material science practices.